

**POLYMER MEMBRANES FOR THE SEPARATION OF COMPLEX
NATURAL HYDROCARBON FEEDS**

A Dissertation
Presented to
The Academic Faculty

by

Ronita Mathias

In Partial Fulfillment
of the Requirements for the Degree
Doctor of Philosophy in the
School of Chemical and Biomolecular Engineering

Georgia Institute of Technology
August 2021

COPYRIGHT © 2021 BY RONITA MATHIAS

POLYMER MEMBRANES FOR THE SEPARATION OF COMPLEX NATURAL HYDROCARBON FEEDS

Approved by:

Dr. Ryan P. Lively, Advisor
School of Chemical and Biomolecular
Engineering
Georgia Institute of Technology

Dr. J. Carson Meredith
School of Chemical and Biomolecular
Engineering
Georgia Institute of Technology

Dr. Christopher W. Jones
School of Chemical and Biomolecular
Engineering
Georgia Institute of Technology

Dr. Elsa Reichmanis
School of Chemical and Biomolecular
Engineering
Lehigh University

Dr. M.G. Finn
School of Chemistry and Biochemistry
Georgia Institute of Technology

Dr. Will R. Gutekunst
School of Chemistry and Biochemistry
Georgia Institute of Technology

Date Approved: [June 29, 2021]

To my lifelong pillars of support, my parents, Veronica Monis and Ronald Mathias

ACKNOWLEDGEMENTS

Graduate school has gone by in the blink of an eye, and my fond memories of it are inevitably linked with those who supported me throughout and those I met along the way. My journey could not have begun without my parents' encouragement to pursue my passion for chemical engineering from a young age. Many sacrifices were made for me to be where I am today, and their unwavering support made the arduous days easier to overcome. My brother, Aaron, five years younger than me, deserves credit for lending me his ear when I needed it the most and surprising me with his wisdom.

I want to thank my advisor, Dr. Ryan Lively, for his constant guidance and willingness to discuss research problems. He took me in when I was a stumbling first-year and had not yet fully appreciated the immensity and importance of doctoral research and its trials and tribulations. Ryan's kind and optimistic direction provided much-needed consolation during my many research failures. I am eternally grateful for the opportunity to have been advised by him and to have been a part of the Lively lab.

I would like to thank my thesis committee, Dr. MG Finn, Dr. Chris Jones, Dr. Elsa Reichmanis, Dr. Carson Meredith, and Dr. Will Gutekunst, for their technical assistance and guidance. I would also like to thank ExxonMobil Research and Engineering for their generous funding and regular feedback and discussion. I received especially helpful advice and direction from Dr. Benjamin McCool, Dr. Dhaval Bhandari, Dr. JR Johnson, and Dr. Neel Rangnekar.

The members of the Lively lab have made a lasting impact on me, and while I will refrain from naming every single one who helped me with experiments or engaged in technical discussions with me, I would like to particularly thank Dr. Melinda Jue, Dr. Yao Ma, Dr. Richelle Lyndon, and Hye Youn Jang for their friendship and for keeping me lighthearted. I would also like to thank Dr. Nick Bruno and Dr. Kirstie Thompson, whom I worked closely with and from whom I learned much more than I could have imagined.

My acknowledgements would be incomplete without recognizing Katie Tomassetti, Samudra Nair, and Kimberly Dean for giving me warmth, making me laugh, and checking in with me even when I was deep in the trenches of lab work and the outside world would seemingly cease to exist.

TABLE OF CONTENTS

ACKNOWLEDGEMENTS	iv
LIST OF TABLES	vii
LIST OF FIGURES	ix
SUMMARY	iv
CHAPTER 1. Introduction	1
1.1 The Future of Separation Science	1
1.2 Separation Technology in Complex Petrochemical Separations	2
1.3 Membranes for Crude Oil Separations	3
1.4 Organic Solvent Nanofiltration (OSN) and Organic Solvent Reverse Osmosis (OSRO)	4
1.5 Research Objectives	5
1.5.1 Thin Film Composite Polymer Membranes for Liquid Hydrocarbon Separations	5
1.5.2 Complex Organic Solvent Transport in Polymer Membranes	6
1.5.3 Continuous Hollow Fiber Membrane Fabrication	8
1.6 Dissertation Overview	10
1.7 References	11
CHAPTER 2. Background and Theory	14
2.1 Overview	14
2.2 Liquid Transport in Polymer Membranes	14
2.2.1 Membrane Transport Mechanisms	14
2.2.2 Defining and Evaluating OSN Transport	17
2.2.3 Sorption	20
2.2.4 Diffusion	22
2.2.5 Maxwell-Stefan Transport	23
2.3 Polymers of Intrinsic Microporosity and their Derivatives	24
2.4 Polymer Hollow Fiber Spinning	28
2.4.1 Developing the Polymer Dope	28
2.4.2 Spinning Process Parameters	30
2.5 Dip Coating	34
2.5.1 Dip Coating Defects	36
2.6 References	40
CHAPTER 3. Materials and Experimental Methods	45
3.1 Overview and Collaborator Acknowledgements	45
3.2 Materials	46
3.3 Monomer Synthesis	47
3.4 Polymer Synthesis	54
3.5 Polymer Material Characterization	60

3.5.1	Gel Permeation Chromatography	60
3.5.2	Nuclear Magnetic Resonance Spectroscopy	60
3.5.3	Thermogravimetric Analysis	62
3.5.4	Dynamic Scanning Calorimetry	62
3.5.5	Gas Physisorption	62
3.5.6	Helium Pycnometry	62
3.5.7	Hydrocarbon Vapor Sorption	63
3.5.8	Polymer Solution Viscosity	63
3.6	Polymer Model Generation	63
3.7	Polymer Model Analysis	68
3.8	Computational Polymer Swelling	68
3.9	Membrane Fabrication and Housing	69
3.9.1	Dense Films	69
3.9.2	Flat Thin Film Composites	69
3.9.3	Spiral Wound Modules	72
3.9.4	Hollow Fiber Spinning	74
3.9.5	Roll-to-Roll Dip Coating on Hollow Fibers	75
3.9.6	Hollow Fiber Module Fabrication	75
3.10	Membrane Material Characterization	76
3.10.1	Scanning Electron Microscopy	76
3.10.2	Hydrocarbon Liquid Sorption	77
3.10.3	Atomic Force Microscopy (AFM)	77
3.11	Membrane Performance	77
3.11.1	Flat Sheet Membrane Performance	77
3.11.2	Hollow Fiber Membrane Performance	83
3.12	References	85
CHAPTER 4. The Effect of Spirocyclic Polymer Structure on Porosity and Swelling		87
4.1	Overview	87
4.2	Spirobifluorene Aryl Diamine (SBAD) Series	87
4.2.1	Design and Synthesis of SBAD Polymers	87
4.2.2	SBAD Powder Characterization	91
4.2.3	Computational SBAD Porosity Analysis	96
4.2.4	Computational SBAD Swelling	106
4.3	DUCKY Series	108
4.3.1	Design and Synthesis of DUCKY Polymers	108
4.3.2	DUCKY Powder Characterization	109
4.4	Summary	112
4.5	References	114
CHAPTER 5. Investigating the Membrane-Based Liquid Hydrocarbon Separation Performance of Novel Spirocyclic Polymers		116
5.1	Overview	116
5.2	Spirobifluorene Aryl Diamine (SBAD) Series	116
5.2.1	Dilute Hydrocarbon Separations	116
5.2.2	Complex Hydrocarbon Separations	123

5.3	DUCKY Series	134
5.3.1	Dilute Hydrocarbon Separations	134
5.3.2	Complex Hydrocarbon Separations	142
5.4	Summary and Conclusions	145
5.5	References	147
 CHAPTER 6. Using a Maxwell-Stefan Model to Predict Complex Liquid Hydrocarbon Transport in PIM-1 and SBAD-1		149
6.1	Overview	149
6.2	Introduction	149
6.3	The Maxwell Stefan Transport of Mixed Feeds	153
6.3.1	Volume-based Maxwell-Stefan Model	153
6.3.2	A New Sorption Model: Langmuir + Flory-Huggins	156
6.3.3	Liquid Hydrocarbon Polymer Diffusivity	160
6.4	Simulation and Parameter Fitting of Modeling Framework	163
6.4.1	Sorption Models	163
6.4.2	Penetrant-Polymer Diffusivity, $D_i, n + 1, m$	164
6.4.3	Multi-component Transport Simulation Framework	166
6.5	Pure Molecule Sorption and Diffusion Fits	170
6.6	Predicting Multicomponent Sorption in Polymers	178
6.7	Predicting Multicomponent Transport in PIM-1 and SBAD-1	180
6.8	Conclusions	189
6.9	References	193
 CHAPTER 7. Fabrication of Modular PIM-1 Thin Film Composite Membranes via a Scalable Roll-to-Roll Coating Process		197
7.1	Overview	197
7.2	Introduction	197
7.3	Fabrication of Torlon® Hollow Fiber Support	200
7.4	Roll-to-Roll Dip Coating	205
7.4.1	The Landau Levich Derjaguin Law	205
7.4.2	Minimizing the Thickness of The Film Coating	208
7.4.3	Estimating the Marangoni Thickening Factor	211
7.5	Thin Film Composite Separation Analysis	214
7.6	Conclusions	217
7.7	References	218
 CHAPTER 8. Conclusions and Future Work		221
8.1	Overview	221
8.2	Conclusions and Impacts	221
8.3	Future Work	223
8.3.1	Long-term Membrane Performance in Natural Crude Streams	223
8.3.2	Extending the Modelling of OSRO/OSN to Natural Crude Oil Feeds	225
8.3.3	Optimizing the Torlon® Support Fiber Structure	227
8.3.4	Roll-to-Roll Coating of SBAD-1 and MALLARD	228
8.4	References	230

LIST OF TABLES

Table 3.1	Force field atom type and partial charges assigned to the atoms in the models. Monomer and atoms labels refer to the ones reported in Figure 3.13.	67
Table 4.1	Conditions tested for the polymerization of SBAD-1: 1 (0.1 mmol), diamine (0.1 mmol), catalyst (5 mol%), solvent (0.5 mL) for 24h. Reaction 2 was performed at 0.1 M (1 mL dioxane) to prevent gelation.	90
Table 4.2	Characterization of the amorphous polymer models for the four SBAD polymers and PIM-1. For each polymer, results are averaged over three independent models deriving from different initial random packing. The standard deviation is reported in parenthesis. The diameters of the largest included sphere (D_I), largest free sphere (D_F) and largest included sphere along the free sphere path (D_{IF}) are reported, as well as the surface area (SA) with different diameter probes.	98
Table 5.1	Steady-state rejection of a 7-component mixture comprised of six solutes at 1 mol% in a dilute feed mixture in toluene tested at 10 bar over a 66-hour period for SBAD-1 thin film composites formed via spin coating on Matrimid® supports; and steady-state rejection of a 10-component mixture comprised of 9 solutes included at 1 mol% in a dilute feed mixture in toluene tested at 30 bar over a 24-hour period for SBAD-1 thin film composites formed via roll-to-roll coating on Ultem® supports. Puramem® 280 was tested under the same conditions as described above. The difference in permeance is likely due to differences in film thickness due to the method of production. Negative rejections indicate enrichment of the component in the permeate.	121
Table 5.2	9-component feed mixture that was used as a model for the separation of a middle distillate cut of crude oil and the resulting ratios of concentration in permeate (C_P) over concentration in retentate (C_R) for both membrane coupons and a spiral wound module of SBAD-1.	124
Table 5.3	Percentage enrichment by hydrocarbon class in the permeate from the crude oil feed for SBAD-1 at 55 bar and 130 °C. Enrichment was calculated as the area between cumulative peak volume curves of the permeate and feed as shown in Figure 5.11.	131

Table 5.4	Ethanol permeabilities of the DUCKY series in oligostyrene marker experiments at an applied pressure of 30 bar.	138
Table 5.5	Separation factors for selected molecule pairs from Figure 5.4 and Figure 5.17.	141
Table 6.1	Hansen solubility parameters used to estimate χ_{ij} .(37)(25) Molecules in parentheses were determined as satisfactory substitutes for species that did not have recorded solubility parameters.	160
Table 6.2	Multicomponent separations via SBAD-1 and PIM-1 performed at 22 °C.	181
Table 6.3	Nomenclature for Equations in Chapter 6.	192
Table 7.1	Torlon® hollow fiber spinning parameters in Trial 1. The molecular weight (MW) of PVP used is also highlighted. The reference used Torlon® 4000T-HV while Trial 1 used Torlon® 4000T-LV.	201
Table 7.2	Summary of gas separation analyses of PIM-1 coated Torlon® thin-film composites.	216

LIST OF FIGURES

Figure 1.1	Thin-film composite morphology and size-based OSN/OSRO separation.	6
Figure 1.2	Solution-diffusion mechanism of transport in OSRO separations. In OSRO separations, frictional forces act to couple the diffusivities of molecule pairs such that faster molecules are slowed, and slower molecules are sped up.	8
Figure 1.3	Morphology of a hollow fiber membrane and packed hollow fiber membrane permeation.	9
Figure 2.1	Chemical potential, pressure and activity profiles throughout a membrane based on solution-diffusion and pore-flow modes of transport.	16
Figure 2.2	Example of a molecular weight cut off curve with a MWCO.	20
Figure 2.3	Type II-like isotherm compared to theoretical Dual-Mode and Flory-Huggins sorption isotherms.	21
Figure 2.4	The chemical structure of PIM-1 and derivatives, tetrazole-functionalized (Tz-) and amidoxime-functionalized (37) PIM-1.	27
Figure 2.5	Schematic of a polymer ternary phase diagram. Dotted red lines indicate the path of the one-phase polymer dope during phase inversion of the skin and substructure.	29
Figure 2.6	Formation of a nascent hollow fiber near the spinneret.	32
Figure 2.7	A) Steady state of the dip coating process showing the fluid entrainment followed by solvent evaporation. B) Liquid flow streamlines in the dynamic meniscus region close to the coating bath surface depicting the balance between draining and entraining forces.	35
Figure 2.8	Dip coating in the capillary regime. The substrate is withdrawn slowly enough such that evaporation is faster than the velocity of the drying line. Capillary feeding of the coating solution to the edge of the meniscus results in a buildup of dried coating.	36
Figure 2.9	A) Stripe defect showing alternating horizontal lines of thick and thin coating. B) Schematic of the coffee-ring effect.	37

Figure 3.1	Synthetic pathway toward 7,7'-dibromo-2,2',3,3'-tetramethoxy-9,9'-spirobifluorene (1).	47
Figure 3.13	3,4-dimethoxy-1,1'-biphenyl.	47
Figure 3.14	2-bromo-4,5-dimethoxy-1,1'-biphenyl.	48
Figure 3.15	2,3-dimethoxy-9H-fluoren-9-one.	49
Figure 3.16	2,2',3,3'-tetramethoxy-9,9'-spirobifluorene.	50
Figure 3.17	7,7'-dibromo-2,2',3,3'-tetramethoxy-9,9'-spirobifluorene.	52
Figure 3.7	Reaction scheme for DUCKY series.	54
Figure 3.8	SBAD-1 polymer structure.	55
Figure 3.9	SBAD-2 polymer structure.	56
Figure 3.10	SBAD-3 polymer structure.	57
Figure 3.11	SBAD-4 polymer structure.	58
Figure 3.12	DUCKY series polymer structures and GPC results.	61
Figure 3.13	Representation of the polymer monomers used for building the polymer models, with labelled atoms. A) monomer A for all the SBAD family polymers B-E) monomer B for SBAD-1-4. F) PIM-1 monomeric unit.	66
Figure 3.14	(A) Thin film composite sheet of SBAD-1 on Ultem®. (B) Scaled-up flat sheet membrane roll of SBAD-1 prepared through roll-to-roll coating. (C) Spiral wound SBAD-1 module comprised of 1.8 m x 0.2 m of membrane.	73
Figure 3.15	Schematic of a hollow fiber spinning system setup.	74
Figure 3.16	Simple schematic of the roll-to-roll coating process of hollow fiber membranes.	75
Figure 3.17	Schematic of a cross-flow permeation system.	78
Figure 4.1	Modular reaction scheme showing the polymerization of 7,7'-dibromo-2,2',3,3'-tetramethoxy-9,9'-spirobifluorene, 1, with diamines I-IV giving the SBAD class of materials: SBAD-1-4.	88
Figure 4.2	Solutions of polymers in the SBAD series in chloroform (0.4 mg/mL).	92

Figure 4.3	GPC analyses of SBAD polymers.	92
Figure 4.4	Thermogravimetric analysis (TGA) of all polymers in the SBAD series compared to PIM-1 shown as A) derivative weight change and B) weight normalized to starting sample weight.	93
Figure 4.5	Differential scanning calorimetry (DSC) of polymers in the SBAD series compared to PIM-1. Glass transition states were not observed below the decomposition temperatures observed in Figure 4.4.	94
Figure 4.6	Uptake of (A) N ₂ at 77 K and (B) CO ₂ at 273 K by SBAD polymers compared to PIM-1. (C) Henry's law coefficient (k_D) and (D) Langmuir capacity constant (C'_H) values fit to CO ₂ sorption data, compared to data obtained for a traditional "non-porous" polymer, Torlon [®] . Error for k_D and C'_H were too small to be apparent on the graphs. Inset = key for A and B.	95
Figure 4.7	Chain length distribution in the polymer models.	96
Figure 4.8	Accessible (teal) and non-accessible (magenta) surface area for all polymers in the SBAD series compared to PIM-1 using a 2.2 Å probe diameter.	99
Figure 4.9	Non-accessible (magenta) surface area for all polymers in the SBAD series compared to PIM-1 using a 3.64 Å probe diameter (kinetic diameter of N ₂).	99
Figure 4.10	Calculated pore size distribution of the SBAD series compared to PIM-1.	100
Figure 4.11	Three-dimensional representation of the pore size distribution in the three models for each of the five polymers. Pores are color-coded based on their dimension. Only pores bigger than 1.42 Å radius are displayed.	101
Figure 4.12	Histograms of the angle distributions for the dihedral highlighted in red in the final models for the SBAD polymers and PIM-1. A) Dihedral angle involving the spirocenter B) dihedral angle involving the linkage between the two monomers.	103
Figure 4.13	Stick and space filling representations of two selected chains for each polymer. Hydrogens have been removed for clarity in the stick representation. Color code: carbon in grey, nitrogen in blue, oxygen in red, hydrogen in white, bromine in purple, fluorine in light blue.	104

Figure 4.14	Selected snapshots that highlight π - π stacking interactions between chains inside the polymer models of the SBAD family. One chain is shown in van der Waals representation with carbon in grey, the other is represented in stick with the carbons in light blue. Nitrogen is in blue, oxygen in red, hydrogen in white.	105
Figure 4.15	(A)-(B) Average pore limiting diameter (D_F) of PIM-1, SBAD-1 and SBAD-3 as a function of swelling. In (B), the red and black dashed lines represent the probe diameter of CO ₂ and N ₂ , respectively. (C)-(D) The average solvent accessible surface area of PIM-1, SBAD-1 and SBAD-3 as a function of swelling for CO ₂ (left) and N ₂ (right) probes.	107
Figure 4.16	Uptake of liquid toluene by dense films of SBAD-1, PIM-1 and Torlon® (14), 22°C, 1 atm. Data are the mean of 2 films +/- the range.	108
Figure 4.17	An example of the CuAAC reaction utilized in the synthesis of the DUCKY series.	109
Figure 4.18	Kinetics of DUCKY-5 and DUCKY-6 polymerization reaction via ¹ H NMR analysis of the monomer conversion rate.	110
Figure 4.19	Thermogravimetric analysis (TGA) of polymers in the DUCKY series shown as derivative weight change (solid lines) and weight normalized to starting sample weight (dotted lines).	111
Figure 4.20	Uptake of (A) N ₂ at 77 K and (B) CO ₂ at 273 K by DUCKY polymers. (C) Henry's law coefficient (k_D) and (D) Langmuir capacity constant (C'_H) values fit to CO ₂ sorption data, compared to data obtained for PIM-1. Inset = key for A and B.	112
Figure 5.1	Side view of thin film-composites: dense polymer layer coated on porous crosslinked polyetherimide. A) SBAD-2 B) SBAD-3 C) SBAD-4 D) PIM-1	117
Figure 5.2	(A) Transient toluene permeance, (B) transient 1,3,5-triisopropyl benzene (TIPB) rejection and (C) steady-state TIPB rejection vs. toluene permeance of SBAD and PIM-1 membranes when a 1/99 mol% feed of TIPB/toluene is applied at 22°C, 15 bar.	118
Figure 5.3	Molecular weight cut-off curves of SBAD-1 at 30 bar (threshold = 335 g·mol ⁻¹), PIM-1 at 5 bar (1220 g·mol ⁻¹), and PIM-1 data reported at 30 bar (786 g·mol ⁻¹) for polystyrene standards in toluene at 22°C. The high flux in PIM-1 in our work limited the applied pressure difference to 5 bar in order to maintain < 5% stage cuts. Data reported by Cook et al. at the same conditions (6) as	120

SBAD-1 was shown for direct comparison. Comparison of SBAD-1 and PIM-1 oligostyrene rejection over three days.

- Figure 5.4 Hydrocarbon molecular weight cutoff curve (threshold = 253 g-mol⁻¹) for SBAD-1 using a 1 mol% concentration of individual solutes of two the mixtures listed in Table 5.1. Cutoff was determined by fitting all data points above 60% rejection to a log/log curve (equation of curve: $10^{((\log(y)-0.9549)/0.4158)} = x$) and interpolating to 90% rejection. 122
- Figure 5.5 Dependence of rejection on aromaticity and molecular weight (MW, g-mol⁻¹) where the effect of aromaticity (sorption) and molecular weight (diffusion) are coupled as represented by $(1 + \text{Carbon}_{aromatic}/\text{Carbon}_{total})/MW$. 123
- Figure 5.6 Ratio of concentrations in permeate vs. retentate (Cp/Cr) of components in a complex, model crude oil (composition is shown in Table 5.2) for both thin film composite membrane coupon of SBAD-1 fractionated at 40 bar (22°C) and a spiral wound module of SBAD-1 fractionated at 40 bar (20°C). Molecules above the reference line were more concentrated in the permeate compared to the feed while the molecules below, were more concentrated in the retentate. A permeance of 0.022±0.013 L-m⁻²-h⁻¹-bar⁻¹ for the coupon and 0.076±0.003 L-m⁻²-h⁻¹-bar⁻¹ for the module was obtained. 125
- Figure 5.7 Some notable separation factors for SBAD-1 based on data shown in Figure 5.6. 126
- Figure 5.8 Ratio of concentrations in permeate vs. retentate (Cp/Cr) of components in the complex mixture outlined in Table 5.2 for a thin film composite of SBAD-1 fractionated at various temperatures and pressures. Repeat at 45 bar was completed by recycling the membrane back to 35°C and 45 bar after treatment at 55 bar and showed increased separation performance. The temperature- and pressure-based study spanned a period of 2 months. 127
- Figure 5.9 Boiling point distribution of feed, permeate and retentate from SBAD-1 membrane fractionation of shale-based crude oil. Inset: Picture of feed (left) and permeate (right) from SBAD-1 membrane fractionation of real shale-based light whole crude oil. 128
- Figure 5.10 GCxGC-FID analysis of membrane fractionation of shale-based crude oil at 130°C and 55 bar showing the feed chromatogram subtracted from the permeate chromatogram. Teal elution peaks are concentrated in the permeate, whereas the magenta elution peaks are concentrated in the membrane retentate. General 129

hydrocarbon classifications are highlighted with dashed red lines to guide the eye. Top right: side view of GCxGC-FID showing the carbon number partition of real crude oil obtained by SBAD-1.

- Figure 5.11 Comparison of cumulative peak volume curves of the permeate and feed for the SBAD-1 enrichment of normal paraffin molecules from a whole crude oil separation. Increasing retention time corresponds with increasing molecular weight. 130
- Figure 5.12 Rejection curves for individual hydrocarbon classes obtained from GCxGC analysis of crude oil separation by SBAD-1. Increasing retention time corresponds to increasing molecular weight within each class. 131
- Figure 5.13 Exemplary membrane cascade for the separation of crude oil into various fractions (13). Desalted crude oil is fed to membrane stage 1 containing a membrane with molecular weight cut-off (MWCO) in the range of 300-400 Da. Stage 1 permeate is fed to membrane stage 2 with a membrane operating in reverse osmosis or pervaporation mode with MWCO < 200 Da. The permeate and retentate from stage 2 have boiling point distributions in the range of naphtha and kerosene/jet fuel, respectively. Stage 1 retentate is the feed for membrane stage 3, which could consist of a membrane with MWCO ~ 1.4 kDa. The permeate from stage 2 has boiling points mainly in the range of 230-340°C, which corresponds to atmospheric gas oil. Atmospheric gas oil can be further processed into gasoline, diesel and light gas oil. Stage 3 retentate is fed to membrane stage 4, which could consist of an ultrafiltration membrane with MWCO ~ 8 kDa. The permeate from stage 4 has boiling points in the range of 340-570°C, which corresponds to vacuum gas oil. The retentate from this stage can be used in heavy fuel oil/residual fuel oil applications. 133
- Figure 5.14 Cross-sectional views of thin film-composites of dense DUCKY polymer layer coated on porous crosslinked polyetherimide. 135
- Figure 5.15 Molecular weight cut-off curves and permeances of DUCKY polymer series at 30 bar for polystyrene standards in (A) toluene and (B) ethanol at 22°C. 136
- Figure 5.16 Separation factors based on Figure 5.14. data for A) toluene/dimer B) toluene/trimer and C) dimer/trimer. 139
- Figure 5.17 Hydrocarbon molecular weight cutoff curve for DUCKY-9 using a 12-component mixture containing 1 mol% concentration of solutes 141

shown in the graph in toluene. A cutoff could not be determined as rejections above 90% were not observed.

- Figure 5.18 Boiling point distribution of feed, permeate and retentate from DUCKY-9 membrane fractionation of shale-based crude oil. Inset: Picture of permeate at 4% stage cut (left), permeate at 17% stage cut (middle) and feed (right). 142
- Figure 5.19 GCxGC-FID analysis of membrane fractionation of shale-based crude oil at 130°C and 55 bar showing the feed chromatogram subtracted from the permeate chromatogram. Green elution peaks are concentrated in the permeate, whereas the pink elution peaks are concentrated in the membrane retentate. Top left: side view of GCxGC-FID showing the carbon number partition of real crude oil obtained by DUCKY-9. 143
- Figure 5.20 Rejection curves for n-paraffins obtained from GCxGC analysis of crude oil separation by DUCKY-9 compared with SBAD-1. Dotted red lines indicate slope between C10 and C14 molecules. 145
- Figure 6.1 Complex mixture transport via PIM-1 and SBAD-1 membranes. Exemplar non-linear chemical potential profiles of individual molecules in complex mixtures are shown across the thickness of selective polymer membranes with corresponding chemical structures. It is assumed that the support layer does not hinder transport and chemical potential is unchanged throughout the support. Higher nonlinearity is observed for more dilute or low sorbing components, and as the number of components is increased (i.e., the mixture becomes more complex and each molecule becomes less concentrated in the mixture), Fick's law becomes insufficient to describe liquid hydrocarbon transport. Note that the membrane and support thicknesses are not to scale. 153
- Figure 6.2 Sorption regimes and diffusive modes of transport in polymer membranes. A. Dependence of sorption regime and membrane volume on solvent activity. It is important to note that the two guest populations are in equilibrium but Langmuir-style sorption will dominate at low solvent activities and Flory-Huggins-style sorption will dominate at high solvent activities. B. Conventional diffusion mechanism where a molecule makes diffusive jumps through free space in a polymer network. C. Maxwell-Stefan interpretation of mixture diffusion where frictional forces between molecules cause diffusion coupling such that faster molecules are slowed and slower molecules are sped up, leading to a loss in diffusion selectivity. D. Cohort motion mode of transport where 165

molecules diffuse collectively as a unit and no diffusion selectivity is obtained.

- Figure 6.3 Flow diagram showing the numerical method used to solve the proposed Maxwell-Stefan model. The solution match block is “yes” when the sum of the squared nonlinear function values (equations 6.18 and 6.19) is less than the default square root of the function tolerance of 10^{-6} . Equation 6.15 is used for algorithm step I, Equation 6.16 is used for algorithm step II, and Equation 6.17 is used for algorithm step III. Then Equations 6.18 and 6.19 are used for the solution match step. 170
- Figure 6.4 Unary sorption in PIM-1 and SBAD-1. Experimental hydrocarbon sorption isotherms (■) and predictions for PIM-1 (A) and SBAD-1 (B) at 25 °C assuming Dual-mode (---), Flory-Huggins (⋯⋯), and Langmuir + Flory-Huggins (-·-·) sorption models. X-axes indicate relative pressure of the molecule and y-axes represent molecule uptake (cc STP molecule/cc polymer). Data are shown as averages of at least two measurements with standard deviation error bars. Abbreviations are shown for 1-methylnaphthalene (1-MN) and 1,3,5-triisopropylbenzene (TIPB). 172
- Figure 6.5 Kinetic sorption of toluene in PIM-1 at toluene activity = 0.7 (left) and 1-methylnaphthalene in SBAD-1 at 1-methylnaphthalene activity = 0.7 (right). 173
- Figure 6.6 Calculation of Flory-Huggins solvent-polymer interaction parameter ($\chi_{i,n+1}$) using the F-H model for composition-dependent interaction parameters, $\ln(a_i^m) = \ln\phi_i^m + (1 - \phi_i^m) - (1 - \phi_i^m)\frac{\bar{V}_i}{\bar{V}_m} + \chi_{im}(1 - \phi_i^m)^2 + \phi_i^m(1 - \phi_i^m)^2\frac{\partial\chi_{im}}{\partial\phi_i^m}$ (22), and measured sorption isotherms for PIM-1 (A) and SBAD-1 (B) in single penetrant systems. \bar{V}_m was assumed to be $\gg \bar{V}_i$. Here, $\chi_{i,n+1}$ is not fixed at a constant value and is allowed to vary with activity of the penetrant. 174
- Figure 6.7 SEM images showing the approximate thickness of the SBAD-1 membrane (left) film thickness ~ 300 nm and PIM-1 membrane (right) film thickness ~ 1.5 microns. 175
- Figure 6.8 Unary permeation in PIM-1 and SBAD-1. Experimental liquid hydrocarbon unary flux (◆) and predicted flux for thin-film composites at 22 °C with an estimated film thickness of 1500 nm for PIM-1 (A) and 300 nm for SBAD-1 (B) assuming Dual-mode (---), Flory-Huggins (⋯⋯), and Langmuir + Flory-Huggins (-·-·) sorption models. X-axes indicate transmembrane pressure (bar) and y-axes represent flux ($\text{Lm}^{-2}\text{h}^{-1}$). Data are shown as averages of 176

three measurements on separate films with standard deviation error (with the exception of TIPB for which only one sample had measurable permeate flux). Abbreviations are shown for 1-methylnaphthalene (1-MN) and 1,3,5-triisopropylbenzene (TIPB).

- Figure 6.9 Predicted multicomponent sorption of heptane/*o*-xylene mixtures in PIM-1 according to Flory-Huggins (left, blue), Dual-mode (middle, red) and Langmuir + Flory-Huggins (right, black) models compared with experimental measurements (yellow). Legend: heptane, +; *o*-xylene, *; polymer, – 178
- Figure 6.10 Unary diffusion and multicomponent liquid hydrocarbon sorption. A. Volume-based Maxwell Stefan diffusivities, $\mathcal{D}_i^{v,m}$ (cm²/s), in SBAD-1 (●) and PIM-1 (◆) at 22 °C calculated using the Langmuir + Flory-Huggins sorption parameters and unary permeate fluxes at 20 bar. Abbreviations are shown for methylcyclohexane (MCH), 1-methylnaphthalene (1-MN), tert-butylbenzene (TBB) and 1,3,5-triisopropylbenzene (TIPB). B-D. Multicomponent experimental sorption in PIM-1 compared with sorption predictions using single component parameter fits and estimates for competitive sorption effects for Dual-Mode, Flory-Huggins, and Langmuir + Flory Huggins models. Experimental measurements are from submerging dense films of PIM-1 in liquid mixtures at 22 °C and atmospheric pressure. Molecule activities were taken into account when predicting multicomponent sorption here. B. Binary sorption indicated as volume fractions of swollen polymer system. Values in parentheses indicate initial mol fractions of surrounding bulk fluid (heptane:*o*-xylene). C. Ternary sorption indicated as volume fractions of sorbed liquid in PIM-1 dense films in bulk fluid initially composed of toluene, heptane and *p*-xylene in mol fractions of 0.35, 0.36 and 0.29 respectively, and D. Total solvent uptake (g solvent/ g polymer) in the swollen polymer from the ternary sorption condition in C. 179
- Figure 6.11 Partial flux predictions for Separation 1 via PIM-1 at varying combinations of sorption and diffusion assumptions. Markers indicate Dual-mode (red), Flory-Huggins (blue) and Langmuir + Flory-Huggins (black) sorption models. 182
- Figure 6.12 Partial flux predictions for Separation 2 via SBAD-1 at varying combinations of sorption and diffusion assumptions. Markers indicate Dual-mode (red), Flory-Huggins (blue) and Langmuir + Flory-Huggins (black) sorption models. 182
- Figure 6.13 Partial flux predictions for Separation 3 via SBAD-1 at varying combinations of sorption and diffusion assumptions. Markers 183

indicate Dual-mode (red), Flory-Huggins (blue) and Langmuir + Flory-Huggins (black) sorption models.

- Figure 6.14 Permeate flux- and composition-based prediction of multicomponent separations in Table 6.2. A. Comparison of predicted experimental permeate compositions with predicted values for Separations 1, 2, and 3 where the $\mathcal{D}_i^{v,m}$ for all molecules are assumed to be equal (average diffusivity approach: Sc5). For each separation, Dual-mode (red), Flory-Huggins (blue) and Langmuir + Flory-Huggins (black) sorption models are investigated. Dotted parity lines ($x=y$) are included as a guide for comparisons between predicted and experimental values. Error bars are included but are too small to be visible in some cases. B. Heatmaps showing composition based and total flux based RMSPE of each combination of sorption and diffusion assumptions. Y-axes vary sorption between Dual-mode, Flory-Huggins, and Langmuir + Flory-Huggins models while x-axes vary diffusion conditions as: Sc1 = Fickian transport, Sc2 = no diffusion coupling, Sc3 = Vignes diffusion coupling, Sc4 = Vignes diffusion coupling + free volume theory, Sc5 = average diffusivity assumption. 184
- Figure 6.15 Separation 3 (via SBAD-1) partial fluxes predicted using LM-FH and cross-diffusivities ($\mathcal{D}_{ij}^{v,m}$) fit to match permeate compositions. 185
- Figure 6.16 Free-volume theory-based prediction of diffusivity, $\mathcal{D}_i^{v,m}$, as it varies with accessible free volume indicated by solid lines for PIM-1 (left) and SBAD-1 (right) assuming $B = 0.03$. Dotted lines are the self-diffusivities of molecules(38) (excluding 1-methylnaphthalene, tert-butylbenzene and 1,3,5-triisopropylbenzene) and represent an upper limit on diffusivity in the polymers. 187
- Figure 6.17 Separation 1 (via PIM-1) predicted using LM-FH, Vignes diffusion coupling, and free volume theory with varying $B =$ i) 0.005, ii) 0.03 and iii) 0.1. 187
- Figure 6.18 Separation 2 (via SBAD-1) predicted using LM-FH, Vignes diffusion coupling and free volume theory with varying $B =$ i) 0.005, ii) 0.03 and iii) 0.1. Left plot has log-log scale while right plot in linear. 188
- Figure 7.1 SEM images of the cross section (left) and top view (right) of Torlon® 4000T-LV fibers from Trial 1. 202
- Figure 7.2 Ternary phase diagram of Torlon® 4000T-HV adapted from (20) (left). The star represents the low polymer concentration dope being considered for spinning hollow fibers. The blue, green and 203

red lines represent the binodal line, shell side trajectory and bore side trajectory, respectively. Bore side trajectories are drawn for spinning hollow fibers in either 88:12 or 90:10 ratios of NMP:water bore fluid. Dope composition of syringe extruded Torlon® hollow fibers with a low polymer concentration (top right). SEM image (bottom right) shows the surface on the shell side of syringe extruded fibers.

- Figure 7.3 Torlon® hollow fiber spinning parameters (top) and SEM images (bottom) in Trial 2. The left image shows the cross-section of the fabrication hollow fiber and the right images shows the surface morphology on the shell of the fiber. 204
- Figure 7.4 Liquid toluene permeance of Torlon® support obtained from Trial 2 at a transmembrane pressure of 10 bar for three samples (A, B and C). 205
- Figure 7.5 Relationship between viscosity and concentration in dilute polymer/chloroform solutions. PIM-1, MW~**70k**. 208
- Figure 7.6 AFM height images of the Torlon® support surface used in the continuous coating of PIM-1. The image on the left has a 0.5 x 0.5 µm field of view while the image on the right has a 6 x 6 µm field of view. 211
- Figure 7.7 SEM images of PIM-1 coated Torlon® hollow fibers drawn at a rate of 2 m·min⁻¹ from a bath of chloroform with PIM-1 at concentrations a) 0.5 wt% b) 1wt% c) 1.5wt% d) 2wt% e) Comparison of measured and predicted thicknesses of PIM-1 thin film coatings by the LLD law and Marangoni thickness factor of 2 and 4. 212
- Figure 7.8 SEM images of 1 wt% PIM-1 coated Torlon® hollow fibers drawn at a rate of 2 m·min⁻¹ from a bath of 50-50 wt% chloroform and trichloroethylene (top row) and 50-50 wt% chloroform and 1,1,2,2-tetrachloroethane (bottom row). Images of the surface are shown in the left column while images of the cross-section are shown in the right column. 214
- Figure 8.1 Comparison of the viscosity of PIM-1, SBAD-1 and MALLARD in chloroform solutions at 22 °C. 229

SUMMARY

The separation of complex liquid mixtures, which are mixtures without a clear singular solvent, has been an emerging area of membrane science. Crude oil is one such complex industrial mixture that is comprised of several tens of thousands of hydrocarbon molecules but is typically fractionated via energy-intensive thermal processes. In this work, specific light fractions of crude oil were separated via novel spirocyclic polymer membranes, with the potential for bypassing significant energy expenditure associated with distillation. Polymeric materials are of interest for membrane fabrication as they are easily processable, inexpensive, and can be easily functionalized for stability. However, for membrane-based fractionation of crude oil to compete with current distillation processes on an industrial scale, multi-stage cascades containing several high-throughput membranes must be optimized. The capability to predict multi-molecule transport in target materials can accelerate the screening and design of materials for cascades that would otherwise require lengthy R&D timelines. Thus, advanced models were also utilized in this work to predict complex mixture permeation in polymeric membranes based only on pure molecule sorption and diffusion inputs. These simplifying hypotheses could enable an extension of predictive capabilities to N -component mixtures of hydrocarbons, of which there are many industrially relevant streams, not limited to crude oil. One of the limitations to the industrial implementation of this type of membrane-based process is whether the polymer membranes can be fabricated in a scalable manner. Therefore, a roll-to-roll dip-coating process was used to demonstrate the continuous fabrication of thin film composite hollow fiber membranes. In this precursive work, a more established spirocyclic polymer, PIM-1,

was coated on a commercial polymer support to investigate the feasibility of this process for the novel spirocyclic polymers identified for crude oil separations. Upon successful demonstration, the learnings could be used to develop large-scale polymeric membranes capable of excellent separation performance in complex mixtures coupled with fast transport rates.

CHAPTER 1. INTRODUCTION

1.1 The Future of Separation Science

Separation processes are critical components of the various systems that fulfill the need for clean water, basic goods and services, and safe and reliable sources of energy. Historically, products and services have been developed without much regard for the complexity and toxicity of waste that is often generated. However, the onset of climate change, human health concerns, and the subsequent imposition of stricter process regulations have led to increasing scrutiny of issues such as greenhouse gas emission, energy inefficiency, and toxic waste production.⁽¹⁻³⁾ Recently, the National Academies of Sciences, Engineering, and Medicine composed an agenda that details the primary research required to enable a shift in global separation processes that will address these concerns.⁽⁴⁾ The agenda identifies that one of the major shortcomings of current separations research is the lack of fundamental understanding of diverse and complex mixture separations. For example, desalination via reverse osmosis, the poster child of energy-efficient membrane separations, was established over 60 years ago and has since been thoroughly studied and optimized to separate dilute impurities (usually ppm levels) in water.⁽⁵⁾ However, there is limited knowledge on how current membrane materials would perform in mixtures of water with more concentrated molecules in solution or how these materials could be adapted for such applications. This “gap” is astounding, as the slate of separations that involve multiple components and at concentrations that are not reflected by current research is enormous. Several natural mixtures that need to be separated are often concentrated liquids that are "complex" in nature; the term "complex" identifies streams with many components and

often without a clear majority species. These multicomponent mixtures are commonplace in the petrochemical, biotechnology, pharmaceutical manufacturing, and other chemical processing industries, and are in dire need of sophisticated separation technologies that can meet the growing demand for sustainability.

1.2 Separation Technology in Complex Petrochemical Separations

Process streams in the petrochemical industry are far from the ideal lab-scale separation experiment of a binary mixture with a dilute contaminant. Natural gas is mainly made up of methane and ethane but also contains lower concentrations of nonhydrocarbons such as nitrogen, carbon dioxide, noble gases, and trace amounts of water vapor and toxic sulfur-containing compounds.⁽⁶⁾ Crude oil contains thousands of liquid hydrocarbon molecules in varying concentrations categorized into groups or “fractions,” each of which is the primary source for specific commodities such as gasoline, diesel, jet fuel, waxes, and asphalt. In particular, the refining of crude oil is a large-scale process that requires several different complex mixture separations and represents an essential target for sustainability improvements as the initial fractionation of crude oil accounts for nearly 1% of global energy use.⁽⁷⁾ Biocrude is a complex hydrocarbon mixture that is being investigated as an alternative to fossil-based petroleum.⁽⁸⁾ Biocrude is synthesized by anaerobic pyrolysis of dry biomass such as wood, peat, or algae and contains a significantly higher amount of oxygen than petroleum.⁽⁹⁾ This distinction, coupled with the high variability in biomass source, suggests that biocrude would require significant additional treatment compared to petroleum to be considered a suitable substitute.

Current crude oil separations are dominated by thermal processes such as distillation, which are energy-intensive and often have low thermodynamic energy efficiency.⁽¹⁰⁾ However, even with the modernization of separations technology research, traditional chemical plants have seen a slow transition to newer processes as the associated capital cost places too great of a financial burden to be deemed beneficial over energy returns.⁽⁴⁾ Additionally, there is great risk in overhauling an extremely large-scale process for a billion-dollar industry without long-term knowledge of materials lifetime and process stability. Therefore, it is beneficial to propose alternative technology that can supplement a currently operating process and be easily retrofitted and removed, if needed.⁽¹¹⁾ Moreover, a clear materials-to-process commercialization path must be visualized by academic researchers to focus efforts on filling the most significant knowledge gaps, which include materials reproducibility and transient and long-term process dynamics.

1.3 Membranes for Crude Oil Separations

As industries seek to reduce energy and resource consumption associated with separation processes, membranes have emerged as attractive low-energy options either in hybrid separation process configurations or as standalone alternatives. Though crude oil distillation has the potential for high recoveries of molecules in discrete boiling-point ranges, it requires more than 1100 terawatt-hours per year.⁽⁷⁾ Distillation energy and carbon efficiency could be improved if paired with low-energy membrane-based separations that fractionate complex mixtures containing thousands of compounds into smaller groups of molecules. Membrane separations based on molecular differences in size, shape, and membrane-penetrant interactions can generate a 10-fold increase in energy efficiency over practical thermal processes.⁽¹⁰⁾ Seawater reverse-osmosis systems that

currently process greater liquid flows than the largest refineries highlight membrane technology's potential to match the scales required by the hydrocarbon-processing industry. Whereas membrane technologies are established for certain aqueous and gas separations, they have not been developed to fractionate organic molecule mixtures because of the relative scarcity of suitable materials that are easily processable, inexpensive, and stable in harsh environments.⁽¹²⁾ Polymeric membrane materials provide the best combination of these three metrics but to date have not been adequate for the separations of small liquid organic molecules. This is mainly due to the flexible nature of typical polymers, which is exacerbated in organic solvents and prevents efficient discrimination amongst small molecules.⁽¹³⁾

1.4 Organic Solvent Nanofiltration (OSN) and Organic Solvent Reverse Osmosis (OSRO)

Organic solvent nanofiltration (OSN) and organic solvent reverse osmosis (OSRO) are two modes of transport of organic solvents through membranes. OSN typically involves separating small solutes with molecular weights of 200-1000 g/mol, present in dilute quantities, from a solvent, and materials have pores in the range of 0.7-2 nm.⁽¹⁴⁾ On the other hand, OSRO can be described as more of a solvent/solvent separation and often necessitates a rigid membrane capable of distinguishing molecules with slight differences in size (<1 nm).⁽¹⁵⁾ The growth of OSN has been steady since the turn of the 21st century, while organic solvent reverse osmosis OSRO has only gained momentum within the last five years.^(14, 15) The separation of complex liquid hydrocarbon mixtures such as light fractions of crude oil would require membrane operation at the cusp of OSN and OSRO and consequently entails three requirements: a) a small, rigid pore size between 0.5 to 1

nm, b) a high transmembrane pressure to accommodate the high driving forces necessary for transport in these regimes(16) and c) thin selective membrane layers to allow high product fluxes that are limited by the applied driving force in the highly selective regimes. Several polymers have been employed for the OSRO-based separation of organics with vastly different polarities(15), but those for liquid hydrocarbon applications are rare. It is essential not just to create scalable materials and membranes for hydrocarbon OSRO separations but also to expand the testing and standardization of these for comparison in the entire space of complex feeds with many components (>1000) as in crude oil fractions.

1.5 Research Objectives

1.5.1 Thin Film Composite Polymer Membranes for Liquid Hydrocarbon Separations

As discussed above, polymer materials are favored in the design of membrane devices due to their ease of processing and scalability. This work explores the use of glassy spirocyclic polymers, inspired by polymers of intrinsic microporosity (PIMs),(17) that are solution-processable, stable in organic solvents, and most importantly, are capable of reduced chain motion and, therefore, high selectivities for small liquid hydrocarbons. The novel spirocyclic polymers will be fabricated as thin-film composites before testing the separation of small liquid hydrocarbon molecules representing species found in crude oil mixtures. A thin film composite membrane contains a thin selective, often dense, membrane layer coated atop a porous support layer (Figure 1.1). Thin-film composites are valuable assets in OSN/OSRO separations as they allow high product fluxes through thin barriers with minimized resistance.(18) Support layers that are typically made of polymer materials can be phase-inverted to obtain the desired pore structure.(19) The selective layer

can then be coated with controlled thickness via spin coating, dip coating, atomic layer deposition, or interfacial polymerization.(20) Support layers with sufficient porosity are desired to prevent transport resistance towards the product permeate from the topcoat. At the same time, a minimum pore size is required at the interface between the selective layer and the support layer to minimize surface roughness, prevent the creep of coating solutions through the surface, and allow the formation of a smooth, defect-free coating.(21) In general, this minimum surface pore size should be lower than the target thickness of the dried thin film coating. Commonly, thin films have a thickness between 200-1000 nm(22-24), with some ultra-thin films fabricated below 10 nm.(25)

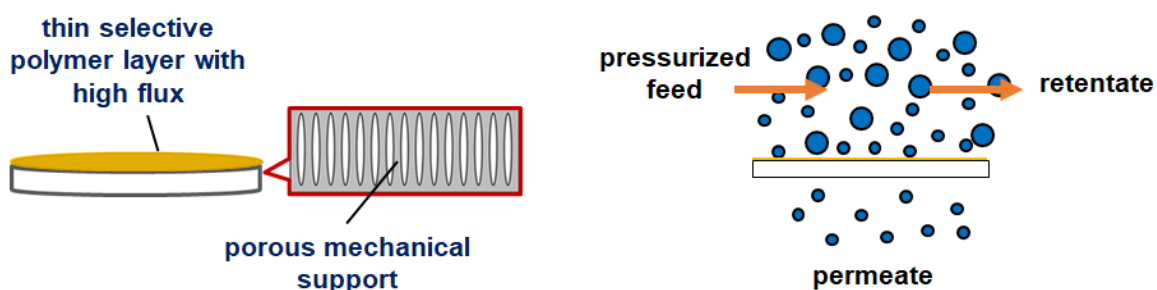


Figure 1.1. Thin-film composite morphology and size-based OSN/OSRO separation.

1.5.2 Complex Organic Solvent Transport in Polymer Membranes

Understanding fundamental organic solvent transport principles enables predictions of important process parameters that can further pave the way for membrane-based process optimization. While the transport of dilute mixtures via OSN and OSRO membranes has been well documented and studied(26), the transport of complex, multicomponent mixtures of organic solvents is less detailed. Pore flow, solution-diffusion models, or a combination

of both typically describe organic solvent nanofiltration (OSN) membranes(27), and OSRO membranes are ideally described by just solution-diffusion approaches(28) (Figure 1.2). In the simplified versions of the solution diffusion model, diffusional and thermodynamic coupling of permeants are ignored, and the transport diffusivity (product of thermodynamically corrected diffusivity and thermodynamic coupling) is assumed to be constant throughout. However, most industrial-relevant mixtures are complex in nature, and transport can thus be affected by intermolecular coupling, solvent-induced swelling and plasticization of polymeric materials, and the concentration dependence of diffusion.(29) Such cases call for a detailed analysis via Maxwell-Stefan equations that account for non-linear changes in the occupied volume of solvents and polymer in a membrane system.(30) Additionally, studies of appropriate sorption models that describe multicomponent liquid sorption ($N > 2$) in glassy polymers are rare and need to be defined and verified. As such, this work implements multicomponent sorption and multicomponent diffusion interaction theories within a Maxwell-Stefan framework to predict the separation of complex liquid hydrocarbons mixtures via polymeric membranes.

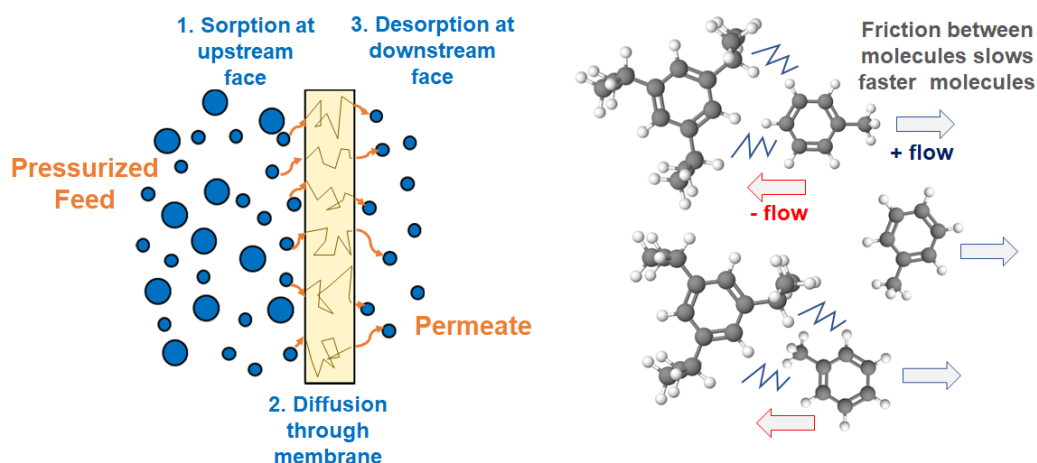


Figure 1.2. Solution-diffusion mechanism of transport in OSRO separations. In OSRO separations, frictional forces act to couple the diffusivities of molecule pairs such that faster molecules are slowed, and slower molecules are sped up.

1.5.3 Continuous Hollow Fiber Membrane Fabrication

As novel polymers are created for new membrane applications, the scalability of the polymer membrane fabrication is a critical factor that determines industrial implementation. Due to their morphology, hollow fibers can be fabricated continuously and offer a high surface area to volume ratio⁽³¹⁾ and a high packing density of multiple fibers, which translates to increased productivity per volume of module. Hollow fiber membranes are cylindrical-tube-like structures with hollow axial voids (Figure 1.3). The outer surface is designated as the shell, and the inner void-adjacent region is called the bore. Fiber outer diameters typically range from 100-600 microns, and a ratio of outer diameter to the inner diameter of around 2 is preferred for thick enough walls to prevent fiber collapse during high-pressure gas or liquid permeation. Hollow fibers also allow asymmetric structures, so they are self-supporting and robust membranes. Hollow fibers

are fabricated in a process known as spinning, where a polymer fluid is extruded through a coannular die called a spinneret. The solution is coextruded with a liquid or gas in the center of the annulus to prevent collapse and create the hollow or bore region. For membrane applications, extrusion can be performed via dry-wet spinning, wet-wet spinning, melt spinning, or electrospinning.(32, 33) Optimizing the spinning of a high-performing hollow fiber membrane requires a highly sophisticated combination of mechanical, thermodynamic, and kinetic considerations and therefore entails a lengthy timeline for new materials or applications.(34) In this work, a commercial polymer, Torlon®, is spun to create porous supports on top of which target spirocyclic polymers are continuously coated; roll-to-roll dip coating is utilized for the continuous coating process. Thus, the scale-up of flat thin-film composite membranes in hollow fiber form is demonstrated via a continuous fabrication process, capable of producing industrial-scale quantities of membranes with desirable separation properties.

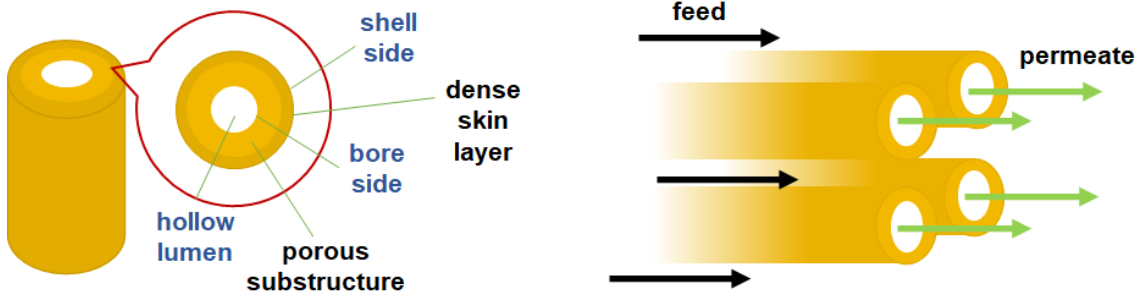


Figure 1.3. Morphology of a hollow fiber membrane and packed hollow fiber membrane permeation.

1.6 Dissertation Overview

This work demonstrates polymer membranes' feasibility for industrial complex liquid hydrocarbon separations, particularly those encountered in crude oil refining. Chapter 2 summarizes the background and theory, including preceding research that provides fundamental support towards the achievements of the thesis. Chapter 3 details the materials and experimental methods that are undertaken to demonstrate the hypotheses of this work. The creation and characterization of two novel series of spirocyclic polymers for the purpose of liquid hydrocarbon separations is summarized in Chapter 4. The performance of selected polymer candidates is then probed in dilute and complex liquid hydrocarbon separations, including natural crude oil fractions in Chapter 5. Chapter 6 details the fundamental theory behind complex mixture transport in polymer membranes, and a Maxwell-Stefan model is hypothesized and validated against experimentally measured complex separations. Finally, Chapter 7 presents the continuous roll-to-roll coating of a spirocyclic polymer on Torlon® hollow fibers, aimed at an industrially attractive mode of membrane production.

1.7 References

1. R. M. Ferguson, Avoiding dangerous climate change. *Choice: Current Reviews for Academic Libraries* **44**, 331-331 (2006).
2. W. Thuiller, Biodiversity - Climate change and the ecologist. *Nature* **448**, 550-552 (2007).
3. L. Fazzo *et al.*, Hazardous waste and health impact: a systematic review of the scientific literature. *Environ Health-Glob* **16**, (2017).
4. E. National Academies of Sciences, and Medicine, A Research Agenda for Transforming Separation Science. *Washington, DC: The National Academies Press*, (2019).
5. Z. Yang *et al.*, A Review on Reverse Osmosis and Nanofiltration Membranes for Water Purification. *Polymers-Basel* **11**, (2019).
6. F. Y. Liang, M. Ryvak, S. Sayeed, N. Zhao, The role of natural gas as a primary fuel in the near future, including comparisons of acquisition, transmission and waste handling costs of as with competitive alternatives. *Chem Cent J* **6**, (2012).
7. "World Balance IEA Sankey Diagram," (International Energy Agency, 2017).
8. G. W. Huber, A. Corma, Synergies between bio- and oil refineries for the production of fuels from biomass. *Angew Chem Int Edit* **46**, 7184-7201 (2007).
9. V. A. Yakovlev *et al.*, Development of new catalytic systems for upgraded bio-fuels production from bio-crude-oil and biodiesel. *Catal Today* **144**, 362-366 (2009).
10. D. S. Sholl, R. P. Lively, Seven chemical separations: to change the world: purifying mixtures without using heat would lower global energy use, emissions and pollution--and open up new routes to resources. *Nature* **532**, 435-438 (2016).
11. K. Wang, B. J. Zhang, Q. L. Chen, Optimization of a crude oil distillation unit based on total-process simulation. *Comput-Aided Chem En* **38b**, 2163-2168 (2016).
12. R. P. Lively, D. S. Sholl, From water to organics in membrane separations. *Nature Materials* **16**, 276-279 (2017).
13. W. J. Koros, C. Zhang, Materials for next-generation molecularly selective synthetic membranes. *Nat Mater* **16**, 289-297 (2017).

14. P. Marchetti, M. F. J. Solomon, G. Szekely, A. G. Livingston, Molecular Separation with Organic Solvent Nanofiltration: A Critical Review. *Chem Rev* **114**, 10735-10806 (2014).
15. C. J. Liu, G. Y. Dong, T. Tsuru, H. Matsuyama, Organic solvent reverse osmosis membranes for organic liquid mixture separation: A review. *J Membrane Sci* **620**, (2021).
16. M. L. Jue, D. Y. Koh, B. A. McCool, R. P. Lively, Enabling Widespread Use of Microporous Materials for Challenging Organic Solvent Separations. *Chem Mater* **29**, 9863-9876 (2017).
17. N. B. McKeown, P. M. Budd, Polymers of intrinsic microporosity (PIMs): organic materials for membrane separations, heterogeneous catalysis and hydrogen storage. *Chemical Society Reviews* **35**, 675-683 (2006).
18. M. F. J. Solomon, Y. Bhole, A. G. Livingston, High flux membranes for organic solvent nanofiltration (OSN)-Interfacial polymerization with solvent activation. *J Membrane Sci* **423**, 371-382 (2012).
19. A. F. Ismail, M. Padaki, N. Hilal, T. Matsuura, W. J. Lau, Thin film composite membrane - Recent development and future potential. *Desalination* **356**, 140-148 (2015).
20. W. J. Lau, A. F. Ismail, N. Misdan, M. A. Kassim, A recent progress in thin film composite membrane: A review. *Desalination* **287**, 190-199 (2012).
21. M. F. Jimenez-Solomon, P. Gorgojo, M. Munoz-Ibanez, A. G. Livingston, Beneath the surface: Influence of supports on thin film composite membranes by interfacial polymerization for organic solvent nanofiltration. *J Membrane Sci* **448**, 102-113 (2013).
22. P. Gorgojo *et al.*, Ultrathin Polymer Films with Intrinsic Microporosity: Anomalous Solvent Permeation and High Flux Membranes. *Adv Funct Mater* **24**, 4729-4737 (2014).
23. S. P. Sun, T. S. Chung, K. J. Lu, S. Y. Chan, Enhancement of Flux and Solvent Stability of Matrimid (R) Thin-Film Composite Membranes for Organic Solvent Nanofiltration. *Aiche J* **60**, 3623-3633 (2014).
24. D. Fritsch, P. Merten, K. Heinrich, M. Lazar, M. Priske, High performance organic solvent nanofiltration membranes: Development and thorough testing of thin film composite membranes made of polymers of intrinsic microporosity (PIMs). *J Membrane Sci* **401**, 222-231 (2012).
25. S. Karan, Z. W. Jiang, A. G. Livingston, Sub-10 nm polyamide nanofilms with ultrafast solvent transport for molecular separation. *Science* **348**, 1347-1351 (2015).

26. M. Galizia, K. P. Bye, Advances in Organic Solvent Nanofiltration Rely on Physical Chemistry and Polymer Chemistry. *Front Chem* **6**, (2018).
27. P. Marchetti, A. G. Livingston, Predictive membrane transport models for Organic Solvent Nanofiltration: How complex do we need to be? *J Membrane Sci* **476**, 530-553 (2015).
28. C. J. Liu *et al.*, Highly improved organic solvent reverse osmosis (OSRO) membrane for organic liquid mixture separation by simple heat treatment. *J Membrane Sci* **618**, (2021).
29. D. R. Paul, Reformulation of the solution-diffusion theory of reverse osmosis. *J Membrane Sci* **241**, 371-386 (2004).
30. R. Krishna, Highlighting Thermodynamic Coupling Effects in Alcohol/Water Pervaporation across Polymeric Membranes. *Acs Omega* **4**, 15255-15264 (2019).
31. J. de Jong, N. E. Benes, G. H. Koops, M. Wessling, Towards single step production of multi-layer inorganic hollow fibers. *J Membrane Sci* **239**, 265-269 (2004).
32. A. L. Ahmad, T. A. Otitoju, B. S. Ooi, Hollow fiber (HF) membrane fabrication: A review on the effects of solution spinning conditions on morphology and performance. *J Ind Eng Chem* **70**, 35-50 (2019).
33. F. E. Ahmed, B. S. Lalia, R. Hashaikeh, A review on electrospinning for membrane fabrication: Challenges and applications. *Desalination* **356**, 15-30 (2015).
34. G. Q. Li, W. Kujawski, R. Valek, S. Koter, A review - The development of hollow fibre membranes for gas separation processes. *Int J Greenh Gas Con* **104**, (2021).

CHAPTER 2. BACKGROUND AND THEORY

2.1 Overview

This chapter provides background and theory that supports the work in this dissertation. Section 2.2 provides fundamental theory on transport in polymeric membranes. The study of polymers of intrinsic microporosity and their derivatives is discussed in Section 2.3. The thermodynamic, kinetic, and mechanical considerations behind the spinning of hollow fiber membranes are discussed briefly in Section 2.4 and finally, dip coating background and common issues are detailed in Section 2.5.

2.2 Liquid Transport in Polymer Membranes

2.2.1 Membrane Transport Mechanisms

Understanding the basics of gas transport through glassy polymeric membranes can provide a useful background for the more complex transport of organic solvents. Gas transport through nonporous polymer membranes can be described using the solution-diffusion model (Equation 2.1) where permeability, \mathbb{P} , is a function of the sorption, \mathbb{S} , and diffusion, D , coefficients of the guest molecules through the membrane.⁽¹⁾

$$\mathbb{P} = \mathbb{S} \cdot D = \frac{J \cdot \ell}{\Delta f} \quad 2.1$$

Here, J is the penetrant flux, ℓ is the thickness of the membrane and Δf is the transmembrane fugacity. The model states that the penetrating species adsorbs onto the feed side of the membranes, diffuses through the membrane, and then desorbs on the permeate side. Smaller molecules tend to have a higher diffusion coefficient while more

soluble molecules (i.e., greater polymer-penetrant interactions) have a higher sorption coefficient. The pure component permeability is calculated from permeation experiments as the flux of the species through the membrane normalized by the driving fugacity, Δf , and the membrane thickness, ℓ . Apart from the permeability of a membrane, the selectivity or rejection of the components in a mixture is an indicator of its separation performance. Ideal selectivity (α) is defined as the ratio of the permeabilities of the two pure components as shown in Equation 2.2, which applies in the case of a downstream vacuum. This ideal selectivity can also be broken down into the product of its diffusion selectivities and sorption selectivities.

$$\alpha_{\frac{A}{B}} = \frac{P_A}{P_B} = \frac{D_A}{D_B} \cdot \frac{S_A}{S_B} \quad 2.2$$

Transport of gases and liquids through porous membranes is defined by the pore-flow model in which species are separated by pressure driven forces through the pores. In this mode of transport, it is assumed that the pore size is larger than the kinetic diameter of the solute and solvent molecules and there exists no concentration gradient within the pores. This mechanism can be described by Darcy's law (Equation 2.3)(2)

$$J = \frac{k\Delta p}{\eta\ell} \quad 2.3$$

where Δp is the transmembrane pressure drop, η is the fluid dynamic viscosity and k is the permeability coefficient that is dependent on membrane structural parameters such as pore size, porosity, and tortuosity. Both solution-diffusion and pore flow models define the flux as a function of the chemical potential gradient across the membrane. In the former,

a concentration-dependent chemical potential gradient is assumed while in the latter, the chemical potential gradient is dependent on a pressure gradient throughout the membrane (Figure 2.1). (1) Due to the mechanical equilibrium requirement in the solution-diffusion approach, the pressure must be constant throughout the thickness of the dense membrane and must be equal to the upstream applied pressure. (3) Consequently, since the downstream pressure is at atmospheric conditions, the pressure difference is expressed as a concentration gradient across the membrane. In the pore flow model, the pressure difference results in a pressure gradient across the membrane and the solvent activity remains constant across the membrane.

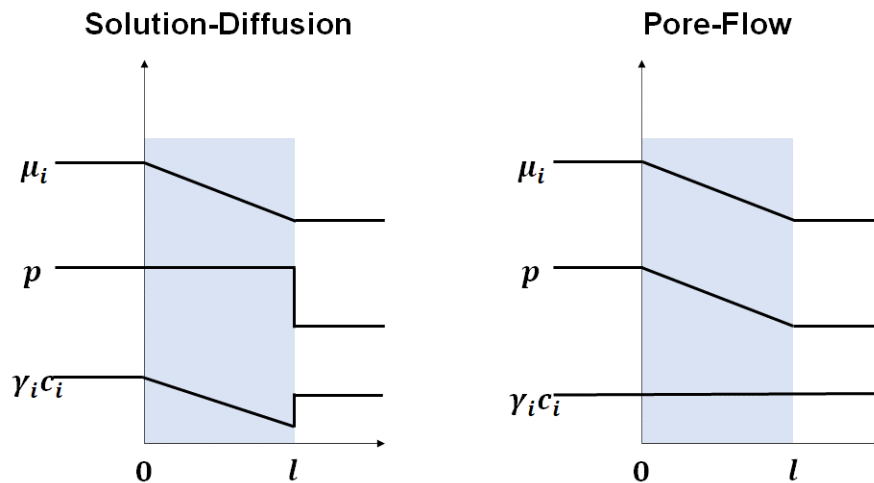


Figure 2.1. Chemical potential, pressure and activity profiles throughout a membrane based on solution-diffusion and pore-flow modes of transport.

2.2.2 Defining and Evaluating OSN Transport

OSN lies at the intersection of pore flow and solution-diffusion transport.(4) The solution-diffusion model is applicable to nonporous polymers when minimal swelling occurs, but in the presence of plasticizing solvents or defective membranes, an addition of a convective term is often appropriate.(5) This term is derived from a simple pore-flow model that describes the sieving transport mechanism depending on pore size. The two terms combine to formulate the solution-diffusion model with imperfections, as shown in Equation 2.4, where c is the concentration of solvent in the membrane, \bar{V} is the partial molar volume of solvent, R is the gas constant, T is the temperature, and B_0 is the specific permeability of the membrane.(5)

$$J = \frac{cD\bar{V}}{RT\ell}(\Delta p - \Delta\pi) + \frac{cB_0}{\eta\ell}\Delta p \quad 2.4$$

Several transport models for OSN have been developed to describe the solute flux based on physicochemical characteristics such as steric hindrance, interactions with pore walls, and relative mobility compared to the solvent. For dilute systems, it is assumed the solvent flux is independent of solute interactions, although realistic separations are certainly more complex. OSN performance, like aqueous membrane separations, is usually defined by permeance and rejection as it varies with applied pressure. When the thickness of the membrane is difficult to determine such as with thin film composite membranes, the performance of the membrane can be characterized by permeance, \mathbb{P}/ℓ , which is accurate in the case of pure components or streams with only very dilute solutes:

$$\frac{\mathbb{P}}{\ell} = \frac{J}{\Delta f} \quad 2.5$$

Since the fugacity across a polymeric membrane may be complicated to calculate due to the high levels of sorption, the transmembrane pressure may be substituted instead and a hydraulic permeance can be calculated(6):

$$\left(\frac{\mathbb{P}}{\ell}\right)^{hydraulic} = \frac{J}{\Delta p} \quad 2.6$$

The rejection of a solute is used to define the membrane performance in OSN and can be calculated based on the difference in concentration of the solute in the permeate and the feed as shown in Equation 2.7:

$$Rejection = \left(\frac{x_f - x_p}{x_p}\right) * 100 \quad 2.7$$

In the case of complex, multicomponent mixtures that may have “negative rejections”, the separation efficacy can be more clearly defined by a separation factor between species *A* and *B*:

$$\beta_{A/B} = \frac{\frac{x_{A,permeate}}{x_{B,permeate}}}{\frac{x_{A,feed}}{x_{B,feed}}} \quad 2.8$$

The molecular weight cut off (MWCO) is used to compare the performance of commercial and novel OSN materials. It is defined as the molecular weight of the smallest

solute that experiences greater than 90% rejection. MWCO curves, such as the one in Figure 2.2, plot the rejection of different molecular weight solutes and are typically broad with a gradual rise in rejection. A curve with a sharper rise in rejection is preferred as it denotes a cleaner separation between solutes with a small difference in molecular size. Recent research has focused primarily on the separation of dye molecules and oligostyrenes with a > 200 Da molecular weight from small molecule solvents.⁽⁴⁾ These serve as a uniform testing protocol across a wide range of membranes but have not been effectively translated to more realistic feedstocks. Non-uniformities in the range of solute-solvent systems investigated by researchers make it difficult to compare membranes across applications. Polystyrene and polyethylene glycol oligomer solutes, that are considered standard solutes for creating molecular weight cut off curves, undergo varying degrees of solvation in different solvents and can differ in size and shape accordingly. The formation of charge-transfer complexes in dye-solvent systems and cluster-formation of solutes in poor solvents are additional hindrances to performance comparisons.

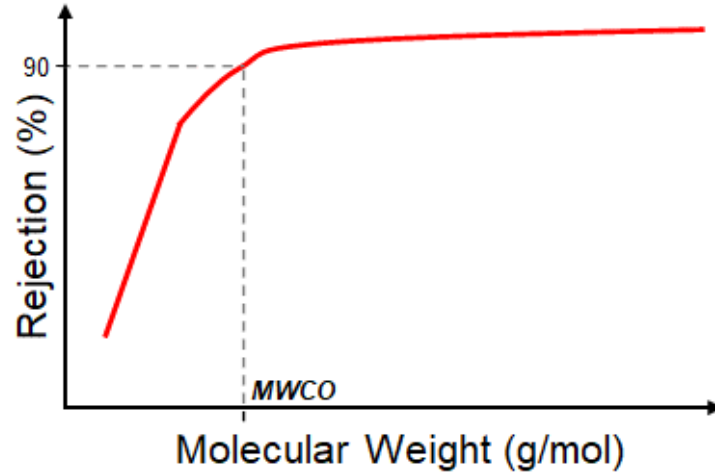


Figure 2.2. Example of a molecular weight cut off curve with a MWCO.

2.2.3 Sorption

Sorption is a thermodynamic property and describes the capture of a molecule by a condensed state (solid or liquid). Gas sorption in polymers has been typically described by the Dual-Mode Sorption model(7) where the low-pressure region of the isotherm represents a Langmuir-like adsorption and the higher-pressure region is described by Henry's law for a gas dissolving in a liquid. The uptake is calculated as the algebraic sum of these components as shown in Equation 2.9, where C^m is the concentration of sorbate in the polymer, k_D is the Henry's law coefficient, $C_{H,sat}^m$ is the Langmuir capacity constant, and b is the Langmuir affinity constant.

$$C^m = k_D f^m + \frac{C_{H,sat}^m b f^m}{1 + b f^m} \quad 2.9$$

For certain strong sorbing gases in glassy polymers such as nitrogen in PIM-1, a steep increase in uptake is expected at high loadings and is symbolic of Flory-Huggins type polymer-penetrant interactions shown in Equation 2.10:(8)

$$\ln\left(\frac{f^m}{f^0}\right) = \ln\phi^m + (1 - \phi^m) + \chi(1 - \phi^m)^2 \quad 2.10$$

where f^0 is the fugacity of the sorbate at saturated vapor conditions at 298 K and ϕ^m is the sorbate volume occupancy in the sorbed polymer system (cm^3 solvent/ cm^3 system). The Flory interaction parameter, χ , is commonly understood to be composition dependent. Type II-like isotherms, shown in Figure 2.3, are most common in systems of condensable vapors (typically liquids at room temperature) and polymers. As such, several researchers have noted the importance of parameterizing a model that combines hole-filling in microporous polymers along with the dissolution of the polymer in the sorbate at high activities as in the Flory-Huggins model.(9, 10)

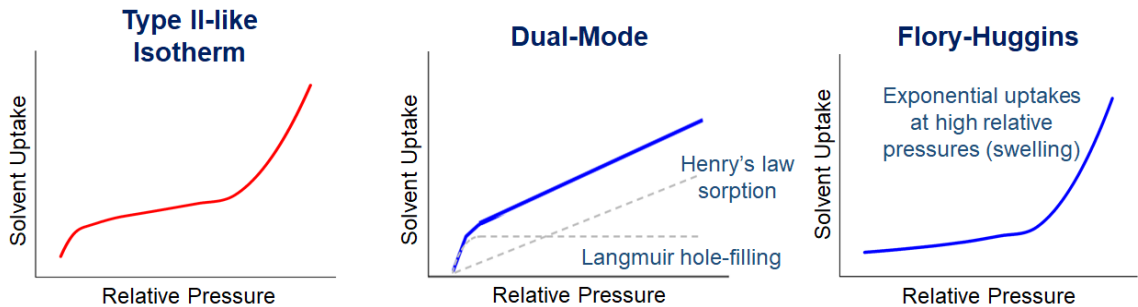


Figure 2.3. Type II-like isotherm compared to theoretical Dual-Mode and Flory-Huggins sorption isotherms.

2.2.4 Diffusion

Diffusion is a kinetic property and describes the movement of a molecule from a region of higher chemical potential to that of lower chemical potential. The diffusional coefficient of a single penetrant is commonly determined by either a steady-state measurement of flux, time-lag observation of sorption and diffusion or transient measurements with a sweep gas.⁽¹¹⁾ Several possible diffusional regimes could exist within the system and can be divided into Case I, Case II, and anomalous diffusion. On one hand, Case I diffusion (Fickian diffusion) is characterized by the diffusion coefficient when the diffusion rate is much slower than the pace at which the polymer chain relaxations occur.⁽¹²⁾ On the other hand, Case II diffusion describes when diffusion is much faster than the rearrangement of the polymer chains.⁽¹³⁾ It becomes more difficult to calculate the diffusion coefficient accurately in this case as the polymer relaxation upon contact with the penetrant is limiting the diffusion. Lastly, anomalous diffusion combines the effects of diffusion through the polymer along with the movement of the polymer chains (Case I and Case II), which share similar time-scales. It is important to consider the effects of polymer swelling, especially in the presence of organic molecules, and account for non-Fickian diffusion within the system. It has been established that diffusion during uptake in PIM-1 falls under anomalous diffusion, which prompts the assumption that its derivatives will perform similarly. ^(14, 15)

2.2.5 Maxwell-Stefan Transport

The solution-diffusion model has often been simplified to a form of Fick's law that can be easily applied to the transport of dilute mixtures as in reverse osmosis applications such as desalination. For multicomponent systems, this can be written as(16)

$$J_i = - \sum_{j=1}^{n-1} D_{ij} \nabla C_j \quad 2.11$$

where n is the total number of components, C_j is the molar concentration of component j , and D_{ij} are multicomponent diffusion coefficients which have a complex dependence on concentration. However, these D_{ij} are dependent on how the system is numbered in the matrix and can take either positive or negative values. Fick's law also stipulates a linear dependence of flux on the system velocity, causing the flux to increase without bounds as the driving force goes to infinity. This is valid within a pore-flow model but the solution-diffusion model requires a bound on the transmembrane concentration gradient that is induced by the driving force.(17) Lastly, in the classical Fickian solution theory, it is assumed that diffusion coefficients are independent of concentration and that the system is thermodynamically ideal.(18) Considering these limitations, application of Fick's law to multicomponent systems is restricted.

Maxwell-Stefan equations have instead been used to described multicomponent transport across various media including light gases, dense liquids and solids, in ionic mixtures and porous structures.(19) The equations can be applied to transport in rigid, porous membranes such as zeolites as well as rubbery, nonporous polymer membranes.

The Maxwell-Stefan theory dictates that chemical potential gradients serve as the driving force for transport through membranes.(20)

$$\frac{x_i}{RT} \nabla_{T,p} \mu_i = - \sum_{j=1}^n \frac{x_i x_j (\mathbf{u}_i - \mathbf{u}_j)}{\mathfrak{D}_{ij}} \quad 2.12$$

where x_i is the mole fraction of component i , \mathbf{u}_i is the component velocity, μ_i is the chemical potential and \mathfrak{D}_{ij} is the Maxwell Stefan diffusivity. Here, \mathfrak{D}_{ij} do represent the inverse of the frictional interactions between component i and j and can depend on the activity of the permeant. Additionally, the nonlinear dependence of flux on the chemical potential gradient is permitted. The Maxwell-Stefan diffusivity of a penetrant through a membrane, \mathfrak{D}_{im} , can also be correlated to the Fickian diffusivity, D_{im} , via a thermodynamic correction factor.(17)

$$D_{im} = \mathfrak{D}_{im} \left(\frac{\partial \ln a_i^m}{\partial \ln x_i} \right) \quad 2.13$$

where, a_i^m is the activity of component i .

2.3 Polymers of Intrinsic Microporosity and their Derivatives

Microporous materials have been studied for use in various applications such as heterogeneous catalysis, gas storage, and molecular separations. Such materials include metal-organic frameworks (MOFs), hypercrosslinked polymers, zeolites, and PIMs, among many others. Polymers of intrinsic microporosity are so named because of the irregular, kinked shape present in the backbone that results in inefficient packing in the solid state

inducing entrapment of large ($\sim 6 \text{ \AA}$) free volume elements.(21) The kinked shape is due to the combination of a ladder backbone and the presence of a spiro-center. The high free volume from these contorted ladder-like structures allow PIMs to have high guest permeabilities. Therefore, they have been widely studied for gas separations and, to some extent, for organic solvent separations. The term intrinsic microporosity defines explicitly a continuous, interconnected network of pores $< 2 \text{ nm}$ in diameter due to the packing of the polymer, although there is debate regarding the interconnected nature of the micropores in PIMs.(22) PIMs are attractive materials for membranes due to their solubility in several polar aprotic casting solvents and synthetically-achievable large molecular weights, which allow them to be solution-processed as free-standing films.(23)

PIM-1, which is the most well-studied PIM (Figure 2.4), has shown promise in gas separations, gas storage, and organic solvent nanofiltration due to its high microporous surface areas of $720\text{-}850 \text{ m}^2/\text{g}$.(24-29) PIM-1 membranes are capable of realizing large organic solvent fluxes with good rejection of organic solutes when there is a $> 500 \text{ Da}$ difference in size in the solute/solvent pair.(30, 31) Thin films of PIMs have been coated on a range of supports, including polyacrylonitrile (PAN), Ultem® 1000 (a polyimide), and alumina.(26, 30, 31) These supports have been tested for OSN with dyes dissolved in alcohols, polystyrene in various aprotic solvents, and solutes such as oligostyrenes and hexaphenylbenzene in nonpolar solvents.(4) Hydraulic permeances in the $1\text{-}20 \text{ liters m}^{-2} \text{ h}^{-1} \text{ bar}^{-1}$ range have been observed, although most PIM materials have not achieved a rejection over 90% or, in other words, a molecular weight cutoff (MWCO) for molecules below 600 Da.

For the prototypical polymer PIM-1, there is a substantial disparity between the apparent pore-size distributions in the “dry” and organic solvent “wet” states. Cryogenic physisorption experiments in solid PIM-1 suggest an average pore size between 3.5 and 5.0 Å. By contrast, the 600 g mol⁻¹ molecular weight cutoff of styrene oligomers in toluene by PIM-1 membranes, corresponds to a pore size of 14 Å in a rigid membrane material such as a ceramic. This discrepancy derives from motion-enabled zones of activation in the semirigid polymer network that undergo swelling and plasticization in organic solvents. A PIM-like polymer that does not exhibit these phenomena should enable separations of small molecules in the organic solvent reverse osmosis (<200 g mol⁻¹) and “tight” organic solvent nanofiltration (200 to 300 g mol⁻¹) regimes. The structural modifications that are valuable in improving the desired separation ability can be identified by developing structure-transport relationships for PIM derivatives.

Researchers have performed at least three different kinds of modifications to PIM-1 to manipulate its gas separation properties. These include a) changing the degree of contortion at the spiro center, b) cross-linking, and c) post-polymerization modification at the nitrile group.(8) Even less flexible polymers can be produced by introducing bulky groups around the spiro center to sterically hinder the rotation.(32, 33) Cross-linking PIM-1 will result in a lower flux of penetrants but also a higher selectivity as it prevents some of the penetrant-induced plasticization that occurs in uncross-linked PIM-1.(34, 35) Amidoxime- (AO) and tetrazole- (Tz) functionalized PIMs (Figure 2.4) exhibit strong hydrogen bonding between the polymer chains, which not only results in a loss of solubility amongst certain protic solvents, but also increases the selectivity of the polar CO₂ over other gases such as N₂ and CH₄.(8) In the case of the Tz-PIM, this is attributed mainly to

the dipole-dipole forces between CO₂ and the amine in the tetrazole group.⁽³⁶⁾ However, in AO-PIM, this is observed to be due to the rigidification of the polymer matrix by inter-chain hydrogen bonding, leading to lower ultramicroporosity (i.e., pores < 6 Å, according to cryogenic N₂ physisorption) and greater size selectivity.⁽⁸⁾ Several researchers have investigated the effects of structural modification to the PIM-1 repeat unit to improve gas separation performance, but these types of studies are less common for organic solvent separations. Although postpolymerization modifications can tune the properties of PIM-1–like materials, structures capable of performing difficult separations without postpolymerization or postfabrication modification would provide more chances to create solutions to these impactful, large-scale challenges.

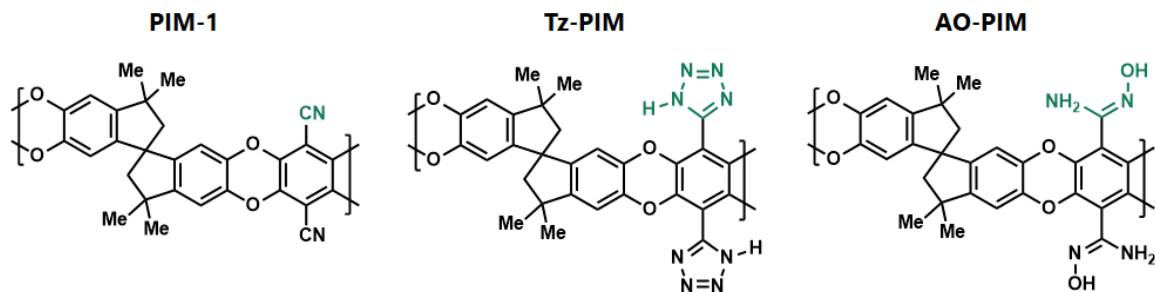


Figure 2.4. The chemical structure of PIM-1 and derivatives, tetrazole-functionalized (Tz-) and amidoxime-functionalized (37) PIM-1.

2.4 Polymer Hollow Fiber Spinning

2.4.1 *Developing the Polymer Dope*

Polymer dopes for spinning hollow fibers typically consist of a combination of the polymer, solvent, nonsolvent, and optionally, a salt or low molecular weight polymer to induce pore formation in the substructure of the fiber. The exact polymer concentrations of spinning dopes are determined by ternary phase diagrams (Figure 2.5)(38, 39) which shows the possible phases a mixture of components can exist in. For polymer dopes, a binodal line separates the one-phase region of the mixture of components from the two-phase region where a polymer rich and a polymer lean phase are obtained. For polymers with unknown phase regimes, such ternary phase diagrams can be created by visual observation of the miscibility of polymer/solvent/nonsolvent mixtures at different compositions. One-phase solutions appear homogenous throughout while solutions in the two-phase region will have separated into two distinct sections. Solutions that are close to the binodal line will appear cloudy or hazy. A secondary envelope exists within the two-phase region and is called the spinodal envelope. The spinodal envelope denotes different types of phase separation mechanisms and the final morphology of the hollow fiber. When a mixture exists between the binodal and spinodal lines, a so-called nucleation and growth process takes over to result in either a polymer-rich phase dispersed in a polymer-lean matrix or a polymer-lean phase in a polymer-rich matrix.(39) When a mixture lies within the spinodal region, the spinodal decomposition process dominates to produce an interpenetrating network of polymer-rich and polymer-lean phases.(39)

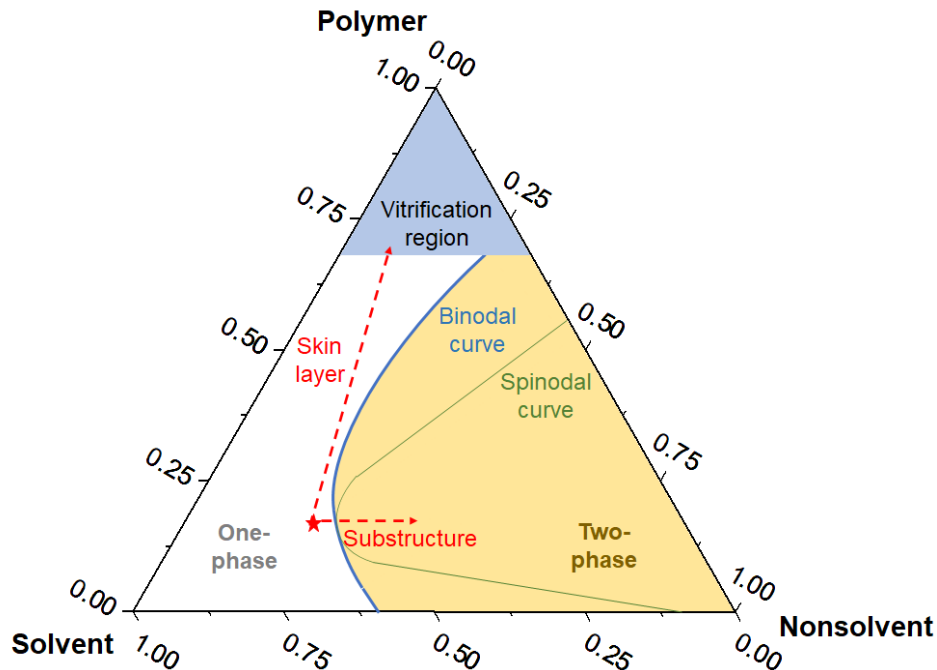


Figure 2.5. Schematic of a polymer ternary phase diagram. Dotted red lines indicate the path of the one-phase polymer dope during phase inversion of the skin and substructure.

The composition of polymer dope chosen for spinning is dependent on the desired morphology of the solid fiber and can be determined by drawing connecting lines on the ternary phase diagram (Figure 2.5). Typically, a thin, dense layer supported by an open spongy substructure provides a desirable performance and mechanical stability.⁽⁴⁰⁾ This dense layer can exist on the shell side or the lumen side. The polymer dope must exist in the one-phase region before extrusion. Once the dope is extruded through a die, a variety of process parameters such as extrusion rate, fiber draw rate and environmental factors such as the air gap between extrusion and quench bath, ambient temperature, ambient humidity, quench bath solvent and quench bath temperature affect the final fiber structure. A dope composition that is close to the binodal line is preferred to induce rapid onset of a

two-phase structure after extrusion.(41) This allows for the formation of a very thin defect-free skin layer atop a spongy interconnected porous network or open-cell substructure. When the dope composition is far from the binodal line and the phase separation is delayed, solvent flows out through the surface into the quench bath for a longer period before a thick skin layer is formed, with a greater chance of defects. With a thick layer hindering solvent-nonsolvent exchange throughout the rest of the fiber, a high local polymer content is obtained underneath and therefore, a dense closed-cell sponge substructure. This type of a fiber membrane is not preferred as both the permeability and selectivity of the resulting fiber are expected to be low.

Finally, polymer dopes must be capable of being drawn out into thin lines through a small aperture, to form the long yet thin configuration that is desired. A preliminary test to determine the drawing tendency of a polymer dope is to perform a syringe extrusion test where pressure is applied to a syringe filled with dope and the extrudate is either allowed to free fall into a quench bath or is drawn by hand through the quench bath. If a continuous line can be drawn without breakage or variation in thickness, the dope can be considered for spinning.

2.4.2 Spinning Process Parameters

During solution spinning, the fluid polymer solution is extruded into cylindrical structures with micron-scale diameters that undergo phase inversion to form solid fibers. As mentioned earlier, fine control of the spinning process parameters permits reproducible fabrication of hollow fibers. The effects of these process parameters are discussed in brief below, although this should not be considered a comprehensive list.

2.4.2.1 Quench Bath

The choice of quench bath liquid and temperature has a significant effect on the kinetics of phase inversion of the skin layer. A strong nonsolvent is recommended in the quench bath when thin, defect-free skin layers are desired. For hydrophilic polymers, water is typically chosen. A strong nonsolvent leads to a quick demixing process and phase inversion, ensuring the formation of a thin dense skin layer.(42) When a weaker coagulant is used, delayed demixing ensues and a more porous and thicker skin layer is formed.(43) The temperature of the quench bath must be optimized for desired skin layer properties; typically, if the temperature is too high, a fast solvent exchange compared to the rate of demixing can cause the formation of pores on the skin layer.(44)

2.4.2.2 Take-up Speed

A high take-up speed enforces elongational tensile stress on the extrudate and the resulting fibers have smaller outer diameters. Further, the increased elongational stress has been observed to increase the chain orientation and packing within the fiber, thereby preventing the formation of macrovoids in the substructure.(45) Moreover, it is hypothesized that a combination of high dope viscosity and high take-up speed prevent nonsolvent intrusion into the extrudate in the radial direction.(46) At low take-up speeds, die swell at the spinneret becomes apparent as the resulting fibers can have outer diameters that are large than the diameter of the spinneret. This die swell is caused by the high pressure that is built up at the spinneret due to the viscosity of the polymer dope.(47)

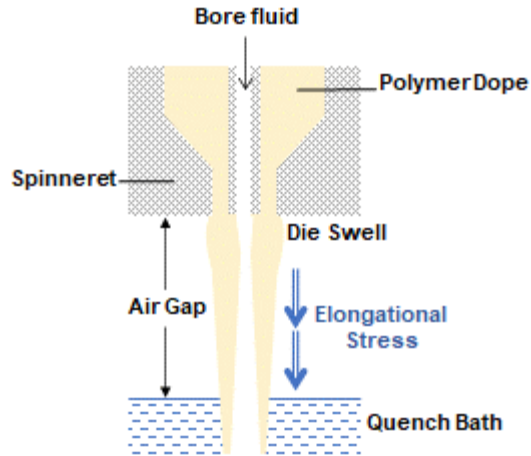


Figure 2.6. Formation of a nascent hollow fiber near the spinneret.

2.4.2.3 Dope Condition and Flowrate

A critical dope viscosity forms the basis of spinning as below a certain viscosity, continuous fibers cannot be formed. Higher solid contents in the dope, which include polymer and nonsolvent additives, lead to higher dope viscosities. On the other hand, increasing the dope temperature will decrease the dope viscosity but increase the solvent exchange rate. A viscous enough dope will suppress macrovoid formation due to chain entanglement and suppression of nonsolvent diffusion.(48) Preventing macrovoid formation is desired as macrovoids reduce the strength of the solid fiber and are subject to compression under pressure during permeation testing which leads to transient (and sometimes at steady-state) undesirably low permeability. The dope extrusion flowrate has similar effects as the dope viscosity. A higher dope extrusion flowrate is typically associated with a less porous surface as well as substructure due to higher solids packing.

2.4.2.4 Bore Fluid

The bore fluid composition and temperature determine the surface morphology of the bore side of the fiber. In addition to creating the bore structure, the bore fluid's main function is to prevent excessive porosity or skin layer formation on the inner surface of the fiber. Typically, a combination of strong solvent and nonsolvent is used to allow solvent exchange before phase inversion for a sufficiently porous structure with minimal transport resistance. Depending on the composition of the bore fluid, the flowrate of the bore fluid can either increase or decrease the porosity and pore size on the bore side of the fiber.(49, 50) Additionally, high solvent concentrations in the bore fluid can increase the porosity of the substructure and affect the porosity of the shell side skin as well.

2.4.2.5 Air Gap

At low take-up speeds, a small air gap will cause the phase inversion of extrudate that is swollen due to die swell at the spinneret. Increasing the air gap can help capture the solid fiber at a lower point in the dope line which is not swollen.(51) Gravitational forces play an important role in the air gap region where the elongational stress increases chain orientation and packing within the fiber.(51) If the air gap is too large and the dope experiences high elongational stress, the dope may break and may not form a continuous line. The presence of moisture in the air gap atmosphere may induce a partial phase inversion of the outer surface, which has the potential for creating ultrathin but often defective skin layers. Moreover, volatile solvents tend to evaporate in this region resulting in changes to the dope composition, most prominently on the shell side. An asymmetric structure is formed where the shell side is less porous or even pore-free (skin layer) and the

bore side is highly porous. Typically, larger air gaps lead to more defect-free (without sub-nm pores) skin layers, while not necessarily affecting the thickness of the skin layers.(6)

2.5 Dip Coating

Dip coating is a simple and effective method for creating composites with thin layers of a desired surface coating and is used across a wide variety of industries. Dip coating is preferred over several other methods of thin film coating due to its simple design, operation, and relatively low cost. The dip coating process relies on fluid rheological properties to enable formation of thin films (Figure 2.7A).(52) The rate of withdrawal determines the thickness of the wet fluid coating on the substrate due to a combination of entrainment and draining forces. Draining forces separate the liquid from the substrate while entraining forces allow the liquid to be retained on the substrate surface. In the fluid mechanical boundary layer above the coating bath interface, the draining and entraining forces are considered to be in equilibrium and the streamlines split according to the magnitude of these forces (Figure 2.7B). This split occurs at the stagnation point, which determines the wet film thickness before drying begins. Therefore, carefully adjusting the stagnation point enables precise control of the thickness of the wet film coating. Above this region, coatings with low volatility will maintain a constant coating thickness until evaporation is induced via heat or convection. When a large quantity of volatiles is present, the thickness of the coating gradually reduces as the solvent escapes, resulting in a wedge shape (Figure 2.7A). Past this, a highly concentrated solution region traps solvent, which can now only escape via diffusion through the gel-like layer. Finally, capillary forces in the almost dry film draw solution into the region, resulting in a thickening of the deposited film before it is fully dried.

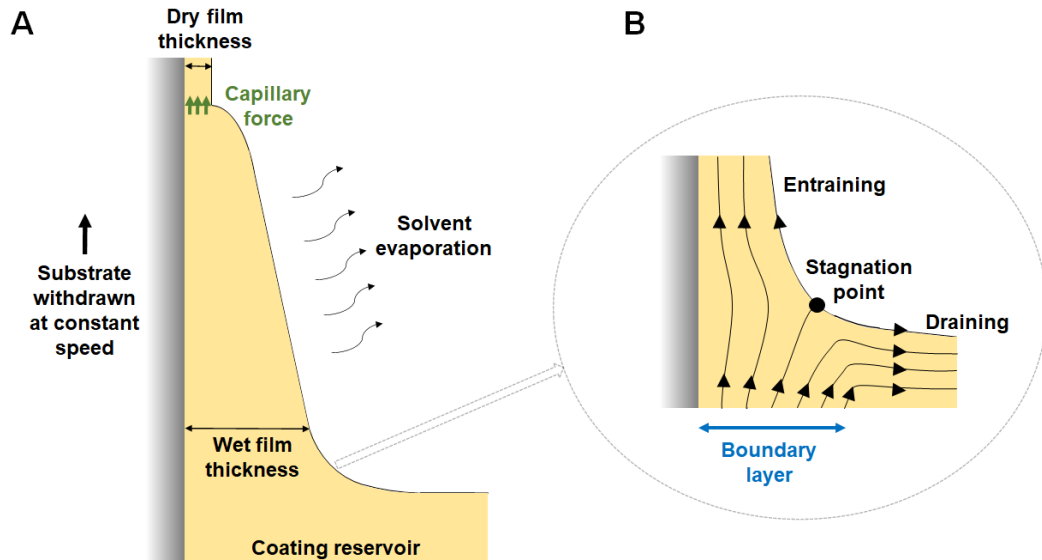


Figure 2.7. A) Steady state of the dip coating process showing the fluid entrainment followed by solvent evaporation. B) Liquid flow streamlines in the dynamic meniscus region close to the coating bath surface depicting the balance between draining and entraining forces.

In the case of very low withdrawal speeds (<0.1 mm/s), the capillary regime is encountered (Figure 2.8). The solvent evaporation is faster than the movement of the substrate line out of the coating bath, which causes a build-up of coating at the edge of the meniscus, known as a “pinned edge”, due to capillary cohesion of the coating solution. While more obvious process parameters such as substrate withdrawal speed and coating solution concentration and composition are the main factors in determining the quality and quantity of coating, other environmental factors such as temperature, humidity, air flow and, importantly, cleanliness will determine whether the films are defect-free and reproducible.

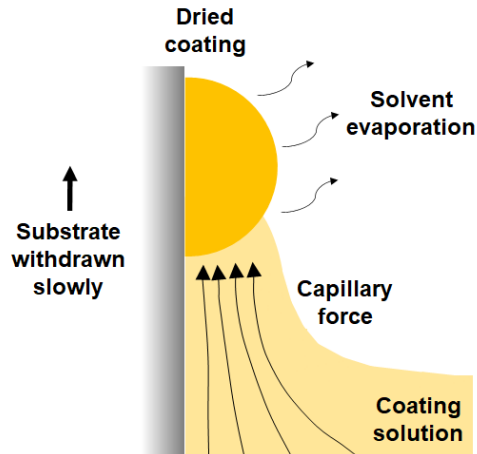


Figure 2.8. Dip coating in the capillary regime. The substrate is withdrawn slowly enough such that evaporation is faster than the velocity of the drying line. Capillary feeding of the coating solution to the edge of the meniscus results in a buildup of dried coating.

2.5.1 Dip Coating Defects

While dip coating is considered a relatively straightforward approach, only precise control over process parameters will allow the formation of an optimized thin film without defects. Dip coating, as a longstanding coating process, has been well studied such that various possible sources of defects have been identified. For the sake of brevity, only the most common defects encountered in dip coating will be discussed here.

2.5.1.1 Stripe Defects

Stripe defects occur when bands of coating are observed to form perpendicularly to the substrate's withdrawal, usually at evenly spaced intervals. A nonuniform or low coating speed with low precision is usually the culprit.⁽⁵³⁾ When the cause is low withdrawal speed, this defect is also known as the "coffee-ring effect" where the formation of the

meniscus occurs as described above in the capillary regime, the substrate is then moved slowly which separates the meniscus from the pinned edge, and a new pinned edge starts to form.(53) Hence, the capillary regime is unfavorable if a consistent film thickness is desired. While the obvious solution may be to increase the withdrawal speed, decreasing the ambient temperature can also reduce this effect by slowing the solvent evaporation rate.

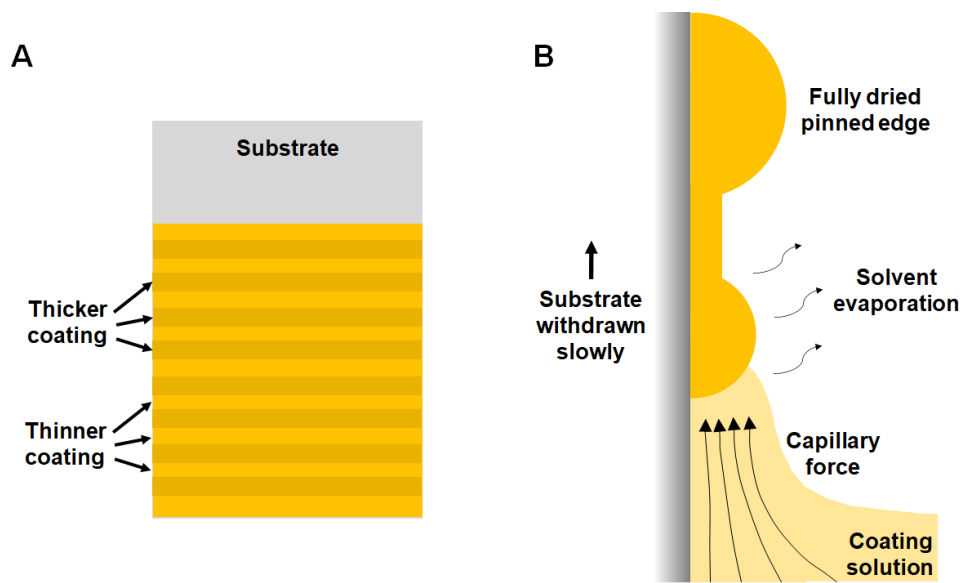


Figure 2.9. A) Stripe defect showing alternating horizontal lines of thick and thin coating. B) Schematic of the coffee-ring effect.

2.5.1.2 Popping

Popping is caused by the blowing out of trapped air or solvent during drying. This is common for dilute coatings in volatile solvents as the outer section of the coating dries quickly, leaving behind trapped solvent in the layers underneath that experiences a high

driving force towards the coating-air interface.(30, 54) The resulting defects may include small volcanoes, craters, pinholes or dimples. These defects are reduced by decreasing the drying temperature or increasing the concentration of the volatile in the atmosphere to slow the rate of evaporation and allow a gradual release of solvent from the coating.

2.5.1.3 Delamination/Dewetting

Dewetting of the coating solution occurs when the coating does not sufficiently cover the substrate due to a high surface tension of the liquid (resulting in highly attractive forces between liquid molecules) or if the surface energy of the substrate is too low.(55) The resulting defect appears as islands or beads of coating. Such a defect can be resolved by using a solvent with a lower surface tension or a substrate with a higher surface energy. Contact angle measurements allow a quick compatibility screening for different substrates where a low contact angle indicates good wettability while a high contact angle ($>90^\circ$) might result in dewetting and is unfavorable.(53)

Delamination is when the dried coating appears lifted off the substrate, leaving a gap between the surfaces. Delamination could occur either due to surface contaminant or due to poor chemical or physical compatibility between the substrate and the coating. Choosing a substrate with similar chemical features or surface energies as the desired coating can prevent such types of defects(56). Further, thorough cleaning of the substrate will also prevent this type of interfacial defect.

2.5.1.4 Cracking

Cracks are often observed after heat is applied to the wet coating to increase the drying rate. They typically appear on the microscale and their occurrence increases with increasing thickness of the film coating. The most common cause for these defects is a mismatch in the thermal expansion of the underlying substrate and the coated film.(55) If the difference in expansion or contraction between the two is significant enough, the coating will experience mechanical stress which leads to cracking. This can be prevented by using a substrate with a similar thermal expansion coefficient to the coating but if the choice of substrate is limited, reducing the thickness of the coating can also reduce the occurrence of cracks.(52, 55)

2.5.1.5 Dust/Foreign Contaminant

Dust or other foreign contaminants such as finger oils can cause small defects such as pinholes or craters. Such contamination can cause a change in local surface energy and either result in a pinhole when the surface energy is low or an aggregation of the coating if the surface energy is high.(53) Thorough cleaning of the substrate and a clean working environment is recommended to prevent such defects during both the coating and drying. It is also recommended that coatings be filtered with a micron-sized pore filter before the coating process.

2.6 References

1. J. G. Wijmans, R. W. Baker, The Solution-Diffusion Model - a Review. *J Membrane Sci* **107**, 1-21 (1995).
2. R. Song, H. A. Stone, K. H. Jensen, J. Lee, Pressure-driven flow across a hyperelastic porous membrane. *J Fluid Mech* **871**, 742-754 (2019).
3. D. R. Paul, Solution-Diffusion Model for Swollen Membranes. *Separ Purif Method* **5**, 33-50 (1976).
4. P. Marchetti, M. F. J. Solomon, G. Szekely, A. G. Livingston, Molecular Separation with Organic Solvent Nanofiltration: A Critical Review. *Chem Rev* **114**, 10735-10806 (2014).
5. M. F. J. Dijkstra, S. Bach, K. Ebert, A transport model for organophilic nanofiltration. *J Membrane Sci* **286**, 60-68 (2006).
6. H. Y. Jang *et al.*, Torlon (R) hollow fiber membranes for organic solvent reverse osmosis separation of complex aromatic hydrocarbon mixtures. *Aiche J* **65**, (2019).
7. P. Li, T. S. Chung, D. R. Paul, Gas sorption and permeation in PIM-1. *J Membrane Sci* **432**, 50-57 (2013).
8. R. Swaidan, B. S. Ghanem, E. Litwiller, I. Pinnau, Pure- and mixed-gas CO₂/CH₄ separation properties of PIM-1 and an amidoxime-functionalized PIM-1. *J Membrane Sci* **457**, 95-102 (2014).
9. A. R. Berens, Solubility of Vinyl-Chloride in Polyvinyl-Chloride). *Angew Makromol Chem* **47**, 97-110 (1975).
10. J. S. Chiou, Y. Maeda, D. R. Paul, Gas and Vapor Sorption in Polymers Just Below T_g. *J Appl Polym Sci* **30**, 4019-4029 (1985).
11. G. R. Gavalas, Diffusion in microporous membranes: Measurements and modeling. *Ind Eng Chem Res* **47**, 5797-5811 (2008).
12. G. Rossi, P. A. Pincus, P. G. Degennes, A Phenomenological Description of Case-II Diffusion in Polymeric Materials. *Europhys Lett* **32**, 391-396 (1995).
13. N. L. Thomas, A. H. Windle, A Theory of Case-II Diffusion. *Polymer* **23**, 529-542 (1982).
14. O. Vopicka *et al.*, Equilibrium and transient sorption of vapours and gases in the polymer of intrinsic microporosity PIM-1. *J Membrane Sci* **434**, 148-160 (2013).

15. M. L. Jue, C. S. McKay, B. A. McCool, M. Finn, R. P. Lively, Effect of Nonsolvent Treatments on the Microstructure of PIM-1. *Macromolecules* **48**, 5780-5790 (2015).
16. R. Taylor, R. Krishna, *Multicomponent mass transfer*. (John Wiley & Sons, 1993), vol. 2.
17. D. R. Paul, Reformulation of the solution-diffusion theory of reverse osmosis. *J Membrane Sci* **241**, 371-386 (2004).
18. R. Krishna, Describing mixture permeation across polymeric membranes by a combination of Maxwell-Stefan and Flory-Huggins models. *Polymer* **103**, 124-131 (2016).
19. R. Krishna, J. A. Wesselingh, Review article number 50 - The Maxwell-Stefan approach to mass transfer. *Chem Eng Sci* **52**, 861-911 (1997).
20. C. P. Ribeiro, B. D. Freeman, D. R. Paul, Modeling of multicomponent mass transfer across polymer films using a thermodynamically consistent formulation of the Maxwell-Stefan equations in terms of volume fractions. *Polymer* **52**, 3970-3983 (2011).
21. P. M. Budd, N. B. McKeown, D. Fritsch, Polymers of intrinsic microporosity (PIMs): High free volume polymers for membrane applications. *Macromol Symp* **245**, 403-405 (2006).
22. N. B. McKeown, Polymers of intrinsic microporosity. *ISRN Materials Science* **2012**, (2012).
23. N. B. McKeown, P. M. Budd, Polymers of intrinsic microporosity (PIMs): organic materials for membrane separations, heterogeneous catalysis and hydrogen storage. *Chemical Society Reviews* **35**, 675-683 (2006).
24. P. M. Budd *et al.*, Gas separation membranes from polymers of intrinsic microporosity. *J Membrane Sci* **251**, 263-269 (2005).
25. P. M. Budd *et al.*, Gas permeation parameters and other physicochemical properties of a polymer of intrinsic microporosity: Polybenzodioxane PIM-1. *J Membrane Sci* **325**, 851-860 (2008).
26. D. Fritsch, P. Merten, K. Heinrich, M. Lazar, M. Priske, High performance organic solvent nanofiltration membranes: Development and thorough testing of thin film composite membranes made of polymers of intrinsic microporosity (PIMs). *J Membrane Sci* **401**, 222-231 (2012).
27. M. L. Jue, R. P. Lively, Targeted gas separations through polymer membrane functionalization. *React Funct Polym* **86**, 88-110 (2015).

28. N. B. McKeown *et al.*, Towards polymer-based hydrogen storage materials: Engineering ultramicroporous cavities within polymers of intrinsic microporosity. *Angew Chem Int Edit* **45**, 1804-1807 (2006).
29. P. M. Budd *et al.*, Polymers of intrinsic microporosity (PIMs): robust, solution-processable, organic nanoporous materials. *Chem Commun*, 230-231 (2004).
30. M. Cook, P. R. J. Gaffney, L. G. Peeva, A. G. Livingston, Roll-to-roll dip coating of three different PIMs for Organic Solvent Nanofiltration. *J Membrane Sci* **558**, 52-63 (2018).
31. P. Gorgojo *et al.*, Ultrathin Polymer Films with Intrinsic Microporosity: Anomalous Solvent Permeation and High Flux Membranes. *Adv Funct Mater* **24**, 4729-4737 (2014).
32. C. G. Bezzu *et al.*, A Spirobifluorene-Based Polymer of Intrinsic Microporosity with Improved Performance for Gas Separation. *Advanced Materials* **24**, 5930-5933 (2012).
33. C. G. Bezzu *et al.*, The synthesis, chain-packing simulation and long-term gas permeability of highly selective spirobifluorene-based polymers of intrinsic microporosity. *Journal of Materials Chemistry A* **6**, 10507-10514 (2018).
34. M. M. Khan *et al.*, Cross-linking of Polymer of Intrinsic Microporosity (PIM-1) via nitrene reaction and its effect on gas transport property. *Eur Polym J* **49**, 4157-4166 (2013).
35. N. Y. Du *et al.*, Azide-based Cross-Linking of Polymers of Intrinsic Microporosity (PIMs) for Condensable Gas Separation. *Macromolecular Rapid Communications* **32**, 631-636 (2011).
36. N. Y. Du, G. P. Robertson, M. M. Dal-Cin, L. Scoles, M. D. Guiver, Polymers of intrinsic microporosity (PIMs) substituted with methyl tetrazole. *Polymer* **53**, 4367-4372 (2012).
37. X.-X. Zhang, J. P. Sadighi, T. W. Mackewitz, S. L. Buchwald, Efficient synthesis of well-defined, high molecular weight, and processible polyanilines under mild conditions via palladium-catalyzed amination. *Journal of the American Chemical Society* **122**, 7606-7607 (2000).
38. C. Cohen, G. B. Tanny, S. Prager, Diffusion-Controlled Formation of Porous Structures in Ternary Polymer Systems. *J Polym Sci Pol Phys* **17**, 477-489 (1979).
39. P. vandeWitte, P. J. Dijkstra, J. W. A. vandenBerg, J. Feijen, Phase separation processes in polymer solutions in relation to membrane formation. *J Membrane Sci* **117**, 1-31 (1996).

40. D. T. Clausi, W. J. Koros, Formation of defect-free polyimide hollow fiber membranes for gas separations. *J Membrane Sci* **167**, 79-89 (2000).
41. J. J. Qin, M. H. Oo, Y. Li, Development of high flux polyethersulfone hollow fiber ultrafiltration membranes from a low critical solution temperature dope via hypochlorite treatment. *J Membrane Sci* **247**, 137-142 (2005).
42. N. Peng *et al.*, Evolution of polymeric hollow fibers as sustainable technologies: Past, present, and future. *Prog Polym Sci* **37**, 1401-1424 (2012).
43. L. Garcia-Fernandez, M. C. Garcia-Payo, M. Khayet, Mechanism of formation of hollow fiber membranes for membrane distillation: 2. Outer coagulation power effect on morphological characteristics. *J Membrane Sci* **542**, 469-481 (2017).
44. K. T. Woo *et al.*, Fabrication of thermally rearranged (TR) polybenzoxazole hollow fiber membranes with superior CO₂/N₂ separation performance. *J Membrane Sci* **490**, 129-138 (2015).
45. K. Y. Wang, D. F. Li, T. S. Chung, S. B. Chen, The observation of elongation dependent macrovoid evolution in single and dual-layer asymmetric hollow fiber membranes. *Chem Eng Sci* **59**, 4657-4660 (2004).
46. N. Peng, T. S. Chung, K. Y. Wang, Macrovoid evolution and critical factors to form macrovoid-free hollow fiber membranes. *J Membrane Sci* **318**, 363-372 (2008).
47. N. Widjojo, T. S. Chung, D. Y. Arifin, M. Weber, V. Warzelhan, Elimination of die swell and instability in hollow fiber spinning process of hyperbranched polyethersulfone (HPES) via novel spinneret designs and precise spinning conditions. *Chem Eng J* **163**, 143-153 (2010).
48. L. Y. Wang, W. F. Yong, L. E. Yu, T. S. Chung, Design of high efficiency PVDF-PEG hollow fibers for air filtration of ultrafine particles. *J Membrane Sci* **535**, 342-349 (2017).
49. F. Tasselli, E. Drioli, Tuning of hollow fiber membrane properties using different bore fluids. *J Membrane Sci* **301**, 11-18 (2007).
50. M. Rahbari-sisakht, A. F. Ismail, T. Matsuura, Effect of bore fluid composition on structure and performance of asymmetric polysulfone hollow fiber membrane contactor for CO₂ absorption. *Sep Purif Technol* **88**, 99-106 (2012).
51. A. L. Ahmad, T. A. Otitoju, B. S. Ooi, Hollow fiber (HF) membrane fabrication: A review on the effects of solution spinning conditions on morphology and performance. *J Ind Eng Chem* **70**, 35-50 (2019).
52. C. J. Brinker, in *Schneller T., Waser R., Kosec M., Payne D. (eds) Chemical Solution Deposition of Functional Oxide Thin Films*. (Springer, Vienna, 2013).

53. J. O. K. Griffin, M., Dip Coating: Practical Guide to Theory and Troubleshooting.
54. C. Z. Liang, J. T. Liu, J. Y. Lai, T. S. Chung, High-performance multiple-layer PIM composite hollow fiber membranes for gas separation. *J Membrane Sci* **563**, 93-106 (2018).
55. B. C. Bonekamp, in *Membrane science and technology series*, A. J. C. Burggraaf, L., Ed. (Elsevier, Amsterdam ; New York, 1996), pp. xviii, 690 p.
56. G. Fourche, An Overview of the Basic Aspects of Polymer Adhesion .1. Fundamentals. *Polym Eng Sci* **35**, 957-967 (1995).

CHAPTER 3. MATERIALS AND EXPERIMENTAL METHODS

3.1 Overview and Collaborator Acknowledgements

This chapter covers the materials and methods behind polymer synthesis, material characterization, membrane fabrication, membrane testing and fundamental transport analyses of polymers. Parts of this chapter are adapted from ‘K. A. Thompson, R. Mathias, D. Kim, J. Kim, N. Rangnekar, J. R. Johnson, S. J. Hoy, I. Bechis, A. Tarzia, K. E. Jelfs, B. A. McCool, A. G. Livingston, R. P. Lively, M. G. Finn, N-Aryl-linked spirocyclic polymers for membrane separations of complex hydrocarbon mixtures. *Science* **369**, 310-315 (2020).’ This work was performed in a highly collaborative approach and the key contributions from coauthors are highlighted below.

SBAD polymer design, synthesis and elemental characterization were conducted by Kirstie Thompson (Georgia Institute of Technology). DUCKY polymer design, synthesis and elemental characterization were conducted by Nicholas Bruno (Georgia Institute of Technology). Polymer model generation and analyses were carried out by Irene Bechis, Andrew Tarzia and Kim E. Jelfs (Imperial College London). Ultem® flat sheet support knife casting, roll-to-roll coating of flat sheets, spiral-wound–module fabrication and spiral-wound–module performance analysis were conducted by Daeok Kim and Jihoon Kim (Imperial College London). The temperature resistance of membranes, whole crude separation and whole crude analysis were conducted by Neel Rangnekar, J.R. Johnson and Scott J. Hoy (ExxonMobil Research and Engineering). Guanghui Zhu (Georgia Institute of Technology) assisted with DUCKY powder physisorption, thin film composite preparation and polystyrene marker testing. PIM-1 polymer for roll-to-roll coating was synthesized by

Yi Ren (Georgia Institute of Technology). Viscosity measurements were performed by Dr. Jianshan Liao (Georgia Institute of Technology), and AFM images were provided by Aaron Liu (Georgia Institute of Technology).

3.2 Materials

Commercially-available diamines [*o*-tolidine (95%) and 1,5-diaminonaphthalene (97%) from Acros Organics; *m*-tolidine (>98%) and 2,5-dimethyl-1,4-phenylenediamine (>98%) from TCI] were rigorously purified before polymerization, as follows. The amine was suspended in H₂O followed by acidification with concentrated HCl. Additional H₂O was added until all amine was dissolved. The acidic diamine solution was then extracted with diethyl ether three times. The aqueous solution was boiled for 30 min while stirring in the presence of decolorizing charcoal (5-10 g, Acros Organics). The solution was allowed to cool to room temperature and the charcoal was removed by vacuum filtration. To the acidic aqueous solution was slowly added 1M NaOH with gentle stirring until the diamine precipitated. The diamine was then separated by vacuum filtration, washed with excess water and dried under vacuum overnight before use.

XantPhos (98%) was purchased from Acros Organics and STREM Chemicals. 1,4-dioxane (99.8% purity, anhydrous) was purchased from Sigma Aldrich in Sure/Seal™ bottles. Torlon® 4000T-LV and Torlon® 4000T-HV powder was obtained from Solvay. Puramem® 280 membranes (Evonik High Performance Polymers) were purchased from Sterlitech Corporation. PIM-1, XantPhos Pd G3 precatalyst, XantPhos Pd G4 precatalyst, and IPr[HCl] were synthesized according to literature procedures (1-4). All other chemicals

were purchased from Sigma Aldrich, Acros Organics, Alfa Aesar, Oakwood Chemical, or TCI and used as received.

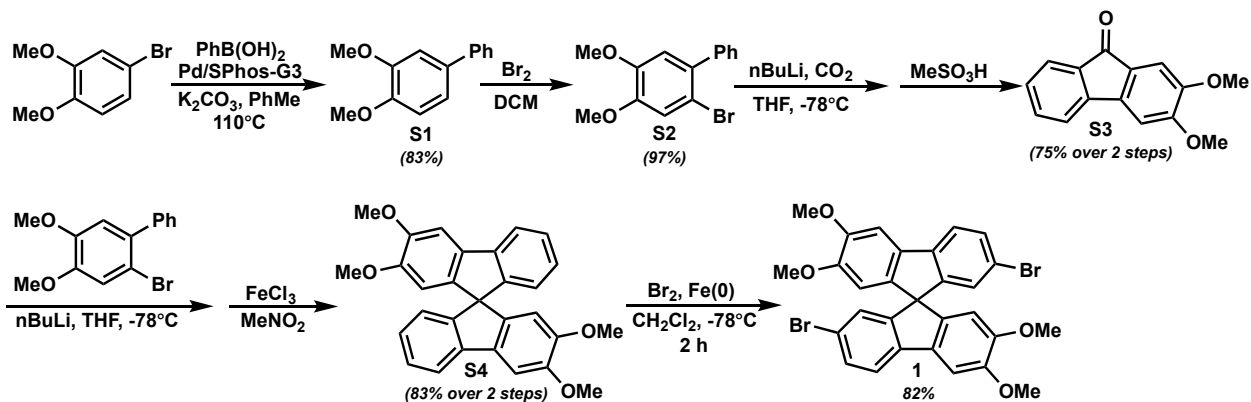


Figure 3.1. Synthetic pathway toward 7,7'-dibromo-2,2',3,3'-tetramethoxy-9,9'-spirobifluorene (1).

3.3 Monomer Synthesis

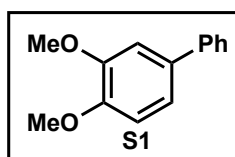


Figure 3.2. 3,4-dimethoxy-1,1'-biphenyl.

3,4-dimethoxy-1,1'-biphenyl: A 500 mL round-bottom flask equipped with a septum and magnetic stir bar was charged with 4-bromoveratrole (21.7 g, 100 mmol, 1.0 equiv), phenylboronic acid (14.5 g, 120 mmol, 1.2 equiv), potassium carbonate (34.5 g, 250 mmol,

2.5 equiv), and toluene (150 mL). The capped flask was sparged with nitrogen for 15 min. Under nitrogen, the precatalyst SPhos-Pd-G4 (39.7 mg, 0.05 mmol, 0.05 mol %) was added in one portion. The flask was then capped and stirred at 110 °C overnight. The reaction mixture was cooled to room temperature, diluted with CH₂Cl₂, and filtered through a plug of Celite on top of silica gel. The resulting solution was concentrated by rotary evaporation and further dried under vacuum to provide the compound as an eggshell white solid (17.9 g, 83% yield). ¹H NMR (400 MHz, CDCl₃) δ 7.63 – 7.55 (m, 2H), 7.45 (dd, *J* = 8.4, 6.9 Hz, 2H), 7.38 – 7.31 (m, 1H), 7.21 – 7.12 (m, 2H), 6.98 (d, *J* = 8.2 Hz, 1H), 3.98 (s, 3H), 3.96 (s, 3H). ¹³C NMR ((126 MHz, CDCl₃) δ 149.07, 148.54, 141.00, 134.20, 128.68, 126.82, 126.80, 119.34, 111.39, 110.39, 55.94, 55.89.

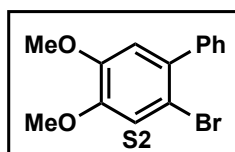


Figure 3.3. 2-bromo-4,5-dimethoxy-1,1'-biphenyl.

2-bromo-4,5-dimethoxy-1,1'-biphenyl: A 250 mL round-bottom flask equipped with a septum and magnetic stir bar was charged with 3,4-dimethoxy-1,1'-biphenyl (15 g, 70 mmol, 1 equiv) followed by the addition of CH₂Cl₂ (100 mL). With vigorous stirring, bromine (3.95 mL, 77 mmol, 1.1 equiv) was added dropwise followed by stirring at room temperature for 1 h. The reaction mixture was quenched with saturated aqueous sodium bicarbonate (~100 mL) followed by saturated sodium sulfite (~50 mL). The layers were

separated, and the organic fraction was washed with water (1 x 50 mL) followed by brine (1 x 50 mL). The organic layer was then dried over anhydrous magnesium sulfate, filtered through a plug of silica gel, and concentrated by rotary evaporation. The crude product was triturated with methanol, filtered, and dried under vacuum to provide the title white solid (23.8 g, 97% yield). ^1H NMR (400 MHz, CDCl_3) δ 7.43 (tdd, $J = 8.6, 6.0, 2.3$ Hz, 5H), 7.15 (s, 1H), 6.86 (s, 1H), 3.94 (s, 3H), 3.89 (s, 3H). ^{13}C NMR (126 MHz, CDCl_3) δ 148.68, 148.20, 141.06, 134.72, 129.48, 127.95, 127.38, 115.67, 113.80, 112.41, 56.20, 56.04.

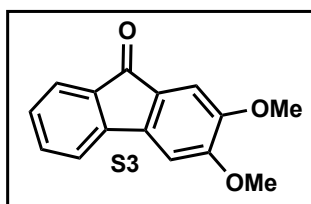


Figure 3.4. 2,3-dimethoxy-9H-fluoren-9-one.

2,3-dimethoxy-9H-fluoren-9-one: A flame dried 1 L round-bottom flask equipped with a magnetic stir bar and rubber septum was charged with 2-bromo-4,5-dimethoxy-1,1'-biphenyl (22 g, 75 mmol, 1 equiv). The flask was evacuated and backfilled with argon three times. Dry tetrahydrofuran (375 mL) was added and the mixture was cooled to -78 °C under argon. A solution of *n*BuLi in hexanes (30 mL, 75 mmol, 1 equiv) was added dropwise. After addition, the mixture was stirred for 2 h at -78 °C. Carbon dioxide, produced from dry ice, was then bubbled through the reaction mixture until the deep yellow color of the reaction mixture dissipated to a pale yellow. The reaction mixture was allowed

to warm to room temperature with a thin gauge needle inserted in the septum to prevent the buildup of pressure. The solvent was removed by rotary evaporation until a solid was obtained. The solid was then dissolved in water and washed with diethyl ether. The aqueous layer was acidified with aqueous HCl and the resulting yellow solid was filtered and dried under vacuum.

The intermediate (**1**) was stirred in mixture of methanesulfonic acid (100 mL) and sulfuric acid (25 mL) at room temperature overnight. The resulting emerald green solution was then poured over ice (approximately 1L) resulting in the precipitation of a vibrant orange solid. The solid was isolated by vacuum filtration, washed with excess water, recrystallized from methanol, and dried under vacuum to provide the title compound as a vivid orange solid (12.6 g, 70% yield). ^1H NMR (500 MHz, CDCl_3) δ 7.56 (dt, $J = 7.2, 0.9$ Hz, 1H), 7.42 (td, $J = 7.4, 1.2$ Hz, 1H), 7.37 (dt, $J = 7.3, 0.9$ Hz, 1H), 7.24 – 7.18 (m, 2H), 7.01 (s, 1H), 4.03 (s, 3H), 3.94 (s, 3H). ^{13}C NMR (126 MHz, CDCl_3) δ 193.16, 154.52, 149.67, 143.90, 139.44, 134.70, 134.19, 128.15, 126.80, 123.72, 119.06, 107.07, 103.36, 56.32, 56.21.

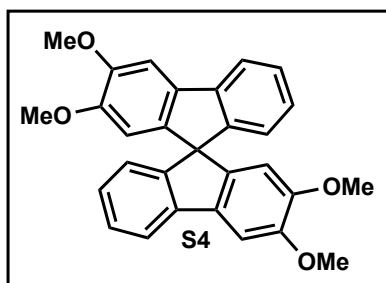


Figure 3.5. 2,2',3,3'-tetramethoxy-9,9'-spirobifluorene.

2,2',3,3'-tetramethoxy-9,9'-spirobifluorene: A flame-dried 500 mL round-bottom flask equipped with a stir bar and rubber septum was charged with 2-bromo-4,5-dimethoxy-1,1'-biphenyl (12.0 g, 41 mmol, 1 equiv). The flask was then evacuated and backfilled with argon three times. Dry tetrahydrofuran (275 mL) was added and the mixture was cooled to -78 °C under argon. A solution of *n*BuLi in hexanes (18 mL, 45.1 mmol, 1.1 equiv) was added dropwise. The reaction was allowed to stir for 2 h after which 2,3-dimethoxy-9H-fluoren-9-one (8.2 g, 34 mmol, 0.83 equiv) was added in one portion. The reaction mixture was allowed to warm to room temperature, stirring overnight. The mixture was quenched with a saturated aqueous ammonium chloride (25 mL) and the tetrahydrofuran was removed from the mixture by rotary evaporation. The aqueous layer was extracted with CH₂Cl₂ (3 x 50 mL) and the combined organic layers were washed with H₂O, dried over MgSO₄, and the solvent removed by rotary evaporation. The resulting off white crude solid was triturated with MeOH and dried under vacuum.

This intermediate (**1**) was transferred to a 250 mL round bottom flask equipped with a stir bar. A small spatula scoop of FeCl₃ was added, along with nitromethane (65 mL). The reaction was allowed to stir for 30 min after which the reaction largely solidified; the remaining solvent was removed by rotary evaporation. The resulting material was dried under vacuum followed by trituration with MeOH. The resulting off-white solid was dried under vacuum to provide the title compound (12.3 g, 83% yield). ¹H NMR (500 MHz, CDCl₃) δ 7.93 – 7.52 (m, 2H), 7.36 (s, 4H), 7.05 (s, 2H), 6.88 – 6.53 (m, 2H), 6.26 (s, 2H), 4.05 (s, 6H), 3.67 (s, 6H). ¹³C NMR (126 MHz, CDCl₃) δ 149.44, 149.26, 149.08, 141.87, 140.75, 134.22, 127.47, 126.50, 123.59, 118.75, 106.73, 102.83, 65.73, 56.11, 55.98.

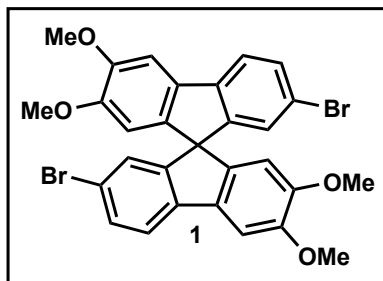


Figure 3.6. 7,7'-dibromo-2,2',3,3'-tetramethoxy-9,9'-spirobifluorene.

7,7'-dibromo-2,2',3,3'-tetramethoxy-9,9'-spirobifluorene: A 100 mL round-bottom flask equipped with a stir bar and rubber septum was charged with 2,2',3,3'-tetramethoxy-9,9'-spirobifluorene (3.7 g, 8.5 mmol, 1 equiv) and Fe(0) (190 mg, 3.4 mmol, 0.4 equiv). The flask was evacuated and backfilled with argon three times. Dry CH₂Cl₂ (30 mL) was added and the reaction mixture was cooled to -78 °C under argon. Bromine (1.3 mL, 25.5 mmol, 3 equiv) was added dropwise and the reaction mixture was allowed to stir for 2 h. The reaction mixture was then poured into excess saturated aqueous sodium sulfite solution while stirring. The solution was extracted with CH₂Cl₂ (3 x 50 mL) and the organic layer was washed with water (1 x 50 mL), brine (1 x 50 mL), dried over MgSO₄, and the solvent was removed by rotary evaporation. The crude material was then purified by column chromatography with a gradual gradient of ethyl acetate and hexanes (10% to 80% EtOAc), providing the title compound as a white solid (4.1 g, 82% yield). ¹H NMR (500 MHz, CDCl₃) δ 7.59 (d, *J* = 8.1 Hz, 2H), 7.49 (dd, *J* = 8.0, 2.0 Hz, 2H), 7.32 (s, 2H), 6.78 (d, *J* = 1.8 Hz, 2H), 6.22 (s, 2H), 4.04 (d, *J* = 2.8 Hz, 6H), 3.69 (s, 6H). ¹³C NMR (126 MHz, CDCl₃) δ 150.27, 149.92, 149.65, 140.85, 139.72, 133.11, 130.89, 126.78, 120.24, 120.10, 106.61, 102.95, 65.36, 56.16, 56.02.

All alkyne monomers for the DUCKY series were synthesized from the common, spirocyclic intermediate **2**, made in one high-yielding step from the inexpensive and widely available bisphenol A at up to 50 g scales. Intermediate **2** could then be brominated with molecular bromine or chlorinated with N-chlorosuccinimide in the presence of thiourea, followed by propargylation to provide monomers **A1** & **A2**, respectively. Halogens on the backbone of the polymers provide handles for future post-polymerization modifications without adding significant steric bulk.

Compound **2** was also alkylated with *tert*-butyl groups with *tert*-butanol and methanesulfonic acid via electrophilic aromatic substitution followed by propargylation to provide the more rigid but still conformationally flexible monomer **A3**. Compound **2** was also alkylated with methyl iodide and brominated to provide intermediate **3**. This compound then underwent a palladium-catalyzed Sonogashira coupling and deprotection to provide monomer **S4**. This monomer is much more rigid as the arylacetylene is much more sterically encumbered both by fewer rotational degrees of freedom as well as the presence of an *ortho* substituent.

Benzyl azide monomers **Z1** & **Z2** were synthesized by S_N2 substitution of the azide anion with the corresponding benzyl bromides. Aryl azide monomers **Z3** & **Z4** were synthesized through the Sandmeyer reaction of the corresponding anilines. All monomers were synthesized at large scales (up to 10 g for **Z1** – **Z4** and 30 g for **A1** – **A4**) and did not require column chromatography, as they could be purified from trituration with methanol and short silica plugs. From **Z1** – **Z4** and **A1** – **A4**, the monomers increase in steric bulk and rigidity, giving us the ability to fine tune the properties of the resulting polymers through different monomer combinations.

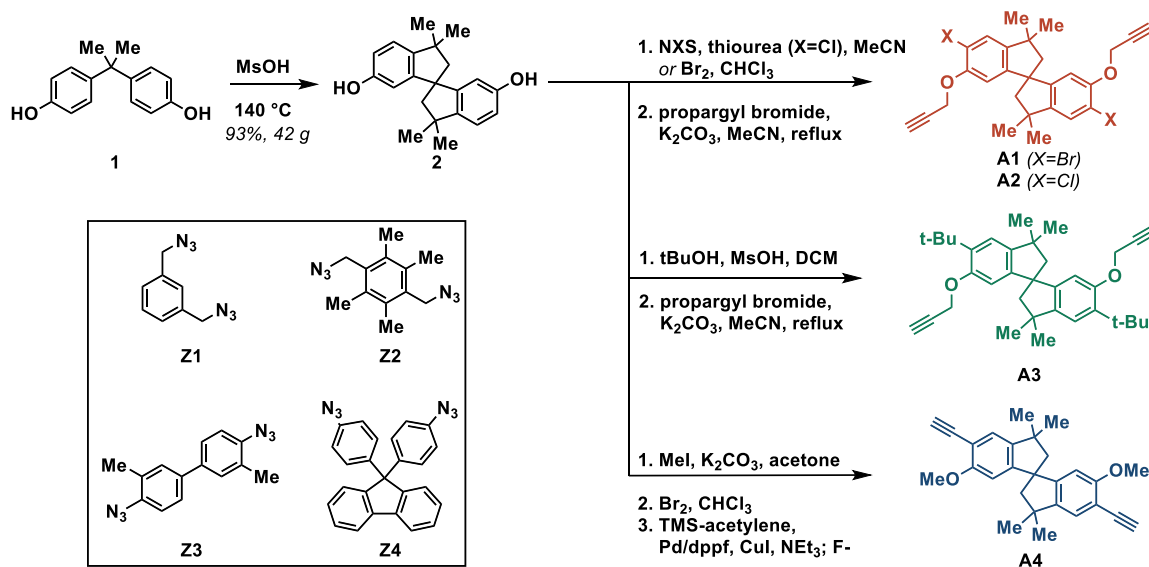


Figure 3.7. Reaction scheme for DUCKY series.

3.4 Polymer Synthesis

Limited reports have been made applying Buchwald-Hartwig as a polymerization method; some notable examples are listed (5-8). For our purposes, bromination of the spirobifluorene monomer as above was followed by careful column chromatography to remove trace quantities of remaining starting material and a tribrominated byproduct. Similarly, rigorous purification of the commercially available diamines as described above was also found to be necessary, presumably due to the ready oxidation of these amines in air.

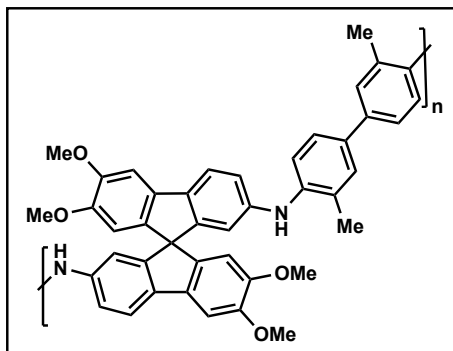


Figure 3.8. SBAD-1 polymer structure.

SBAD-1: A 10 mL microwave vial equipped with a stir bar and crimp cap was charged with *o*-tolidine (212.3 mg, 1 mmol, 1 equiv), 7,7'-dibromo-2,2',3,3'-tetramethoxy-9,9'-spirobifluorene (594.3 mg, 1 mmol, 1 equiv), sodium *tert*-butoxide (288.3 mg, 3 mmol, 3 equiv), and XantPhos-Pd-G4 (48.1mg, 0.05 mmol, 5 mol %). The tube was evacuated and backfilled with argon three times. Dry and air-free dioxane (5 mL, 0.2 M with respect to one monomer) was added and the reaction mixture was allowed to stir for 24 h at 50 °C in an oil bath. The resulting polymer appeared as a solid precipitate, which was isolated by filtration, dried, dissolved in the minimum volume of CHCl₃, and precipitated by addition to methanol (500 mL). The solid was filtered, washed with excess MeOH, and then refluxed in a solution of sodium diethyl dithiocarbamate (~30 mL, 0.25 M) overnight to remove any residual Pd. The polymer was filtered, rinsed with excess MeOH, and dried in a vacuum oven at 80 °C overnight to give a tan solid (521 mg, 81% yield). ¹H NMR (500 MHz, CDCl₃, 318 K) δ 7.56 (d, *J* = 8.1 Hz, 2H), 7.31 – 7.29 (m, 2H), 7.25 (s, 2H), 7.21 (d, *J* = 8.5 Hz, 2H), 7.10 (d, *J* = 8.3 Hz, 2H), 6.99 (dd, *J* = 8.6, 2.2 Hz, 2H), 6.37 (d, *J* = 2.1 Hz, 2H), 6.32 (s, 2H), 5.29 (s, 2H), 3.99 (s, 6H), 3.68 (d, *J* = 3.6 Hz, 6H), 2.17 (s, 6H); ¹³C

NMR (126 MHz, CDCl_3) δ 151.16, 149.45, 148.72, 142.55, 140.45, 140.20, 134.82, 134.57, 133.98, 128.89, 127.49, 124.66, 119.36, 117.81, 116.96, 113.95, 107.42, 102.55, 65.62, 56.14, 43.95, 17.89. Analysis calculated for $\text{C}_{43}\text{H}_{36}\text{N}_2\text{O}_4$ C 80.10, H 5.63, N 4.34 Found C 78.10, H 5.77, N 4.24. GPC (against polystyrene standards, CHCl_3): $M_n = 9.45$ kDa, $M_w = 80.4$ kDa, $D = 8.51$.

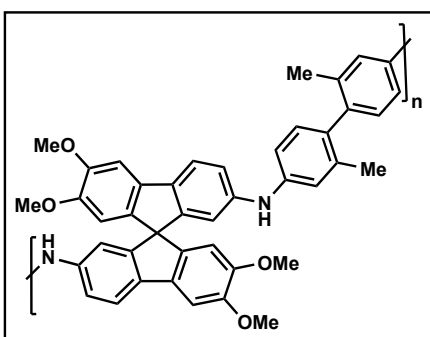


Figure 3.9. SBAD-2 polymer structure.

SBAD-2: A 10 mL microwave vial equipped with a stir bar and crimp cap was charged with *m*-tolidine (159.2 mg, 0.75 mmol, 1 equiv), 7,7'-dibromo-2,2',3,3'-tetramethoxy-9,9'-spirobifluorene (445.7 mg, 0.75 mmol, 1 equiv), sodium *tert*-butoxide (216.2 mg, 2.25 mmol, 3 equiv), and XantPhos-Pd-G4 (36.1mg, 0.038 mmol, 5 mol %). The tube was evacuated and backfilled with argon three times. Dry and air-free dioxane (3.75 mL, 0.2 M with respect to one monomer) was added and the reaction mixture was allowed to stir for 24 h at 80 °C in an oil bath. The polymer appeared as a solid precipitate, which was isolated by filtration, dried under vacuum, dissolved in the minimum volume of CHCl_3 , and precipitated into methanol (500 mL). The solid was filtered, washed with excess MeOH, and refluxed in a solution of sodium diethyl dithiocarbamate (~30 mL, 0.25 M) overnight,

filtered, and rinsed with excess MeOH. The resulting polymer was dried in a vacuum oven at 80 °C overnight providing a tan solid (280 g, 58% yield.) ^1H NMR (500 MHz, CDCl_3) δ 7.80 – 7.39 (m, 3H), 7.11 (s, 3H), 6.79 (d, $J = 54.9$ Hz, 6H), 6.36 (d, $J = 38.0$ Hz, 4H), 5.91 – 5.19 (m, 2H), 3.99 (d, $J = 6.9$ Hz, 6H), 3.84 – 3.41 (m, 6H), 1.88 (s, 6H). ^{13}C NMR (126 MHz, CDCl_3) δ 151.16, 149.47, 148.79, 142.03, 141.96, 140.42, 140.41, 137.14, 134.97, 134.57, 133.87, 130.53, 119.32, 118.14, 117.08, 114.26, 107.42, 102.63, 65.59, 56.17, 56.10, 19.90. GPC (against polystyrene standards, CHCl_3): $M_n = 10.3$ kDa, $M_w = 29.3$ kDa, $D = 2.85$.

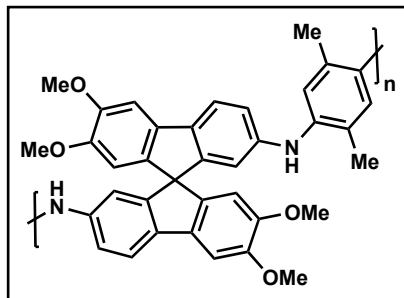


Figure 3.10. SBAD-3 polymer structure.

SBAD-3: A 10 mL microwave vial equipped with a stir bar and crimp cap was charged with 2,5-dimethyl-1,4-phenylenediamine (102.2 mg, 0.75 mmol, 1 equiv), 7,7'-dibromo-2,2',3,3'-tetramethoxy-9,9'-spirobifluorene (445.7 mg, 0.75 mmol, 1 equiv), sodium *tert*-butoxide (216.2 mg, 2.25 mmol, 3 equiv), and XantPhos-Pd-G4 (36.1mg, 0.038 mmol, 5 mol %). The tube was evacuated and backfilled with argon three times. Dry and air free dioxane (3.75 mL, 0.2 M with respect to one monomer) was added and the reaction mixture

was allowed to stir for 24 h at 80 °C in an oil bath. The polymer appeared as a solid precipitate, which was isolated by filtration, dried under vacuum, dissolved in the minimum volume of CHCl₃, and precipitated into methanol. The solid was filtered, washed with excess MeOH, and refluxed in a solution of sodium diethyl dithiocarbamate (~30 mL, 0.25 M) overnight, filtered, and rinsed with excess MeOH (500 mL). The resulting polymer was dried in a vacuum oven at 80 °C overnight providing a tan solid (421 g, 98% yield). ¹H NMR (500 MHz, CDCl₃) δ 7.73 – 7.38 (m, 2H), 7.26 – 7.02 (m, 2H), 6.98 – 6.57 (m, 4H), 6.30 (dq, *J* = 23.5, 11.8 Hz, 4H), 5.38 – 4.79 (m, 2H), 4.12 – 3.73 (m, 6H), 3.67 (d, *J* = 21.3 Hz, 6H), 2.12 – 1.65 (m, 6H). ¹³CNMR (126 MHz, CHCl₃) Complex spectra due to polymer oxidation. Analysis calculated for C₃₇H₃₂N₂O₄ C 78.15, H 5.67 N 4.93 Found C 77.33 H 6.43 N 4.00. GPC (against polystyrene standards, CHCl₃): M_n= 10.3 kDa, M_w= 64.6 kDa, D= 6.25.

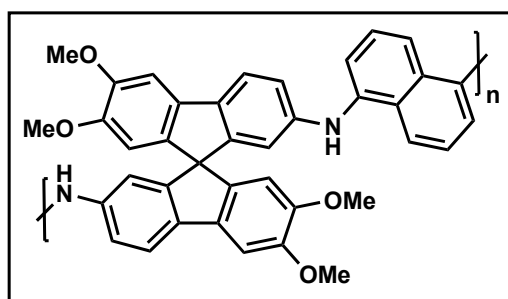


Figure 3.11. SBAD-4 polymer structure.

SBAD-4: A 10 mL microwave vial equipped with a stir bar and crimp cap was charged with 1,5-diaminonaphthalene (158 mg, 1 mmol, 1 equiv), 7,7'-dibromo-2,2',3,3'-

tetramethoxy-9,9'-spirobifluorene (594 mg, 1 mmol, 1 equiv), sodium *tert*-butoxide (289 mg, 3 mmol, 3 equiv), and XantPhos-Pd-G4 (48.1mg, 0.05 mmol, 5 mol %). The tube was evacuated and backfilled with argon three times. Dry and air free dioxane (10 mL, 0.1 M with respect to one monomer) was added and the reaction mixture was allowed to stir for 48 h at 80 °C in an oil bath. The polymer appeared as a solid precipitate, which was isolated by filtration, dried under vacuum, dissolved in the minimum volume of CHCl₃, and precipitated into methanol (500 mL). The solid was filtered, washed with excess MeOH, and refluxed in a solution of sodium diethyl dithiocarbamate (~10 mL, 0.25 M) overnight, filtered, and rinsed with excess MeOH. The resulting polymer was dried in a vacuum oven at 80 °C overnight providing a tan solid (373 g, 63% yield). ¹H NMR (500 MHz, CDCl₃) δ 7.81 – 7.35 (m, 4H), 7.28 – 6.66 (m, 8H), 6.64 – 6.05 (m, 4H), 5.82 (s, 2H), 4.19 – 3.77 (m, 6H), 3.77 – 3.35 (m, 6H). ¹³C NMR (126 MHz, CDCl₃) δ 151.17, 149.47, 148.79, 143.09, 140.46, 139.57, 135.02, 134.54, 133.80, 128.03, 125.42, 119.40, 117.16, 114.13, 107.44, 103.17, 103.00, 102.61, 65.63, 56.15, 56.12. GPC (against polystyrene standards, CHCl₃): M_n= 7.90 kDa, M_w= 57.0 kDa, D= 7.22.

Polymers DUCKY-1 – DUCKY-10 were all synthesized at 1 g scales via the CuAAC reaction in chloroform with (Ph₃P)₂CuOAc as the catalyst. Polymerizations conducted in more coordinating solvents such as THF and DMF had lower rates of reaction and provided polymers with lower molecular weights. Additionally, when other similar copper sources (e.g. (Ph₃P)₃CuBr and (Ph₃P)₃CuCl) were used, no observable reaction took place. Propargyloxy-containing monomers **A1–A3** were polymerized at room temperature with 2 mol% Cu at 0.5 M while arylacetylene-containing monomer **A4** was polymerized at 60 °C with 5 mol% Cu at 0.2 M. The lower concentration is due to the somewhat lower solubility

of the arylacetylene-derived polymers. All of the DUCKY polymers synthesized except for DUCKY-2 exhibit high yields (>90%) and molecular weights (up to 180K), solubilities up to 43 wt% in common organic solvents (DCM, CHCl₃, THF, NMP, DMF, etc.), and excellent film forming properties. After isolation, DUCKY-2 became insoluble in all solvents tested, presumably due to a much higher degree of π - π stacking compared to other DUCKY polymers. Across the board the arylacetylene-containing polymers exhibit lower molecular weights than their propargyloxy counterparts. This is likely due to the increased steric bulk and fewer rotational degrees of freedom making the alkynes less accessible to the copper catalyst. Additionally, to demonstrate the scalability of the polymerization method polymers DUCKY-6 (50g), DUCKY-9 (15g), and DUCKY-10 (20g) were synthesized at large scales and provided polymers with comparable yields and molecular weights to the 1 g polymerizations.

3.5 Polymer Material Characterization

3.5.1 Gel Permeation Chromatography

Gel permeation chromatography (GPC) was carried out using a TSKgel SuperHZM-M (6.0 mm I.D. x 15 cm, 3.5 μ m) column with a flow rate of 0.45 mL/min. Molecular weight was determined from a calibration of polystyrene standards.

3.5.2 Nuclear Magnetic Resonance Spectroscopy

Nuclear magnetic resonance (NMR) spectra were obtained on a Bruker AMX-400 and or Bruker DRX-500 instrument in CDCl₃ and referenced to the signals of residual protons in the NMR solvent.

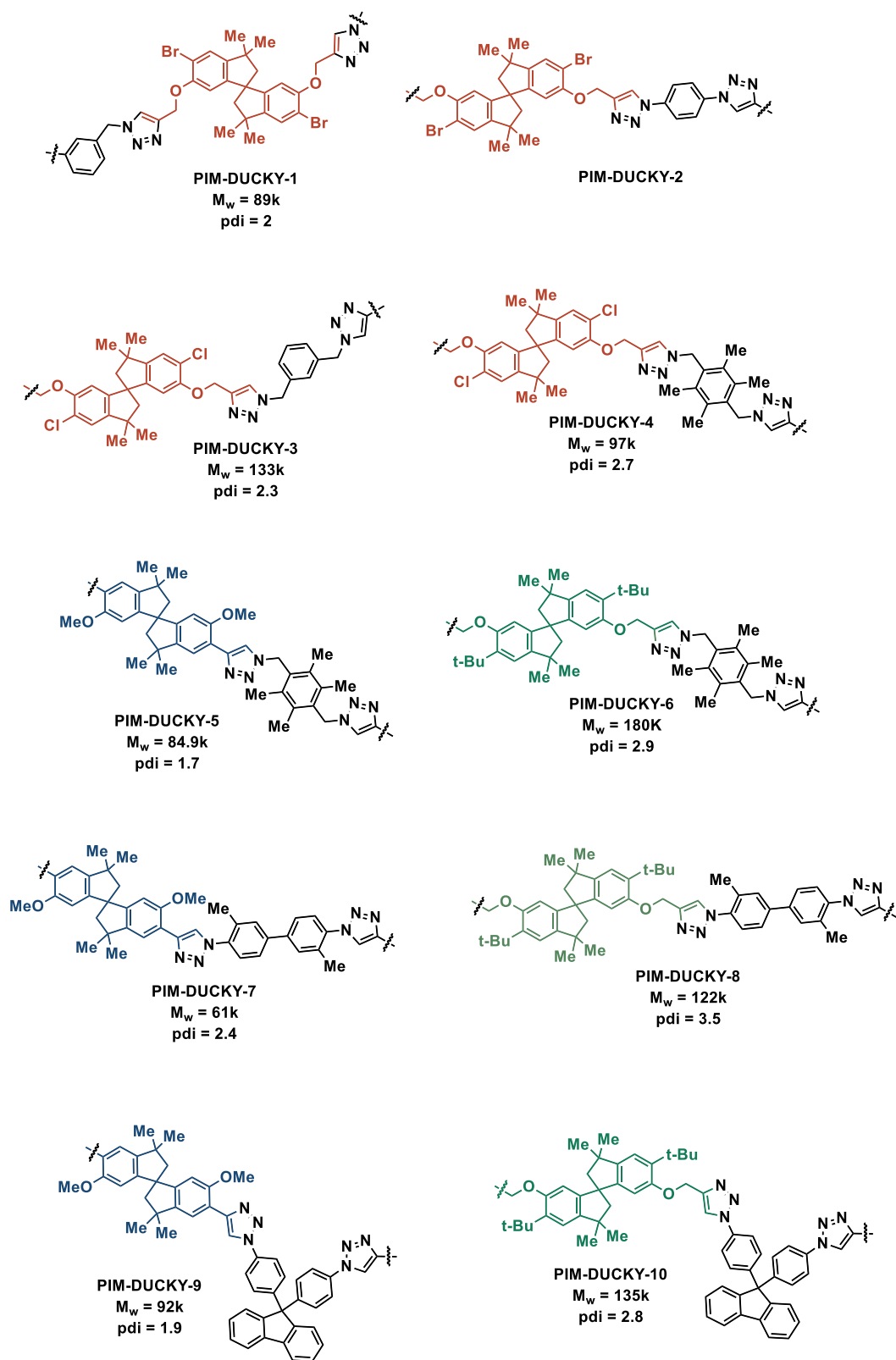


Figure 3.12. DUCKY series polymer structures and GPC results.

3.5.3 *Thermogravimetric Analysis*

Thermogravimetric analysis (TGA) was used to evaluate the thermal stability of the polymers and determine the amount of non-solvent present in the powder after drying at 110 °C for 1 hour. The powders were heated to 900°C at 5°C/min under a nitrogen purge rate of 10 mL/min (TGA Q500, TA Instruments) and subsequently cooled at 10°C/min to room temperature.

3.5.4 *Dynamic Scanning Calorimetry*

Dynamic scanning calorimetry (DSC) was performed by heating samples to 900 °C at a rate of 5 °C/min under 120 mL/min of N₂ (STA 449F3 F3 Jupiter, NETZSCH) to determine the glass transition and melting points of each polymer.

3.5.5 *Gas Physisorption*

Sorption of N₂ (at 77 K) and CO₂ (at 273 K) were measured at relative pressures ranging from 1E-6 to 1 bar with an ASAP 2020 (Micromeritics) analyzer. The polymer powders were degassed for 12 h under vacuum at 110 °C immediately prior to analysis.

3.5.6 *Helium Pycnometry*

Dried SBAD-1 powder samples were analyzed via helium gas at 22 °C (AccuPyc II 1340 FoamPyc V3.00, Micromeritics). An average skeleton density of 1.29 g/cm³ was calculated from 10 cycles.

3.5.7 Hydrocarbon Vapor Sorption

SBAD-1 and PIM-1 powder obtained directly from synthesis were used for vapor sorption experiments. The powder was dried under 29 mm Hg vacuum and 110 °C overnight before analysis and dried again *in situ* at 110 °C under flowing nitrogen for 200 minutes before sorption. The vapor sorption instrument (VTI SA+, TA Instruments) utilized Wagner equation constants to determine the saturation vapor pressure of a liquid and the relative pressure ($p_i/p_{i,sat}$) was controlled by mixing dry nitrogen gas and the headspace of a saturator containing hydrocarbon liquid. Measurements were performed at 25 °C and in triplicate except where noted.

3.5.8 Polymer Solution Viscosity

The rheological measurements were performed on a rotational rheometer (MCR 302, Anton Paar) with a double gap geometry (DG26.7). The effective bob length is 40 mm. The inner bob diameter is 24.6 mm, inner cup diameter 23.8 mm, outer bob diameter 26.7 mm and outer cup diameter 27.6 mm. The temperature for all measurements was at 23 °C. The chloroform was added to the rim of cup to reduce the evaporation of the polymer solution in the cup. The viscosity is measured at shear rates from 1 to 1000 s⁻¹ and then from 1000 to 1 s⁻¹. The reported viscosity is the average value of the points from both intervals.

3.6 Polymer Model Generation

The amorphous structural models for the PIMs were generated with the simulated polymerization algorithm Polymatic (9). Three independent models for each polymer were

generated by randomly packing monomers in a periodic box of 70 Å with a one-to-one ratio at an initial low density of 0.3 - 0.4 g cm⁻³, as done in previous work (10). Previous work has also shown that three models are sufficient for sampling different structures and thus creating representative models that characterize the porosity of these systems, because the standard deviation between models is small (10). For the construction of PIM-1, previously published procedures were used as reference (9). The structures were described using the polymer consistent force field (pcff) (11). Partial charges were calculated for the repeat units by fitting atomic charges from the output of Gaussian16 (12) calculations at the HF/6-31G* level of theory. The molecular models used to derive the charges include the repetition of each monomer twice, in order to derive charges for both the units inside the chain and at the end of the chain, saturated with capping functional groups. In the polymerization phase, bonds were formed between reactive atoms on different monomers within a cutoff of 6 Å. The reactive groups were the aromatic carbon connected to bromine in the spirobifluorene dibromide monomer and the nitrogen for the diamine monomers. The structure was minimized after every new bond was formed, while intermediate molecular dynamics (13) steps in the canonical ensemble were performed once every five new bonds were formed, to allow the structure to adapt and the polymerization to continue, reaching high degrees of polymerization and therefore longer chains. The MD steps were performed at 1000 K for 10 ps using a timestep of 1 fs. Additional opposite fractional charges of 0.3 *e* were added to opposite reactive sites for all the PIMs to aid the polymerization.

Geometric restrictions for PIM-1 were tested to obtain realistic structures, as described elsewhere (9), however, it was found that these restrictions resulted in low

degrees of polymerization of the structures compared to reported structures, whereas removing the restrictions resulted in similar degrees of polymerization to those previously reported (9). The models were carefully examined for any signs of incorrect bonding that the restrictions are supposed to avoid, but did not find any problems in the absence of the restrictions. All qualitative discussion of the differences between PIM-1 and the other four models held regardless of whether restrictions were employed or not. Bromine and hydrogen atoms were used to saturate unreacted active sites on the spirobifluorene and diamine monomers, respectively, after polymerization of SBAD-1, SBAD-2, SBAD-3 and SBAD-4. Fluorine and hydrogen atoms were used to saturate the unreacted aromatic carbon and unreacted oxygen atoms in PIM-1, respectively. The monomers and the capping groups used for each system are reported in Figure 3.13. Selected atom types and derived partial charges for all the atoms in the monomers are reported in Figure 3.13 and Table 3.1.

The final polymerized structures were then annealed through a 21-step molecular dynamics equilibration, an established protocol for generating physically sensible structures of microporous polymers (9). A final temperature value (T_{Final}) of 300 K, a maximum temperature value (T_{Max}) of 1000 K, a final pressure value (P_{Final}) of 1 bar and a maximum pressure value (P_{Max}) of 5×10^5 bar were used for the annealing step. The LAMMPS package (14) was used to perform all the energy minimization and molecular dynamics across the structure generation procedure. Ewald summation was used to compute the long-range electrostatic interactions, the Lennard-Jones (2) potential was used to represent the short-range van der Waals interactions. The cut-off distance for the LJ interactions and the real part of the Ewald summation was set to 15 Å. Constant pressure

and temperature were maintained using a Nosé-Hoover thermostat and barostat during molecular dynamics steps.

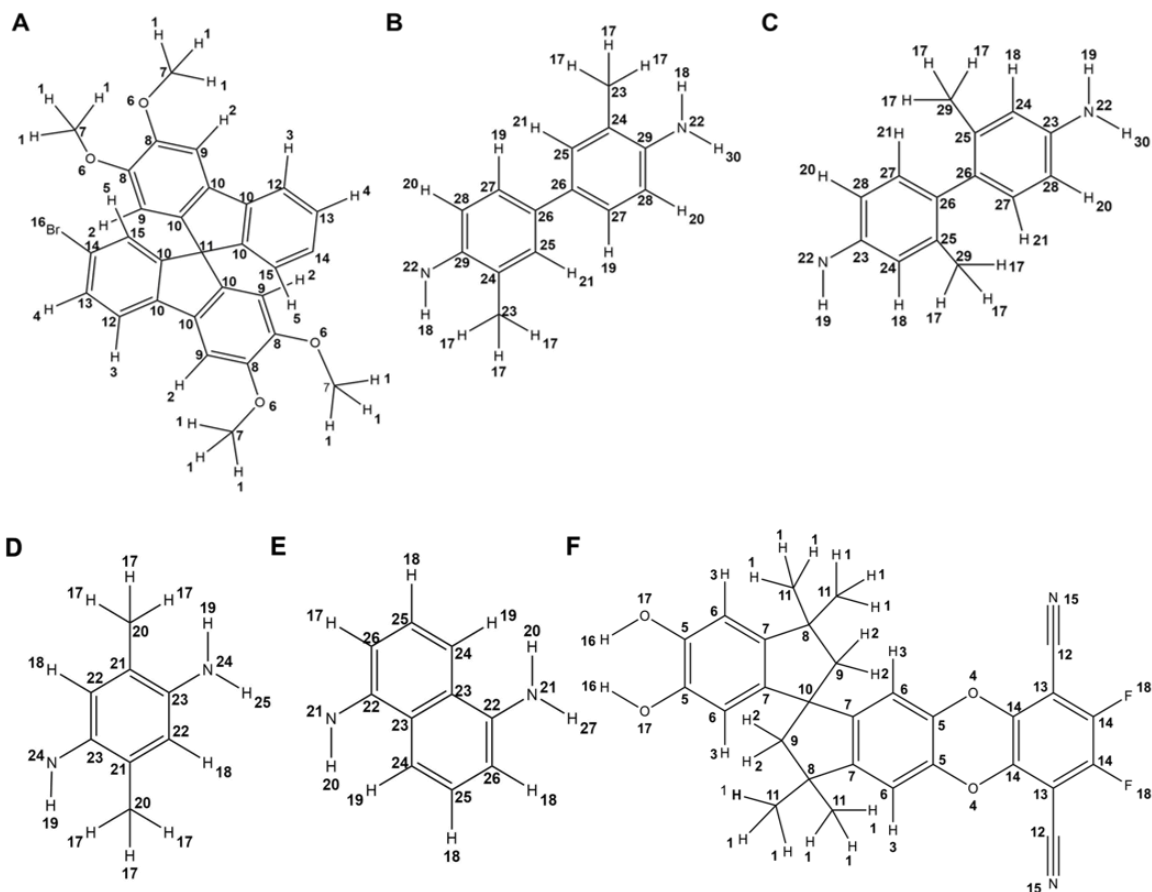


Figure 3.13. Representation of the polymer monomers used for building the polymer models, with labelled atoms. A) monomer A for all the SBAD family polymers B-E) monomer B for SBAD-1-4. F) PIM-1 monomeric unit.

Table 3.1. Force field atom type and partial charges assigned to the atoms in the models. Monomer and atoms labels refer to the ones reported in Figure 3.13.

SBAD -1	A	type	charge	B	Type	charge	SBAD- 2	A	type	charge	C	type	charge
	1	hc	0.0451	17	Hc	0.1010		1	hc	0.0591	17	hc	0.1360
	2	hc	0.1631	18	Hn	0.3803		2	hc	0.1592	18	hc	0.2510
	3	hc	0.1438	19	Hc	0.1758		3	hc	0.1415	19	hn	0.2805
	4	hc	0.1531	20	Hc	0.1896		4	hc	0.1505	20	hc	0.2389
	5	hc	0.1545	21	Hc	0.1982		5	hc	0.1769	21	hc	0.1888
	6	oc	-0.3543	22	Nb	-0.6420		6	oc	-0.3317	22	nb	-0.7447
	7	c	0.0360	23	C	-0.2702		7	c	-0.0317	23	cp	0.5588
	8	cp	0.2171	24	Cp	0.1564		8	cp	0.2210	24	cp	-0.5845
	9	cp	-0.2612	25	Cp	-0.3461		9	cp	-0.2572	25	cp	0.3582
	10	c5	-0.0281	26	Cp	0.1172		10	c5	-0.0344	26	cp	-0.1866
	11	c	0.3471	27	Cp	-0.2389		11	c	0.3878	27	cp	-0.0239
	12	cp	-0.1434	28	Cp	-0.2165		12	cp	-0.1699	28	cp	-0.4375
	13	cp	-0.3561	29	Cp	0.1932		13	cp	-0.3310	29	c	-0.3069
	14	cp	0.4020	30	Hn	0.3767		14	cp	0.4341	30	hn	0.3708
	15	cp	-0.2871					15	cp	-0.3320			
16	br	-0.1075				16	br	-0.1070					
SBAD -3	A	type	charge	D	Type	charge	SBAD- 4	A	type	charge	E	type	charge
	1	hc	0.0569	17	Hc	0.0905		1	hc	0.0584	17	hc	0.1923
	2	hc	0.1572	18	Hc	0.2155		2	hc	0.1720	18	hc	0.1780
	3	hc	0.1483	19	Hn	0.3814		3	hc	0.1548	19	hc	0.1429
	4	hc	0.1342	20	C	-0.1739		4	hc	0.1643	20	hn	0.3423
	5	hc	0.1595	21	Cp	0.0775		5	hc	0.1673	21	nb	-0.5284
	6	oc	-0.3323	22	Cp	-0.3398		6	oc	-0.3424	22	cp	0.2257
	7	c	-0.0184	23	Cp	0.2056		7	c	0.0031	23	cp	0.0309
	8	cp	0.2164	24	Nb	-0.6378		8	cp	0.2097	24	cp	-0.1780
	9	cp	-0.2529	25	Hn	0.3760		9	cp	-0.2562	25	cp	-0.1504
	10	c5	-0.0391					10	c5	-0.0034	26	cp	-0.2553
	11	c	0.4147					11	c	0.1675	27	hn	0.3724
	12	cp	-0.1968					12	cp	-0.2319			
	13	cp	-0.2707					13	cp	-0.2860			
	14	cp	0.3943					14	cp	0.3038			
	15	cp	-0.3010					15	cp	-0.2648			
16	br	-0.1090				16	br	-0.1182					

3.7 Polymer Model Analysis

The final structures obtained after annealing were used for the analysis. All the obtained results are averaged over the three different models for each structure. For the porosity analysis, Zeo++ (15, 16) was used, which uses a Voronoi decomposition to calculate void space, pore size distribution and the interconnectivity between voids given a certain probe radius. The structure is treated as rigid, therefore the flexibility of the system is not taken into account in the porosity evaluation. The accessible and non-accessible surface area in the structures were calculated with a probe diameter of 2 Å, 2.2 Å, 3.30 Å (kinetic diameter of CO₂) and 3.64 Å (kinetic diameter of N₂)(17). The calculations were performed using the high accuracy flag. Surface areas were calculated using 5000 samples (number of MC samples per atom). Pore size distributions were calculated using 50000 samples per cell. For the pore size distribution, 200000 samples were used. For the accessible and inaccessible surface area, 3000 – 4000 samples per atom were used.

3.8 Computational Polymer Swelling

Each annealed model of PIM-1, SBAD-1 and SBAD-3 was artificially swollen using the approach developed by Colina et al. (40). The swelling procedure generates models at different swelling percentages by expanding the systems' periodic box length (L) by a dilation factor, f . The annealed structure was considered a model with 0% swelling. The change in volume ($\Delta V/V$) due to swelling (or swelling percentage) is given by

$$\frac{\Delta V}{V} = \frac{(fL)^3}{L^3} - 1 \quad 3.1$$

After expansion, the atom positions are remapped to equivalent relative positions in the new simulation box. Values of f in this work ranged from 1.000-1.225, and the corresponding $\Delta V/V$ values ranged from 0.00% to 83.83%. The swollen system was then equilibrated using two sequential MD simulations in the NVT (canonical) ensemble at 600 K for 100 ps and 300 K for 50 ps, respectively. An artificial swelling procedure was applied because simulating adsorption-based swelling was deemed computationally intractable. Crucially, the artificial swelling procedure does not include sorbates. The role of swelling on the potential porosity of PIM-1, SBAD-1 and SBAD-3 was examined using the geometrical porosity calculated by Zeo++ (using the same sampling and probe sizes as the non-swollen models).

3.9 Membrane Fabrication and Housing

3.9.1 Dense Films

A dense film of SBAD-1 was prepared by pouring a 10 wt% chloroform solution of the polymer into a leveled Teflon dish in a glove bag saturated with chloroform vapor. The disk was allowed to stand for 24 h, and the film was then allowed to dry as the atmosphere was gradually depleted of solvent vapor over the course of 3 days. The film was then further dried under vacuum (-29 mm Hg) at 110 °C overnight.

3.9.2 Flat Thin Film Composites

Flat thin film composites were synthesized through various methods including spin coating, blade coating and roll-to-roll dip coating with the latter two methods achieving a greater amount of success compared to the former. Due to this, spin coating was only

pursued for a few samples before a transition was made to blade coating for small scale testing and to roll-to-roll dip coating for large scale testing.

3.9.2.1 Spin Coating

Crosslinked Matrimid® supports were fabricated following a previously established protocol.⁽¹⁸⁾ Matrimid® powder was first dried overnight under vacuum at 110 °C. A dope of Matrimid® was prepared in a combination of volatile and non-volatile solvents, non-solvents and a pore-former. Each of these components plays an important role in determining the porosity within the asymmetric membrane structure. A composition ratio (wt%) of 16:69:10: 3:1:1 of Matrimid®, NMP, THF, ethanol, water and lithium nitrate was used and mixed in a 20 mL vial. The dope was sealed with electrical tape and left on a roller overnight until fully mixed. The dope vial was then taken off the roller and degassed by letting it stand upright for 12 hours. The dope was then poured onto a cleaned, smooth glass substrate on top of a leveled table and an automatic mover was used to draw the dope across the plate at a rate of 20mm/s using a doctor blade with a height of 250 microns. 20 seconds were allowed for the THF to evaporate off the top of the film before the glass plate was placed in a bath containing DI water, which immediately led to phase inversion of the film. It is essential that the glass plate is kept level throughout the moving and submersion process. After 20 minutes in the first DI water bath, when the membrane had floated off the plate, it was placed into a bath containing fresh DI water for 24 hours. The support membrane was then solvent exchanged in methanol 3 times to remove any residual solvent or lithium nitrate. A 5wt% solution of p-xylylenediamine was prepared in methanol and Matrimid® supports were submerged in this solution to crosslink for 24 hours. The support was then solvent exchanged in methanol again 3 times before allowing to air dry and then

dried in a vacuum oven at 110 °C overnight. Thin film composite membranes were prepared using a spin coater (WS-650Mz-23NPPB-UD-3, Laurell Technologies). 1 mL of a 0.3 wt% polymer solution in tetrahydrofuran was chilled in a fridge to 4 °C overnight. A circular coupon of the crosslinked Matrimid® support was centered onto the rotating table in the spin coater and suctioned using a vacuum pump. Before casting, nitrogen was allowed to purge through the spin coater for 15 minutes. Ten to fifteen Kimwipes were then soaked in chloroform and placed in the edges of the spin coater to create a saturated chloroform environment for a few minutes. 0.5 mL of the polymer solution was first aliquoted onto the center of the support, spinning at a speed of 1000 rpm. The support was allowed to rotate for 60 seconds at this speed after which, the procedure was repeated to generate a '2-layer' film. The thin film composite is then allowed to air dry for 1 day.

3.9.2.2 Roll-to-Roll Knife Casting

Membrane supports were prepared using polyetherimide (PEI, ULTEM 1000) powder that was evacuated at 100 °C 12 h before use. A 23 wt% dope solution of PEI was prepared by dissolving the powder in a binary mixture of GBL/NMP (70/30 on a weight basis) by stirring at 70 °C for one day and then filtered using nylon net filter (11 µm pore size, Millipore) and stored for a day at room temperature to remove bubbles. Membranes were cast from the PEI dope solution on polyethylene terephthalate (PET) non-woven backing (Hirose) by using a continuous casting machine (SeptraTek, Korea) with a casting knife set at 170 µm. The casted film was plunged into a water bath set to 19°C to induce phase inversion. To enhance the chemical stability of PEI membranes for the usage in various organic solvents, PEI polymeric chains were crosslinked using diaminopropane (DAP) by immersing in a solution of 1 wt% of DAP in MeOH for 1 day, then placed in a solution of

5 wt% of DAP in MeOH for 22 h. At the end of the reaction, membranes were thoroughly rinsed with water and IPA and then dried at room temperature.

3.9.2.3 Blade Coating

Thin film composites were produced from chloroform solutions of each polymer (0.5-2 wt%) filtered through 0.2 μm PTFE syringe filters (VWR) and chilled to 4 °C overnight. Using a 25 μm stainless steel bar applicator (Gardco), each solution was blade-coated onto a flat crosslinked polyetherimide (PEI) prepared as described above. The nascent polymer film was allowed to dry overnight at room temperature in a fume hood before circular coupons with an effective surface area of 14 cm^2 were cut out for testing.

3.9.2.4 Roll-to-Roll Dip Coating on Flat Supports

Polymer solutions were prepared at 0.8 wt% in chloroform and filtered through 200nm PTFE (FGLP04700, Merk) filters. Thin film composites were then prepared by coating onto crosslinked polyetherimide supports (average pore size: 9nm) via a roll-to-roll process line (RK Print, UK) as described elsewhere (19) at a casting speed of 5m/min and a drying temperature of 55 °C in an air-convection dryer.

3.9.3 *Spiral Wound Modules*

To prepare a membrane module of SBAD-1 (Figure 3.14), membranes (prepared through roll-to-roll processing) were soaked in a solution of PEG400-IPA (1:1) for 24h then dried at room temperature until all IPA was removed. A membrane sheet (dimensions 0.3m x 1.7m) was cut from the prepared membrane roll, laid out, and folded in half with the coating layer facing inward. A sheet of feed spacer from Top Zeven, Netherlands

(Polypropylene 2680, 28 mil thickness) was then placed between the folded membrane sheet. The permeate spacer from Sefar, Switzerland (PROPYLTEX 05-210/32, 295 μm thickness) was then attached to a perforated tube. Next, the “membrane-feed spacer-membrane sandwich” was glued on three sides at 70 °C forming an envelope open to the permeate tube. The solvent-stable glue designated EMET0001 was purchased from Evonik MET Limited (UK). After the envelope was completely wrapped around the permeate tube, extra glue was pasted along the straps on the outer surface of the roll to keep the spiral configuration and prevent unwrapping. The final rolled modules were approximately 0.0457 m in diameter and 0.3048 m long (1.8" \times 12"). Each module was made up of one membrane leaf ($\sim 0.4\text{m}^2$, $\sim 1.5\text{ m} \times \sim 0.25\text{ m}$) resulting in an effective area of $\sim 0.2\text{ m}^2$.

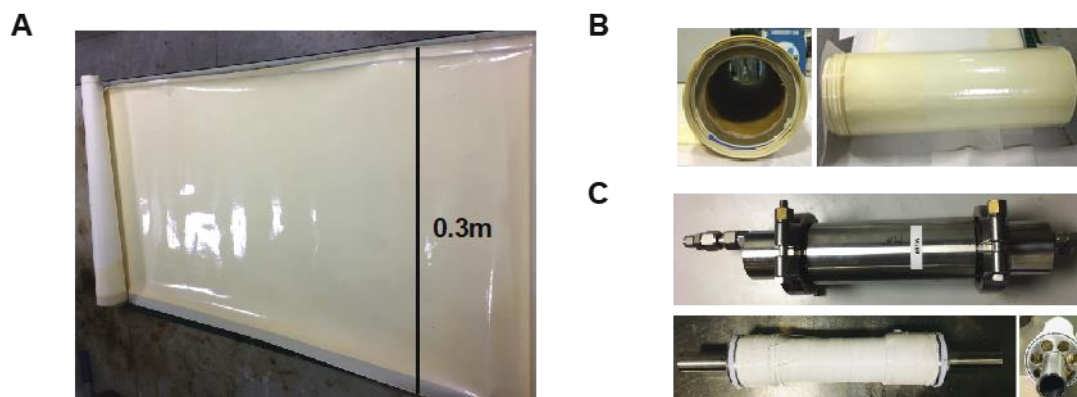


Figure 3.14. (A) Thin film composite sheet of SBAD-1 on Ultem®. (B) Scaled-up flat sheet membrane roll of SBAD-1 prepared through roll-to-roll coating. (C) Spiral wound SBAD-1 module comprised of 1.8 m x 0.2 m of membrane.

3.9.4 Hollow Fiber Spinning

Torlon® hollow fiber supports were fabricated using a spinning system illustrated in Figure 3.15. A core polymer solution is extruded with a bore fluid through a custom-built spinneret under pressure provided by high pressure syringe pumps (Teledyne Isco). The extrudate is then submerged into a quench bath containing water at a set temperature, which acts as a nonsolvent and phase inverts the polymer. The vitrified polymer is guided under a pulley in the quench bath and onto a take-up drum placed externally, where a controlled drum rotation speed affects the fiber draw rate from the quench bath. Several factors in the spinning method affect the morphology of the resulting fiber (20) and in the work presented here, the main adjustments were made to the polymer dope concentration and the fiber draw rate.

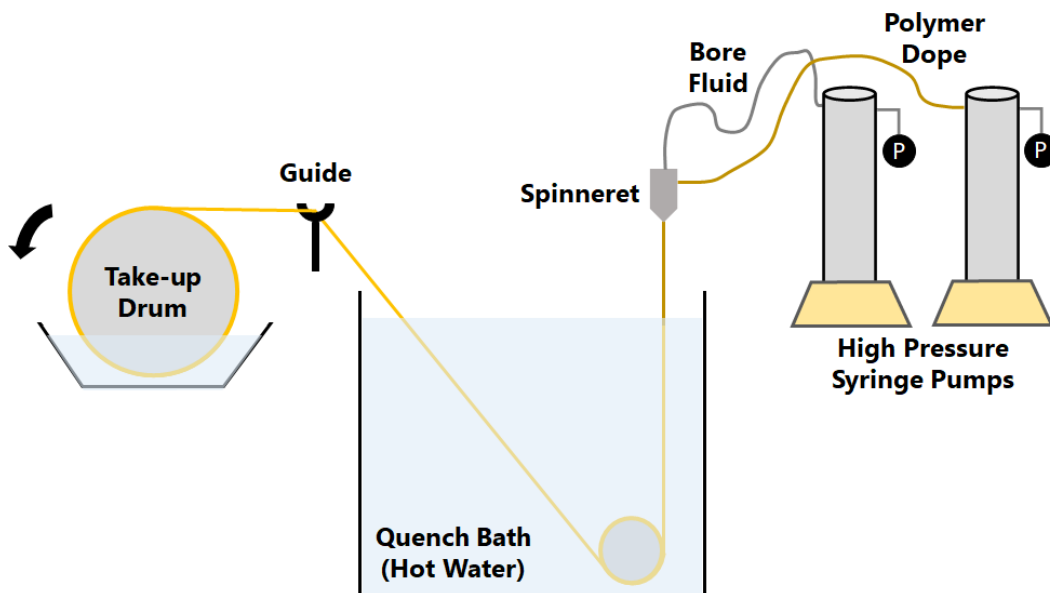


Figure 3.15. Schematic of a hollow fiber spinning system setup.

3.9.5 Roll-to-Roll Dip Coating on Hollow Fibers

The roll-to-roll coating of hollow fibers was performed on a custom-built equipment illustrated in Figure 3.16. The spool of support Torlon® fibers was unwound with the means of pulleys, where the fiber is first guided into a coating solution bath, then an oven with controlled temperature and finally, a take-up drum with a controlled take-up rate. Coating solution concentration, oven temperature and fiber draw rate are the main parameters to be adjusted in this process.

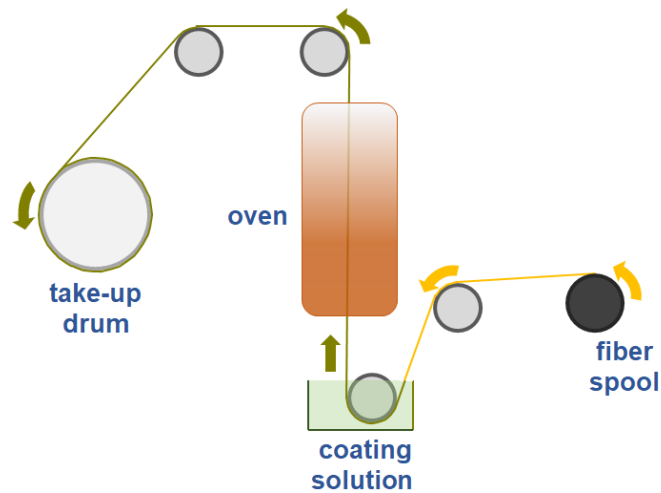


Figure 3.16. Simple schematic of the roll-to-roll coating process of hollow fiber membranes.

3.9.6 Hollow Fiber Module Fabrication

The thin film composite hollow fibers were sealed in stainless steel housing that was capable of withstanding high operating pressures. The modules were fabricated from $\frac{1}{4}$

inch stainless Swagelok® tubing and fittings: two union tees (316 SS), three port connectors (316 SS) and three nuts with ferrules (316 SS). The union tees were first connected with a single port connector and nut. 15 cm fibers were cut and fixed in place within this housing using Teflon tape on either ends of the tees. Tweezers were used to pack the Teflon tape around the fibers and into the openings of the tees such that no epoxy would leak through. J-B Weld Marineweld epoxy mix was then syringed through a pipette tip into one end of a tee until filled. This end was then connected to another port connector and nut, making sure to allow the fiber to run through and out of the connector. More epoxy was syringed into the connector until filled and no air bubbles were present. After 6 hours, the other end was sealed in a similar manner. The sealant was allowed to cure for at least 24 hours before testing for gas or liquid permeation.

3.10 Membrane Material Characterization

3.10.1 Scanning Electron Microscopy

Field Emission Scanning Electron Microscopy (FE-SEM) was used to obtain ultra-high-resolution images of the thin film composites (Hitachi SU8010). Samples were cut with a sharp razor blade and placed on aluminum mounts using carbon tape. A turbomolecular pumped coater (Quorum Q-150 T ES) was used to sputter coat the samples with a layer of a gold/palladium alloy under a deposition current of 10 mA for 45 seconds. Images were obtained with a voltage of 3kV and a current of 10 μ A at a working distance of 8 mm.

3.10.2 Hydrocarbon Liquid Sorption

Liquid sorption was measured by submerging weighed flat dense film fragments in pure and mixed liquid hydrocarbons at room temperature (22 °C) for at least 1 month for SBAD-1 and 3 days for PIM-1. The resulting solvated films were weighed after wiping the surface dry with a Kimwipe. Each measurement was performed twice. Measurements with sorption under 5 wt% were not included in the final data as reliable mass uptakes could not be obtained.

3.10.3 Atomic Force Microscopy (AFM)

Atomic force microscopy (Dimension Icon, Bruker) was performed on the shell side surface of hollow fiber membranes. The images were obtained in tapping mode with n-type silicon cantilever/tip (HQ:NSC14/No Al, MikroMasch) with an 8 nm radius. The images were captured at a scan rate of 0.990 Hz and a resolution of 512 x 512 pixels.

3.11 Membrane Performance

3.11.1 Flat Sheet Membrane Performance

3.11.1.1 Synthetic Hydrocarbon Feeds

Liquid permeation was measured with a custom-built cross flow system (Figure 3.17) pressurized by an HPLC pump (Azura P 4.1S, Knauer). Circular flat thin film composite coupons were inserted into the top section of the sample cells containing solvent-resistant Kalrez o-rings to prevent the membranes from being cut by the hard metal. The intended feed side of the membrane is allowed to face the o-ring and a porous stainless steel disc

(Sterlitech) is placed behind the membrane for mechanical support during permeation. The top and bottom sections of the cells were then sealed with high pressure bolt clamps (Grainger). The sealed cells are connected into the cross flow system via ¼ inch stainless steel Swagelok nuts. The three cells could be run independently as bypass lines were created between the feed and retentate valves.

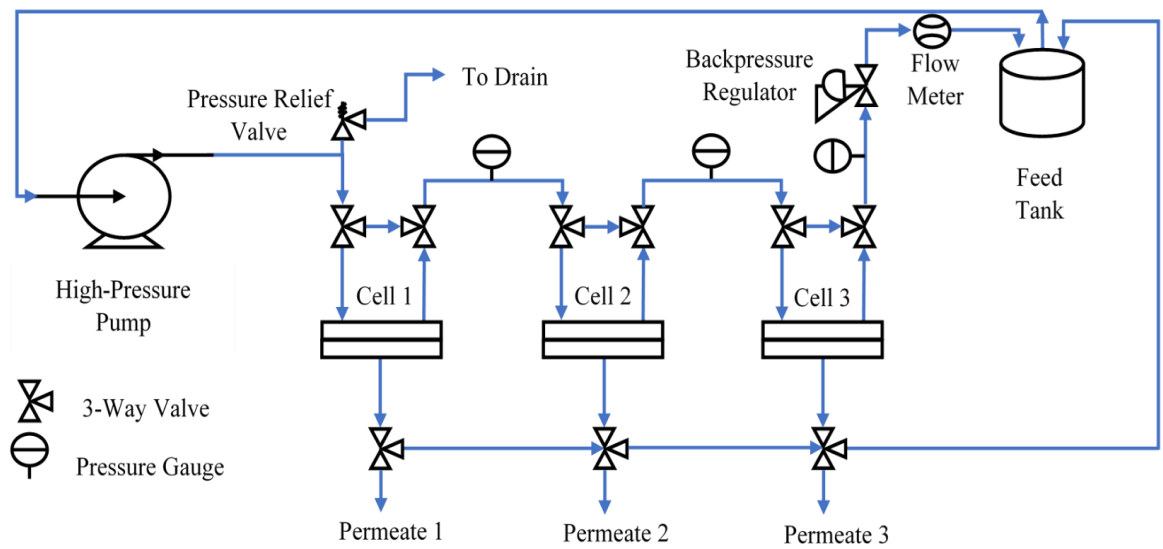


Figure 3.17. Schematic of a cross-flow permeation system.

Both feed and retentate valves are directed towards the cell and the permeate valve is directed towards the feed tank before the pump is switched on and allowed to flow liquid through the system at a constant flow rate. Once all air is removed from the system, as indicated by the disappearance of bubbles in the flowmeter, the backpressure regulator, which is depressurized initially, is slowly pressurized to the target pressure. A quick

pressurization or depressurization can rupture polymer membranes. The maximum operating pressure of the system is 69 bar so the hydrocarbon liquids were only pressurized upto 60 bar at a feed flow rate of 10 mL/min. The permeate port was flushed with a few mLs of permeate before samples were collected. Aliquots from the permeate port were taken at 24 h intervals until the permeance and rejection were stabilized for 24 h. The permeance (specifically, the hydraulic permeance), $\frac{\mathbb{P}_i}{\ell}$, is the total flux, J_i , of the permeating species through the membranes, normalized by the applied pressure, Δp .

$$\frac{\mathbb{P}_i}{\ell} = \frac{J_i}{\Delta p} \quad 3.2$$

The stage cut, defined as the ratio of permeate flow rate to feed flow rate, was maintained below 5% to reduce concentration polarization effects on the feed side of the membrane; concentration polarization can reduce the observed rejection of the solute. The separation of liquid hydrocarbon solutes was determined using gas chromatography (Agilent 7890B), where the rejection was calculated as the difference in concentration of the solute in the feed and permeate, normalized by the concentration in the feed.

$$Rejection (\%) = \frac{(C_{feed} - C_{permeate})}{C_{feed}} * 100 \quad 3.3$$

Separation factors for a component pair, A-B, were calculated as:

$$Separation Factor_{A/B} = \frac{C_{A,P}}{C_{A,R}} \cdot \frac{C_{B,R}}{C_{B,P}} \quad 3.4$$

Samples from each membrane sheet were tested in triplicate to assess the reproducibility of the separation performance.

Standardized molecular weight cutoff performance was measured using 0.05 g•L⁻¹ of α -methylstyrene dimer (Sigma Aldrich, UK) and 0.5 g•L⁻¹ each of PS 580 and PS 1090 (Polymer Labs, UK), dissolved in toluene. The rejections of oligomers were analyzed by high-pressure liquid chromatography (Agilent HPLC) with a UV/Vis detector set at a wavelength of 264 nm. The MWCO was determined by interpolating the rejections of the marker solutes and is defined as the smallest molecular weight that corresponds to a 90% rejection.

The impact of pressure and temperature variation on the separation of a model crude mixture was tested. A circular coupon of SBAD-1 was loaded into a stainless steel cross-flow cell. The cell was placed into a custom-built cross-flow system equipped with feed and recirculation pumps, back-pressure regulators on permeate and retentate lines, a hot-box purged with nitrogen to maintain uniform temperature and automated permeate and retentate sampling system. A constant feed-rate of 300 mL/hr was maintained under full-recycle, i.e. permeate and retentate were recycled back to the feed container. The retentate back-pressure regulator was initially set to 45 bar while permeate was maintained at atmospheric pressure. The hot-box temperature was initially set to 25°C. Permeate and retentate samples were collected every 24 hours and analyzed by gas chromatography. After steady-state was achieved (no change in permeate and retentate composition), the hot-box temperature was increased to 35°C. This process was repeated at 50°C and 75°C. This set of experiments at four temperatures was repeated at 50 bar and 55 bar retentate pressures.

3.11.1.2 Natural Hydrocarbon Feeds

A 49 mm diameter coupon of SBAD-1 was loaded into a Sterlitech HP4750X stirred dead-end cell (active membrane area = 14.6 cm²) with a custom-made heating jacket and nitrogen line for application of head pressure. The cell was initially loaded with 50g of toluene which was allowed to permeate overnight at room temperature and 800 psig N₂ head pressure. The cell was then depressurized and loaded with 100 g of shale-based light whole crude oil and 800 psig N₂ head pressure was again applied. The cell was stirred at a constant rate of 400 rpm. A cold trap cooled by dry ice was set up to collect the permeate in order to prevent loss of the light ends. The temperature of the cell was slowly increased up to 130°C until permeate flow was observed. After sufficient permeate had been collected, the cell was cooled and depressurized. The permeate, retentate and feed samples were analyzed using simulated distillation (SIMDIS) and 2-dimensional gas chromatography (GCxGC).

The GCxGC system consisted of an Agilent 6890 gas chromatograph (Agilent Technologies, Wilmington, DE) configured with a split/splitless inlet, oven, and flame ionization detector, and a Zoex ZX1 looped jet thermal modulation assembly (Zoex Corp., Houston, TX). The column system was a combination of three different columns connected in series. The first column was a weakly-polar BPX-5 (30 m length, 0.25 mmID, 0.25 µm film), followed by an intermediate-polarity BPX-50 (1.5 m length, 0.1 mmID, 0.1 µm film) interface column, and an additional intermediate-polarity BPX-50 (1.9 m length, 0.1 mmID, 0.1 µm film) analytical column. All columns were purchased from SGE Analytical (SGE Analytical Science, Austin, TX). The ZX1 modulator uses a combination of alternating cold and hot nitrogen gas jets regulated by liquid nitrogen heat-exchange and

electric auxiliary heating to trap and release “slices” of eluent from the first column onto the second column. This trapping occurs on the interface column which is looped through the intersection of both gas jets in the oven.

A 2.0 μL sample was injected neat into the split/splitless inlet with a 20:1 split ratio at 360°C. The carrier gas was helium running in constant flow mode at 1.9 mL per minute. The oven was programmed from 60°C to 390°C at 3°C per minute for a total run time of 110 minutes. The modulator hot jet is programmed from 180°C to 390°C at 3°C per minute and then held for 40 minutes until the end of the run. The modulation period was 10 s with a hot jet pulse length of 400 ms. The FID sample rate was 100 Hz. Instrument control and FID data collection was conducted using Agilent Chemstation.

FID signal processing was conducted using GC Image software (GC Image, LLC, Lincoln, NE). GC Image constructed the two-dimensional and three-dimensional GCxGC plot images from the Chemstation FID channel file using built-in baseline correction, peak detection, and peak integration algorithms. Three-dimensional comparison images were also constructed using built-in functionality.

GCxGC chromatograms were split according to molecular class (normal paraffins, branched paraffins, naphthenes and aromatics) and normalized cumulative peak volume was plotted against retention time for both feed and permeate for each class. A polynomial (depending on goodness of fit) was fit to each curve and integrated between the limits of lowest and highest retention time to obtain the area under the curve. For each class, the area under the normalized cumulative peak volume curve for the feed was subtracted from that for the permeate. This difference in area was then expressed as a percentage of the area

under feed curve to obtain the “% enrichment” of each class in the permeate relative to the feed.

For calculation of class-wise rejection, the peak volumes for each class were binned into 5-minute retention time intervals for both feed and permeate. The rejection at a given retention time was then calculated as shown in Equation 3.3 where C_p is the peak volume of permeate and C_f is the peak volume of feed at the same retention time. The rejection curves for each class as well as total rejection were then plotted against retention time.

3.11.2 Hollow Fiber Membrane Performance

3.11.2.1 Hollow Fiber Gas Permeation

Hollow fiber membranes were tested in a constant pressure, gas permeation system at 35 °C. The gas is fed to the sealed shell side of the membrane and permeate is collected through the bore. Samples were measured in triplicate to assess reproducibility. Samples were allowed to permeate for at least 4 hours before permeate was collected in 1-hour intervals until steady-state was reached. The permeate flow rate was measured using a soap bubble flowmeter.

3.11.2.2 Hollow Fiber Liquid Permeation

Pure liquid permeation was measured using a high-pressure syringe pump (Teledyne Isco, 500D) in dead-end filtration mode while mixture permeation was measured using a dual pump continuous flow system (Teledyne Isco, 500E). The feed was supplied to the shell side of the hollow fibers while the permeate was collected from the bore-side of the module. In the single pump system, the retentate remained on the shell side of the module.

In the dual-pump system, the retentate was allowed to flow back to the feed vessel and the feed was continuously circulated to prevent concentration polarization. The stage cut was adjusted using a needle valve in the retentate line and kept below 1%. A minimum of 2 days was allowed before permeate samples were collected to allow steady-state transport to be reached. Permeate samples were collected as described in the flat membrane case.

3.12 References

1. N. B. McKeown, P. M. Budd, Polymers of intrinsic microporosity (PIMs): organic materials for membrane separations, heterogeneous catalysis and hydrogen storage. *Chemical Society Reviews* **35**, 675-683 (2006).
2. N. C. Bruno, N. Niljianskul, S. L. Buchwald, N-Substituted 2-Aminobiphenylpalladium Methanesulfonate Precatalysts and Their Use in C–C and C–N Cross-Couplings. *The Journal of Organic Chemistry* **79**, 4161-4166 (2014).
3. N. C. Bruno, M. T. Tudge, S. L. Buchwald, Design and preparation of new palladium precatalysts for C-C and C-N cross-coupling reactions. *Chem Sci* **4**, 916-920 (2013).
4. L. Hintermann, Expedient syntheses of the N-heterocyclic carbene precursor imidazolium salts IPr center dot HCl, IMes center dot HCl and IXY center dot HCl. *Beilstein J Org Chem* **3**, (2007).
5. X.-X. Zhang, J. P. Sadighi, T. W. Mackewitz, S. L. Buchwald, Efficient synthesis of well-defined, high molecular weight, and processible polyanilines under mild conditions via palladium-catalyzed amination. *Journal of the American Chemical Society* **122**, 7606-7607 (2000).
6. B.-J. Jung, J.-I. Lee, H. Y. Chu, L.-M. Do, H.-K. Shim, Synthesis of novel fluorene-based poly (iminoarylene) s and their application to buffer layer in organic light-emitting diodes. *Macromolecules* **35**, 2282-2287 (2002).
7. Y. Liao, H. Wang, M. Zhu, A. Thomas, Efficient Supercapacitor Energy Storage Using Conjugated Microporous Polymer Networks Synthesized from Buchwald–Hartwig Coupling. *Advanced Materials* **30**, 1705710 (2018).
8. Y. Liao, J. Weber, B. M. Mills, Z. Ren, C. F. Faul, Highly efficient and reversible iodine capture in hexaphenylbenzene-based conjugated microporous polymers. *Macromolecules* **49**, 6322-6333 (2016).
9. L. J. Abbott, K. E. Hart, C. M. Colina, Polymatic: a generalized simulated polymerization algorithm for amorphous polymers. *Theor. Chem. Acc.* **132**, (2013).
10. M. F. Jimenez-Solomon, Q. Song, K. E. Jelfs, M. Munoz-Ibanez, A. G. Livingston, Polymer nanofilms with enhanced microporosity by interfacial polymerization. *Nat. Mater.* **15**, 760-767 (2016).
11. H. Sun, Force field for computation of conformational energies, structures, and vibrational frequencies of aromatic polyesters. *J. Comput. Chem.* **15**, 752-768 (1994).

12. M. Frisch *et al.*, Gaussian 16. *Revision A* **3**, (2016).
13. J. L. Duda, I. H. Romdhane, R. P. Danner, Diffusion in Glassy-Polymers - Relaxation and Antiplasticization. *J Non-Cryst Solids* **172**, 715-720 (1994).
14. S. Plimpton, Fast Parallel Algorithms for Short-Range Molecular Dynamics. *J. Comput. Phys.* **117**, 1-19 (1995).
15. T. F. Willems, C. H. Rycroft, M. Kazi, J. C. Meza, M. Haranczyk, Algorithms and tools for high-throughput geometry-based analysis of crystalline porous materials. *Microporous Mesoporous Mater.* **149**, 134-141 (2012).
16. M. Pinheiro, R. L. Martin, C. H. Rycroft, M. Haranczyk, High accuracy geometric analysis of crystalline porous materials. *CrystEngComm* **15**, 7531-7538 (2013).
17. L. M. Robeson, Correlation of separation factor versus permeability for polymeric membranes. *J. Membr. Sci.* **62**, 165-185 (1991).
18. G. H. Zhu *et al.*, Molecularly Mixed Composite Membranes for Advanced Separation Processes. *Angew Chem Int Edit* **58**, 2638-2643 (2019).
19. M. Cook, P. R. J. Gaffney, L. G. Peeva, A. G. Livingston, Roll-to-roll dip coating of three different PIMs for Organic Solvent Nanofiltration. *J. Membr. Sci.* **558**, 52-63 (2018).
20. A. L. Ahmad, T. A. Otitoju, B. S. Ooi, Hollow fiber (HF) membrane fabrication: A review on the effects of solution spinning conditions on morphology and performance. *J Ind Eng Chem* **70**, 35-50 (2019).

CHAPTER 4. THE EFFECT OF SPIROCYCLIC POLYMER STRUCTURE ON POROSITY AND SWELLING

4.1 Overview

This chapter discusses SBAD and DUCKY series' powder material characterization and computational simulation of SBAD polymers' pore structure. Parts of this chapter are adapted from 'K. A. Thompson, R. Mathias, D. Kim, J. Kim, N. Rangnekar, J. R. Johnson, S. J. Hoy, I. Bechis, A. Tarzia, K. E. Jelfs, B. A. McCool, A. G. Livingston, R. P. Lively, M. G. Finn, N-Aryl-linked spirocyclic polymers for membrane separations of complex hydrocarbon mixtures. *Science* **369**, 310-315 (2020)'.

4.2 Spirobifluorene Aryl Diamine (SBAD) Series

4.2.1 Design and Synthesis of SBAD Polymers

Previous gas separation work by McKeown and colleagues was noted, in which a spirobifluorene monomer was found to frustrate chain packing and rigidify ladder-type polymer structures beyond equivalent materials made using a spirobisindane monomer (*I*), resulting in higher polymer free volume and permeability relative to PIM-1. Moreover, swelling and plasticization were reduced, resulting in no apparent loss of separation selectivity compared to PIM-1. Therefore, a similar spirobifluorene building block was employed but it was realized that this modification alone would likely be unable to address the challenge posed by swelling in organic solvent separation compared to gas-phase separations. Thus, it was sought to enhance packing efficiency within certain segments of the backbone by using a modestly flexible linkage, choosing the aryl-N-aryl connection.

This design allowed the use of catalytic C-N bond formation as the polymerization process, rather than the nucleophilic aromatic substitution reaction that gives rise to the dibenzodioxin linkage of PIM-1. The palladium-catalyzed Buchwald-Hartwig amination reaction is a robust method for the coupling of aryl halides and amines that has been used extensively in medicinal, materials, and natural products chemistry (2); its application to polymer synthesis has been more limited. A single spirobifluorene dibromide (**1**, Figure 4.1) was chosen as the A-A monomer and a range of commercially available aromatic diamines as the B-B component (compounds **I-IV** in Figure 4.1). Polymerization using the XantPhos Pd G4 palladacycle catalyst (**3**) was optimized (Table 4.1) with respect to temperature and concentration, providing the spirobifluorene aryl diamine (SBAD) series (Figure 4.1).

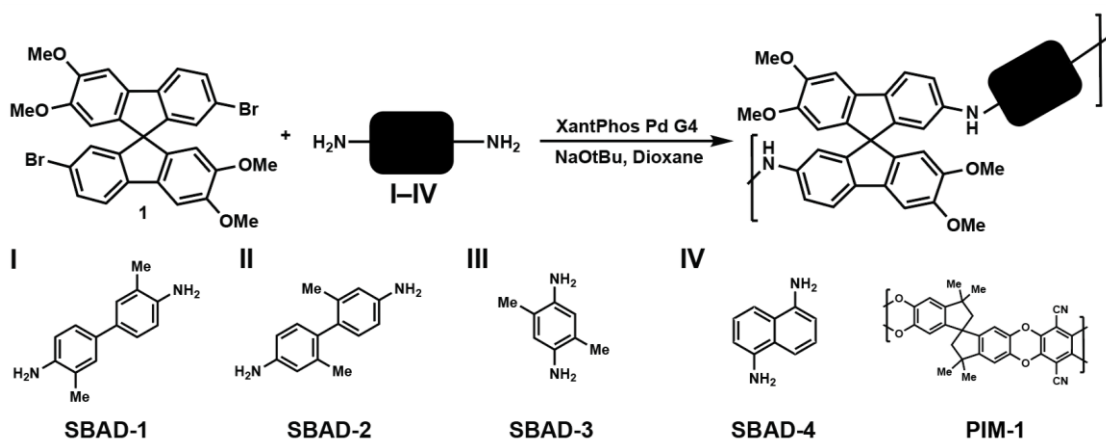


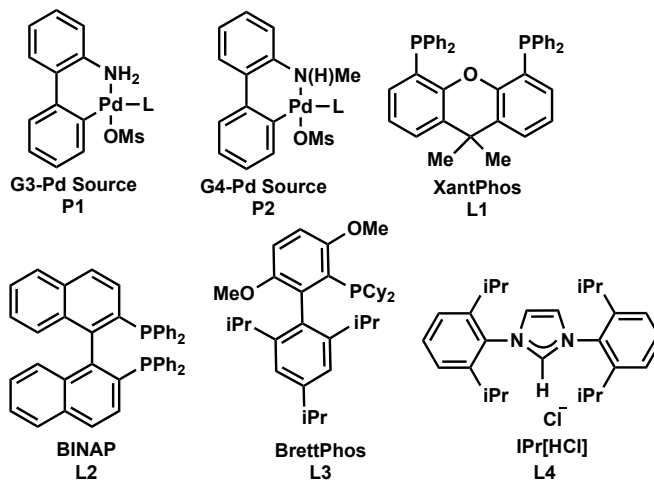
Figure 4.1. Modular reaction scheme showing the polymerization of 7,7'-dibromo-2,2',3,3'-tetramethoxy-9,9'-spirobifluorene, **1, with diamines **I-IV** giving the SBAD class of materials: SBAD-1-4.**

The Buchwald-Hartwig polymerization of **1** and *o*-tolidine (3,3'-dimethylbenzidine, compound **I** in Figure 4.1) was explored with several known catalysts for this reaction, as summarized in Table 4.1. The palladacycle XantPhos Pd G4 (**4**) proved to be the most effective, giving the highest polymer molecular weight in good yield. (High molecular weights are desirable because longer chains form higher quality films, whereas short chains are more likely to cause cracking or to be too soluble in the organic mixtures to be separated.) Consistent with prior reports (**4**, **5**), polymerization catalyzed by the XantPhos Pd G3 pre-catalyst was much slower, requiring ten days to reach similar conversion and molecular weight (data not shown). Pd(dba)₂ was also found to be inefficient in this process (Table 4.1, entries **4** and **5**).

While polymerization reactions at 50 °C consistently produced soluble polymeric products, increasing the reaction temperature to 100 °C produced polymer gels that were largely insoluble. While this may be due to the intrinsic properties of larger chains, it is also possible that chain crosslinking occurred under these conditions, even a small amount of which can be expected to dramatically decrease solubility. Decreasing overall concentration at high reaction temperature (Table 4.1, reaction **2**) eliminated the gelation problem, but also compromised chain length. To balance these effects, three of the four polymers were prepared at 80 °C. Unfortunately, the use of BrettPhos – known for its selective coupling of primary over secondary amines (**6**) – did not provide a significant degree of polymerization.

Table 4.1. Conditions tested for the polymerization of SBAD-1: 1 (0.1 mmol), diamine (0.1 mmol), catalyst (5 mol%), solvent (0.5 mL) for 24h. Reaction 2 was performed at 0.1 M (1 mL dioxane) to prevent gelation.

Entry	Catalyst	Temp. (°C)	Solvent	M _w (kDa)
1	P1-L1	50	Dioxane	No Conv
2	P2-L1	100	Dioxane*	16.7
3	P2-L1	50	Dioxane	80.4
4	L1•Pd(dba) ₂	50	Dioxane	8.0
5	L2•Pd(dba) ₂	50	Dioxane	4.2
6	P2-L1	140	DMAc	25.5
7	P2-L3	50	Dioxane	1.4
8	P1-L3	110	Toluene	9.3
9	P2-L1	110	Toluene	8.8
10	P2-L1	50	THF	113
11	L4•[PhCN] ₂ PdCl ₂	110	Toluene	2.3
12	L4•[PhCN] ₂ PdCl ₂	100	Dioxane	4.6



4.2.2 SBAD Powder Characterization

All SBAD polymers were readily soluble in volatile solvents (THF, chloroform, CH₂Cl₂, Figure 4.2) and were easily cast into films. The SBAD-3 and SBAD-4 polymers were much more colored (vibrant magenta and deep indigo, respectively) than the others in both the solid state and solution. This may reflect their greater degrees of π -conjugation across the diamine linkage, allowing for small amounts of N-oxidation to lead to stronger donor-acceptor chromophores in the polymer backbone. The presence of such oxidized linkages may contribute to the more complex appearances of the NMR spectra and TGA analyses shown later in this chapter.

GPC analysis revealed a component of high apparent molecular weight, thought to correspond to a small amount of branched material derived from a second N-H insertion event at one or more amine sites along the polymer chain (Figure 4.3). The number-average molecular weights of the polymers derived from the optimized procedures described above (calibrated against polystyrene, and so of uncertain absolute value) were all low, reflecting degrees of polymerization below 20, but dispersities were very large. This likely reflects two factors: (a) while the catalyzed Buchwald-Hartwig reaction is fast, the thermodynamic driving force of each coupling step is not large, and (b) branching via C-N bond formation to secondary amine centers is possible, and only a small amount of branching at secondary amine centers is necessary to dramatically inflate the observed weight-average molecular weight and dispersity. The polymerization results are highly reproducible, thus branching, if it occurs, is likely an intrinsic feature of the polymerization reaction. Even a small amount of branching at secondary amine centers can dramatically inflate observed weight-average molecular weights and dispersities (7).



Figure 4.2. Solutions of polymers in the SBAD series in chloroform (0.4 mg/mL).

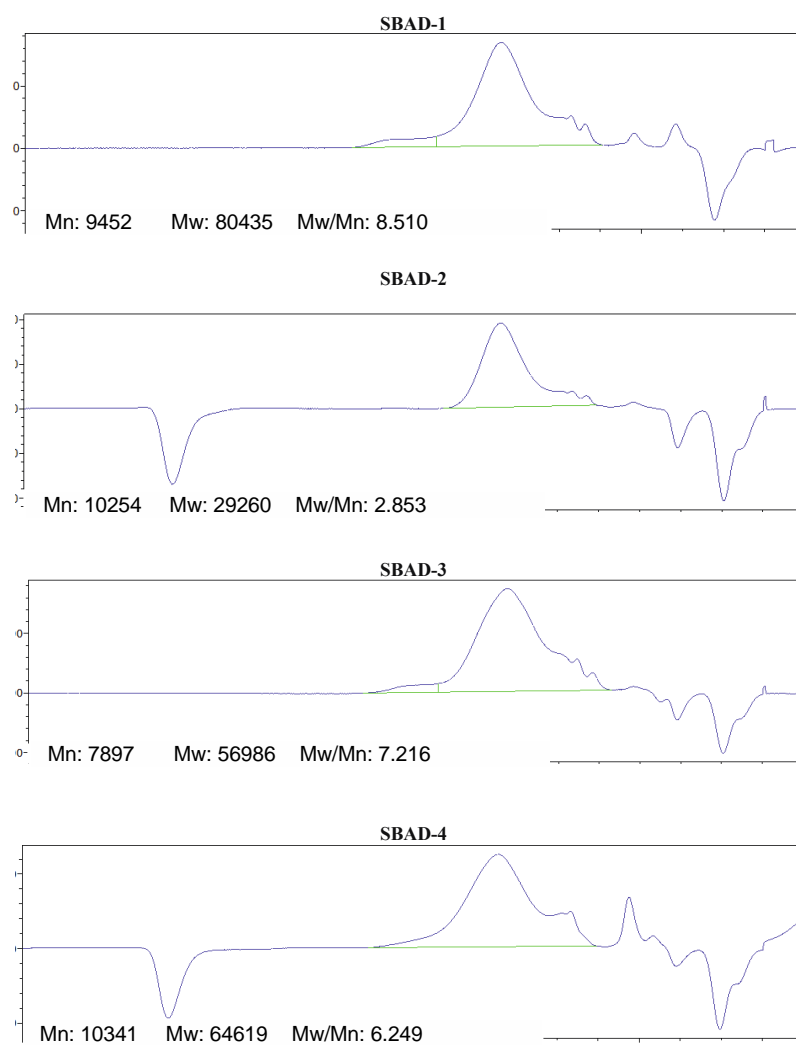


Figure 4.3. GPC analyses of SBAD polymers.

The SBAD polymers demonstrated high thermal stabilities, with no observable glass transition temperatures (Figure 4.4 -Figure 4.5), as has often been reported for PIM systems (8). These materials also exhibited low uptakes of N₂ at 77K (Figure 4.6) but had only moderately lower CO₂ sorption than PIM-1 at 273K (Figure 4.6B), suggesting the existence of isolated microporous free volume elements. CO₂ is a known plasticizer of PIM-1 at higher activities with a kinetic diameter lower than N₂. As shown in Figure 4.6, the SBAD isotherms are more comparable to that of PIM-1 in the case of CO₂ (although still lower) and have lower slopes at higher CO₂ activities.

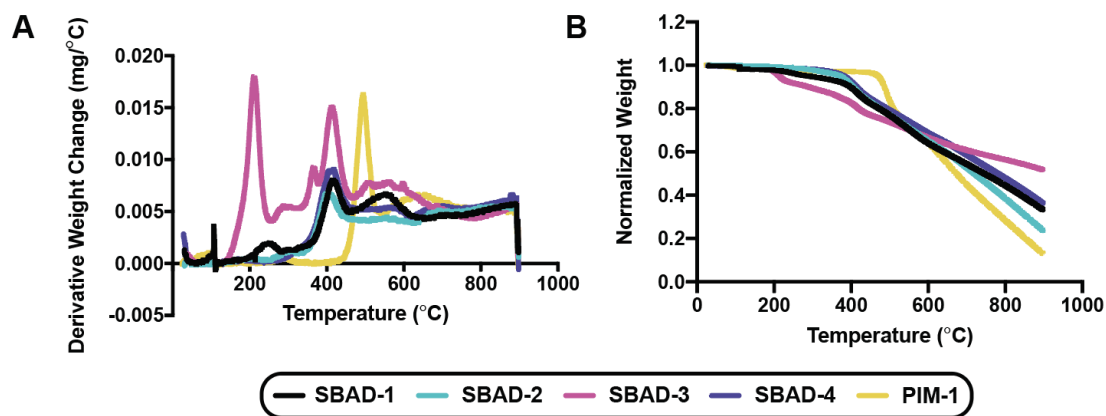


Figure 4.4. Thermogravimetric analysis (TGA) of all polymers in the SBAD series compared to PIM-1 shown as A) derivative weight change and B) weight normalized to starting sample weight.

The accessible free volume and swelling effect of CO₂ is quantified through the dual-mode sorption model shown in Equation 4.1. The CO₂ sorption isotherm can be fit to this model, which is characterized by the algebraic sum of Henry's law for a gas dissolving in

a solid and a Langmuir equation for gas adsorbing in the free volume sites of the polymer network (9).

$$C = C_D + C_H = k_D p + \frac{C'_H b p}{1 + b p} \quad 4.1$$

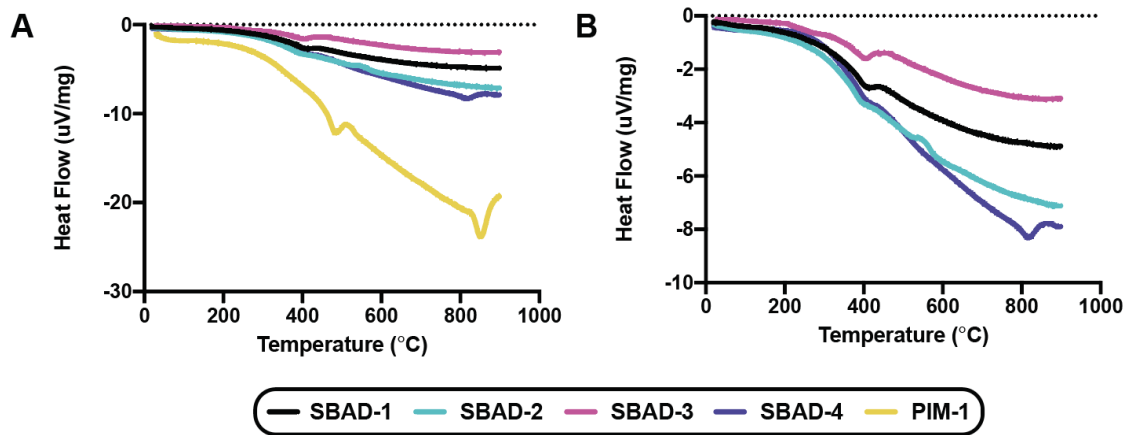


Figure 4.5. Differential scanning calorimetry (DSC) of polymers in the SBAD series compared to PIM-1. Glass transition states were not observed below the decomposition temperatures observed in Figure 4.4.

The Henry's law coefficient, k_D can be correlated to the sorption or swelling affinity of the polymer in a gas. The Langmuir capacity constant, C'_H , is related to the unrelaxed free volume of the glassy polymer. Figure 4.6B and C shows the calculated k_D and C'_H values, respectively, obtained by best fit to the CO₂ sorption data compared to data obtained for a non-porous polymer such as Torlon[®] at the same temperature. Lower k_D values confirm that SBAD polymers undergo less CO₂-induced swelling than PIM-1, but

are not as resistant as Torlon[®], which is extensively H-bonded throughout its network (10). The SBAD C'_H values were all somewhat lower than those for PIM-1 (~4x difference) but significantly higher than those for Torlon[®]. These CO₂ vapor physisorption results suggest that the SBAD polymers possess higher cohesive energy densities than PIM-1 and are thereby likely to be more resistant to solvent-induced swelling.

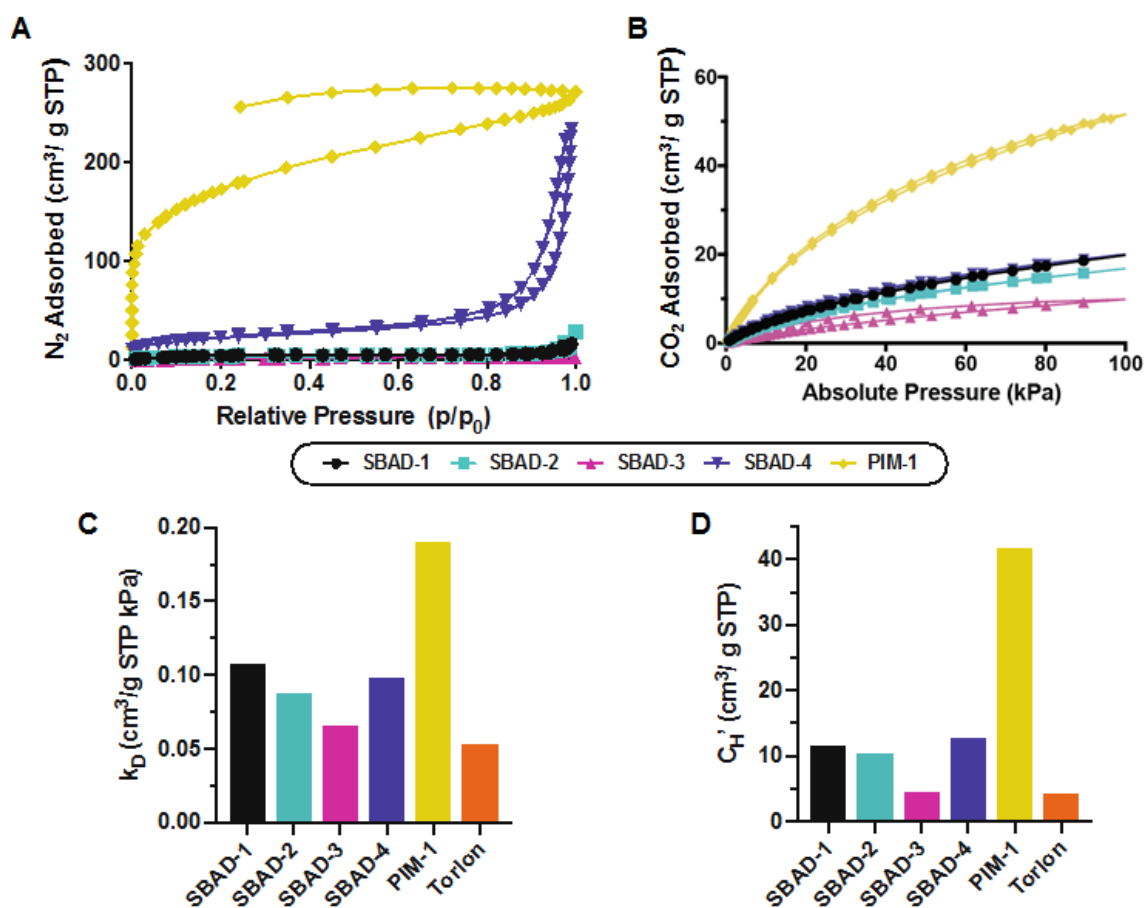


Figure 4.6. Uptake of (A) N₂ at 77 K and (B) CO₂ at 273 K by SBAD polymers compared to PIM-1. (C) Henry's law coefficient (k_D) and (D) Langmuir capacity constant (C'_H) values fit to CO₂ sorption data, compared to data obtained for a traditional “non-porous” polymer, Torlon[®]. Error for k_D and C'_H were too small to be apparent on the graphs. Inset = key for A and B.

4.2.3 Computational SBAD Porosity Analysis

To further probe the pore structure of these materials, computational models for the polymers in the dry state were generated using the polymerization algorithm Polymatic (11). Three models were generated for each system to sample different structural arrangements and ensure the models were representative of the bulk material. The properties of the models were then characterized (Figure 4.7) (12).

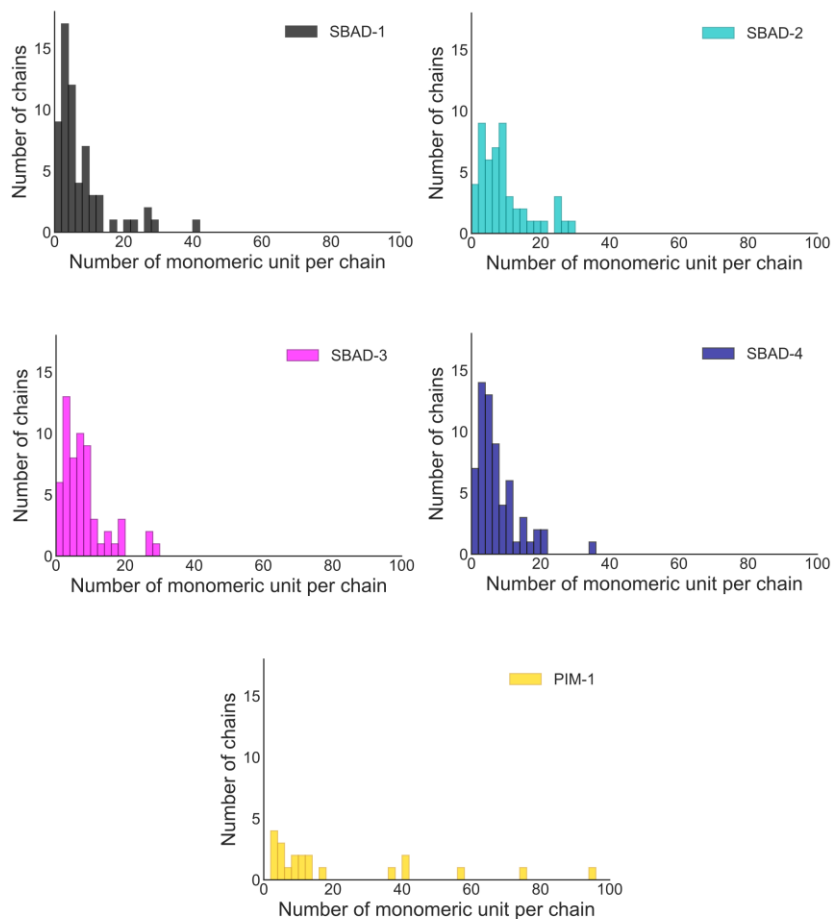


Figure 4.7. Chain length distribution in the polymer models.

Table 4.2 reports the values of the density of the initial random packing of monomers in the model box, together with the percentage of polymerization reached and the final value of bulk density after the annealing procedure. The standard deviations between different models for the same polymer are reported in parenthesis. PIM-1 models reached the highest percentage of polymerization, which results in longer chains within the model, as can be seen from Figure 4.7 which shows the chain length distribution inside the models. In Table 4.2, the diameters of the largest included sphere (D_I), largest free sphere (D_F) and largest included sphere along the free sphere path (D_{IF}) is reported for all the models. In particular, the D_F value defines the largest probe that can diffuse from one side to the other side of the model through interconnected pores.

The diameter of the largest probe that can pass through an interconnected pore network in the PIM-1 models is $3.2 \pm 0.3 \text{ \AA}$, whereas the equivalent value for the SBAD series is $2.3 \pm 0.1 \text{ \AA}$. Given the D_F values in Table 4.2, none of the polymer models present accessible pores for a probe radius of 1.82 \AA , corresponding to the kinetic diameter of N_2 , contrary to experimental results. However, the analysis of the static model does not take into account the chain movement that can occur upon gas adsorption due to chain flexibility, and only a small amount of motion would conceivably be required for the PIM-1 models ($D_F = 3.18 (0.34)$) to become interconnected to a nitrogen sized molecule.

PIM-1 has the highest value of total surface area (including both accessible and non-accessible voids) with respect to every tested probe diameter. This is reported visually in Figure 4.8 and Figure 4.9 for 2.2 \AA and 3.64 \AA probe diameters. Figure 4.10 reports the pore size distribution inside all of the models, calculated using a probe diameter of 2 \AA . The figure shows the existence of narrow distributions of ultra-micropores between $2\text{-}8 \text{ \AA}$

for SBAD-1 and -3 and 2-10 Å for SBAD-2 and -4, whereas PIM-1 has an apparently broader distribution between 2-12 Å. Even tighter distributions of ultra-micropores are seen in traditional glassy polymers (13), but the pore sizes are often too small for meaningful organic solvent separations. Thus, the presence of intermediate non-interconnected pores exhibited by the SBAD materials could offer significant penetrant-penetrant differentiation of small-molecule organic solvents at reasonable fluxes if diffusion from one pore to the next were reasonably fast.

Table 4.2. Characterization of the amorphous polymer models for the four SBAD polymers and PIM-1. For each polymer, results are averaged over three independent models deriving from different initial random packing. The standard deviation is reported in parenthesis. The diameters of the largest included sphere (D_I), largest free sphere (D_F) and largest included sphere along the free sphere path (D_{IF}) are reported, as well as the surface area (SA) with different diameter probes.

	SBAD-1	SBAD-2	SBAD-3	SBAD-4	PIM-1
Initial packing density ($\text{g}\cdot\text{cm}^3$)	0.381	0.381	0.396	0.429	0.334
% of polymerization reached	93.1 (0.9)	94.8 (0.9)	93.5 (0.7)	93.0 (0.7)	95.3 (0.7)
No. of bonds formed	279 (3)	283 (3)	280 (2)	279 (2)	143 (1)
Final bulk density ($\text{g}\cdot\text{cm}^3$)	1.052 (0.007)	1.045 (0.008)	1.002 (0.004)	1.080 (0.005)	0.999 (0.029)
No. chains in the model	21 (3)	17 (3)	20 (2)	21 (2)	7 (1)
D_I (Å)	6.64 (0.76)	7.95 (1.16)	6.83 (0.39)	7.57 (1.74)	10.53 (1.70)
D_F (Å)	2.30 (0.08)	2.30 (0.13)	2.28 (0.02)	2.23 (0.03)	3.18 (0.34)
D_{IF} (Å)	6.21 (1.11)	6.97 (0.62)	6.16 (0.65)	7.24 (1.85)	9.18 (1.93)
SA (2.00 Å probe) $\text{cm}^2\cdot\text{g}^{-1}$	1381 (31)	1455 (17)	1498 (30)	1361 (33)	1959 (48)
SA (2.20 Å probe) $\text{cm}^2\cdot\text{g}^{-1}$	1073 (29)	1147 (14)	1183 (34)	1063 (40)	1687 (57)
SA (3.30 Å probe – CO_2) $\text{cm}^2\cdot\text{g}^{-1}$	232 (18)	277 (11)	278 (32)	235 (52)	717 (77)
SA (3.64 Å probe – N_2) $\text{cm}^2\cdot\text{g}^{-1}$	138 (15)	175 (7)	171 (24)	143 (48)	550 (81)

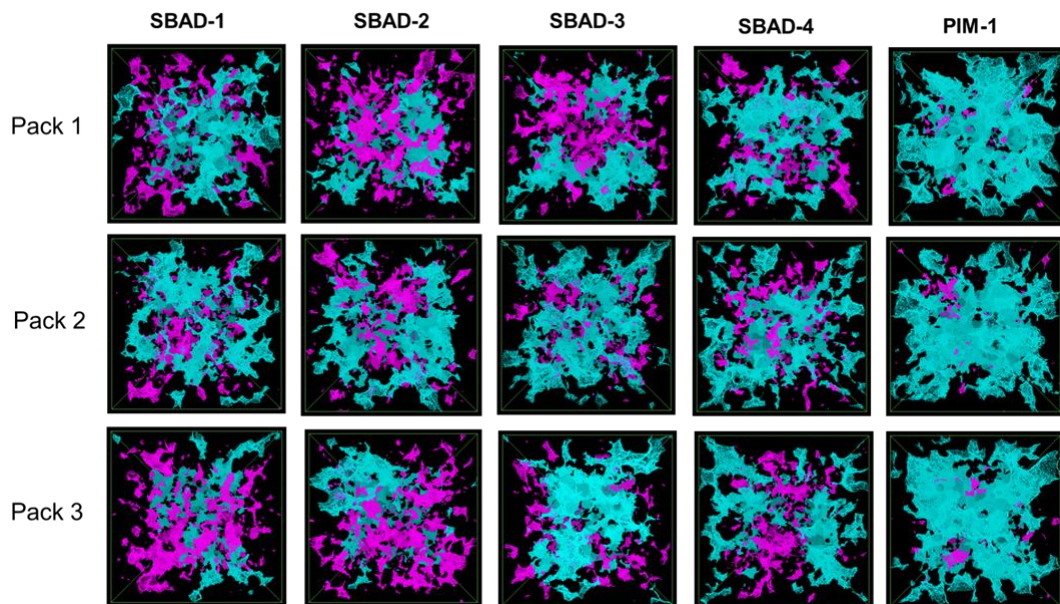


Figure 4.8. Accessible (teal) and non-accessible (magenta) surface area for all polymers in the SBAD series compared to PIM-1 using a 2.2 Å probe diameter.

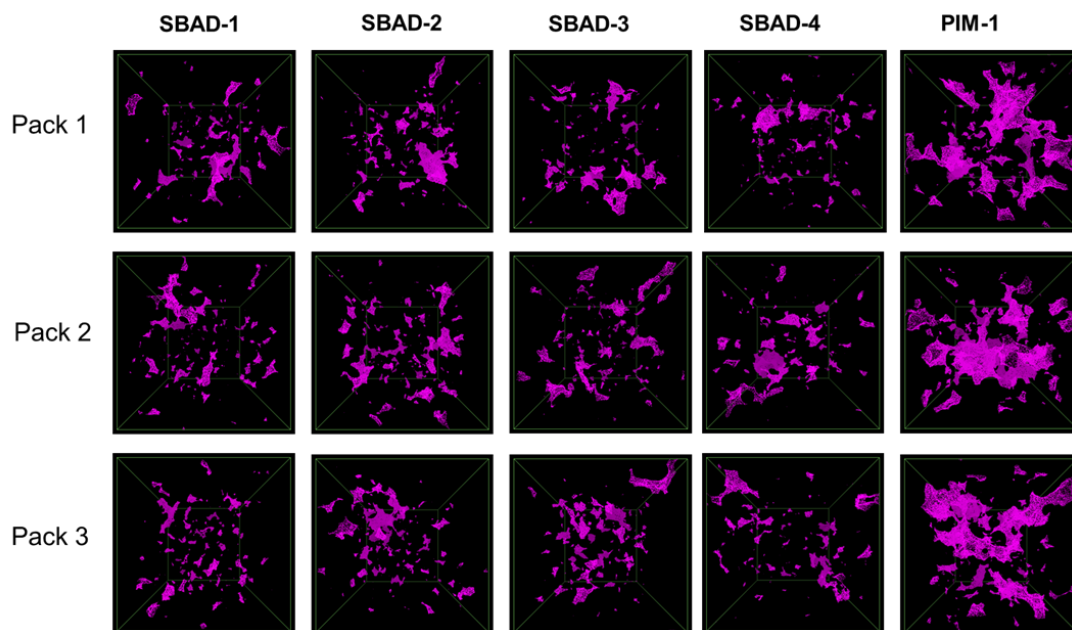


Figure 4.9. Non-accessible (magenta) surface area for all polymers in the SBAD series compared to PIM-1 using a 3.64 Å probe diameter (kinetic diameter of N₂).

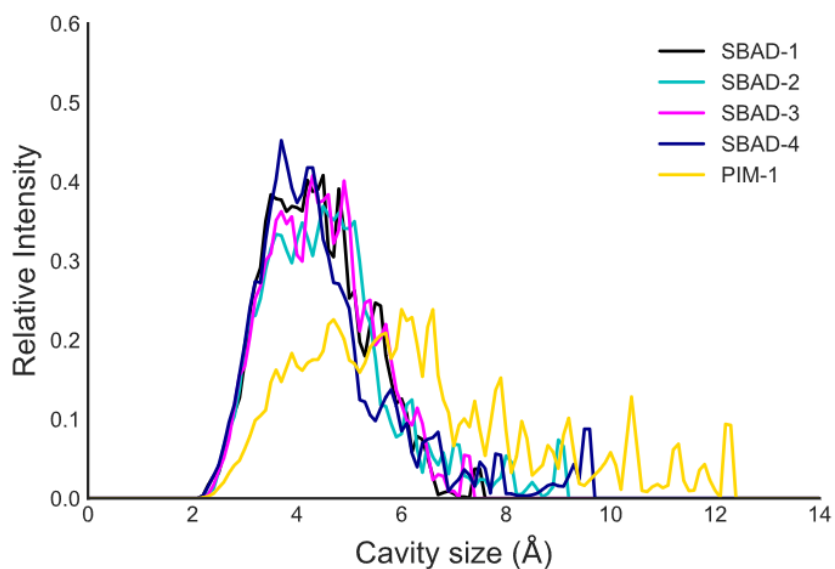


Figure 4.10. Calculated pore size distribution of the SBAD series compared to PIM-1.

The sampled pores and their location in each structure are reported in Figure 4.11, where they are color-coded according to their size. The new class of SBAD polymers shows less interconnected porosity compared to PIM-1. This results from a more efficient packing of the polymer chains in the bulk structure, as shown by the average final densities for all the SBAD polymer models being higher than that obtained for the PIM-1 models (Table 4.2).

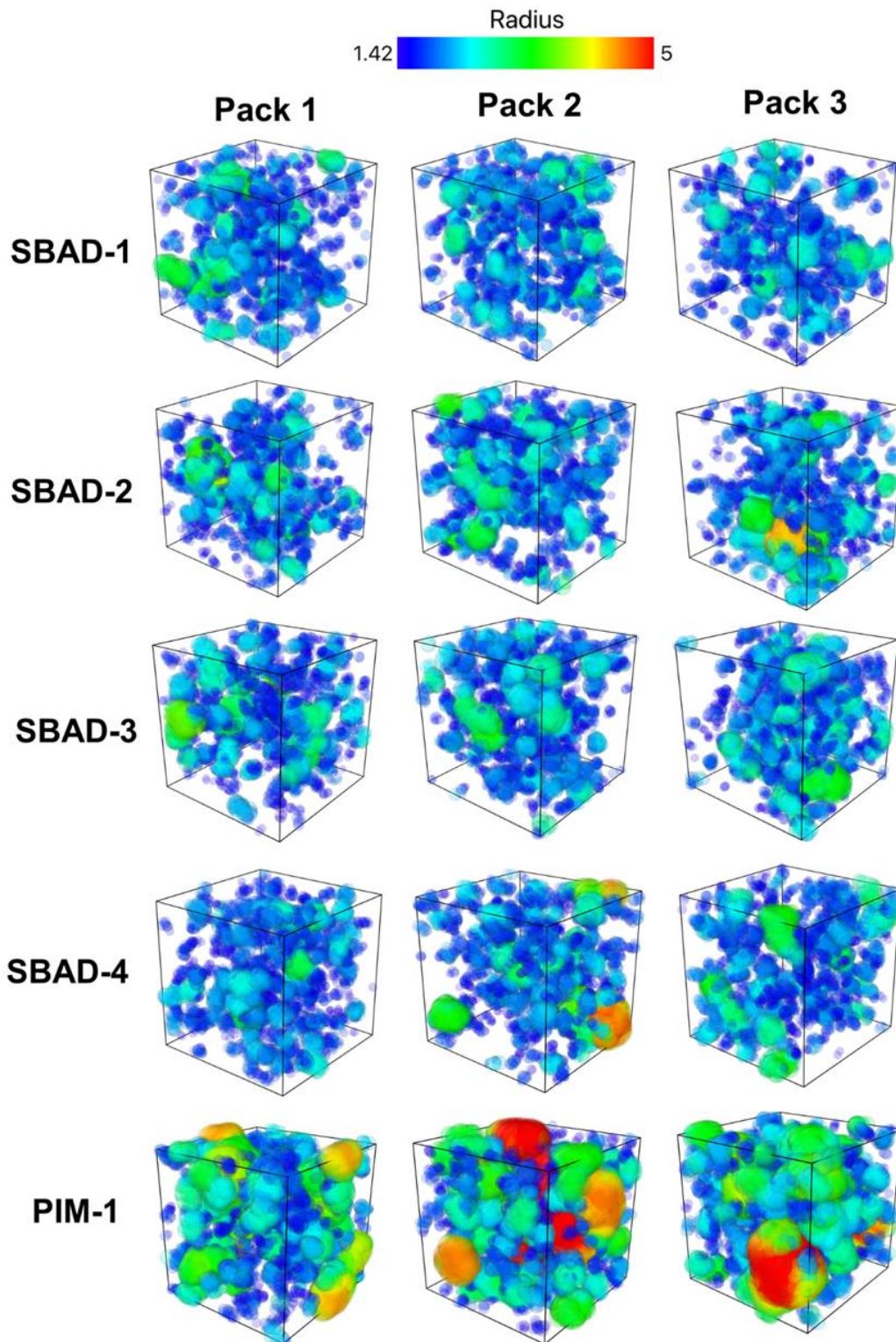


Figure 4.11. Three-dimensional representation of the pore size distribution in the three models for each of the five polymers. Pores are color-coded based on their dimension. Only pores bigger than 1.42 Å radius are displayed.

Whether SBAD polymer chains having the potential to form hydrogen bonding also influences the more efficient packing and consequent lowering of porosity in the SBAD systems compared to PIM-1 was investigated. However, analysis of the radial distribution function of hydrogen bond donor and acceptor atoms in the models did not show any evidence of this. The distribution of the values of two significant dihedral angles in all the models were plotted to confirm the higher flexibility in the new SBAD polymers compared to PIM-1 (Figure 4.12), the first including the spiro center, the second involving the linkage between the two monomers in the polymeric unit (as highlighted in Figure 4.12). It is found that the PIM-1 distribution of the dihedral angle involving the spiro center is slightly narrower, which is an indication of the PIM-1 chains having lower flexibility. In the case of the dihedral angle involving the linkage between the two monomers, the double linked nature of this linkage in PIM-1 restricts the values of the angle around 180° , while in the case of the SBAD series there is an even distribution of the dihedral angle around 0° and 180° , coming from the different orientation that the diamine monomer can adopt with respect to the spirobifluorene monomer when the single amine linkage is formed. This helps enforce the more ladder-like chain morphology in the case of PIM-1.

The main differences between the structural arrangement of the SBAD chains compared to PIM-1 are better highlighted by visual inspection. Figure 4.13 shows the images of selected single chains for all the constructed models. Two chains were selected for each polymer that are representative of the typical chain shape and arrangement in all the models for that system. However, it has to be kept in mind that every chain is different and unique in both its length and spatial arrangement. As can be seen from the stick representation of the chains (Figure 4.13), PIM-1 shows the expected ladder-like structure,

while SBAD polymers seem to arrange themselves more in a spiral-like way. In general, PIM-1 chains maintain a more linear arrangement, while the SBAD polymers tend to twist on themselves to form clusters. The SBAD polymers also have a higher degree of aromatic and conjugated systems, which can form inter- and intra-chain π - π interactions that can lead to a tighter packing. Figure 4.14 shows examples of these chain-chain aromatic interactions.

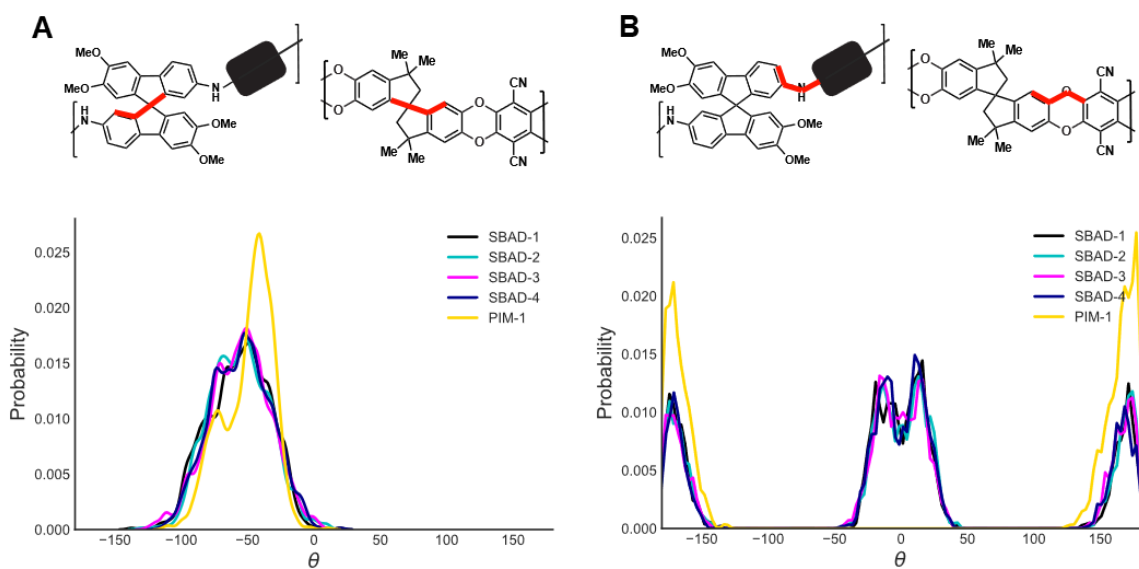


Figure 4.12. Histograms of the angle distributions for the dihedral highlighted in red in the final models for the SBAD polymers and PIM-1. A) Dihedral angle involving the spirocenter B) dihedral angle involving the linkage between the two monomers.

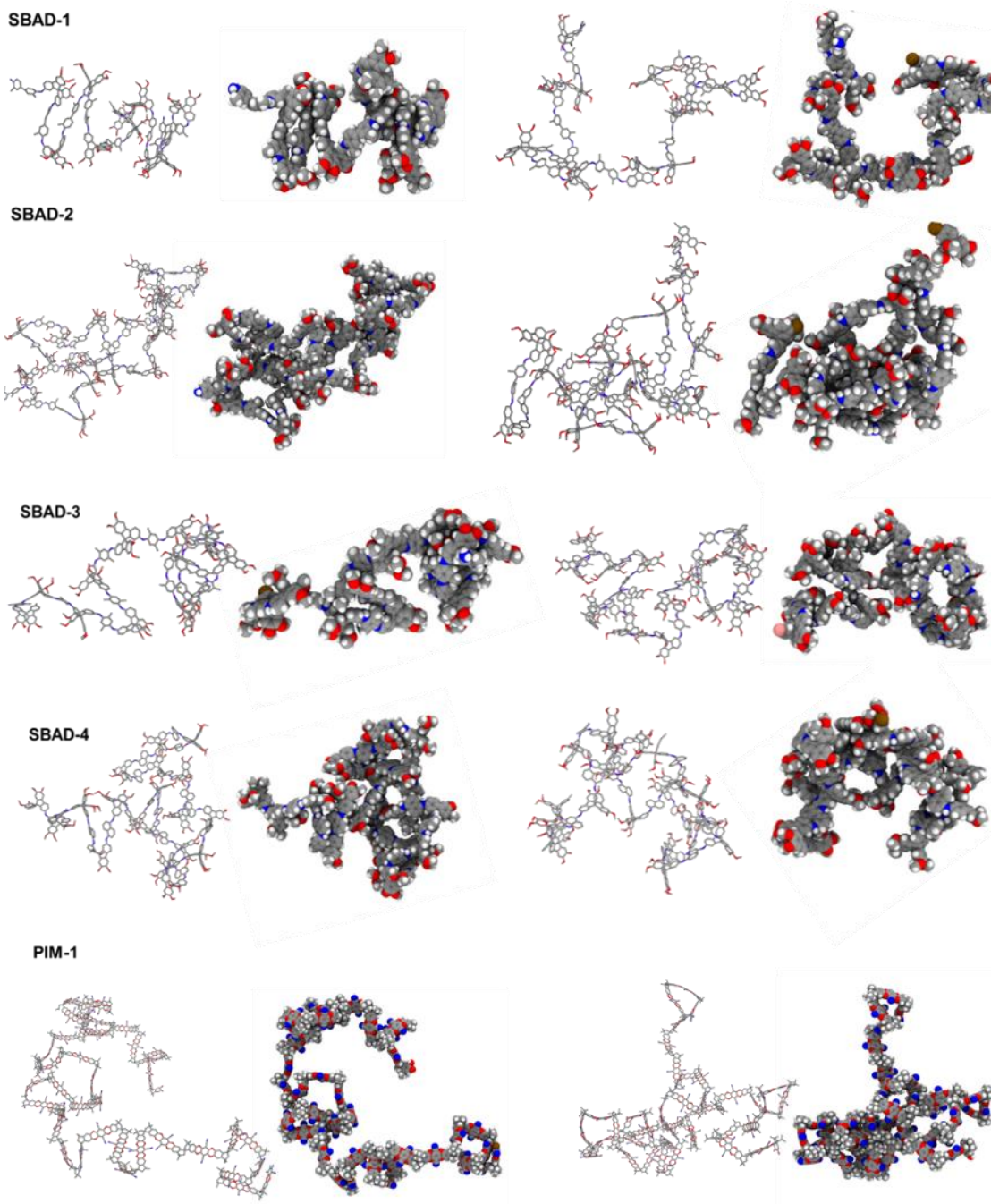


Figure 4.13. Stick and space filling representations of two selected chains for each polymer. Hydrogens have been removed for clarity in the stick representation. Color code: carbon in grey, nitrogen in blue, oxygen in red, hydrogen in white, bromine in purple, fluorine in light blue.

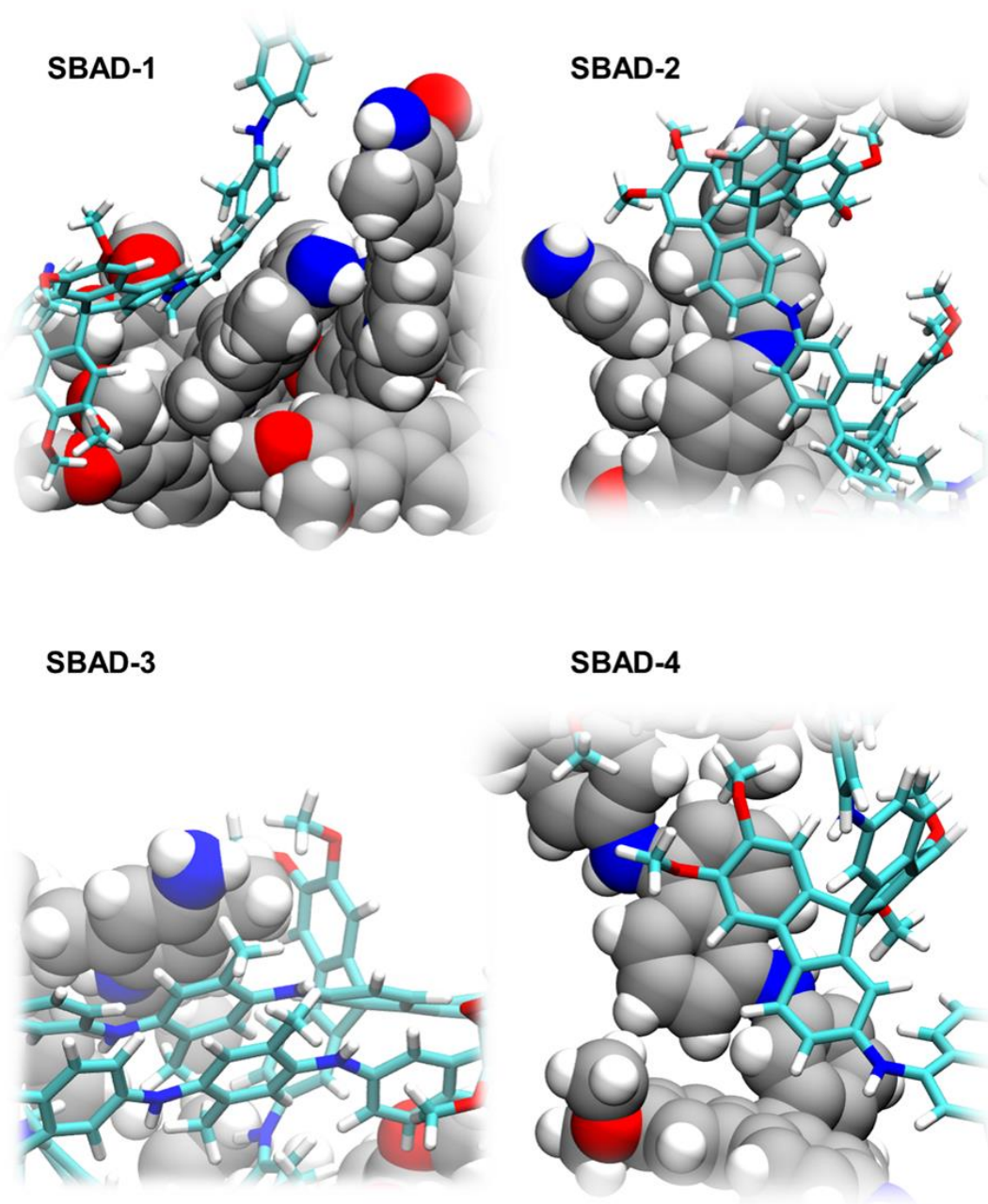


Figure 4.14. Selected snapshots that highlight π - π stacking interactions between chains inside the polymer models of the SBAD family. One chain is shown in van der Waals representation with carbon in grey, the other is represented in stick with the carbons in light blue. Nitrogen is in blue, oxygen in red, hydrogen in white.

4.2.4 Computational SBAD Swelling

Figure 4.15 (A) and (B) show the effect of computational swelling, outlined in Section 3.8, on the average pore limiting diameter (D_F) of the models. In all cases, D_F increases as a function of swelling, but for SBAD-1 and SBAD-3, D_F does not become larger than the diameter of CO_2 and N_2 until between 12-14% swelling. Therefore, in these models, SBAD-1 and SBAD-3 maintain non-interconnected voids (and low porosity) for low swelling values, unlike PIM-1. This result is further highlighted by the calculated accessible surface areas for probe sizes of CO_2 and N_2 in Figure 4.15 (C) and (D), respectively. PIM-1 shows accessible porosity to these probes at 3% swelling, while SBAD-1 and SBAD-3 have no accessible surface area until 12-14% swelling. We may conclude that only a small amount of flexible breathing motions or polymer swelling would be required for nitrogen (diameter 3.64 Å (12)) to diffuse through PIM-1, but much larger dilations would be required with the SBAD series (Figure 4.8 - Figure 4.9). This is consistent with the observed nitrogen physisorption isotherms above showing high uptakes for PIM-1 compared to the SBAD series at low relative pressures, which is the range that is typically used to calculate micropore distributions. By defining “interconnected pores” as those that are accessible by N_2 at 77K within a reasonable timeframe (2 days), it is apparent that “interconnected microporosity” is a characteristic feature of PIM-1 that is suppressed in the SBAD polymers. This effect is likely due to the absence of the dibenzodioxin linkage and ladder-like morphology of PIM-1 (Figure 4.12 - Figure 4.13), replaced in the SBAD series with more flexible single-bond C-N linkages, allowing for the formation of π - π stacking interactions between and within chains (Figure 4.14) and more efficient chain packing. It is important to note that the artificial swelling procedure does

not entirely capture the physical process of swelling, i.e., swelling is not the only physical process causing the porosity of the PIMs in this study. Even though this artificial swelling approach is crude, the findings highlight preliminary indicators of the impact of polymer chemistry on the evolution of porosity due to dilations in in PIM materials.

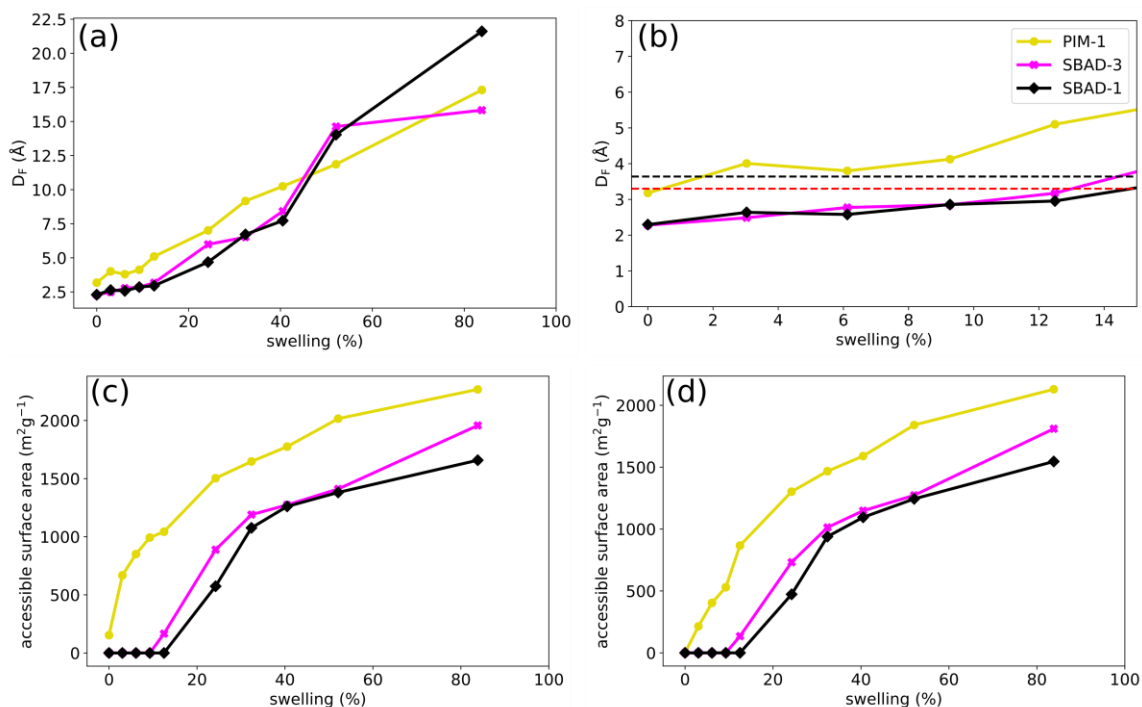


Figure 4.15. (A)-(B) Average pore limiting diameter (D_F) of PIM-1, SBAD-1 and SBAD-3 as a function of swelling. In (B), the red and black dashed lines represent the probe diameter of CO_2 and N_2 , respectively. (C)-(D) The average solvent accessible surface area of PIM-1, SBAD-1 and SBAD-3 as a function of swelling for CO_2 (left) and N_2 (right) probes.

In the “wet” state, separating small organic molecules requires that the membrane material exhibit resistance to significant solvent-induced swelling (e.g., Torlon®, a highly solvent-stable polyamide-imide, Figure 4.16). Solvent-induced dilation experiments showed that SBAD-1 experienced substantially less mass change than PIM-1 at unit

activity of toluene, suggesting that the SBAD materials retain their narrow distribution of ultramicropores even when exposed to solvents.

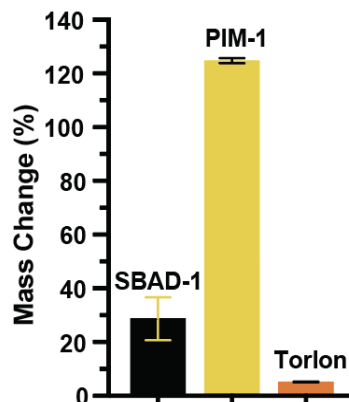


Figure 4.16. Uptake of liquid toluene by dense films of SBAD-1, PIM-1 and Torlon® (14), 22°C, 1 atm. Data are the mean of 2 films +/- the range.

4.3 DUCKY Series

4.3.1 Design and Synthesis of DUCKY Polymers

The copper-catalyzed azide-alkyne cycloaddition (CuAAC) reaction is a formal 1,3 cycloaddition reaction between an azide and terminal alkyne to provide 1,4 triazoles. The CuAAC reaction is often orthogonal to other chemistries frequently employed for the synthesis and modification of a wide variety of polymers and its 1,4-disubstituted triazole products are highly stable towards heat, oxidation, and hydrolysis. The CuAAC reaction can be very rapid and is irreversible, making it a powerful method for post-polymerization functionalization.⁽¹⁵⁾ However, it is far less commonly employed as a polymerization method, due to the relatively poor solubility of the main chain polytriazole products.⁽¹⁶⁾

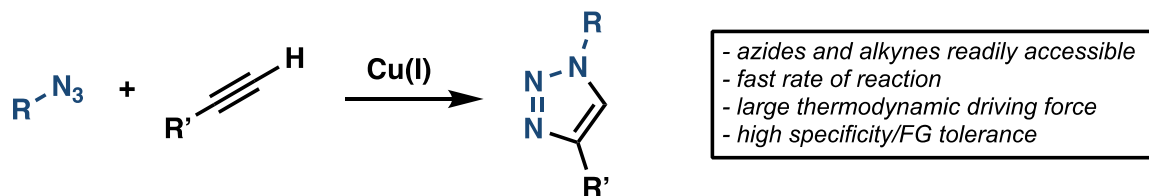


Figure 4.17. An example of the CuAAC reaction utilized in the synthesis of the DUCKY series.

Spirocyclic monomers are commonly used in a class of PIM materials useful for gas and liquid separations, as their rigidity and kinked shape introduce porosity into the resulting polymers. It was reasoned that introducing triazoles into PIM-like materials could open new avenues for their synthesis. It is shown in this chapter and in Chapter 5 that such polymers made with a non-traditional C-N bond linkage (SBAD series) have advantageous properties. At the same time, having a spirocenter in the monomer could solve the polymeric triazole problem and provide soluble, high molecular weight polytriazole materials with synthetic ease, giving entry to a new class of highly tunable materials for membrane applications.

4.3.2 DUCKY Powder Characterization

Preliminary investigations into the kinetics of the reactions via ^1H NMR indicate that the polymerizations are extremely fast, with the more rigid DUCKY-5 polymer reaching 50% conversion in 20 minutes and less rigid DUCKY-6 reaching 50% conversion in 2 minutes (Figure 4.18). It is worth noting that the reactions are likely even faster when run

on the benchtop as it was necessary to perform them at slightly lower concentrations and temperatures in the NMR.

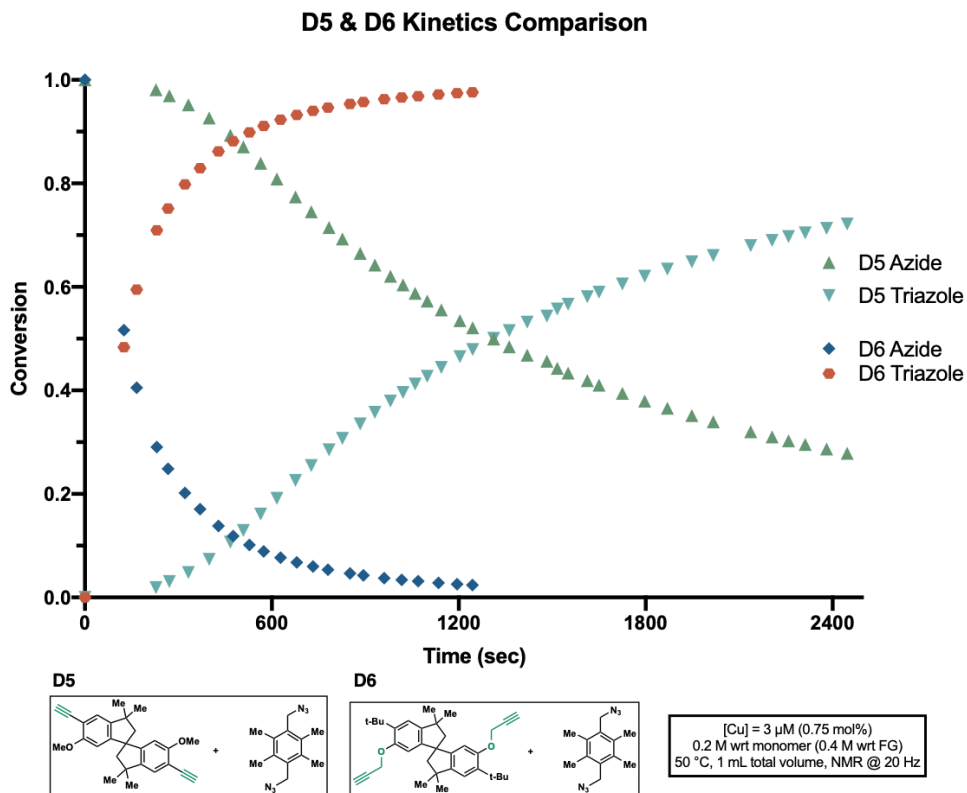


Figure 4.18. Kinetics of DUCKY-5 and DUCKY-6 polymerization reaction via ^1H NMR analysis of the monomer conversion rate.

The DUCKY polymers are thermally stable up to ~ 300 °C under pure nitrogen conditions (Figure 4.19). While this is lower than the thermal stability of PIM-1 (Figure 4.4), it is often sufficient for crude oil separation applications, especially in the range of naphtha and kerosene molecules.

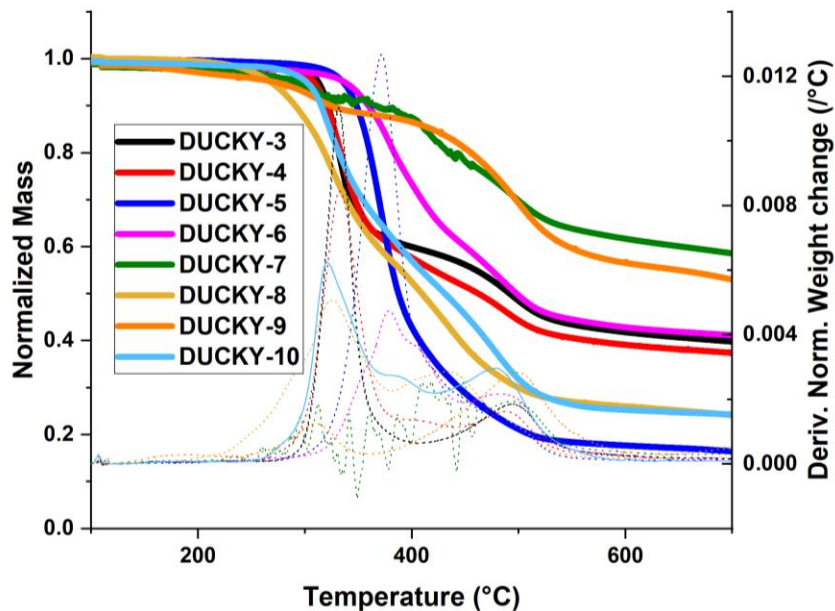


Figure 4.19. Thermogravimetric analysis (TGA) of polymers in the DUCKY series shown as derivative weight change (solid lines) and weight normalized to starting sample weight (dotted lines).

Physisorption of N_2 at 77K and CO_2 sorption at 273K was found to be in similar ranges as the SBAD series (Figure 4.20). Interestingly, polymers without ether linkages (DUCKY-6,7 and 9) showed the highest uptakes of CO_2 , which may be a result of the inefficient packing of polymer chains due to the reduced freedom of rotation. DUCKY-3 has the lowest CO_2 sorption, which is likely due to the highest packing efficiency from a combination of a flexible ether group and no functional groups on the aromatic rings in the comonomer to create steric hindrance. Figure 4.20C and D shows the calculated k_D and C'_H values for the DUCKY series obtained by best fit of the dual mode sorption model to the CO_2 sorption data. Lower k_D values confirm that DUCKY polymers undergo less CO_2 -induced swelling than PIM-1, similar to the SBAD series. Again, as with SBAD, these

results suggest that the DUCKY polymers could be more resistant to solvent-induced swelling than PIM-1.

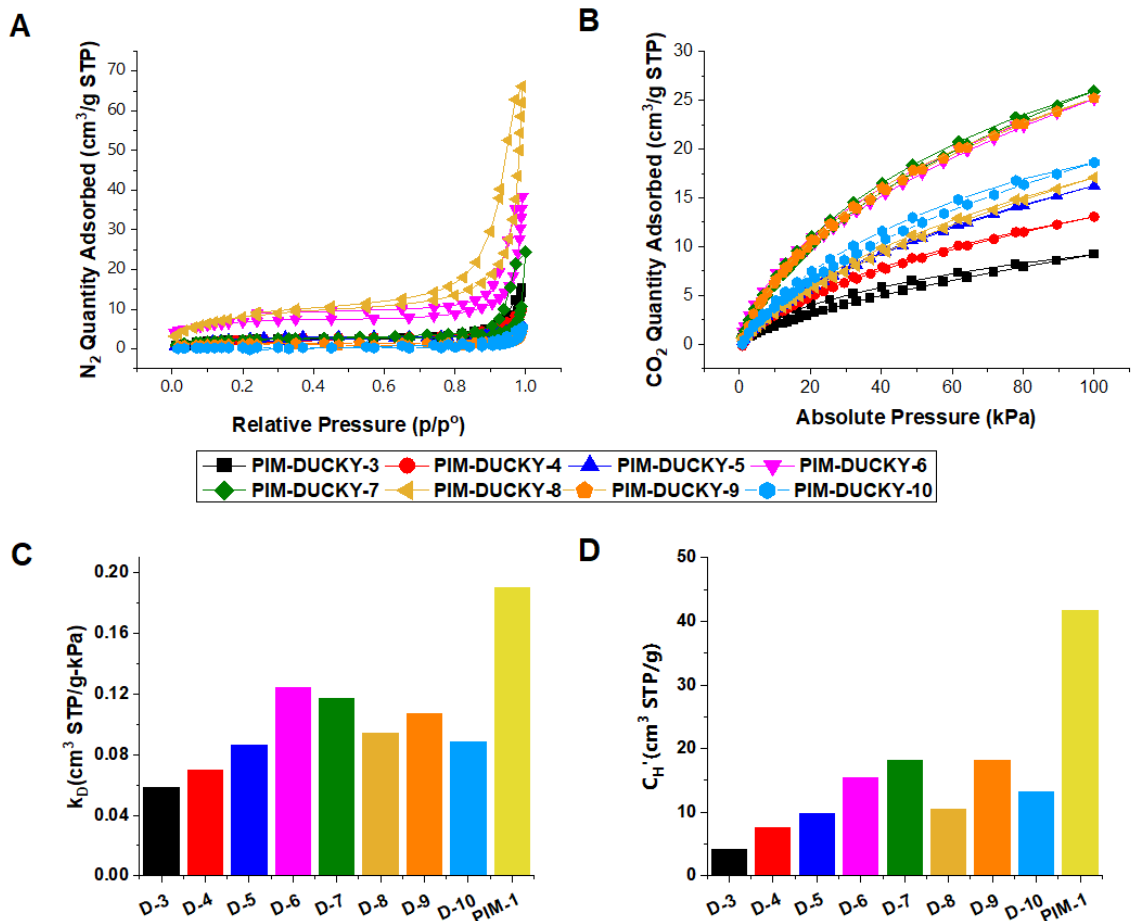


Figure 4.20. Uptake of (A) N_2 at 77 K and (B) CO_2 at 273 K by DUCKY polymers. (C) Henry's law coefficient (k_D) and (D) Langmuir capacity constant (C_H') values fit to CO_2 sorption data, compared to data obtained for PIM-1. Inset = key for A and B.

4.4 Summary

Novel spirocyclic polymers were designed from gas and OSN separation principles in PIM-derived polymers. Modular synthesis schemes allowed for the creation of a range of

polymers with small changes in the polymer backbone, that could then be investigated for structure-property relationships. The SBAD and DUCKY series exhibit lower porosities and lower gaseous swelling than PIM-1 and show promise for decreased dilation- and plasticization-based loss of selectivity in OSN/OSRO applications. This can be attributed to a combination of a change from the PIM-1 ladder structure to a linear backbone which allows for slightly more efficient packing and the presence of rigid N-aryl linkages that are hypothesized to lend swelling and plasticization resistance. Provided the polymers can form continuous films, the novel spirocyclic polymers can be fabricated into membranes to investigate their applicability in liquid hydrocarbon separations, particularly aromatics like toluene, which have been reported to swell PIM-1 by over a 100%.*(17, 18)*

4.5 References

1. C. G. Bezzu *et al.*, A Spirobifluorene-Based Polymer of Intrinsic Microporosity with Improved Performance for Gas Separation. *Advanced Materials* **24**, 5930-5933 (2012).
2. P. Ruiz-Castillo, S. L. Buchwald, Applications of palladium-catalyzed C–N cross-coupling reactions. *Chem Rev* **116**, 12564-12649 (2016).
3. N. C. Bruno, N. Niljianskul, S. L. Buchwald, N-Substituted 2-Aminobiphenylpalladium Methanesulfonate Precatalysts and Their Use in C–C and C–N Cross-Couplings. *The Journal of Organic Chemistry* **79**, 4161-4166 (2014).
4. N. C. Bruno, N. Niljianskul, S. L. Buchwald, N-Substituted 2-Aminobiphenylpalladium Methanesulfonate Precatalysts and Their Use in C–C and C–N Cross-Couplings. *J. Org. Chem.* **79**, 4161-4166 (2014).
5. K. Jiang, L. Zhang, Y. Zhao, J. Lin, M. Chen, Palladium-Catalyzed Cross-Coupling Polymerization: A New Access to Cross-Conjugated Polymers with Modifiable Structure and Tunable Optical/Conductive Properties. *Macromolecules* **51**, 9662-9668 (2018).
6. B. P. Fors, D. A. Watson, M. R. Biscoe, S. L. Buchwald, A Highly Active Catalyst for Pd-Catalyzed Amination Reactions: Cross-Coupling Reactions Using Aryl Mesylates and the Highly Selective Monoarylation of Primary Amines Using Aryl Chlorides. *J. Am. Chem. Soc.* **130**, 13552-13554 (2008).
7. A. B. Foster *et al.*, Understanding the Topology of the Polymer of Intrinsic Microporosity PIM-1: Cyclics, Tadpoles, and Network Structures and Their Impact on Membrane Performance. *Macromolecules* **53**, 569-583 (2020).
8. M. Heuchel, D. Fritsch, P. M. Budd, N. B. McKeown, D. Hofmann, Atomistic packing model and free volume distribution of a polymer with intrinsic microporosity (PIM-1). *J Membrane Sci* **318**, 84-99 (2008).
9. T. A. Barbari, W. J. Koros, D. R. Paul, Gas-Transport in Polymers Based on Bisphenol-A. *J. Polym. Sci. B Polym. Phys.* **26**, 709-727 (1988).
10. M. R. Kosuri, W. J. Koros, Defect-free asymmetric hollow fiber membranes from Torlon®, a polyamide–imide polymer, for high-pressure CO₂ separations. *J. Membr. Sci.* **320**, 65-72 (2008).
11. L. J. Abbott, K. E. Hart, C. M. Colina, Polymatic: a generalized simulated polymerization algorithm for amorphous polymers. *Theor Chem Acc* **132**, (2013).

12. T. F. Willems, C. Rycroft, M. Kazi, J. C. Meza, M. Haranczyk, Algorithms and tools for high-throughput geometry-based analysis of crystalline porous materials. *Micropor Mesopor Mat* **149**, 134-141 (2012).
13. C. Nagel *et al.*, Free volume distributions in glassy polymer membranes: Comparison between molecular modeling and experiments. *Macromolecules* **33**, 2242-2248 (2000).
14. H. Y. Jang *et al.*, Torlon (R) hollow fiber membranes for organic solvent reverse osmosis separation of complex aromatic hydrocarbon mixtures. *Aiche J* **65**, (2019).
15. R. A. Evans, The rise of azide-alkyne 1,3-dipolar 'click' cycloaddition and its application to polymer science and surface modification. *Aust J Chem* **60**, 384-395 (2007).
16. A. J. Qin *et al.*, Polytriazoles with Aggregation-Induced Emission Characteristics: Synthesis by Click Polymerization and Application as Explosive Chemosensors. *Macromolecules* **42**, 1421-1424 (2009).
17. M. L. Jue, C. S. McKay, B. A. McCool, M. Finn, R. P. Lively, Effect of Nonsolvent Treatments on the Microstructure of PIM-1. *Macromolecules* **48**, 5780-5790 (2015).
18. R. Swaidan, B. S. Ghanem, E. Litwiller, I. Pinnau, Pure- and mixed-gas CO₂/CH₄ separation properties of PIM-1 and an amidoxime-functionalized PIM-1. *J Membrane Sci* **457**, 95-102 (2014).

CHAPTER 5. INVESTIGATING THE MEMBRANE-BASED LIQUID HYDROCARBON SEPARATION PERFORMANCE OF NOVEL SPIROCYCLIC POLYMERS

5.1 Overview

This chapter details SBAD and DUCKY polymer membrane fabrication analysis, membrane testing with dilute liquid hydrocarbon feeds and membrane testing with an industrial shale-based crude oil feed. Parts of this chapter are adapted from ‘K. A. Thompson, R. Mathias, D. Kim, J. Kim, N. Rangnekar, J. R. Johnson, S. J. Hoy, I. Bechis, A. Tarzia, K. E. Jelfs, B. A. McCool, A. G. Livingston, R. P. Lively, M. G. Finn, N-Aryl-linked spirocyclic polymers for membrane separations of complex hydrocarbon mixtures. *Science* **369**, 310-315 (2020)’.

5.2 Spirobifluorene Aryl Diamine (SBAD) Series

5.2.1 Dilute Hydrocarbon Separations

Mechanically robust thin film composite membranes were fabricated on crosslinked polyetherimide supports with no observable interlayer delamination (Figure 5.1). Thicknesses of the polymer thin films coated with 2 wt% polymer solutions in chloroform were recorded in the nanometer – micron range. Although the PIM-1 solution was less concentrated during casting, thicker films were observed compared to the SBAD series which could be due to lower polymer solution penetration through the support during casting as a result of its higher viscosity and lower polymer density.(1)

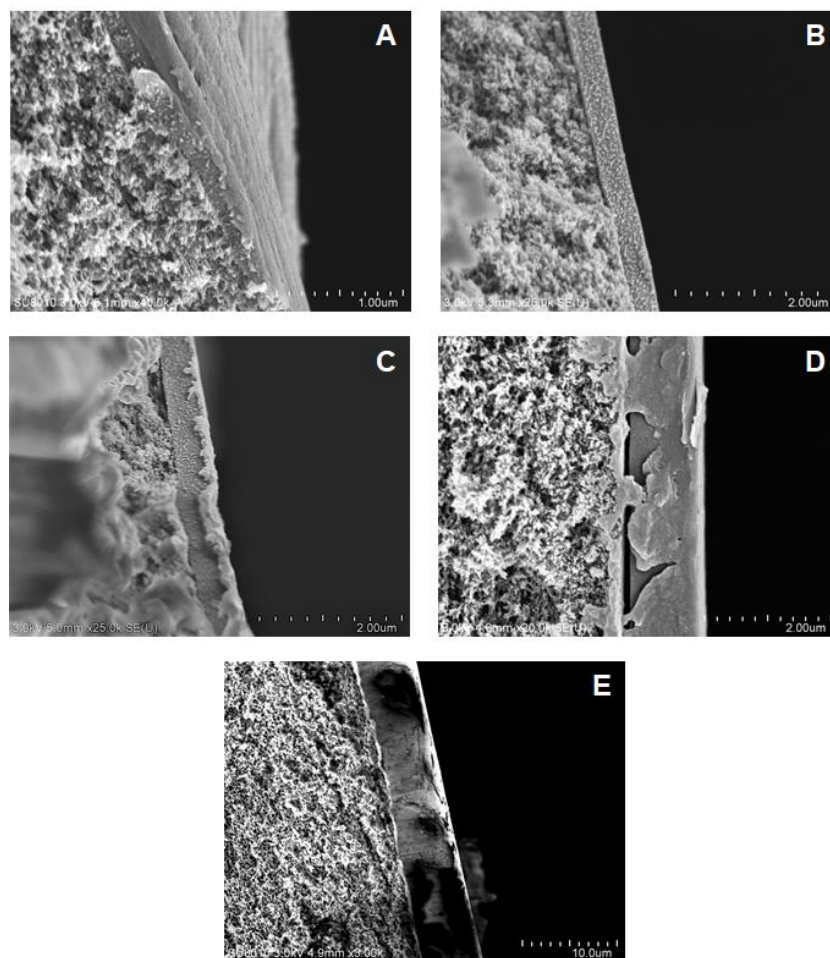


Figure 5.1. Side view of thin film-composites: dense polymer layer coated on porous crosslinked polyetherimide. A) SBAD-2 B) SBAD-3 C) SBAD-4 D) PIM-1.

The molecular separation performance of these materials was surveyed with binary mixture separations of 1,3,5-triisopropylbenzene (TIPB) in toluene (Figure 5.2). TIPB serves as a surrogate solute molecule for organic solvent separations, with a molecular weight (204.35 Da) at the lower end of the typical nanofiltration range (200-1000 g·mol⁻¹) in which PIMs have often been tested.(2) Membrane performance was evaluated via cross flow filtration after more than 48 hours of continuous permeation of the mixture. As shown

in Figure 5.2, all of the SBAD polymers exhibited significantly greater rejections at steady-state than PIM-1, with permeances in the range of 0.1-0.7 L-m⁻²-h⁻¹-bar⁻¹. SBAD-1 showed the highest TIPB rejection of 80% throughout the duration of the experiment and SBAD-3 was the least effective, despite having similar predicted micropore size distributions as the other materials.

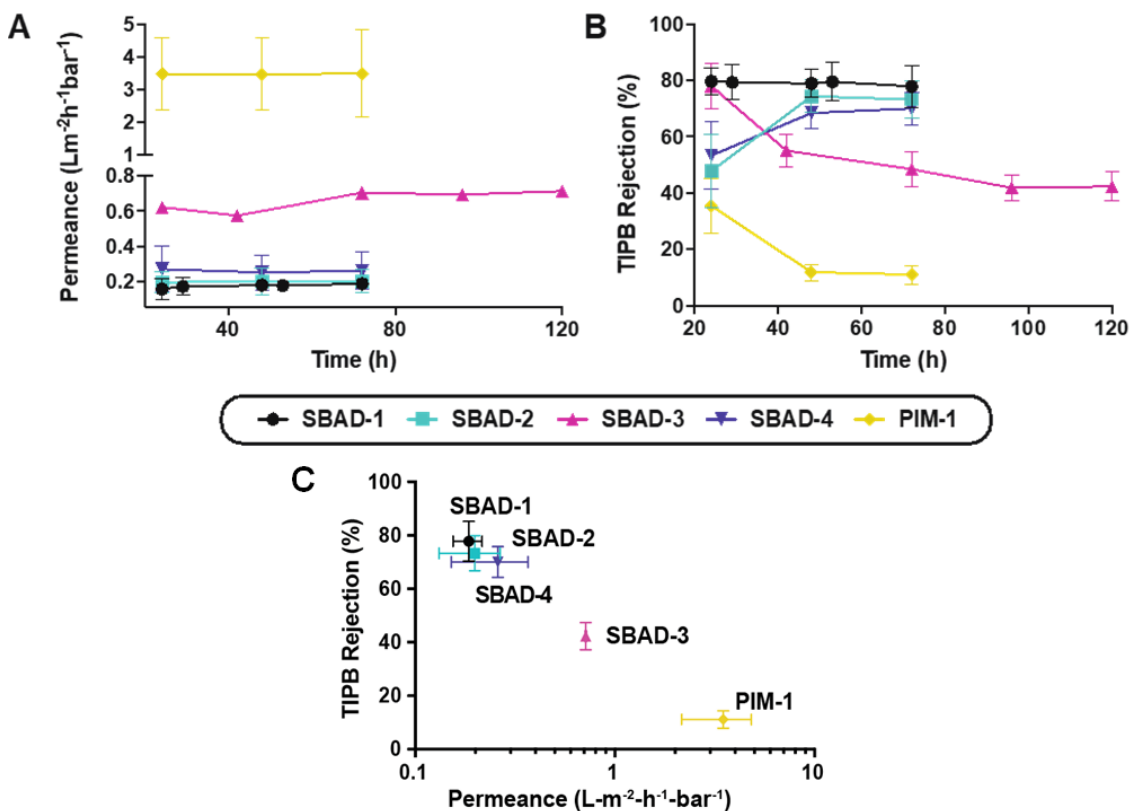


Figure 5.2. (A) Transient toluene permeance, (B) transient 1,3,5-triisopropyl benzene (TIPB) rejection and (C) steady-state TIPB rejection vs. toluene permeance of SBAD and PIM-1 membranes when a 1/99 mol% feed of TIPB/toluene is applied at 22°C, 15 bar.

The most relevant structural difference appeared to be the larger biphenyl bridge structure used in SBAD-1, 2, and 4 vs. the smaller phenyl bridge in SBAD-3. The

improvement in TIPB rejection with the larger bridge suggests that aromatic chain-chain interactions, more available with biphenyl linkages, are advantageous. The rejection properties of SBAD-2 and SBAD-4 increased over 48 hours, reaching steady-state values only slightly lower than SBAD-1 (Figure 5.2B). Such time-dependent behavior is consistent with solvent-induced polymer relaxation towards a less swollen state (3). Only a handful of commercial organic solvent nanofiltration membranes and other polymeric membranes with complex fabrication procedures are capable of high rejections of ~ 200 g-mol⁻¹ solutes and have toluene permeances in the same range (4). As SBAD-1 demonstrated the highest rejections, it was chosen for scale-up and further evaluation with more complex mixtures.

SBAD-1 and PIM-1 were compared in a standardized measurement of molecular weight cut-offs using oligostyrene markers in toluene (Figure 5.3). SBAD-1 was significantly better than PIM-1 in the separation of small solutes (molecular weight cut-off of 335 vs. 1220 g-mol⁻¹, respectively), albeit at a much lower permeance (0.2 L-m⁻²-h⁻¹-bar⁻¹ vs. 3.49 L-m⁻²-h⁻¹-bar⁻¹). The molecular weight cut-off of PIM-1 increased over the course of 3 days while that of SBAD-1 remained constant.

The separation performance of SBAD-1 using a group of non-polar hydrocarbon (Table 5.1) molecules in the organic solvent reverse osmosis and nanofiltration ranges that are representative of hydrocarbons found in light crude oils is shown in Fig. 2C.(5) A hydrocarbon molecular weight cut-off of approximately 253 g-mol⁻¹ (Figure 5.4) was calculated. Below 150 g-mol⁻¹, greater aromaticity (ratio of aromatic carbons to aliphatic carbons) of the solute was found to diminish rejection, perhaps due to greater sorption interactions with the aromatic rings present in the polymer backbone.

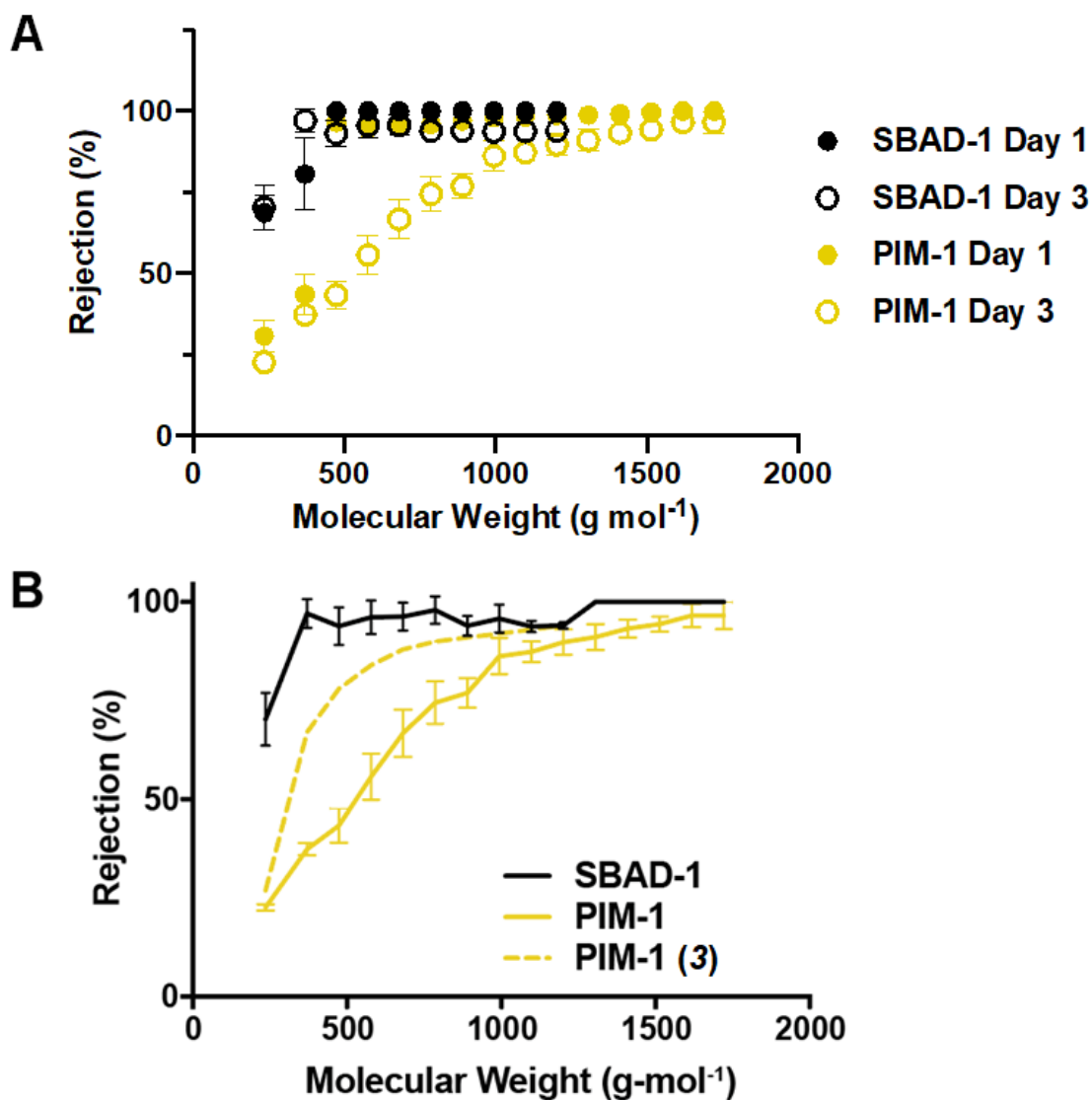


Figure 5.3. Molecular weight cut-off curves of SBAD-1 at 30 bar (threshold = 335 g mol^{-1}), PIM-1 at 5 bar (1220 g mol^{-1}), and PIM-1 data reported at 30 bar (786 g mol^{-1}) for polystyrene standards in toluene at 22°C. The high flux in PIM-1 in our work limited the applied pressure difference to 5 bar in order to maintain < 5% stage cuts. Data reported by Cook et al. at the same conditions (6) as SBAD-1 was shown for direct comparison. Comparison of SBAD-1 and PIM-1 oligostyrene rejection over three days.

Table 5.1. Steady-state rejection of a 7-component mixture comprised of six solutes at 1 mol% in a dilute feed mixture in toluene tested at 10 bar over a 66-hour period for SBAD-1 thin film composites formed via spin coating on Matrimid® supports; and steady-state rejection of a 10-component mixture comprised of 9 solutes included at 1 mol% in a dilute feed mixture in toluene tested at 30 bar over a 24-hour period for SBAD-1 thin film composites formed via roll-to-roll coating on Ultem® supports. Puramem® 280 was tested under the same conditions as described above. The difference in permeance is likely due to differences in film thickness due to the method of production. Negative rejections indicate enrichment of the component in the permeate.

		<i>SBAD-1</i>	<i>Puramem®</i> 280
7-comp mixture	<u>Species</u>	<u>MW (g·mol⁻¹)</u>	<u>Rejection (%)</u>
	p-xylene	106.17	-4.2 ± 0.9
	o-xylene	106.17	-1.3 ± 0.7
	Mesitylene	120.19	12 ± 0.6
	Naphthalene	128.17	-5.7 ± 1.4
	Biphenyl	154.21	-3.3 ± 1.5
	1,3,5-triisopropylbenzene	204.36	83 ± 1.1
	Permeance (L·m⁻²·h⁻¹·bar⁻¹)		0.24 ± 0.05
10-comp mixture	Isooctane	114.22	68 ± 0.7
	Propylbenzene	120.20	23 ± 2.1
	Tetralin	132.20	34 ± 1.1
	n-butylcyclohexane	140.27	66 ± 0.6
	1-methylnaphthalene	142.20	33 ± 0.4
	Dodecane	170.33	75 ± 0.4
	Dodecylbenzene	246.43	86 ± 0.7
	Pristane	268.51	97 ± 1.3
	n-docosane	310.60	96 ± 1.2
	Permeance (L·m⁻²·h⁻¹·bar⁻¹)		0.15 ± 0.03

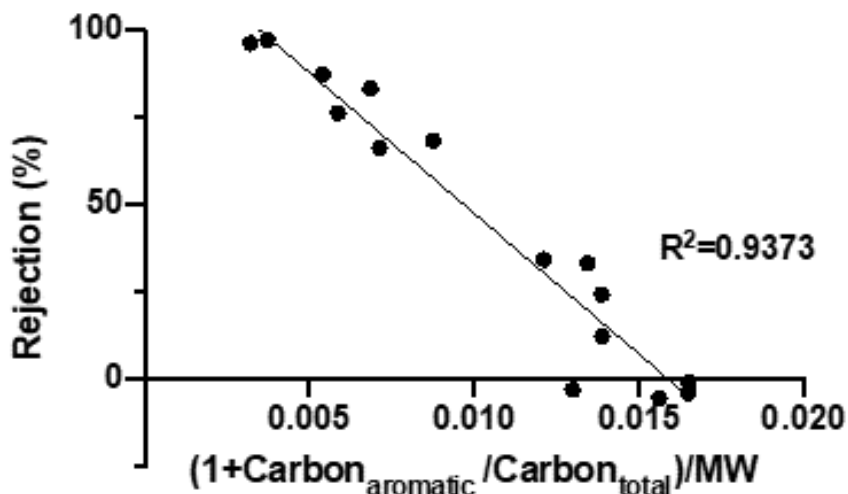


Figure 5.5. Dependence of rejection on aromaticity and molecular weight (MW, $\text{g}\cdot\text{mol}^{-1}$) where the effect of aromaticity (sorption) and molecular weight (diffusion) are coupled as represented by $(1 + \text{Carbon}_{\text{aromatic}} / \text{Carbon}_{\text{total}}) / \text{MW}$.

5.2.2 Complex Hydrocarbon Separations

The naphtha and kerosene fractions of crude oil, representing a good candidate for membrane-based hydrocarbon fractionation.(7, 8) A thin-film composite membrane sheet of SBAD-1 was produced through roll-to-roll coating of the polymer onto a prefabricated Ultem® support. Membrane coupons from the sheet (diameter 47 mm) were subjected to a complex feed of hydrocarbons that serve as a model naphtha-kerosene fraction (Table 5.2). Several large spiral wound modules (Figure 3.3) (containing 1.8 m x 0.2 m of membrane) were also fabricated from the sheet to highlight the scalability of these materials.

Table 5.2. 9-component feed mixture that was used as a model for the separation of a middle distillate cut of crude oil and the resulting ratios of concentration in permeate (C_P) over concentration in retentate (C_R) for both membrane coupons and a spiral wound module of SBAD-1.

	MW (g-mol ⁻¹)	Feed Concentration (mol%)	C_P/C_R	
			Coupon	Module
toluene	92.14	17	1.18 ± 0.02	1.09 ± 0.00
methylcyclohexane	98.19	28	0.90 ± 0.01	0.97 ± 0.02
<i>n</i> -octane	114.22	22	1.11 ± 0.02	0.98 ± 0.00
isooctane	114.22	15	0.82 ± 0.05	0.92 ± 0.02
<i>tert</i> -butylbenzene	134.21	2.2	1.25 ± 0.03	0.99 ± 0.00
decalin	138.25	11	1.03 ± 0.00	0.94 ± 0.01
1-methylnaphthalene	142.20	2.0	1.40 ± 0.05	1.06 ± 0.00
TIPB	204.35	1.6	0.52 ± 0.07	0.77 ± 0.00
isocetane	226.45	1.3	0.34 ± 0.06	0.73 ± 0.01

Figure 5.6 shows the membrane performance as the ratio of permeate to retentate concentrations plotted against the molecular weights of the components. A permeance of 0.022 ± 0.013 L-m⁻²-h⁻¹-bar⁻¹ for the coupon and 0.076 ± 0.003 L-m⁻²-h⁻¹-bar⁻¹ for the module was obtained. This permeance is lower than the dilute mixture experiment (Table 5.1) due to the increase in concentration of less permeable molecules in the complex, multicomponent mixture.⁽⁹⁾ However, good separation of molecules of different molecular weights, independent of molecular class, as well as for molecules from different classes without a molecular weight advantage was obtained.

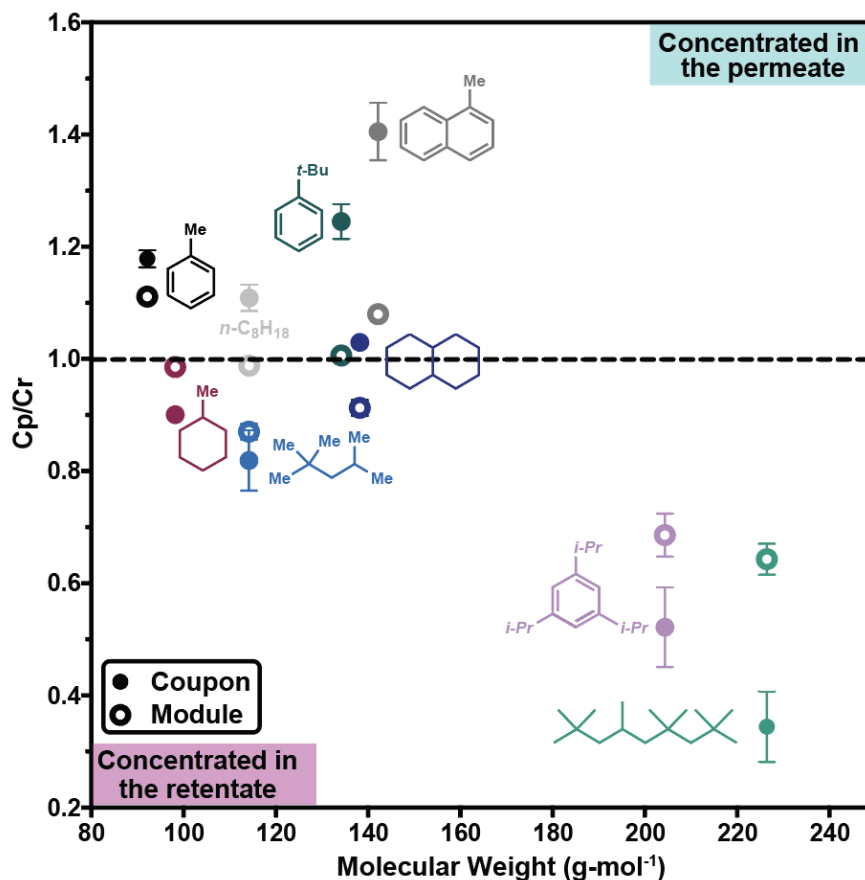


Figure 5.6. Ratio of concentrations in permeate vs. retentate (C_p/C_r) of components in a complex, model crude oil (composition is shown in Table 5.2) for both thin film composite membrane coupon of SBAD-1 fractionated at 40 bar (22°C) and a spiral wound module of SBAD-1 fractionated at 40 bar (20°C). Molecules above the reference line were more concentrated in the permeate compared to the feed while the molecules below, were more concentrated in the retentate. A permeance of 0.022 ± 0.013 L-m⁻²-h⁻¹-bar⁻¹ for the coupon and 0.076 ± 0.003 L-m⁻²-h⁻¹-bar⁻¹ for the module was obtained.

Some notable separation factors (based on coupon data) are shown in Figure 5.7, illustrating the potential of SBAD-1 for membrane-based concentration of solutes of both low molecular weights and high aromaticity. The values highlighted are comparable with separation factors obtained for liquid xylene isomers using carbon molecular sieve

membranes (10). Aromatic-rich permeates streams (observed in this work) are useful for the production of plastics and provide a rich source of industrial organic solvents. Fractionation of crude oil into groups of smaller and larger molecules also has direct value in generating products classified by the number of carbons present such as gasoline (C5-12 alkanes and cycloalkanes) and jet fuel (C10-18 alkanes and aromatics). The retentate stream shown in Fig. 3A contains both of these.

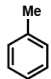
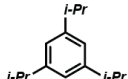
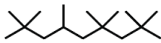
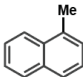
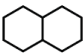
Separation Factors		
	VS.	 2.3
$n\text{-C}_8\text{H}_{18}$	VS.	 3.2
	VS.	 1.4

Figure 5.7. Some notable separation factors for SBAD-1 based on data shown in Figure 5.6.

Additionally, exposure to temperatures up to 75 °C did not negatively affect membrane performance. Figure 5.8 validates the increase of separation factors with increasing pressure as is generally observed in OSN. However, the separation factors were independent of temperature except when the performance suffered at a much higher temperature (75 °C). Recycling the membrane back to 35°C and 45 bar after treatment at

55 bar increased the separation performance, which could be due to slow temporal changes in transport rates through the membrane. Ultimately, this shows that the high temperatures and pressures did not damage the membrane and cause permanent loss in performance.

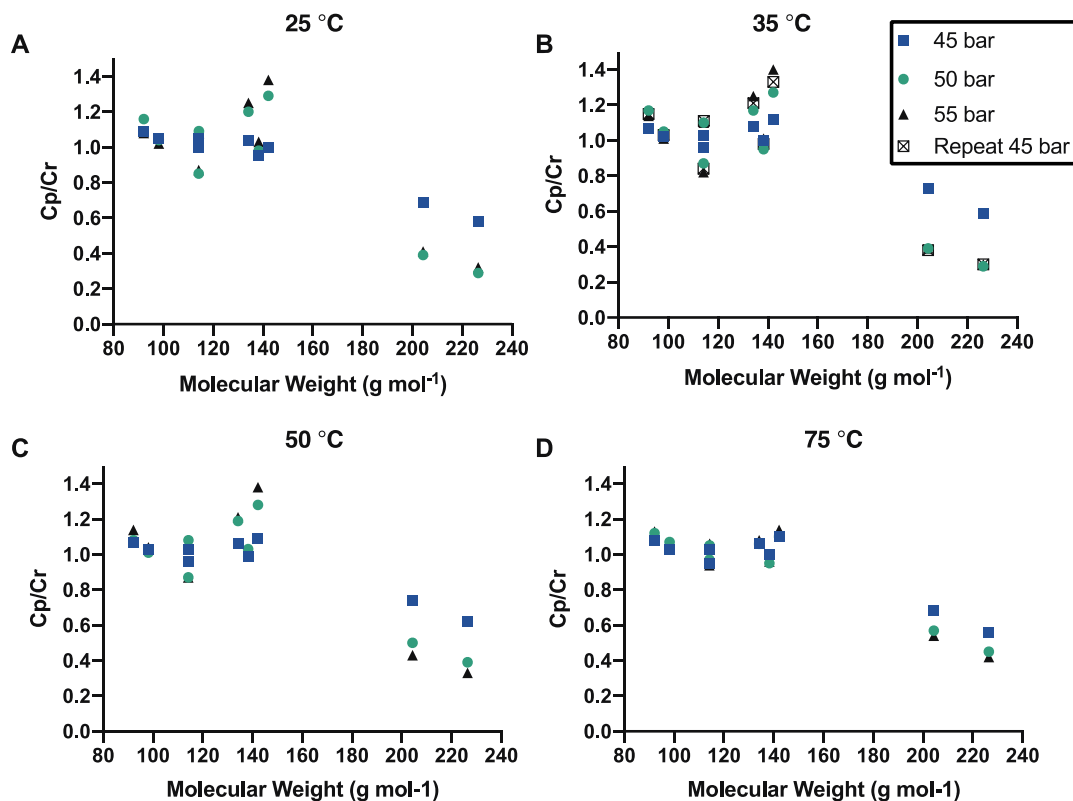


Figure 5.8. Ratio of concentrations in permeate vs. retentate (C_p/C_r) of components in the complex mixture outlined in Table 5.2 for a thin film composite of SBAD-1 fractionated at various temperatures and pressures. Repeat at 45 bar was completed by recycling the membrane back to 35°C and 45 bar after treatment at 55 bar and showed increased separation performance. The temperature- and pressure-based study spanned a period of 2 months.

SBAD-1 was also challenged with a light shale crude oil to illustrate the potential of membrane materials as an alternative for the fractionation of crude oil. Figure 5.9 shows

the boiling point distribution of molecules in the feed, permeate and retentate. Approximately 38% of the mixture boiled below 200°C in the feed tested in this work. After passing through a thin film composite of SBAD-1 the permeate was found to be significantly enriched in the lighter molecules present in the feed, such that more than 60% of the permeate boiled below 200°C. The inset shows a picture of the crude oil and the lighter colored permeate indicating removal of color bodies that are typically high in molecular weight. (11)

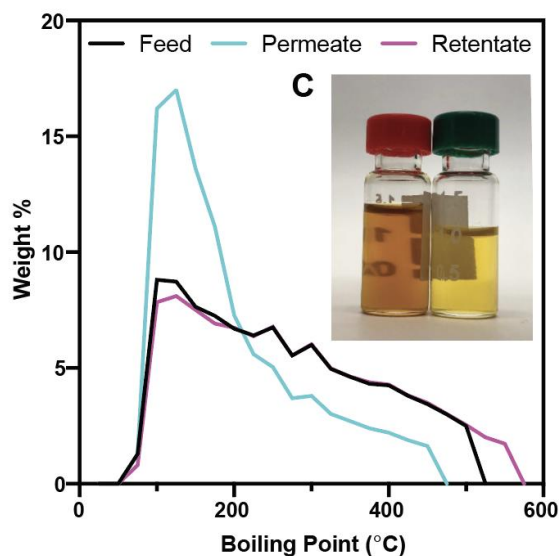


Figure 5.9. Boiling point distribution of feed, permeate and retentate from SBAD-1 membrane fractionation of shale-based crude oil. Inset: Picture of feed (left) and permeate (right) from SBAD-1 membrane fractionation of real shale-based light whole crude oil.

Figure 5.10 visualizes the differences in GCxGC-FID chromatograms(12) of the feed and permeate, with the three axes representing boiling point (time scale in minutes),

polarity (time scale in seconds), and response factor (z-axis). The GCxGC-FID data indicates enrichment of molecules lighter than carbon numbers of 12 or around molecular weight of 170 Da. The membrane permeance is low ($0.016 \text{ L}\cdot\text{m}^{-2}\cdot\text{h}^{-1}\cdot\text{bar}^{-1}$) as the thin film fabrication process has not yet been optimized to create more productive composites. Overall, the SBAD-1 membrane-based separation demonstrated selectivity for low molecular weight saturated molecules in the naphtha and early kerosene boiling range with slight permeation of higher molecular weight linear paraffins. This result is similar to a boiling point separation of a complex hydrocarbon mixture, but without expending the energy associated with vaporization.

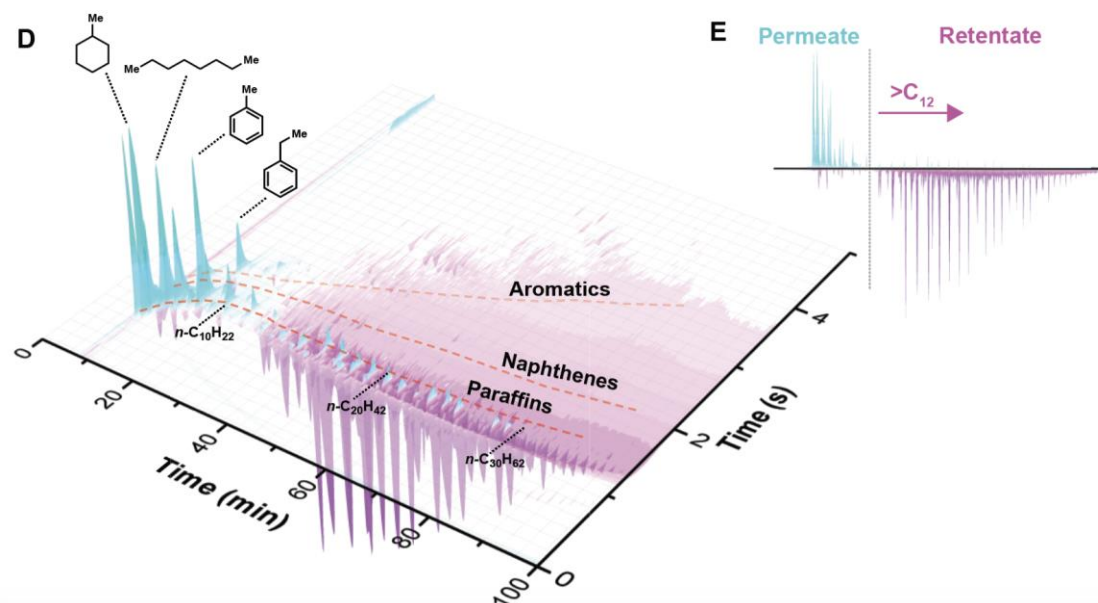


Figure 5.10. GCxGC-FID analysis of membrane fractionation of shale-based crude oil at 130°C and 55 bar showing the feed chromatogram subtracted from the permeate chromatogram. Teal elution peaks are concentrated in the permeate, whereas the magenta elution peaks are concentrated in the membrane retentate. General hydrocarbon classifications are highlighted with dashed red lines to guide the eye. Top right: side view of GCxGC-FID showing the carbon number partition of real crude oil obtained by SBAD-1.

A clear “inter-class” separation of the crude was observed with a preferential order of permeation: naphthenes, linear paraffins, aromatics, and branched paraffins (Figure 5.11 and Table 5.3). Moreover, “intra-class” size-based separation also occurred for each of these individual classes of hydrocarbons, such that the permeate was enriched in the low boiling (or “light”) compounds in the crude oil (Figure 5.12). Although the fouling effects from the real crude feed were not specifically explored, the permeance and separation factors changed minimally over a period of two months during synthetic crude testing at temperatures ranging from 25 °C to 75 °C (Figure 5.8).

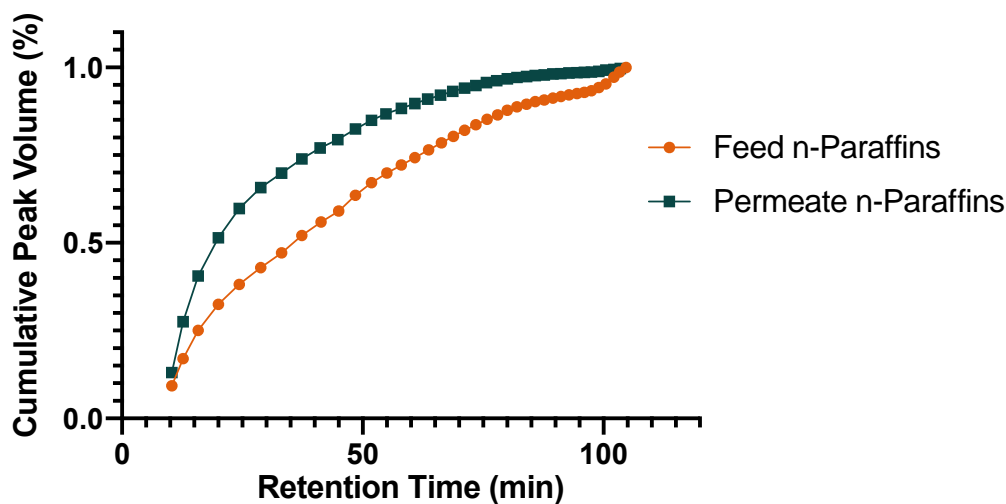


Figure 5.11. Comparison of cumulative peak volume curves of the permeate and feed for the SBAD-1 enrichment of normal paraffin molecules from a whole crude oil separation. Increasing retention time corresponds with increasing molecular weight.

Table 5.3. Percentage enrichment by hydrocarbon class in the permeate from the crude oil feed for SBAD-1 at 55 bar and 130 °C. Enrichment was calculated as the area between cumulative peak volume curves of the permeate and feed as shown in Figure 5.11.

	Permeance	Class	% Enrichment From Feed
SBAD-1	0.016 (L·m ⁻² ·h ⁻¹ ·bar ⁻¹)	iso-paraffins	13.5
		Aromatics	15.7
		n-paraffins	21.0
		Naphthenes	22.5

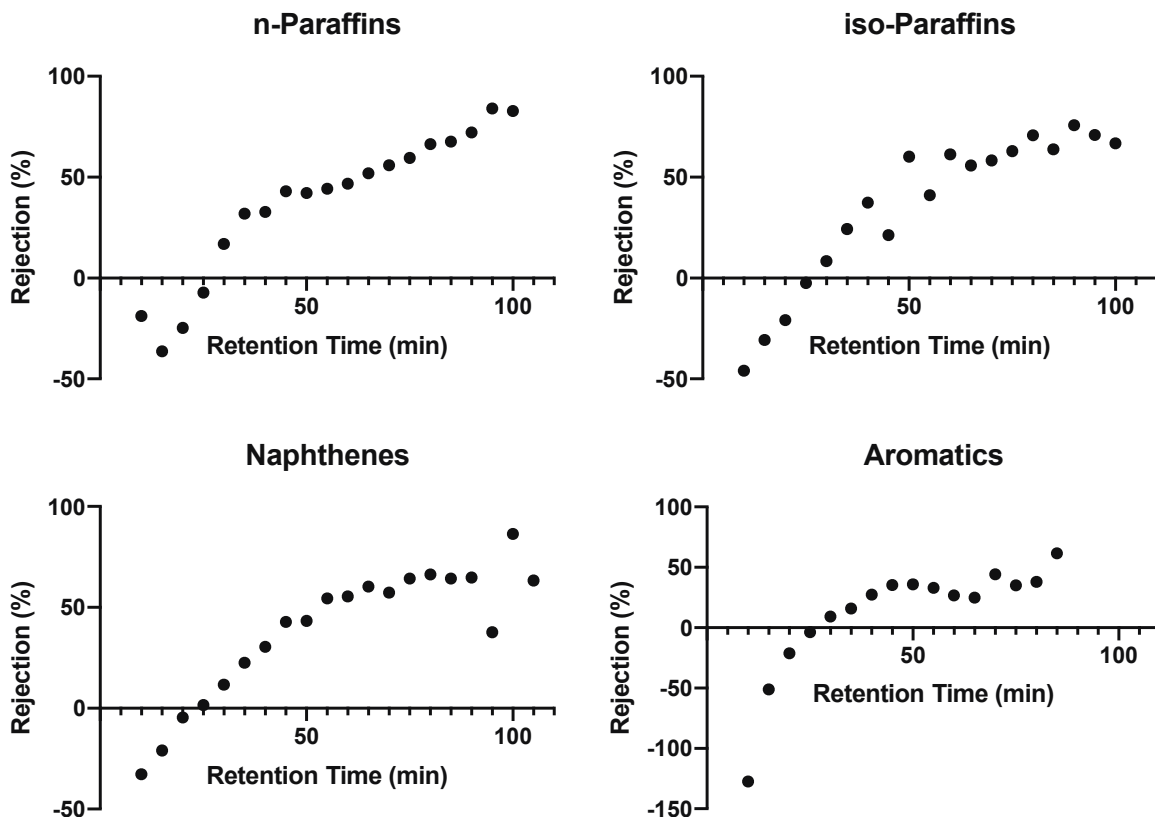


Figure 5.12. Rejection curves for individual hydrocarbon classes obtained from GCxGC analysis of crude oil separation by SBAD-1. Increasing retention time corresponds to increasing molecular weight within each class.

An interesting distinction emerges when comparing traditional binary separation experiments (i.e., toluene/TIPB) and dilute multicomponent hydrocarbon separations with the complex mixture fractionation experiments (i.e., fractionation of lab-made and real crude oil). While molecular weight cut-off and rejection are important figures of merit for dilute separations such as water purification and nanofiltration, the utility of this metric is less clear in the case of complex mixture fractionation where there is no discrete solvent or solute: every molecule in crude oil is a solvent. In this case, each molecule in the mixture experiences highly nonideal coupling effects (e.g., diffusion and sorption) during permeation. Moreover, the osmotic effects in this crude oil system are complex and certainly contribute towards reducing the fluxes relative to the diluted mixtures. The membrane-based crude oil separation occurs via a combination of diffusion-based selection processes as well as solvent-membrane (and solvent-solvent) interactions, which further reinforces the importance of testing real mixtures. Beyond testing industrial feeds, it will be important to establish how these materials fit into an energy-efficient membrane fractionation process (13). To produce distillation-like products through membrane fractionation, a cascade of membrane materials such as SBAD-1, capable of fractionating feeds across a specific range of hydrocarbon sizes, will be necessary (Figure 5.13).

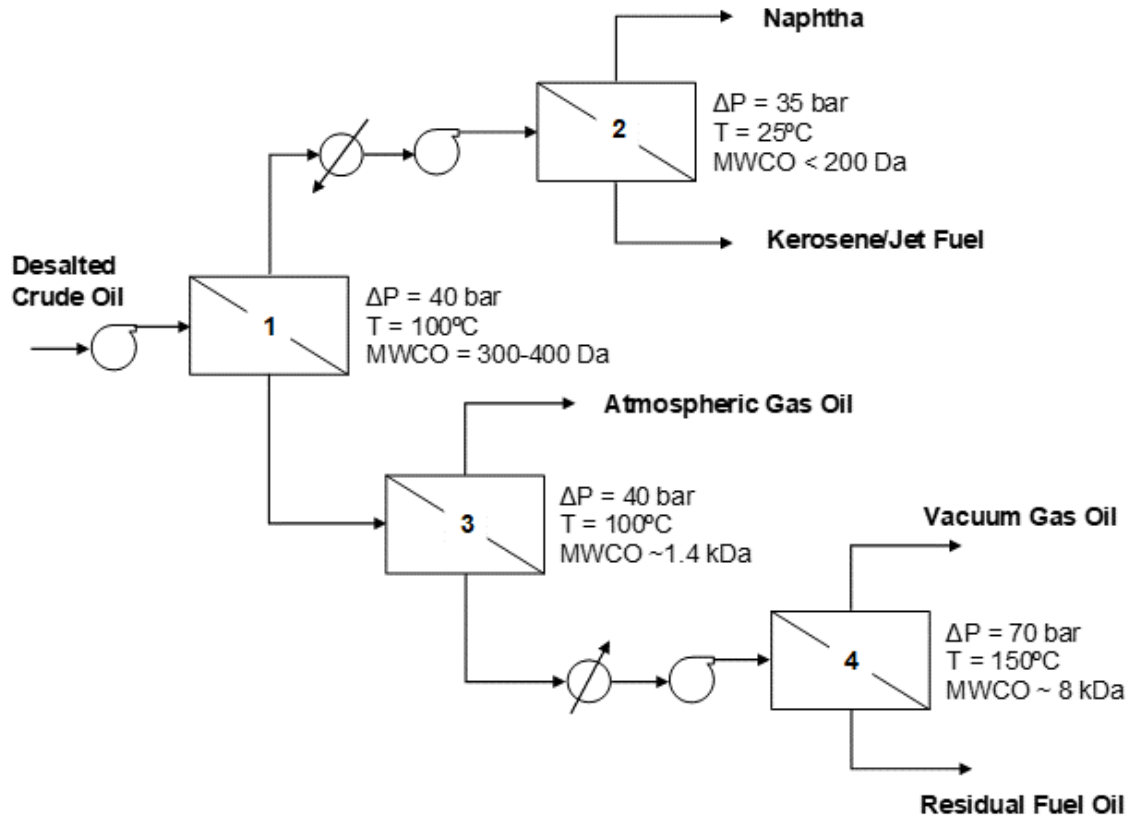


Figure 5.13. Exemplary membrane cascade for the separation of crude oil into various fractions (13). Desalted crude oil is fed to membrane stage 1 containing a membrane with molecular weight cut-off (MWCO) in the range of 300-400 Da. Stage 1 permeate is fed to membrane stage 2 with a membrane operating in reverse osmosis or pervaporation mode with MWCO < 200 Da. The permeate and retentate from stage 2 have boiling point distributions in the range of naphtha and kerosene/jet fuel, respectively. Stage 1 retentate is the feed for membrane stage 3, which could consist of a membrane with MWCO ~ 1.4 kDa. The permeate from stage 2 has boiling points mainly in the range of 230-340°C, which corresponds to atmospheric gas oil. Atmospheric gas oil can be further processed into gasoline, diesel and light gas oil. Stage 3 retentate is fed to membrane stage 4, which could consist of an ultrafiltration membrane with MWCO ~ 8 kDa. The permeate from stage 4 has boiling points in the range of 340-570°C, which corresponds to vacuum gas oil. The retentate from this stage can be used in heavy fuel oil/residual fuel oil applications.

5.3 DUCKY Series

5.3.1 Dilute Hydrocarbon Separations

Thin film composites of DUCKY polymers were fabricated on top of crosslinked polyetherimide (Figure 5.14). Smooth, continuous thin films with thicknesses less than 700 nm were obtained. Blade coatings were universally performed with 1wt% polymer solutions in chloroform and a blade with a 25.4-micron thickness. Still, a significant variation in thicknesses (between 25 to 650 nm) across samples indicates that the manual blade coating method is not consistent. This can be attributed to the inconsistencies in a) time delays between pouring the solution across the flat support and beginning the blade drawing, b) the speed at which the blade is drawn manually, and c) the area on the coated support from which the membrane sample is taken for analysis.⁽¹⁴⁾

The thin film composites were tested with dilute solutions of oligostyrene standard solutes in toluene and ethanol (Figure 5.15). MWCOs of the DUCKY series are higher than SBAD-1 (greater than 350 g/mol) and can reach up to 1200 g/mol depending on polymer structure. There is a clear correlation between the inferred structural rigidity of the polymer structure (Figure 3.12) and the sharpness of the MWCO. For instance, DUCKY-9 is hypothesized to have the most structural rigidity in the entire series due to reduced freedom of rotation from the combination of the tetrazole linkage and the 9,9-diphenyl-9H-fluorene in the comonomer. The resulting MWCO curve for DUCKY-9 in toluene has the sharpest increase in rejections at low molecular weights, where a rejection of 45% for the dimer jumps to 90% for the trimer.

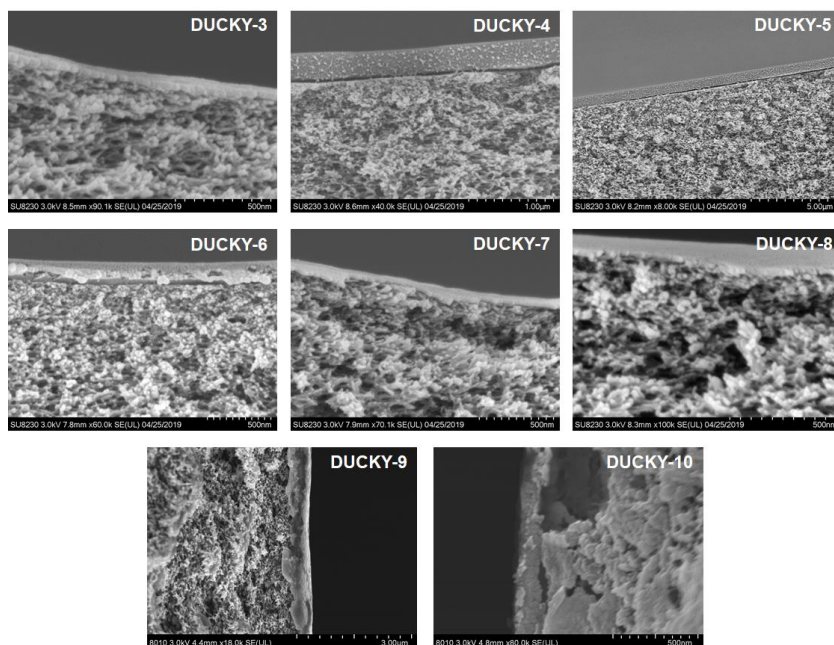


Figure 5.14. Cross-sectional views of thin film-composites of dense DUCKY polymer layer coated on porous crosslinked polyetherimide.

The lack of sharp cutoffs for DUCKY-6 and DUCKY-7 in toluene suggests that the sharp cutoff for DUCKY-9 cannot be attributed to the absence of the flexible ether linkage alone. On the other hand, DUCKY-10, which has the 9,9-diphenyl-9H-fluorene comonomer but also contains an ether linkage, does not have the sharp cutoff. This leads to the hypothesis that the result observed for DUCKY-9 is due to the combination of the rigid tetrazole linkage (without ether group) and the rigid 9,9-diphenyl-9H-fluorene structure. An interesting observation is the drastic change in DUCKY-3 performance in ethanol from the performance in toluene. The rejections of the oligostyrenes drop from >60% for the dimer to below 20% for solutes in the entire range tested.

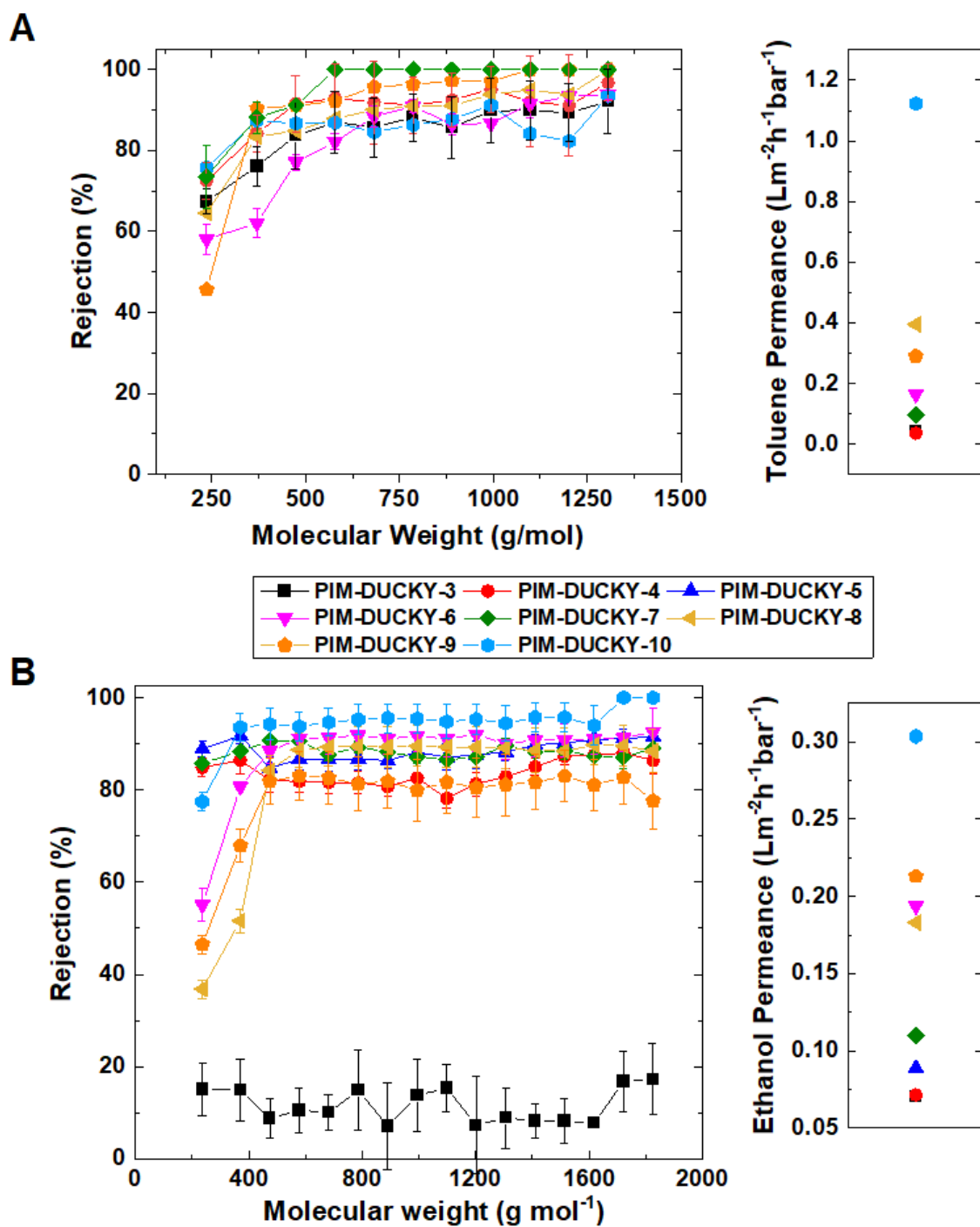


Figure 5.15. Molecular weight cut-off curves and permeances of DUCKY polymer series at 30 bar for polystyrene standards in (A) toluene and (B) ethanol at 22°C.

A similar observation was made for PIM-1 where rejections in toluene reached 90% for solutes > 700 g/mol but remained below 20% for solutes in methanol up to 1400 g/mol.⁽⁶⁾ In this work by Cook et al., this behaviour of PIM-1 was attributed to the weak solubility interactions between methanol and PIM-1, which lowered the permeation rate. DUCKY-4, which is similar in structure to DUCKY-3 but lacks the additional steric hindrance around the benzyl group from four methyl functionalities, does not exhibit the same behavior as DUCKY-3. If the differences in thin film thicknesses of the various membranes are accounted for based on Figure 5.14, then DUCKY-3 membranes have reduced ethanol and toluene permeabilities (Table 5.4) compared to DUCKY-4. It is not immediately clear why the increased steric hindrance around the phenyl linking group would play a significant role in changing in ethanol and toluene permeation. A possible explanation for the rejections dropping significantly across the entire molecular weight range in ethanol and not toluene is that the oligostyrenes have a smaller hydrodynamic diameter in ethanol due to poor solubility⁽¹⁵⁾ and thus, a decreased ethanol permeability could easily lead to a dramatic drop in styrene rejections if the polymer network is flexible.⁽¹⁶⁾

The separation factors of various small molecule pairs from Figure 5.15A are plotted against toluene permeance in Figure 5.16. These styrene marker experiments show that for hydrocarbon separations that involve molecules > 370 g/mol, both DUCKY-9 and DUCKY-10 are expected to offer the most favourable properties, with the former giving the highest separation factor and the latter offering the highest permeance with separation factors that are comparable to the rest of the series. However, when the toluene/dimer

separation is concerned, DUCKY-9 appears to be the least attractive candidate. DUCKY-10 remains favourable due to a high permeance and a high separation factor.

Table 5.4. Ethanol permeabilities of the DUCKY series in oligostyrene marker experiments at an applied pressure of 30 bar.

DUCKY #	Thickness (nm)	Ethanol Permeability ($10^{-9} \text{ Lm}^{-1}\text{h}^{-1}\text{bar}^{-1}$)	Toluene Permeability ($10^{-9} \text{ Lm}^{-1}\text{h}^{-1}\text{bar}^{-1}$)
3	37	2.6	1.5
4	305	21.8	11.1
5	640	56.8	-
6	125	24.2	20.6
7	26	2.9	2.5
8	380	69.6	150.0
9	263	56.0	76.5
10	143	43.4	160.6

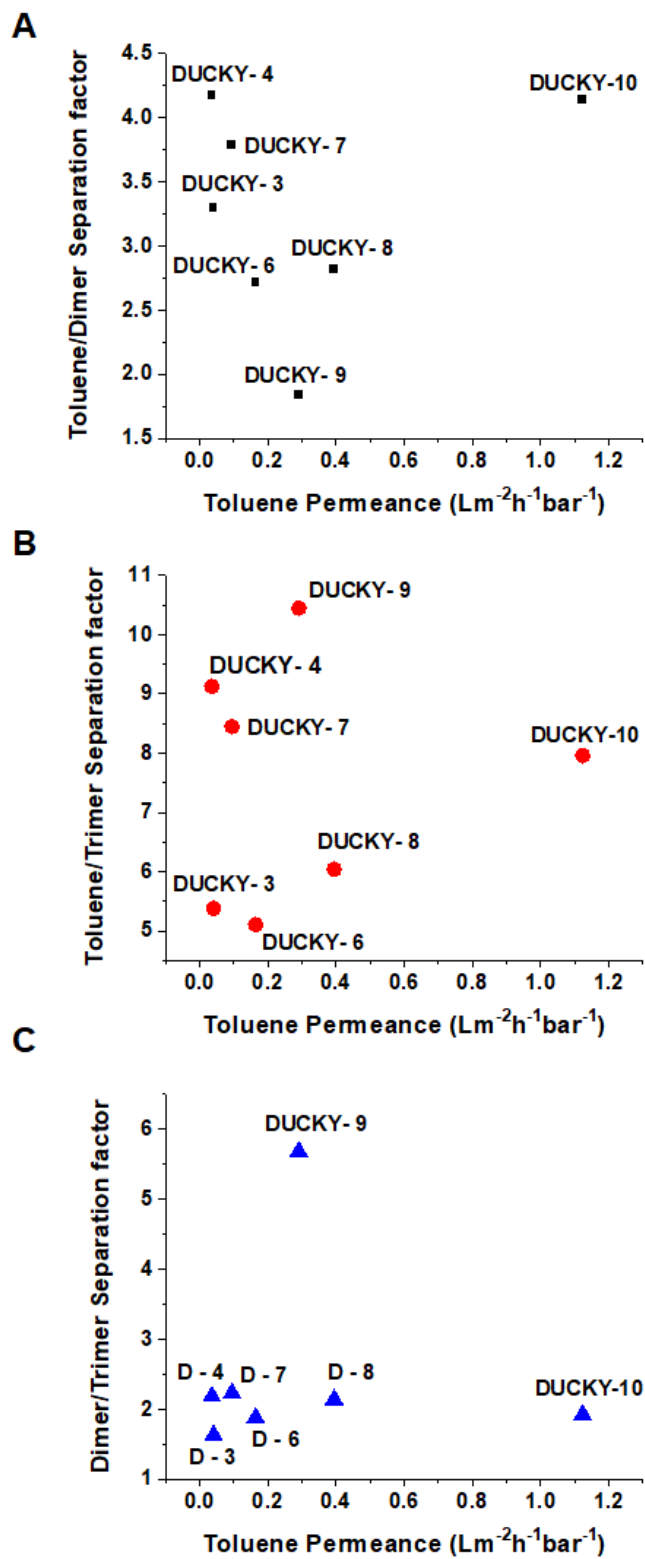


Figure 5.16. Separation factors based on Figure 5.14. data for A) toluene/dimer B) toluene/trimer and C) dimer/trimer.

The uniquely sharp MWCO of DUCKY-9 makes it an attractive option for multi-solute separations in specific molecular weight ranges. To further explore the applicability of this polymer in crude oil-type mixtures, 11 representative hydrocarbon molecules were tested in dilute amounts (1 mol%) in toluene (Figure 5.17). A toluene permeance of $0.39 \text{ Lm}^{-2}\text{h}^{-1}\text{bar}^{-1}$ was obtained, which is more than twice the value obtained for SBAD-1 membranes for a similar separation of nine molecules from toluene (Table 5.1), even though the thickness of the films were observed to be in a similar range (Figure 5.1 and Figure 5.14). The rejections of large molecules are not quite as high as those observed for SBAD-1 in Figure 5.4, but the separation factors for specific molecule pairs are greater. Specifically, DUCKY-9's class-based aliphatic/aromatic separation in the same weight range is less pronounced, and instead, perhaps due to the rigidity in the polymer backbone, it has a more evident molecular weight-based separation.

Table 5.5 shows the separation factors for iso-octane/TIPB, tetralin/TIPB, and dodecane/TIPB, which range in molecular weight differences between 34 - 90 g/mol or carbon numbers of C8 - 15. It is in this range that the rejection curve is the steepest for the representative hydrocarbons. Thus, DUCKY-9 was also tested with the light shale-based crude oil to investigate whether a better separation of small molecules can be obtained compared to SBAD-1.

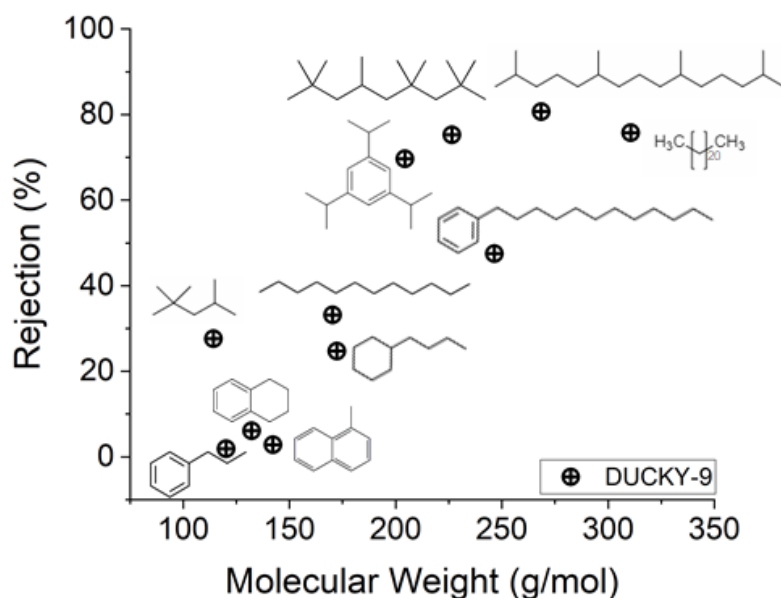


Figure 5.17. Hydrocarbon molecular weight cutoff curve for DUCKY-9 using a 12-component mixture containing 1 mol% concentration of solutes shown in the graph in toluene. A cutoff could not be determined as rejections above 90% were not observed.

Table 5.5. Separation factors for selected molecule pairs from Figure 5.4 and Figure 5.17.

Molecule Pair	Separation Factors	
	SBAD-1	DUCKY-9
iso-octane/TIPB	1.88	2.39
tetralin/TIPB	3.88	3.10
dodecane/TIPB	1.47	2.20

5.3.2 Complex Hydrocarbon Separations

DUCKY-9 was then also tested with the same shale-based crude mixture as SBAD-1 at a temperature of 130 °C and a pressure of 55 bar (Figure 5.18), which was the same set of conditions that SBAD-1 was tested under. Permeate was collected at a stage cut of 4% as well as 17% in a batch/dead-end filtration process. The total permeance at 4% stage cut was found to be $0.012 \text{ L}\cdot\text{m}^{-2}\cdot\text{h}^{-1}\cdot\text{bar}^{-1}$ which is comparable with SBAD-1. The inset in Figure 5.18 shows the color of the permeate samples alongside the feed. The permeate was found to be much lighter. This indicates a significant loss of color bodies such as polyaromatic molecules with high molecular weights.

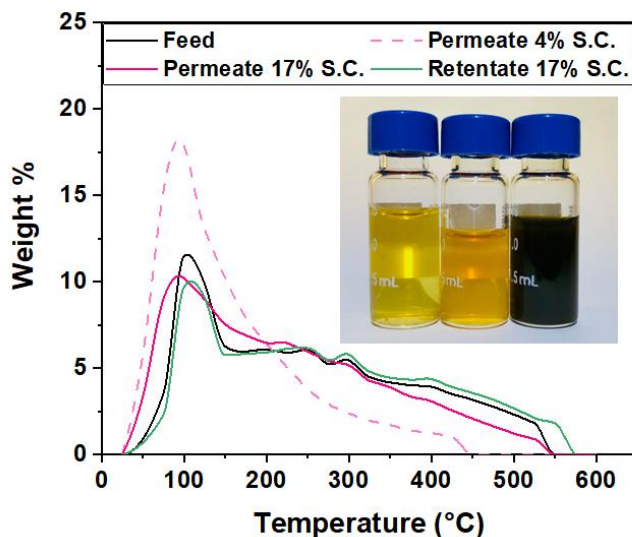


Figure 5.18. Boiling point distribution of feed, permeate and retentate from DUCKY-9 membrane fractionation of shale-based crude oil. Inset: Picture of permeate at 4% stage cut (left), permeate at 17% stage cut (middle) and feed (right).

Surprisingly, an even larger fraction of the permeate at 4% stage cut was concentrated in light molecules by DUCKY-9 than SBAD-1 with 71.5% of the permeate boiling below

200 °C compared to 60%. The simulated distillation of the feed here only showed a slight difference from the feed used for SBAD-1 with 35.25% of the molecules boiling below 200 °C compared to 38%. It is apparent that the selectivity suffers as stage cut is increased and can be seen from the similarity in composition between the feed and the permeate at 17% stage cut.

The GCxGC-FID chromatograms of the feed and permeate at 4% stage cut are shown in Figure 5.19, where the time scale in minutes represents the boiling point, the time scale in seconds shows the polarity and the z-axis shows the response factor.

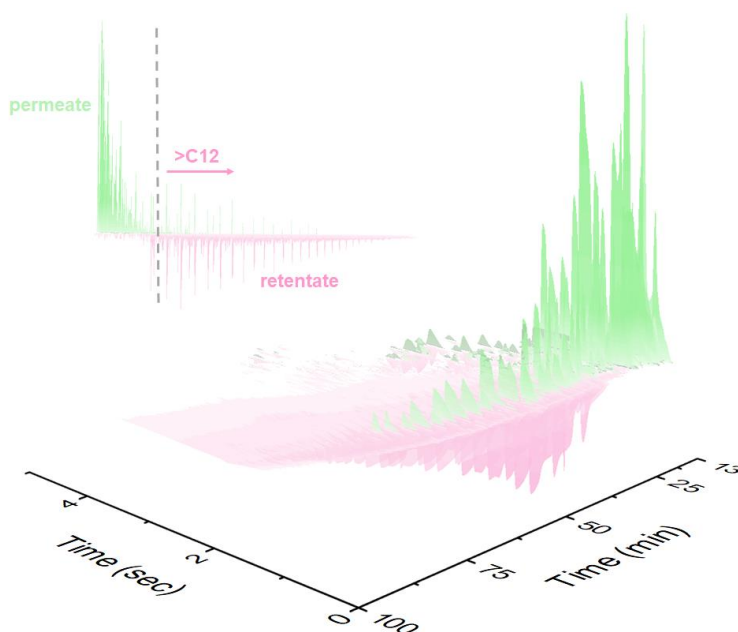


Figure 5.19. GCxGC-FID analysis of membrane fractionation of shale-based crude oil at 130°C and 55 bar showing the feed chromatogram subtracted from the permeate chromatogram. Green elution peaks are concentrated in the permeate, whereas the pink elution peaks are concentrated in the membrane retentate. Top left: side view of GCxGC-FID showing the carbon number partition of real crude oil obtained by DUCKY-9.

Similar to SBAD-1, there is an enrichment of molecules lighter than carbon numbers of 12 (170 Da). However, the inset shows a less clean cut of the permeate from the retentate; green peaks have larger response factors and pink peaks have smaller response factors for molecules with a carbon number greater than 12 compared to Figure 5.10. It is suspected that overcrowding of molecules in the stationary phase of the first GC column led to the appearance of alternate and equally tall permeate and retentate peaks in this region.⁽¹⁷⁾ Simply put, an overconcentration of material can cause competitive sorption in the capillary column and therefore, a shift in the retention times. If this shift is not uniform across the range of molecules that are analyzed, then no single offset applied to the dataset can resolve the issue in visualizing the data as presented in Figure 5.19.

Instead, we may extract data from the simulation distillation experiment to plot the rejection curves for DUCKY-9 and SBAD-1 by class. Figure 5.20 shows this comparison for normal paraffin molecules. As in the dilutes separations, DUCKY-9 exhibits a steeper change in rejections for the range of molecules with C10-C15. Above this carbon number, the rejections are comparable. It is well known that the current challenge for multicomponent organic solvent separations is the ability to fractionate feeds into groups of distinct molecules as a result of high selectivities amongst molecules that are close in molecular weight or size.⁽¹⁸⁾ This is more likely with a sharper molecular weight cutoff and so DUCKY-9 emerges as an attractive candidate compared to SBAD-1 for the

separation of aliphatic molecules in the kerosene and naphtha range without suffering a loss in permeance, despite the increase rigidity of the polymer network.

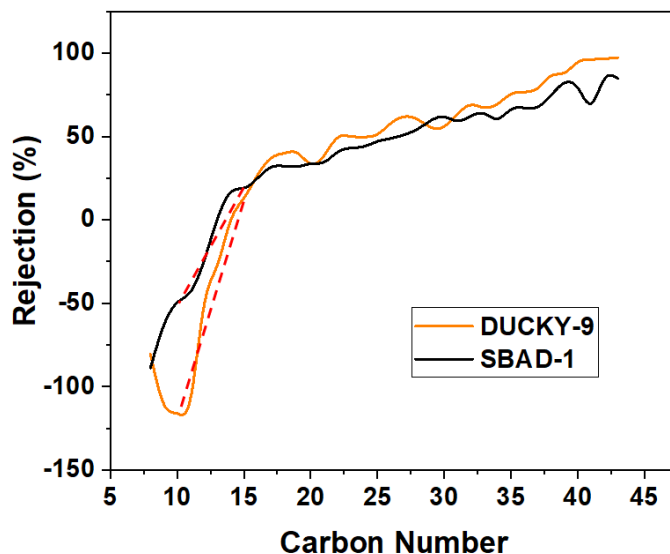


Figure 5.20. Rejection curves for n-paraffins obtained from GCxGC analysis of crude oil separation by DUCKY-9 compared with SBAD-1. Dotted red lines indicate slope between C10 and C14 molecules.

5.4 Summary and Conclusions

The results described here highlight that the dibenzodioxin connection between spirocyclic monomers that characterizes PIM-1-like materials is not necessary to enable meaningful small-molecule membrane-based separations. It can be speculated that the advantageous properties of SBAD- and DUCKY-based membranes derive from the nature of the aromatic nitrogen-carbon linkage, which has long been known to demonstrate hindered rotation(19). This connection between spirocyclic and aromatic building blocks

gives rise to bulk rigidity and low swelling, isolated and large micropores, and enough segmental mobility to allow migration of molecules between micropores at rates influenced by both molecular size and molecular type. Together, these properties make the SBAD and DUCKY family promising for the separation of small-sized molecules spanning the organic solvent reverse osmosis and the lower end of the organic solvent nanofiltration range (100-350 g-mol⁻¹) in complex mixtures such as crude oil. Most other membranes that operate in similar regimes require post-polymerization or post-fabrication modifications (e.g., crosslinking) that can be costly and difficult to scale up(4, 20). In contrast, the polymers used here can be tailored with simple changes in composition and performance. The proposed dependence of polymer performance on both pore structure and dynamic motion enables complex mixture fractionation that may be scalable and translatable to real crude oil fractions.

While both SBAD-1 and DUCKY-9 demonstrate the separation of molecules in a similar weight range (100-300 g/mol), it is the nature of the separation performed by each polymer that differs. SBAD-1 displays a prominent class-based separation, favoring the transport of aromatic molecules over aliphatic molecules. However, DUCKY-9 presents a more classical molecular weight-based separation of solutes, with a sharp cutoff among C10-C15 molecules. The application of either polymer would be defined by whether the greater demand is for purely aliphatic or aromatic streams or a clear carbon number cutoff. For the shale-based crude oil separation attempted here, the desired naphtha and kerosene products are more well described by tight molecular weight ranges. Thus, it may seem that the sharp MWCO of DUCKY-9 along with its higher permeance is favored in such crude oil applications.

5.5 References

1. D. Z. Wu, L. Zhao, V. K. Vakharia, W. Salim, W. S. W. Ho, Synthesis and characterization of nanoporous polyethersulfone membrane as support for composite membrane in CO₂ separation: From lab to pilot scale. *J Membrane Sci* **510**, 58-71 (2016).
2. J. Winter, B. Barbeau, P. Berube, Nanofiltration and Tight Ultrafiltration Membranes for Natural Organic Matter Removal-Contribution of Fouling and Concentration Polarization to Filtration Resistance. *Membranes-Basel* **7**, (2017).
3. J. L. Duda, I. H. Romdhane, R. P. Danner, Diffusion in Glassy-Polymers - Relaxation and Antiplasticization. *J Non-Cryst Solids* **172**, 715-720 (1994).
4. P. Marchetti, M. F. J. Solomon, G. Szekely, A. G. Livingston, Molecular Separation with Organic Solvent Nanofiltration: A Critical Review. *Chem Rev* **114**, 10735-10806 (2014).
5. E. Niyonsaba, K. E. Wehde, R. Yerabolu, G. Kilaz, H. I. Kenttamaa, Determination of the chemical compositions of heavy, medium, and light crude oils by using the Distillation, Precipitation, Fractionation Mass Spectrometry (DPF MS) method. *Fuel* **255**, (2019).
6. M. Cook, P. R. J. Gaffney, L. G. Peeva, A. G. Livingston, Roll-to-roll dip coating of three different PIMs for Organic Solvent Nanofiltration. *J Membrane Sci* **558**, 52-63 (2018).
7. M. Alyani, J. Towfighi, S. M. Sadrameli, Effect of process variables on product yield distribution in thermal catalytic cracking of naphtha to light olefins over Fe/HZSM-5. *Korean J Chem Eng* **28**, 1351-1358 (2011).
8. M. S. Shehata, M. M. ElKotb, H. Salem, Combustion Characteristics for Turbulent Pre vaporized Premixed Flame Using Commercial Light Diesel and Kerosene Fuels. *J Combust* **2014**, (2014).
9. H. Y. Jang *et al.*, Torlon (R) hollow fiber membranes for organic solvent reverse osmosis separation of complex aromatic hydrocarbon mixtures. *Aiche J* **65**, (2019).
10. D. Y. Koh, B. A. McCool, H. W. Deckman, R. P. Lively, Reverse osmosis molecular differentiation of organic liquids using carbon molecular sieve membranes. *Science* **353**, 804-807 (2016).
11. M. Raymond, W. L. Leffler, *Oil & gas production in nontechnical language*. (PennWell, Tulsa, Oklahoma, ed. 2nd Edition., 2017), pp. xxii, 343 pages.
12. L. Mondello, *Fundamental principles of comprehensive 2D GC*. 2012.

13. D. A. B. B.A. McCool, Y.V. Joshi, US Patent App No. 20190367820A1. (2019).
14. S. F. Kistler, P. M. Schweizer, *Liquid film coating : scientific principles and their technological implications*. (Chapman & Hall, London ; New York, 1997), pp. xi, 783 p.
15. W.-F. Su, *Principles of polymer design and synthesis*. Lecture notes in chemistry, (Springer, Heidelberg ; New York, 2013), pp. xiii, 306 pages.
16. M. Galizia, K. P. Bye, Advances in Organic Solvent Nanofiltration Rely on Physical Chemistry and Polymer Chemistry. *Front Chem* **6**, (2018).
17. J. Harynuk, T. Gorecki, J. de Zeeuw, Overloading of the second-dimension column in comprehensive two-dimensional gas chromatography. *J Chromatogr A* **1071**, 21-27 (2005).
18. P. Marchetti, L. Peeva, A. Livingston, The Selectivity Challenge in Organic Solvent Nanofiltration: Membrane and Process Solutions. *Annu Rev Chem Biomol* **8**, 473-497 (2017).
19. A. Mannschreck, H. Muensch, Internal rotation about the N-aryl bond in ortho-disubstituted anilines and anilinium ions. *Tetrahedron Letters* **9**, 3227-3230 (1968).
20. E. K. McGuinness, F. Y. Zhang, Y. Ma, R. P. Lively, M. D. Losego, Vapor Phase Infiltration of Metal Oxides into Nanoporous Polymers for Organic Solvent Separation Membranes. *Chem Mater* **31**, 5509-5518 (2019).

CHAPTER 6. USING A MAXWELL-STEFAN MODEL TO PREDICT COMPLEX LIQUID HYDROCARBON TRANSPORT IN PIM-1 AND SBAD-1

6.1 Overview

This chapter proposes a framework to enable workable predictions of permeate flux and composition in complex hydrocarbon liquids transported through SBAD-1 and PIM-1. This chapter is adapted from ‘R. Mathias, D. J. Weber, K. A. Thomspson, B. D. Marshall, M. G. Finn, J. K. Scott, R. P. Lively, A framework for predicting the fractionation of complex liquid feeds via polymer membranes. *Journal of Membrane Science* (2021)’. The numerical methods and computational simulation in this work were conceptualized and implemented by Dylan J. Weber (Georgia Institute of Technology).

6.2 Introduction

The ability to predict multicomponent transport in many different classes of membranes is essential to accelerate the development of materials for such cascade systems that would otherwise require lengthy experimental timelines for material synthesis, membrane fabrication, and separation testing. Significant attention has been paid to experimental and theoretical aspects of membrane-based separations of dilute mixtures(1, 2); however, there is a lack of methods available for modeling complex mixture permeation data or predicting complex mixture permeations based on easily accessible experimental parameters. Complex liquid permeation of similarly-sized molecules, wherein multiple components are present in high concentrations (such as in crude oil separations), has not

yet been successfully modeled and matched with experimental data in a scalable manner for polymer systems. The challenge is accurately describing both multicomponent liquid occupancy throughout a polymer membrane and diffusional cross-coupling for multiple species with similar physicochemical properties. Several studies have modeled liquid transport in polymer membranes via pore-flow and solution-diffusion models.(2-4) Pore-flow models assume no change in solvent activity across the thickness of a membrane, which does not match experimental observations for microporous or dense polymer materials, especially in the case of reverse osmosis regimes.(5, 6) It is now general consensus that the permeation of molecules through dense membranes is best described by the solution-diffusion model, whose driving force is a pressure-induced concentration gradient and not a pressure gradient across the membrane thickness.(2, 7)

Several researchers have published detailed studies of small organic molecule flux through OSN and OSRO membranes that provide the backdrop for understanding complex organic transport.(8-11) A number of researchers have applied Paul and Ebra-Lima's solution-diffusion model in Fick's law form(12) to describe the transport of pure molecules or dilute mixtures through polymeric membranes and observed a close agreement with experimental data.(13, 14) Although Fick's law is easily combined with mass balances and requires less complex equations to solve than the Maxwell-Stefan model, the omission of cross-coupling effects, the assumption of thermodynamic ideality and neglecting the dependence of Fickian diffusivity on concentration bring about significant error in describing multicomponent transport.(15-17) The Maxwell-Stefan model does not possess the shortcomings of this classical solution-diffusion model, which is why the solution-diffusion form of the Maxwell-Stefan model is preferred to describe multicomponent liquid

separations via polymer membranes.(18-20) However, such predictive studies with liquid mixtures containing three or more species in $\gg 1\%$ concentrations are scarce.

Ribeiro et al. first described the Maxwell-Stefan transport equations with volume fraction terms in conjunction with the Flory-Huggins sorption model to predict the permeation of binary mixtures of $\text{CO}_2/\text{C}_2\text{H}_6$ across crosslinked polyethylene oxide membranes.(21) Krishna further developed explicit analytic expressions such that these fluxes could be described in two-dimensional matrix notation.(22) He used this notation to predict fluxes for Ribeiro et al.'s $\text{CO}_2/\text{C}_2\text{H}_6$ experiments as well as water/alcohol pervaporation via cellulose acetate and polyimide membranes. While this approach showed potential for experimental simplicity as mutual diffusion parameters did not have to be experimentally measured, it requires further validation for complex, nonpolar feeds such as those found in crude oil. Here Krishna's approach is used as a starting point to predict the separation of liquid hydrocarbon mixtures containing up to nine similarly-sized molecules with two microporous, glassy polymer materials: a polymer of intrinsic microporosity, PIM-1, and a spirobifluorene aryl diamine, SBAD-1 (Figure 6.1).(23, 24)

It is demonstrated that complex mixture separations can be adequately predicted (i.e., permeate fluxes and compositions within 25% of experimental values) via a Maxwell-Stefan framework with single component molecule-polymer sorption and diffusion parameters as the only experimental input requirements. These values were obtained from a combination of unary gravimetric vapor sorption, unary liquid swelling experiments, and unary liquid permeation. A new sorption model that additively combines Langmuir- and Flory-Huggins-type sorption contributions is proposed to fit the unique sorption in glassy polymers and serves as a generalizable model, capable of extension to low- and high-

swelling polymers. Comparisons to other thermodynamic models such as classical Flory-Huggins (FH) and Dual-mode sorption (DMS) are made based on unary, binary, and ternary sorption experiments as well as unary and mixture membrane permeation experiments. Vignes mixing rules are investigated as empirical correlations of binary diffusion interactions amongst hydrocarbons. Finally, free volume theory and an alternative average diffusivity concept are investigated to capture the influence of polymer dilation and plasticization on molecule diffusivities. It is demonstrated that complex mixture separations can be adequately predicted (i.e., within an average of 10% of the experimental values of permeate compositions and an average of 35% for permeate fluxes) via a Maxwell-Stefan framework with single component molecule-polymer sorption and diffusion parameters as the only experimental input requirements. These values were obtained from a combination of unary gravimetric vapor sorption, unary liquid swelling experiments, and unary liquid permeation. A new sorption model that additively combines Langmuir- and Flory-Huggins-type sorption contributions is proposed to fit the unique sorption in glassy polymers and serves as a generalizable model, capable of extension to low- and high-swelling polymers. Comparisons to other thermodynamic models such as classical Flory-Huggins (FH) and Dual-mode sorption (DMS) are made based on unary, binary, and ternary sorption experiments as well as unary and mixture membrane permeation experiments. Vignes mixing rules are investigated as empirical correlations of binary diffusion interactions amongst hydrocarbons. Finally, free volume theory and an alternative average diffusivity concept are investigated to capture the influence of polymer dilation and plasticization on molecule diffusivities.

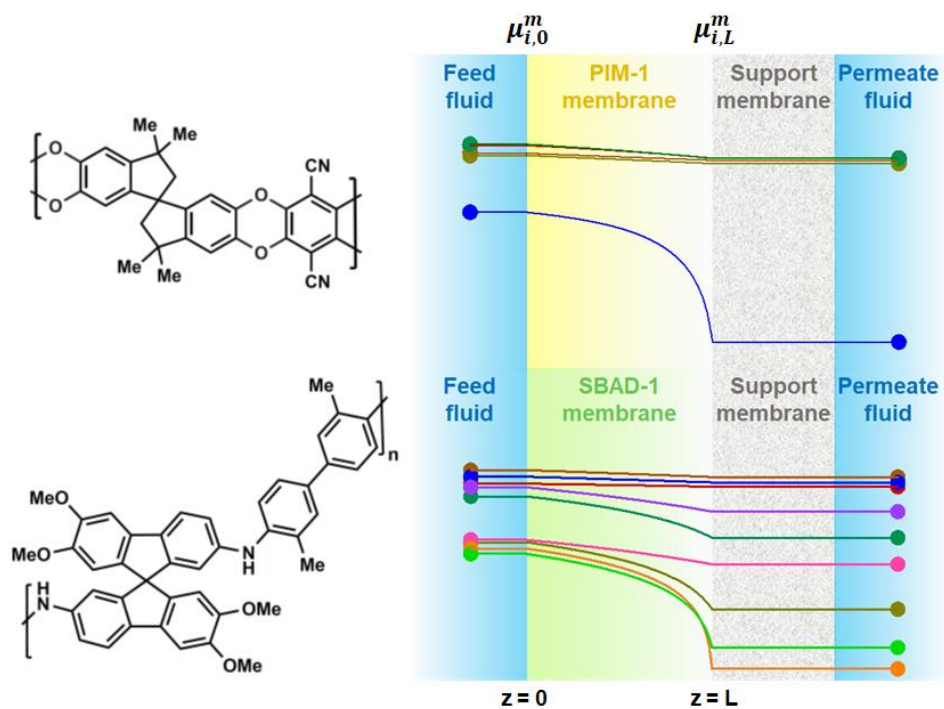


Figure 6.1. Complex mixture transport via PIM-1 and SBAD-1 membranes. Exemplar non-linear chemical potential profiles of individual molecules in complex mixtures are shown across the thickness of selective polymer membranes with corresponding chemical structures. It is assumed that the support layer does not hinder transport and chemical potential is unchanged throughout the support. Higher nonlinearity is observed for more dilute or low sorbing components, and as the number of components is increased (i.e., the mixture becomes more complex and each molecule becomes less concentrated in the mixture), Fick's law becomes insufficient to describe liquid hydrocarbon transport. Note that the membrane and support thicknesses are not to scale.

6.3 The Maxwell Stefan Transport of Mixed Feeds

6.3.1 Volume-based Maxwell-Stefan Model

As described above, the Maxwell-Stefan framework is appropriate for describing coupled transport across a membrane by designating chemical potential or concentration gradients as the driving force instead of transmembrane pressure differences. The

Maxwell-Stefan model is commonly described in terms of the penetrant and membrane mole fractions. However, since concentration gradients in polymers are often described by the Flory-Huggins model (which is formulated with volume fractions), it has been suggested that the Maxwell-Stefan model for polymers also be described with volume fraction terms.(25) The description of transmembrane fluxes as a function of volume fractions within a Maxwell-Stefan formulation was set up by Ribeiro et al.(21) The two-dimensional matrix form of this from Krishna(22) is followed and extended it to n penetrants in a polymer membrane:

$$(N^V) = -[B]^{-1} \text{diag}(\phi^m)_{1:n} \frac{d(\mu^m/RT)_{1:n}}{dz} = -[B]^{-1}[\Gamma] \frac{d(\phi^m)_{1:n}}{dz} \quad 6.1$$

where z is the spatial dimension across the membrane thickness, (N^V) is the n -dimensional vector of permeant volumetric fluxes, and μ^m and ϕ^m are $(n + 1)$ -dimensional vectors of component chemical potentials and volume fractions in the sorbed polymer phase (m), respectively, where the $(n + 1)^{\text{st}}$ component is the polymer itself. The subscript $1:n$ refers to the first n components of the corresponding vector (i.e., those for the permeants only). The $(n \times n)$ diffusion matrix $[B]$ describes solvent-polymer and solvent-solvent diffusion and is defined as

$$[B]_{ii} = \sum_{j=1; j \neq i}^n \frac{\phi_j^m}{\mathbb{D}_{ij}^{v,m}} + \frac{\phi_{n+1}^m}{\mathbb{D}_{i,n+1}^{v,m}}, \quad [B]_{ij, i \neq j} = -\frac{\phi_i^m}{\mathbb{D}_{ij}^{v,m}} \quad 6.2$$

where $\mathbb{D}_{i,n+1}^{v,m}$ is the volume-based Maxwell-Stefan diffusivity of component i in the polymer (typically assumed to be independent of concentration). The mole-based

diffusivity typically used in Maxwell-Stefan equations is related to $\mathbb{D}_{ij}^{v,m}$ by $\mathbb{D}_{ij}^m = \frac{\mathbb{D}_{ij}^{v,m} \hat{V}}{\bar{V}_j}$,

where \bar{V}_j is the molar volume of component j and \hat{V} is the molar volume of the mixture,

described by $\hat{V} = \sum_{j=1}^{j=n+1} x_j^m \bar{V}_j$. (22) The mole-based Maxwell-Stefan diffusivities are

symmetric in accordance with Onsager's reciprocal relations(26) such that $\frac{\mathbb{D}_{ij}^{v,m}}{\bar{V}_j} = \frac{\mathbb{D}_{ji}^{v,m}}{\bar{V}_i}$.

The $(n \times n)$ sorption matrix $[\Gamma]$ describes sorption interactions in the membrane and is defined as

$$\Gamma_{ij} = \phi_i^m \frac{\partial \ln a_i^m}{\partial \phi_j^m} = \frac{\phi_i^m}{f_i^m} \frac{\partial f_i^m}{\partial \phi_j^m} \quad 6.3$$

where f_i^m is the fugacity of i in the sorbed polymer phase. Note that the second equality in Equations 6.1 is derived by applying the chain rule to μ^m as a function of the independent variables $(\phi^m)_{1:n}$, leading to the terms in Γ . There are no derivatives with respect to ϕ_{n+1}^m in Γ because ϕ_{n+1}^m is dependent on $(\phi^m)_{1:n}$ through the fact that all volume fractions must sum to one. Similarly, the system of Equations 6.1 does not include an $(n + 1)^{\text{st}}$ equation because it is redundant through the Gibbs-Duhem relationship. Instead, Equations 6.1 is augmented with the independent $(n + 1)^{\text{st}}$ differential equation

$$\frac{d(\phi^m)_{n+1}}{dz} = - \sum_{j=1}^n \frac{d(\phi^m)_j}{dz} \quad 6.4$$

When only the diagonal elements are considered for the sorption and diffusion matrices, evaluated at some constant pure component reference volume fraction, $\phi^{m,*}$, 6.1 reduces to classical Fick's Law as

$$(N^V) = -\text{diag}([B(\phi^{m,*})])^{-1} \text{diag}([\Gamma(\phi^{m,*})]) \frac{d(\phi^m)_{1:n}}{dz} \quad \mathbf{6.5}$$

The resulting uncoupled system of ODEs can be integrated directly; however, when comparing with Maxwell-Stefan approaches here, a consistent numerical method described in Section 6.3.3 is used.

The diffusional cross-coupling of molecular pairs in multicomponent separations has been documented,(27-29) but is difficult to predict from first principles. Thus, empirical approaches are commonly used. Vignes estimated that this coupling is exponentially dependent on the concentration of one component in a binary pair and initially introduced an equation to describe interdiffusion in binary mixtures(30) where he found the new mixing rule to be most appropriate for non-polar molecules. This equation was later found to be applicable to multicomponent mixtures(15, 31) with an error of around 10% for non-polar mixtures. Here, the effect of solvent occupancy on the diffusion-based coupling of molecules is described using the following Vignes-style mixing rule

$$\frac{\mathbb{D}_{ij}^{v,m}}{\bar{V}_j} = (\mathbb{D}_{i,n+1}^{v,m}/\bar{V}_i) \left(\frac{\phi_i^m}{\phi_i^m + \phi_j^m} \right) (\mathbb{D}_{j,n+1}^{v,m}/\bar{V}_j) \left(\frac{\phi_j^m}{\phi_i^m + \phi_j^m} \right) \quad \mathbf{6.6}$$

Other empirical correlations such as the Darken expression(32) can be used, but the Vignes mixing rule was deemed to be appropriate here.

6.3.2 A New Sorption Model: Langmuir + Flory-Huggins

Inspired by the dual mode sorption model, it is proposed that the sorption of hydrocarbon vapors and liquids in glassy polymers can be more accurately described over

the full range of solvent activities by a combination of Langmuir micropore-filling and Flory-Huggins swelling type sorption(33) (LM-FH) contributions, viz.,

$$C_i^m = C_{i,Langmuir}^m + C_{i,Flory-Huggins}^m \quad \mathbf{6.7}$$

where C_i^m is the total sorbed polymer phase (m) molar concentration of component i , $C_{i,Langmuir}^m$ is the sorbed polymer phase (m) molar concentration in the glassy polymer micropores due to Langmuir-type sorption, and is $C_{i,Flory-Huggins}^m$ is the sorbed polymer phase (m) molar concentration in the swollen polymer matrix due to Flory-Huggins (FH) type sorption. In fact, the concept of additively combining Langmuir hole-filling with lattice theory-based dissolution has been theorized much earlier by Barrer et al. but with a formulation that resembles DMS more closely than the formulation proposed in Equation 8.(34) In developing the proposed LM-FH sorption model, the dry polymer system is conceptualized as having polymer and void regions, while at high activities we may imagine the system to be made up of polymer and sorbed guest molecule regions (Figure 6.2). We can assume that sorbates take up the entire free volume space present in the polymer above a certain activity corresponding to the transition of the polymer from the Langmuir-dominant regime to the Flory-Huggins-dominant regime (which often coincides with a glassy to rubbery transition). The volume basis for each term in Equation 6.7 is made consistent with the Maxwell-Stefan equation and this conversion is described in further detail in the Appendix (A1). While the proposed LM-FH sorption model is similar to DMS in that both models describe a combination of a pore-filling and dissolution mechanisms, the convexity of sorption at higher activities for certain hydrocarbon molecules is not accurately captured by the Henry's sorption component of DMS. The competitive sorption

of multiple penetrants into free volume elements in a glass can be described by the multi-site Langmuir model as

$$C_{i,Langmuir} = \frac{C_{H,sat,i} b_i f_i^m}{1 + \sum_{i=1}^n b_i f_i^m} \quad 6.8$$

The lattice swelling of a polymer due to multiple components is described by the expanded Flory-Huggins model shown below where the polymer phase is the $(n + 1)^{st}$ component and there are n solvents in the system

$$\begin{aligned} \ln(a_i^m) &= \ln\left(\frac{f_i^m}{f_i^o}\right) \\ &= \ln(\phi_{i,FH}^m) + (1 - \phi_{i,FH}^m) - \sum_{\substack{j=1 \\ j \neq i}}^{n+1} \frac{\bar{V}_i}{\bar{V}_j} \phi_{j,FH}^m \\ &\quad + \left(\sum_{j=1}^{i-1} \chi_{ji} \phi_{j,FH}^m \frac{\bar{V}_i}{\bar{V}_j} + \sum_{j=i+1}^{n+1} \chi_{ij} \phi_{j,FH}^m \right) \left(\sum_{\substack{j=1 \\ j \neq i}}^{n+1} \phi_{j,FH}^m \right) \\ &\quad - \sum_{\substack{j=1 \\ j \neq i}}^{n+1} \sum_{\substack{k=j+1 \\ k \neq i}}^{n+1} \chi_{jk} \frac{\bar{V}_i}{\bar{V}_j} \phi_{j,FH}^m \phi_{k,FH}^m \end{aligned} \quad 6.9$$

where f_i^o is the fugacity of i as a saturated vapor at 298 K and $\phi_{i,FH}^m = \phi_{i,Flory-Huggins}^m$ is the Flory-Huggins-contributed solvent occupancy in the sorbed polymer system. Flory interaction parameters are commonly understood to be composition-dependent. Yang and Lue(35) have explicitly shown that sorption is defined more accurately when $\chi_{i,n+1}$ and χ_{ij} are considered to be functions of concentration and are asymmetric such that χ_{12} is not

equal to χ_{21} . However, hyperbolic and polynomial functions that need to be fit to obtain $\chi_{i,n+1}-\phi_i$ and $\chi_{ij}-\phi_i$ relationships involve extensive mixture sorption experiments to verify and more complex numerical methods to apply in a Maxwell-Stefan framework with N components. For simplicity, we will assume that $\chi_{i,n+1}$ is constant across different loading conditions and is equal to the $\chi_{i,n+1}$ observed at unit activity (when the polymer is in contact with pure liquid). The binary solvent-solvent Flory-Huggins interaction parameters can be estimated using a modified form of Hansen solubility theory(36), viz.,

$$\chi_{ij} = \frac{(\bar{V}_i \bar{V}_j)^{1/2}}{RT} \left[(\delta_{D,i} - \delta_{D,j})^2 + 0.25(\delta_{P,i} - \delta_{P,j})^2 + 0.25(\delta_{H,i} - \delta_{H,j})^2 \right] \quad \mathbf{6.10}$$

Detailed multicomponent sorption experiments and analyses are required to confirm the validity of this simplified approach and will be the focus of future work. Table 6.1 shows the Hansen solvent parameters used in this study.(37) The more alike two solvents are, the lower the difference between the parameters will be and the lower the binary chi parameters will be, resulting in greater binary sorption coupling.

Table 6.1. Hansen solubility parameters used to estimate χ_{ij} .(37)(25) Molecules in parentheses were determined as satisfactory substitutes for species that did not have recorded solubility parameters.

Hansen solubility parameters (MPa^{1/2})			
	Dispersion	Polarity	Hydrogen Bonding
toluene	18	1.4	2
<i>n</i>-octane	15.5	0	0
<i>iso</i>-octane	14.1	0	0
methylcyclohexane	16	0	1
decahydronaphthalene (average of isomers)	18.4	0	0
1,3,5- triisopropylbenzene (mesitylene)	18	0	0.6
1-methylnaphthalene	20.6	0.8	4.7
<i>tert</i>-butylbenzene (<i>n</i>-isomer)	17.4	0.1	1.1
<i>iso</i>-cetane (<i>n</i>-isomer)	16.3	0	0
heptane	15.3	0	0
<i>p</i>-xylene	17.6	1	3.1
<i>o</i>-xylene	17.8	1	3.1

6.3.3 Liquid Hydrocarbon Polymer Diffusivity

Penetrant-polymer Maxwell-Stefan diffusivities can be calculated via experimentally measured pure molecule permeation, pure molecule sorption, and fundamental two-component transport equations that are derived from Equations 6.1, 6.2 and 6.3. However,

significantly different polymer swelling in the presence of a range of solvents could result in a wide range of mixture-accessible free volumes; these depend on the various possible upstream and downstream concentration ratios for a given set of molecules. This complicates simple attempts to estimate separation performance of a multicomponent mixture because the diffusion of each molecule through the polymer matrix could also vary with the accessible free volume in the system. Several versions of the free volume theory have been previously used in gas transport studies to correlate penetrant diffusivity with the accessible free volume of the dry polymer. Here, one such model was used to correlate the same, viz.,(38)

$$D_{i,n+1}^{v,m} = A_i \exp\left(-\frac{B_i}{v_F}\right) \quad 6.11$$

where A_i is a molecule-polymer system dependent constant, B_i is a molecule-dependent constant and is related with the molecule size, and v_F is the polymer free volume. Assuming the diffusivities of liquid species are also similarly dependent on accessible volume due to membrane swelling, we can derive the following correlation for each molecule:

$$\frac{D_{i,n+1,polymer\ state\ II}^{v,m}}{D_{i,n+1,polymer\ state\ I}^{v,m}} = \exp\left[B\left(\frac{1}{v_{FI}} - \frac{1}{v_{FII}}\right)\right] \quad 6.12$$

Thus, solvent-polymer Maxwell-Stefan diffusivities that are calculated from permeation experiments with known polymer states (i.e., degree of swelling) can be used in conjunction with Equation 6.12 to estimate diffusivities in mixtures where the degree of polymer swelling is dependent on multicomponent sorption and is different from the

swelling induced by the pure solvent. Here we may take v_{F_I} as the unit activity volume fraction of component i and $v_{F_{II}}$ to be the mixture accessible volume (i.e., $v_{F_{II}} = \sum_{j=1}^n \phi_j^m = 1 - \phi_{n+1}^m$).

Going a step further in relating diffusivities with polymer state upon sorption, Damle and Koros observed a loss of diffusion selectivity in glassy polymers that strongly dilate and plasticize in the presence of condensable adsorbates.(39) On the feed side, the mixture undergoes equilibrium partitioning into the membrane, which is swollen and has negligible microvoids, so sorption is most appropriately described by Flory-Huggins lattice interactions. Inside the membrane, small collections of molecules act as a unit since the membrane is sufficiently swollen or plasticized, such that they collectively diffuse together. While the Maxwell-Stefan framework naturally takes the thermodynamic and cross-diffusional coupling into account, it was noticed that setting all the penetrant-membrane diffusivities to some volume corrected average value gave the best results compared to any other approach (Sc1-4). Since $\mathfrak{D}_{i,n+1}^{v,m}$ is proportional to the inverse drag coefficient, this approach is setting all the friction forces experienced by the permeants to be almost equivalent. When tracking the motion of an individual molecule, it would have a velocity or a displacement that is equivalent to all other molecules as they are moving in this unit. The mixture then partitions into the adjacent permeate phase according to the FH sorption model again. This is different from the Maxwell-Stefan approach of a single molecule "hop" from sorption site to sorption site, which is the classic picture for gases and polymers that have not plasticized or dilated. The cohort-style diffusivity can be calculated using a Vignes-style volume-corrected interpolation formula of the pure component Maxwell-Stefan molecule-polymer diffusivities, viz.,

$$\mathbb{D}_{i,n+1,average}^{v,m} = \frac{\sum_{i=1}^n \mathbb{D}_{i,n+1}^{v,m}}{n} \quad 6.13$$

Many complex averaging and weighting approaches have been tested and this version gave the best results for our initial description of the complex mixture permeation framework.

6.4 Simulation and Parameter Fitting of Modeling Framework

6.4.1 Sorption Models

The Langmuir capacity can be estimated by visual observation of the curvature of the isotherms and is typically designated as the initial step uptake at a relative pressure of ~0.3 (better fits were obtained by using the uptake at a relative pressure of 0.5 for *iso*-octane and 1-methylnaphthalene in SBAD-1 for this calculation). The Flory-Huggins contribution is then calculated by subtracting $C_{H,sat}^m$ from the total sorption at unit activity, which effectively removes sorption in the microvoids such that these contributions are not double counted. For each solvent, $\chi_{i,polymer}$ can then be calculated based on this Flory-Huggins sorption contribution via Equation 6.9. This single parameter (assumed to be constant) is sufficient to describe the Flory-Huggins contribution at different solvent activities. Finally, the Langmuir sorption parameter, b_i , is obtained by performing a least-squares fit of Equation 6.7 to the total experimental sorption isotherm. In the case of the F-H sorption model, where the dry polymer fractional free volume is assumed to be negligible, $\chi_{i,polymer}$ is calculated using sorption at unit activity in Equation 6.9. For the DMS model, the three model parameters are fit simultaneously via a least-squares fit of Equation 2.9 to the experimental sorption isotherm. The error in calculated sorption model parameters was

estimated by fitting to upper and lower bounds of the raw sorption isotherms measured from duplicate and triplicate data.

6.4.2 Penetrant-Polymer Diffusivity, $\mathfrak{D}_{i,n+1}^{v,m}$

Experimental unary fluxes at a fixed transmembrane pressure were used in combination with each sorption model (FH, DMS, and LM-FH) to calculate three sets of $\mathfrak{D}_i^{v,m}$ corresponding to each sorption model. This was done via the Maxwell-Stefan equation reduced to a binary system of one penetrant in a polymer (Equation 6.1, $n = 1$). These $\mathfrak{D}_i^{v,m}$ values were then utilized in the Maxwell-Stefan framework along with the respective sorption models to predict unary fluxes at higher transmembrane pressures for model validation. These diffusivities are then used as the inputs into the multicomponent transport models. As described in Section 6.2.3, $\mathfrak{D}_i^{v,m}$ is expected to be a function of polymer free volume and is adjusted for polymer swelling in multicomponent transport via Equation 6.12. The free volume theory dictates that B is unique to each molecule and is dependent on penetrant size. Evaluating appropriate B values for each molecule requires at least two distinct experimentally-measured diffusivities for each penetrant at different accessible free volumes of the polymer. This increases the experimental effort required by the predictive framework and is also difficult to calculate for molecules that do not noticeably swell polymers. Therefore, several different possible B values are explored and, in each sorption model case, a single value was consistently applied to all penetrants for simplicity. This method enables modification of a single component diffusivity (measured at a condition of v_{F_I}) to a case where the polymer is swollen to a much different degree due to the sorption of many different molecules resulting in the $v_{F_{II}}$ polymer condition.

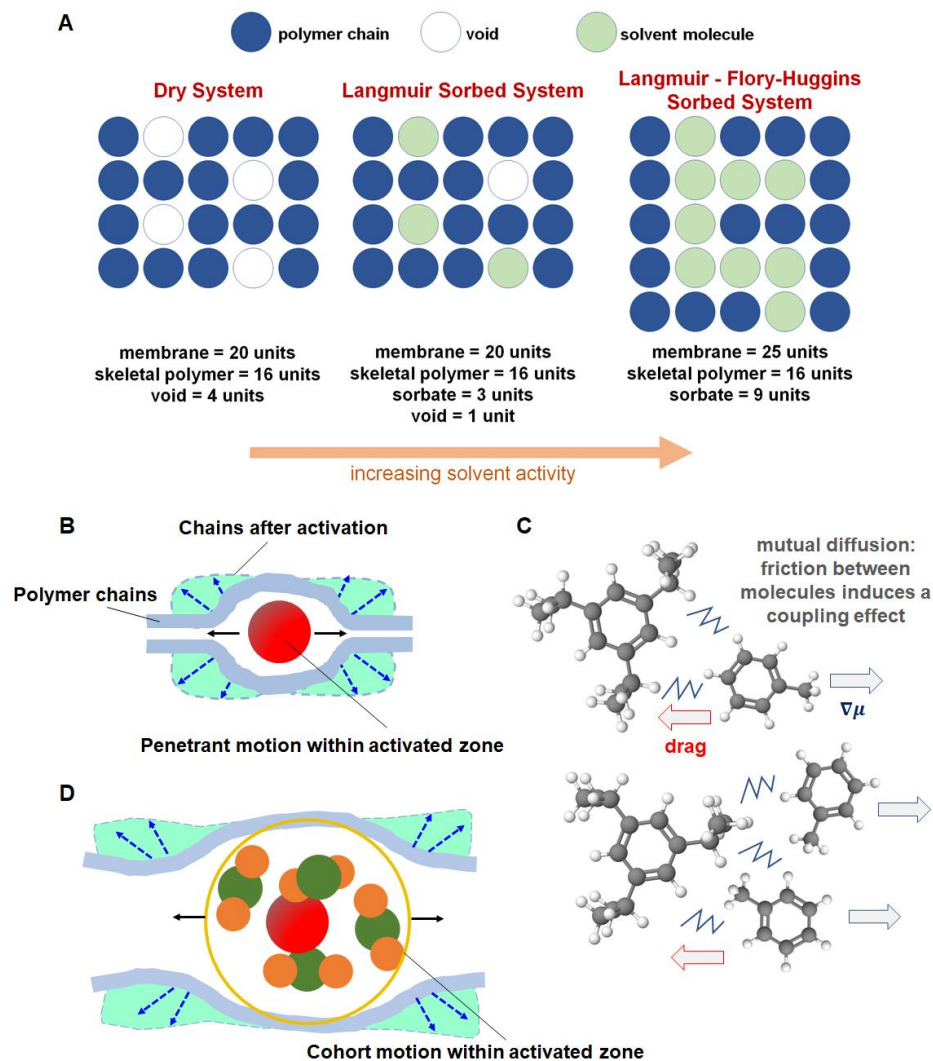


Figure 6.2. Sorption regimes and diffusive modes of transport in polymer membranes. **A.** Dependence of sorption regime and membrane volume on solvent activity. It is important to note that the two guest populations are in equilibrium but Langmuir-style sorption will dominate at low solvent activities and Flory-Huggins-style sorption will dominate at high solvent activities. **B.** Conventional diffusion mechanism where a molecule makes diffusive jumps through free space in a polymer network. **C.** Maxwell-Stefan interpretation of mixture diffusion where frictional forces between molecules cause diffusion coupling such that faster molecules are slowed and slower molecules are sped up, leading to a loss in diffusion selectivity. **D.** Cohort motion mode of transport where molecules diffuse collectively as a unit and no diffusion selectivity is obtained.

6.4.3 Multi-component Transport Simulation Framework

The Maxwell-Stefan framework discussed above was implemented to obtain multi-component permeation predictions using the Dual-Mode sorption model, the Flory-Huggins sorption model, and the proposed Langmuir + Flory-Huggins sorption model. Additionally, several different transport models were tested, which affect how the B and Γ matrices are specified in the Maxwell-Stefan framework. These are described in the following scenarios:

- a) Scenario 1 (Sc1): Fick's Law flux formulation as in Equation 6.5, with $\phi^{m,*}$ evaluated for single component permeant at 20 bar.
- b) Scenario 2 (Sc2): Maxwell-Stefan approach in Equations 6.1-6.3 without diffusional cross-coupling (i.e., $[B] \rightarrow \text{diag}([B])$)
- c) Scenario 3 (Sc3): identical to Sc2 but with a Vignes correlation (Equation 6.6) to describe diffusion cross-coupling
- d) Scenario 4 (Sc4): identical to Sc3 but with $\mathcal{D}_i^{v,m}$ adjusted for polymer swelling via the free volume theory (Equation 6.12), where $B = 0.03$ is assumed to be a constant value for all molecules for experimental simplicity.
- e) Scenario 5 (Sc5): identical to Sc2 but with $\mathcal{D}_i^{v,m}$ replaced via the sorp-vection average diffusivity concept (Equation 6.13).

The proposed framework makes the following assumptions:

- i. the partial molar volume of each component is equivalent to its molar volume at pure conditions, 298 K, 1 atm
- ii. ideal solution conditions throughout the external feed and permeate fluids that are in contact with the dense polymers

The proposed framework for modeling transport through the asymmetric membrane involves three parts. First, the upstream membrane phase volume fractions are solved for by setting the activities in the solution and membrane phase equal as(17)

$$a_{i,0}^m = a_{i,0}^{fl} \quad \mathbf{6.14}$$

where $a_{i,0}^m$ is the activity of component i in the active layer and $a_{i,0}^{fl}$ is the activity of component i in the bulk fluid phase, both evaluated at $z = 0$. The activity coefficients of fluid mixtures on the upstream face of the membrane were calculated using ASPENTech and UNIQUAC (or PC-SAFT) methods. However, the results did not affect the separation predictions in a meaningful way, thus the ideal solution theory was used throughout the external fluid systems. This simplification is likely valid for highly similar hydrocarbon-only streams like the ones considered here but would almost certainly need to be revisited for more complex streams containing highly different compounds.

Next, to model the permeate side, the fluid at the downstream end of the active membrane layer is assumed to be in equilibrium with the fluid composition throughout the porous support layer. Setting the activities of these fluids equal and assuming that the transmembrane pressure Δp occurs at the downstream interface between the active and porous layers(12),

$$a_{i,L}^m = a_{i,L}^s \exp \left[-\bar{V}_i \left(\frac{\Delta p}{RT} \right) \right] \quad 6.15$$

where $a_{i,L}^m$ is the activity of component i in the active layer and $a_{i,L}^s$ is the activity of component i in the support layer, both evaluated at $z = L$. However, following Pan's approach for asymmetric membranes, the bulk permeate is assumed not to mix with the fluid in the support layer. Therefore, the porous layer mole fractions ($x_{i,L}^s$) are unknowns and cannot be used to directly compute the composition in the active layer at $z = L$ via Equation 6.15. Instead, these mole fractions are related to the partial molar fluxes through the active layer viz.,(40)

$$N_i = x_{i,L}^s \sum_{j=1}^n N_j = \frac{N_i^V}{\bar{V}_i} = x_{i,L}^s \frac{N_{Tot}^V}{\sum_{j=1}^{j=n} x_{j,L}^s \bar{V}_j} \quad 6.16$$

Finally, transport through the active membrane layer is modeled by Equation 6.1. Substituting Equation 6.16 into Equation 6.1 and rearranging gives the system of ODEs

$$\frac{d(\phi^m)_{1:n}}{dz} = -[\Gamma]^{-1}[B](x_L^s \bar{V}) \frac{N_{Tot}^V}{\sum_{j=1}^{j=n} x_{j,L}^s \bar{V}_j} \quad 6.17$$

where $(x_L^s \bar{V})$ is the n -dimensional vector formed by elementwise multiplication of the support layer fluid mole fractions with the respective component molar volumes.

This creates a two-point boundary-value problem that is solved using a novel shooting algorithm described in Figure 6.3. Specifically, the n permeant compositions in the bulk fluid within the support layer at $z = L$ is first guessed, as well as the total flux, N_{Tot}^V . Next,

Equation 6.17 and 6.4 are integrated (i.e., “shoot”) across the membrane active layer using the initial conditions $\phi_{i,0}^m$ determined by the feed-side sorption equilibrium calculation discussed above. This furnishes values for the component volume fractions on the permeate side of the active layer, $\phi_{i,L}^m$. Next, these values are used to calculate new values of the support layer compositions, $x_{i,L}^s$. Comparing these values to the initial guesses yields n nonlinear equations

$$x_L^s(\phi_L^m) - x_L^{s,guess} = 0 \quad \mathbf{6.18}$$

where $x_L^s(\phi_L^m)$ is the support layer composition vector calculated from the final integrator value of the membrane phase volume fractions evaluated at $z = L$, and $x_L^{s,guess}$ is the solver iterative guess of those component support layer compositions. Enforcing that these mole fractions sum to one provides the $(n + 1)^{\text{st}}$ nonlinear equation

$$1 - \sum_{j=1}^n x_{j,L}^s(\phi_L^m) = 0 \quad \mathbf{6.19}$$

Finally, these $n + 1$ equations are solved simultaneously for the $n + 1$ unknowns x_L^s and N_{Tot}^V . In previous work, approximation or full discretization of the above system of ordinary differential equations has been used to obtain a solution.(3, 41) However, those methods are insufficient in the case of complex multicomponent mixtures, concentration-dependent diffusivities, strong cross-coupling, and nonlinear sorption models. A separate publication is currently in preparation describing the complete numerical method used and detailed comparisons with alternative approaches.

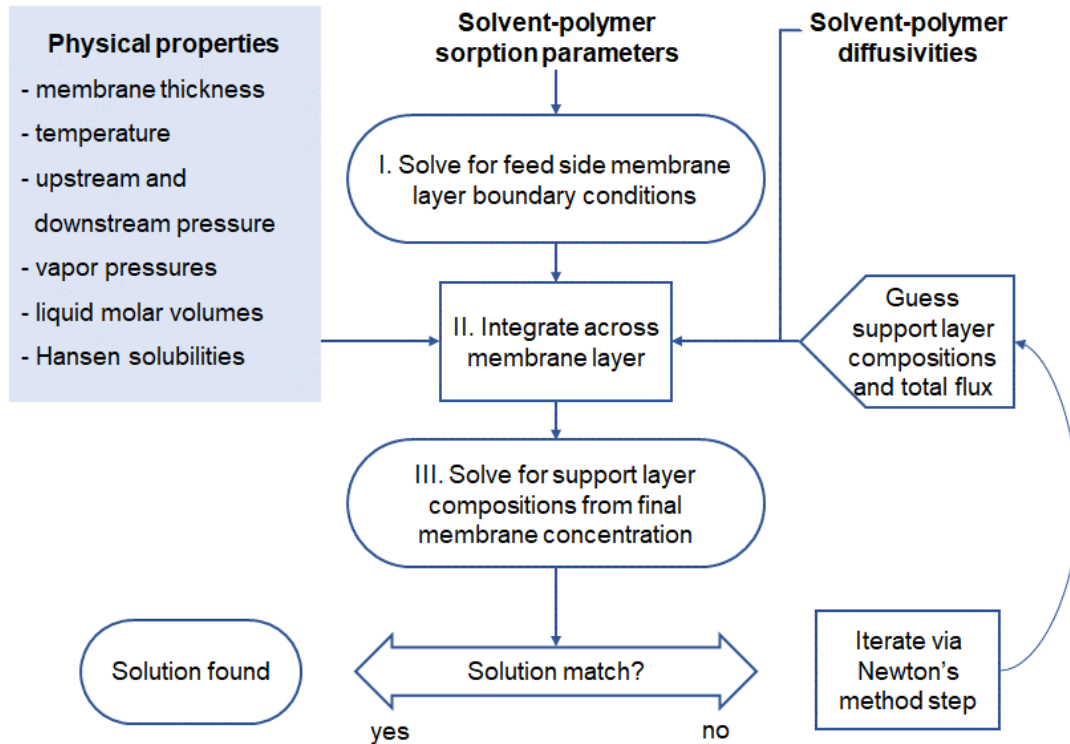


Figure 6.3. Flow diagram showing the numerical method used to solve the proposed Maxwell-Stefan model. The solution match block is “yes” when the sum of the squared nonlinear function values (equations 6.18 and 6.19) is less than the default square root of the function tolerance of 10^{-6} . Equation 6.15 is used for algorithm step I, Equation 6.16 is used for algorithm step II, and Equation 6.17 is used for algorithm step III. Then Equations 6.18 and 6.19 are used for the solution match step.

6.5 Pure Molecule Sorption and Diffusion Fits

A key factor in the multicomponent transport framework is a sorption isotherm that accurately captures the uptake of multiple penetrants in a polymer system. Unary experimental hydrocarbon sorption isotherms and model fits for PIM-1 and SBAD-1 are shown in Figure 6.4. The higher experimental error observed for low sorbing molecules

such as *iso*-cetane is expected as the data approaches the lower end of the instrument accuracy range. It should be noted that due to slow transport in SBAD-1, certain sorption data likely did not reach full equilibrium (Figure 6.5). These include sorption of methylcyclohexane, 1-methylnaphthalene, *tert*-butylbenzene, 1,3,5-triisopropylbenzene and *iso*-cetane. Despite this, the data at each relative pressure that was collected within reasonable timeframes (up to 2 weeks of equilibration time per point) were used to fit the desired sorption parameters with the understanding that the model isotherms will likely be underpredicting the true uptakes. Beyond a relative pressure of 0.3, vapor uptakes of *tert*-butylbenzene were difficult to measure due to accumulation and condensation of the fluid within the instrument chamber and so, limited experimental data is available for this molecule. In general, LM-FH and DMS enable good predictions of sorption at different activities while the FH model with constant $\chi_{i,n+1}$ underpredicts sorption within the entire range of activities. Figure 6.6 shows how $\chi_{i,n+1}$ must vary with the volume fraction of the penetrant to obtain more accurate predictions of sorption via the FH model. For certain highly sorptive molecules, such as *o*-xylene in PIM-1 and 1-methylnaphthalene in SBAD-1, the proposed LM-FH sorption model delivers better isotherm fits than DMS. Based on this observation, we may expect the multicomponent sorption of liquid hydrocarbons to be captured best by LM-FH.

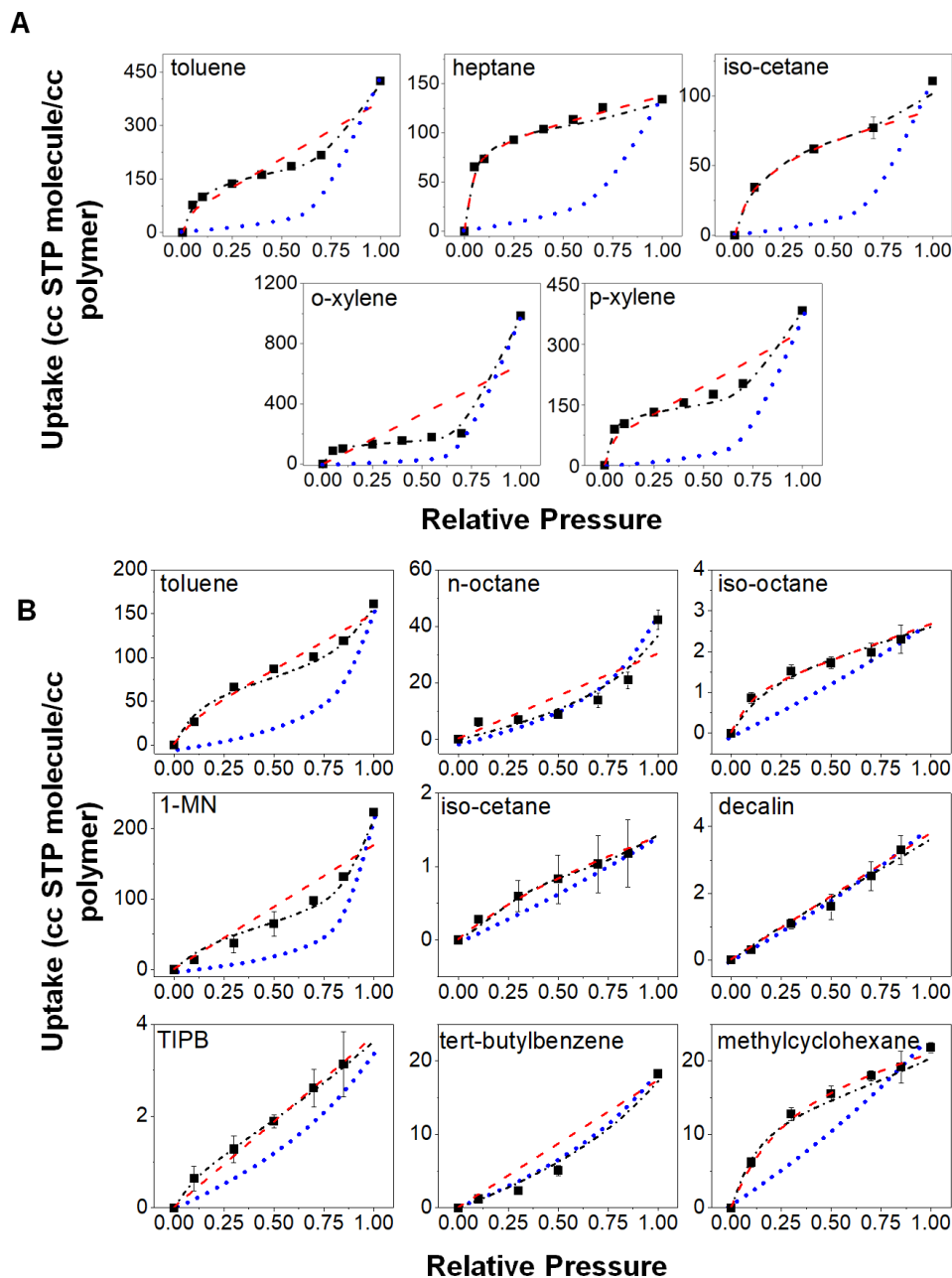


Figure 6.4. Unary sorption in PIM-1 and SBAD-1. Experimental hydrocarbon sorption isotherms (■) and predictions for PIM-1 (A) and SBAD-1 (B) at 25 °C assuming Dual-mode (---), Flory-Huggins (....), and Langmuir + Flory-Huggins (-.-) sorption models. X-axes indicate relative pressure of the molecule and y-axes represent molecule uptake (cc STP molecule/cc polymer). Data are shown as averages of at least two measurements with standard deviation error bars. Abbreviations are shown for 1-methylnaphthalene (1-MN) and 1,3,5-triisopropylbenzene (TIPB).

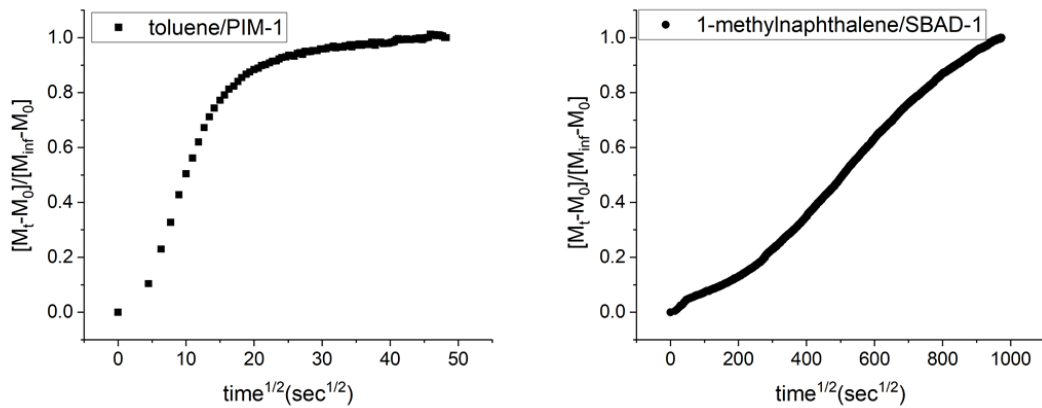


Figure 6.5. Kinetic sorption of toluene in PIM-1 at toluene activity = 0.7 (left) and 1-methylnaphthalene in SBAD-1 at 1-methylnaphthalene activity = 0.7 (right).

It is essential for a model that describes the transport of complex liquid feeds to be capable of describing permeation of simple feeds - the simplest being a pure liquid. Therefore, the Maxwell-Stefan model is first applied to unary liquid hydrocarbon permeation at a range of different transmembrane pressures as described in Section 6.2.3 (Figure 6.8). The membranes used in these experiments were thin film composites of PIM-1 and SBAD-1 with thickness of approximately 300 nm and 1500 nm, respectively.

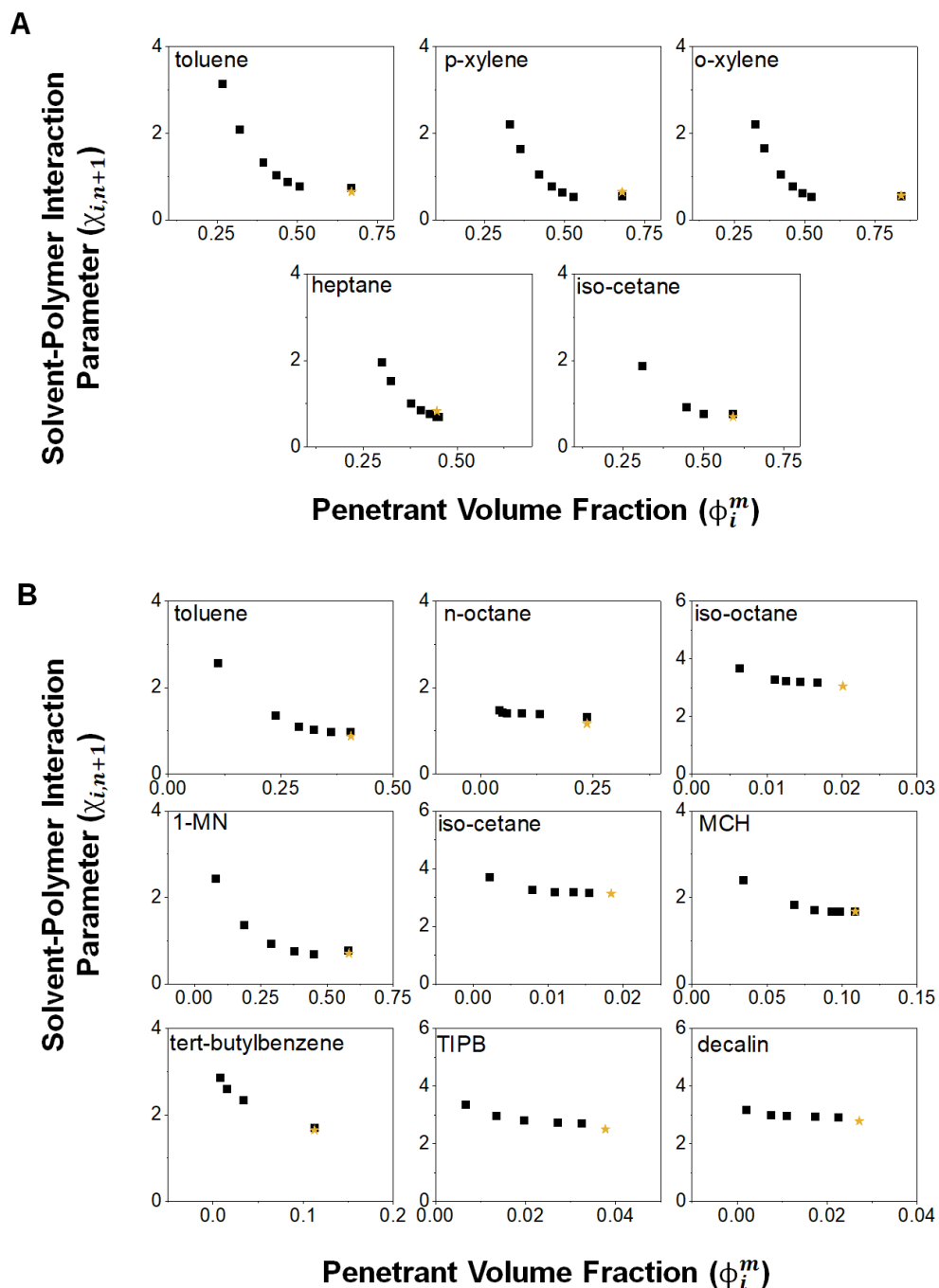


Figure 6.6. Calculation of Flory-Huggins solvent-polymer interaction parameter ($\chi_{i,n+1}$) using the F-H model for composition-dependent interaction parameters, $\ln(a_i^m) = \ln\phi_i^m + (1 - \phi_i^m) - (1 - \phi_i^m)\frac{\bar{V}_i}{\bar{V}_m} + \chi_{im}(1 - \phi_i^m)^2 + \phi_i^m(1 - \phi_i^m)^2\frac{\partial\chi_{im}}{\partial\phi_i^m}$ (22), and measured sorption isotherms for PIM-1 (A) and SBAD-1 (B) in single penetrant systems. \bar{V}_m was assumed to be $\gg \bar{V}_i$. Here, $\chi_{i,n+1}$ is not fixed at a constant value and is allowed to vary with activity of the penetrant.

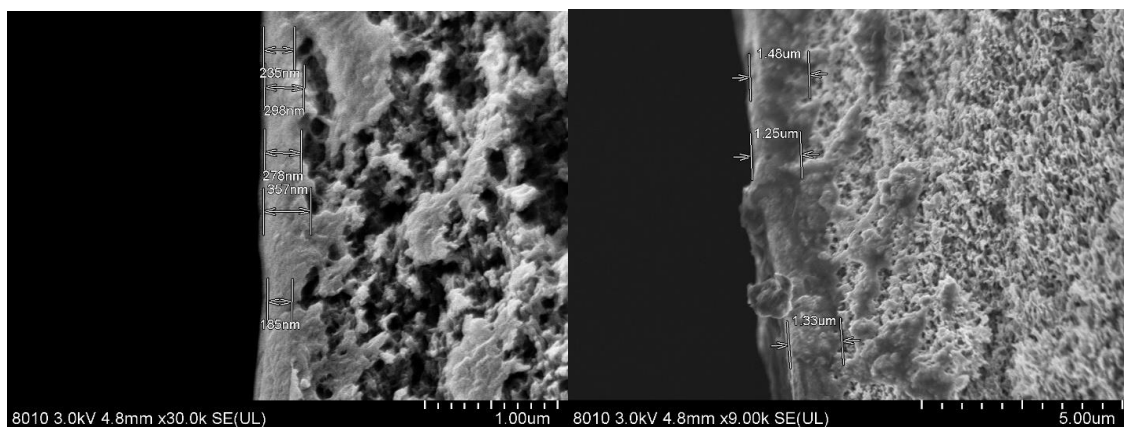


Figure 6.7. SEM images showing the approximate thickness of the SBAD-1 membrane (left) film thickness ~ 300 nm and PIM-1 membrane (right) film thickness ~ 1.5 microns.

The pure component diffusivities $\mathcal{D}_{i,n+1}^{v,m}$ were estimated using the experimental unary permeation flux for each solvent-polymer pair at a transmembrane pressure of 20 bar (30 bar for *iso*-octane) (Figure 6.8 and Figure 6.10A). The calculated $\mathcal{D}_i^{v,m}$ were then used to predict and compare with experimentally measured fluxes at higher transmembrane pressures of 30, 40, 50, and 60 bar. It should be noted that the high error in the experimental permeation for PIM-1 was likely due to the varying thickness of the thin films in the thin film composite membranes. To reduce the contribution of experimental error to the predictive framework, the same set of membranes were utilized in all permeation experiments, including complex mixture separations. Figure 6.8 shows that the predicted fluxes fit closely with experimentally measured values in the case of all three sorption models.

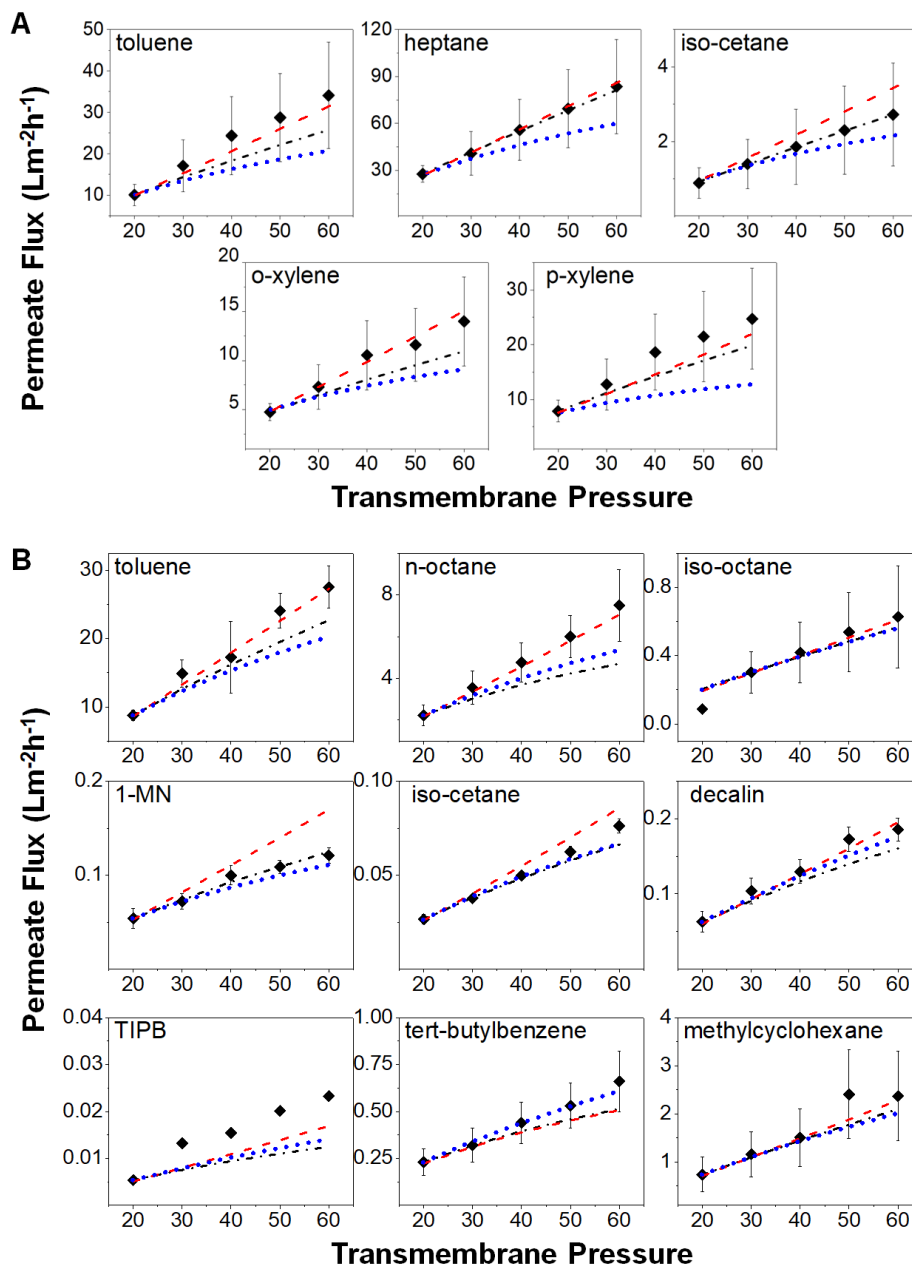


Figure 6.8. Unary permeation in PIM-1 and SBAD-1. Experimental liquid hydrocarbon unary flux (\blacklozenge) and predicted flux for thin-film composites at 22 °C with an estimated film thickness of 1500 nm for PIM-1 (A) and 300 nm for SBAD-1 (B) assuming Dual-mode (---), Flory-Huggins (....), and Langmuir + Flory-Huggins (-.-) sorption models. X-axes indicate transmembrane pressure (bar) and y-axes represent flux ($\text{Lm}^{-2}\text{h}^{-1}$). Data are shown as averages of three measurements on separate films with standard deviation error (with the exception of TIPB for which only one sample had measurable permeate flux). Abbreviations are shown for 1-methylnaphthalene (1-MN) and 1,3,5-triisopropylbenzene (TIPB).

An anomaly exists in the experimental values for 1,3,5-triisopropylbenzene (TIPB), where the fluxes were so low that an accurate measurement was only recorded for one sample (which was the highest) and error bars could not be calculated. In general, all sorption models enable unary flux predictions that are within error of experimental values. For aromatic molecules such as toluene, *p*-xylene and *o*-xylene in PIM-1 and tert-butylbenzene and 1-methylnaphthalene in SBAD-1, where a clear preference of the LM-FH model was observed in Figure 6.4, no such preference is seen in the prediction of their fluxes in Figure 6.8. It is observed that TIPB flux predictions are out of the range of experimental values. The good matches for all other hydrocarbon fluxes and the excellent TIPB sorption predictions suggest that the measured TIPB fluxes (which are very low) are on the order of the leak rate in the permeation cell resulting in unexpectedly higher values.

Figure 6.10A correlates $\mathcal{D}_i^{v,m}$ with molecule liquid molar volumes and as expected, higher Maxwell-Stefan diffusivities are calculated for molecules with lower liquid volumes. There is an almost linear negative correlation of the data except for one outlier: 1-methylnaphthalene. It is possible that due to the long timescales of 1-methylnaphthalene diffusion within SBAD-1 that the five-day unary permeation experiments were not at the same sorption state as assumed from Figure 6.4. Lower 1-methylnaphthalene uptake in the membrane would result in lower measured fluxes, which would then lead to lower calculated $\mathcal{D}_{1-MN,SBAD-1}^{v,m}$. It is concluded that for this molecule, further long-term sorption and permeation experiments may be needed to more accurately estimate $\mathcal{D}_{1-MN,SBAD-1}^{v,m}$. Moreover, the diffusivities of toluene and iso-cetane in PIM-1 are higher than those in SBAD-1 which align with the expected higher fractional free volume in PIM-1 compared to SBAD-1.

6.6 Predicting Multicomponent Sorption in Polymers

Beyond single component sorption, it is important that the new sorption models adequately describe mixture sorption phenomena. While a complete analysis of multicomponent sorption is beyond the scope of this paper due to the large amount of experimental data that is required, a few binary liquid sorption measurements of heptane and *o*-xylene (Figure 6.9, Figure 6.10B) and one ternary mixture sorption of toluene, *p*-xylene and *iso*-cetane (Figure 6.10C-D) in PIM-1 are compared with predictions from the three sorption models. For the binary uptakes, we observe equally good predictions by the FH and LM-FH sorption models. In the case of ternary sorption, the total uptake (g mixture/g polymer) seems to match predictions in the order of LM-FH > DMS > FH with the latter being out of the range of experimental error. All sorption models predict the composition of the sorbed species in the ternary system to a similar degree of accuracy. We may include, based on this limited dataset, that the LM-FH mixture sorption model – parameterized with single component data – results in the closest agreement with the experimental uptakes out of the three sorption models.

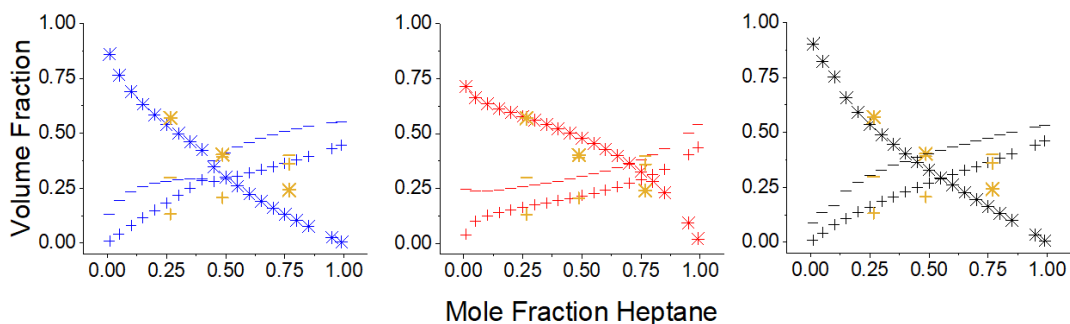


Figure 6.9. Predicted multicomponent sorption of heptane/*o*-xylene mixtures in PIM-1 according to Flory-Huggins (left, blue), Dual-mode (middle, red) and Langmuir + Flory-Huggins (right, black) models compared with experimental measurements (yellow). Legend: heptane, +; *o*-xylene, *; polymer, –

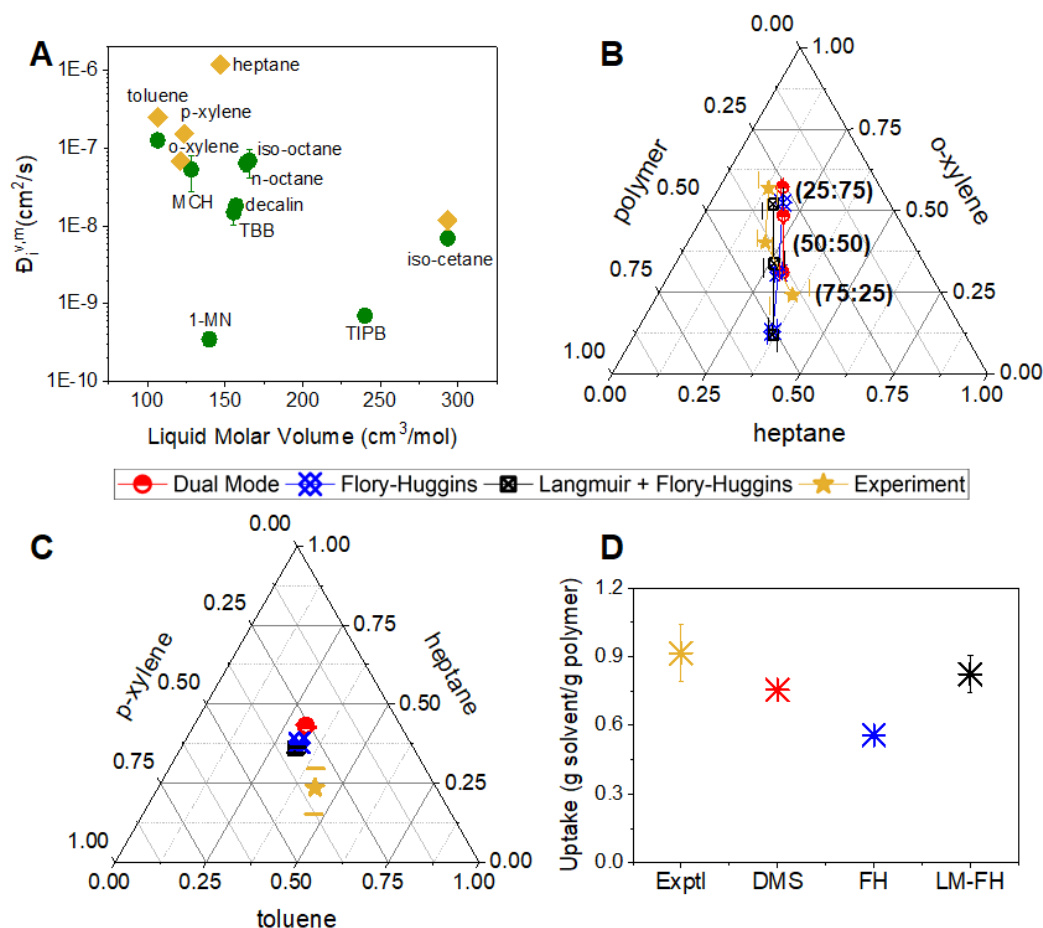


Figure 6.10. Unary diffusion and multicomponent liquid hydrocarbon sorption. **A.** Volume-based Maxwell Stefan diffusivities, $\mathcal{D}_i^{v,m}$ (cm^2/s), in SBAD-1 (\bullet) and PIM-1 (\blacklozenge) at 22°C calculated using the Langmuir + Flory-Huggins sorption parameters and unary permeate fluxes at 20 bar. Abbreviations are shown for methylcyclohexane (MCH), 1-methylnaphthalene (1-MN), tert-butylbenzene (TBB) and 1,3,5-triisopropylbenzene (TIPB). **B-D.** Multicomponent experimental sorption in PIM-1 compared with sorption predictions using single component parameter fits and estimates for competitive sorption effects for Dual-Mode, Flory-Huggins, and Langmuir + Flory Huggins models. Experimental measurements are from submerging dense films of PIM-1 in liquid mixtures at 22°C and atmospheric pressure. Molecule activities were taken into account when predicting multicomponent sorption here. **B.** Binary sorption indicated as volume fractions of swollen polymer system. Values in parentheses indicate initial mol fractions of surrounding bulk fluid (heptane:*o*-xylene). **C.** Ternary sorption indicated as volume fractions of sorbed liquid in PIM-1 dense films in bulk fluid initially composed of toluene, heptane and *p*-xylene in mol fractions of 0.35, 0.36 and 0.29 respectively, and **D.** Total solvent uptake (g solvent/ g polymer) in the swollen polymer from the ternary sorption condition in **C.**

6.7 Predicting Multicomponent Transport in PIM-1 and SBAD-1

Experimentally-measured permeate fluxes and compositions for three complex mixtures via PIM-1 and SBAD-1 membranes are detailed in Table 6.2. The three separations vary in complexity: a five-component separation via PIM-1, a nine-component separation via SBAD-1 and a three-component separation via SBAD-1. SBAD-1, being less susceptible to dilation than PIM-1, as observed in Figure 6.4, results in better separation of mixtures (significant decrease in concentration of large molecules such as *iso*-cetane and TIPB). It is of interest to include both polymers in the Maxwell-Stefan transport predictions because of their differing behavior in solvents, despite both being glassy and rigid in the dry state. The transport of these mixtures is predicted via the varying sorption and diffusion scenarios described in Section 6.3.3 and the resulting predicted partial fluxes are summarized in Figure 6.11, Figure 6.12, and Figure 6.13. The experimental partial flux of a molecule is calculated as the product of its volume-based composition in the permeate and the total permeate volume flux. It is informative to define the success of a transport model by how precise the predicted permeate compositions are and to a lesser extent, by how precise the predicted total permeate fluxes are. This precision can be calculated for any single experiment via Root Mean Square Percentage Error (RMSPE) calculations where

$$RMSPE = \left(\frac{\sum_{i=1}^n \left[\frac{|Predicted\ value_i - Experimental\ value_i|}{Experimental\ value_i} \right]^2}{n} \right)^{\frac{1}{2}} [\%] \quad 6.20$$

Table 6.2. Multicomponent separations via SBAD-1 and PIM-1 performed at 22 °C.

Separation 1 via PIM-1 at a transmembrane pressure of 30 bar			
Permeate flux (L/m²/h) =	6.33 ± 3.96		
	Feed Conc.	Permeate Conc.	Permeate Conc. Error
	mol fraction	mol fraction	%
Toluene	0.257	0.267	0.37
Heptane	0.216	0.210	0.95
<i>p</i> -xylene	0.205	0.212	0.47
<i>o</i> -xylene	0.264	0.269	0.74
<i>iso</i> -cetane	0.058	0.042	4.8
Separation 2 via SBAD-1 at a transmembrane pressure of 40 bar			
Permeate flux (L/m²/h) =	0.88 ± 0.52		
	Feed Conc.	Permeate Conc.	Permeate Conc. Error
	mol fraction	mol fraction	%
Toluene	0.171	0.201	1.5
Methylcyclohexane	0.281	0.253	0.79
1-methylnaphthalene	0.020	0.028	3.6
Decalin	0.107	0.110	0.91
<i>n</i> -octane	0.221	0.245	2.0
<i>iso</i> -octane	0.150	0.123	6.5
tert-butylbenzene	0.022	0.027	3.7
1,3,5-triisopropylbenzene	0.016	8.2x10 ⁻³	12
<i>iso</i> -cetane	0.013	4.5x10 ⁻³	22
Separation 3 via SBAD-1 at a transmembrane pressure of 30 bar			
Permeate flux (L/m²/h) =	0.40 ± 0.12		
	Feed Conc.	Permeate Conc.	Permeate Conc. Error
	mol fraction	mol fraction	%
Toluene	0.284	0.318	1.9
<i>iso</i> -octane	0.388	0.422	1.4
<i>iso</i> -cetane	0.328	0.260	4.2

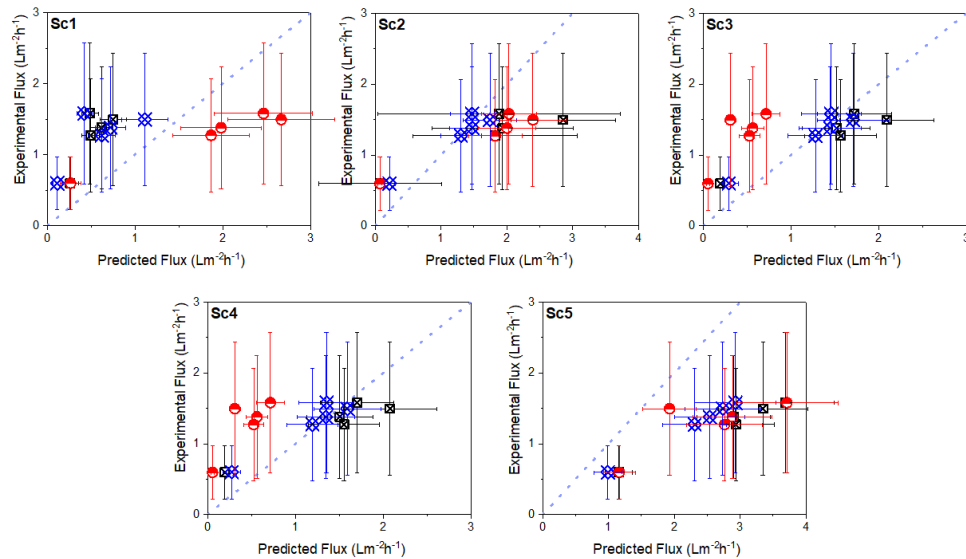


Figure 6.11. Partial flux predictions for Separation 1 via PIM-1 at varying combinations of sorption and diffusion assumptions. Markers indicate Dual-mode (red), Flory-Huggins (blue) and Langmuir + Flory-Huggins (black) sorption models. X-axis error bars are propagated from error in penetrant-polymer diffusivities (from unary flux measurements) and y-axis error bars are propagated from error in mixture separation flux measurements.

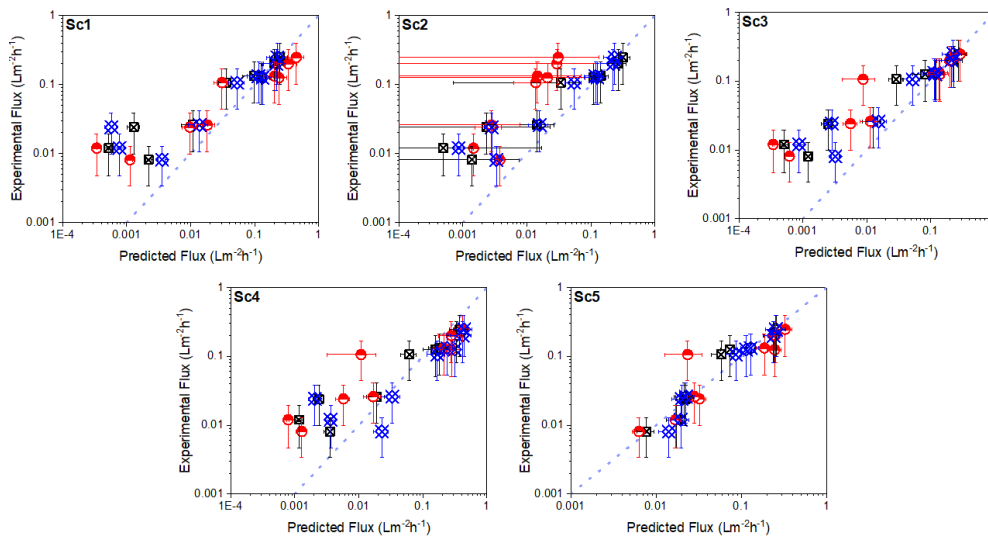


Figure 6.12. Partial flux predictions for Separation 2 via SBAD-1 at varying combinations of sorption and diffusion assumptions. Markers indicate Dual-mode (red), Flory-Huggins (blue) and Langmuir + Flory-Huggins (black) sorption models. X-axis error bars are propagated from error in penetrant-polymer diffusivities (from unary flux measurements) and y-axis error bars are propagated from error in mixture separation flux measurements.

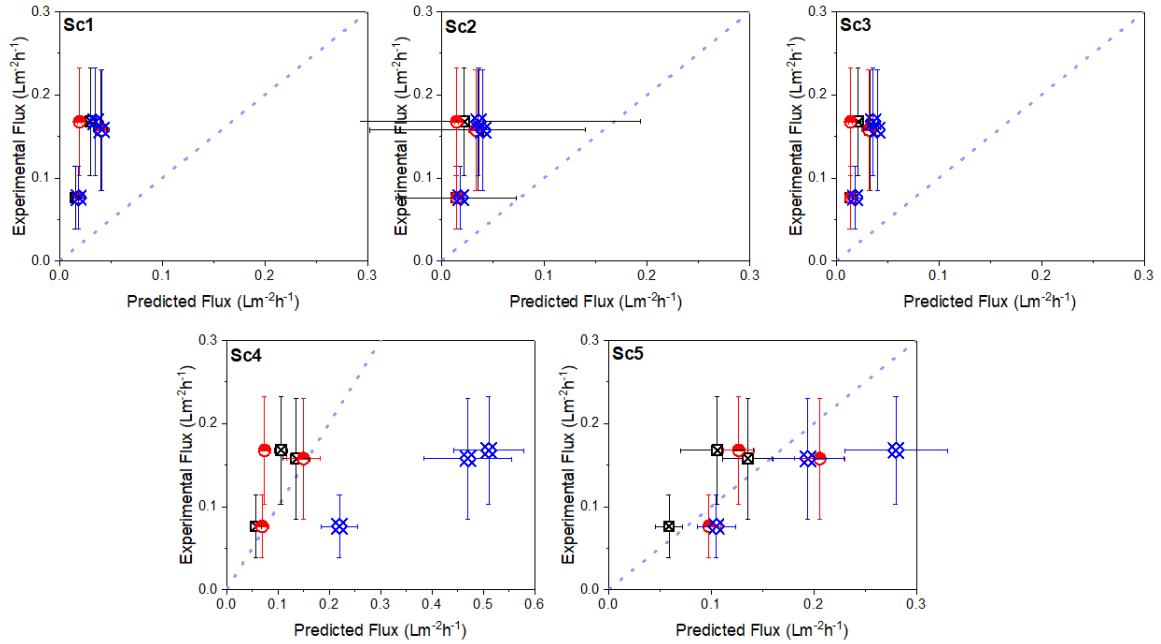


Figure 6.13. Partial flux predictions for Separation 3 via SBAD-1 at varying combinations of sorption and diffusion assumptions. Markers indicate Dual-mode (red), Flory-Huggins (blue) and Langmuir + Flory-Huggins (black) sorption models. X-axis error bars are propagated from error in penetrant-polymer diffusivities (from unary flux measurements) and y-axis error bars are propagated from error in mixture separation flux measurements.

The best overall agreement of permeate composition and total permeate flux with experimental data is obtained with the LM-FH sorption model and Sc4 where the free volume theory is used within the Maxwell-Stefan framework to adjust $\mathcal{D}_i^{v,m}$ with polymer swelling. When the permeate composition needs to be more accurate but the flux can have a larger band of error, the cohort-style average diffusivity approach (Sc5) excels with all sorption models, particularly LM-FH. For thin film membranes, such as the ones used in this work, it is not uncommon to encounter membranes with 30-40% variability in thickness. Despite the dependence of permeate flux on membrane thickness, the permeate compositions are expected to be independent of thickness if a defect-free membrane is

utilized. The low experimental error in permeate compositions (Figure 6.14A) is reflective of defect-free membranes. Therefore, greater importance is placed on the precision of permeate composition predictions than permeate flux predictions.

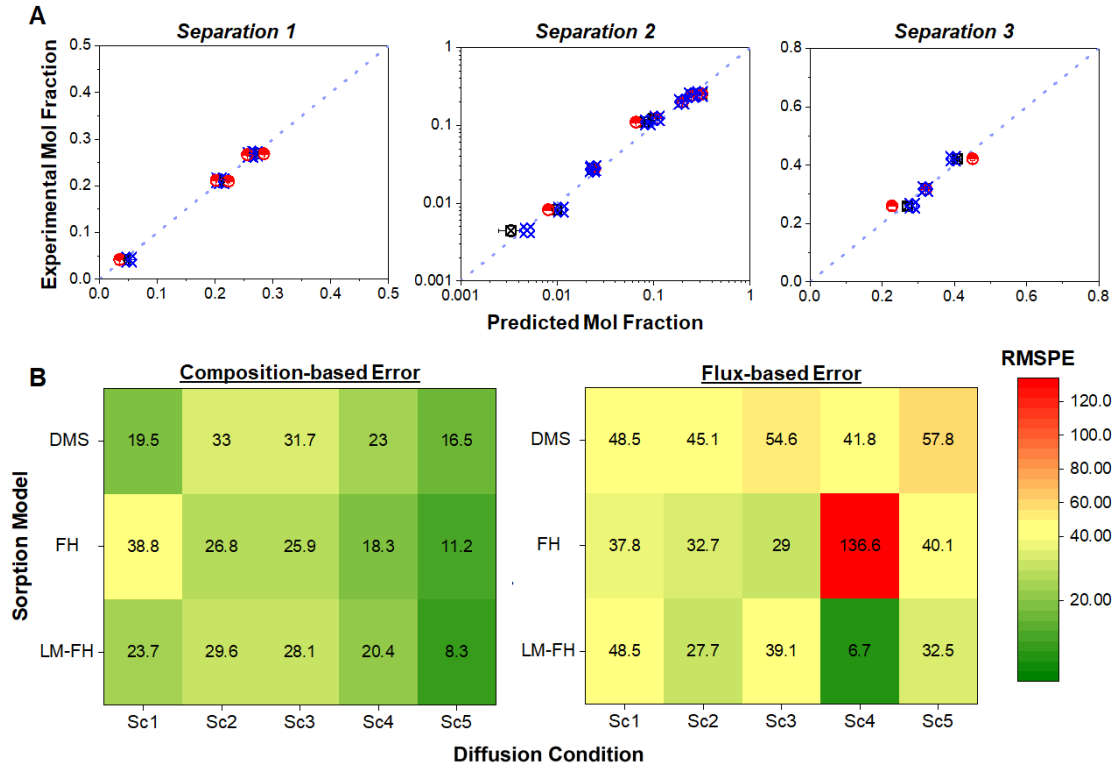


Figure 6.14. Permeate flux- and composition-based prediction of multicomponent separations in Table 6.2. **A.** Comparison of predicted experimental permeate compositions with predicted values for Separations 1, 2, and 3 where the $D_i^{v,m}$ for all molecules are assumed to be equal (average diffusivity approach: Sc5). For each separation, Dual-mode (red), Flory-Huggins (blue) and Langmuir + Flory-Huggins (black) sorption models are investigated. Dotted parity lines ($x=y$) are included as a guide for comparisons between predicted and experimental values. Error bars are included but are too small to be visible in some cases. **B.** Heatmaps showing composition based and total flux based RMSPE of each combination of sorption and diffusion assumptions. Y-axes vary sorption between Dual-mode, Flory-Huggins, and Langmuir + Flory-Huggins models while x-axes vary diffusion conditions as: Sc1 = Fickian transport, Sc2 = no diffusion coupling, Sc3 = Vignes diffusion coupling, Sc4 = Vignes diffusion coupling + free volume theory, Sc5 = average diffusivity assumption.

Interestingly, the simple Fick's law formulation (Sc1) generates better predictions of the permeate composition via the DMS and LM-FH model than the Maxwell-Stefan framework (Sc2) although the latter predicts the total flux slightly more accurately. On the other hand, the FH sorption model behaves as expected with Fick's law (Sc1) performing worse than Maxwell-Stefan (Sc2) in both permeate composition and permeate flux predictions. Vignes cross-coupling only provides minimal improvements in the accuracy of permeate composition predictions and, in fact, generates worse permeate flux predictions. This indicates that the Vignes equation does not sufficiently describe the various intermolecular coupling of diffusive transport of molecules in a liquid mixture through a glassy polymer. Even when the cross-diffusivities $\mathfrak{D}_{ij}^{v,m}$ are deliberately fit to match the experimental compositions (Figure 6.15), there is still an undesirably large discrepancy in the flux predictions suggesting that manipulation of cross-diffusivities is insufficient to capture the transport in these glassy polymers.

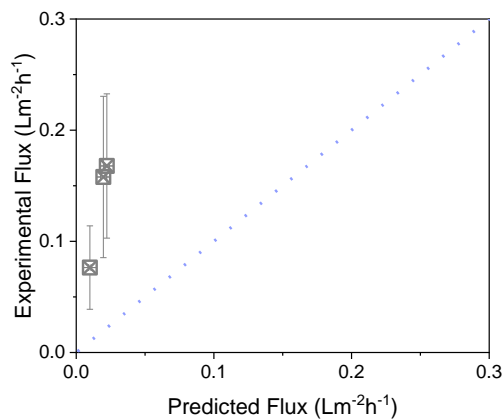


Figure 6.15. Separation 3 (via SBAD-1) partial fluxes predicted using LM-FH and cross-diffusivities ($\mathfrak{D}_{ij}^{v,m}$) fit to match permeate compositions.

As discussed in Section 6.3.3, the $\mathcal{D}_i^{v,m}$ can be correlated with the degree of polymer swelling. Said more plainly, the pure component diffusivity is strongly dependent on the state of dilation of the polymer, and the polymer will exist at different states of dilation depending on the solvent mixture it is in contact with. Our simplified free volume theory expression (Equation 6.12) enables a first pass estimate of this complex process (estimates of $\mathcal{D}_{i,II}^{v,m}$ for a range of swollen FFVs is shown in Figure 6.16 and are maintained below self-diffusivities.⁽⁴²⁾ A clear issue associated with assuming a constant B parameter is that the polymer's diffusion selectivity for specific molecular pairs is maintained at various states of dilation, whereas it is almost certain that the selectivity will be reduced at higher levels of dilation. For this reason, individual B values may be estimated by fitting the equation to self-diffusivities, although this approach was not pursued in an effort to simplify the framework such that it can be more easily generalized and applied. The B value of 0.03 was chosen as the optimum value in a range of arbitrary values investigated (Figure 6.17 and Figure 6.18). In Sc4, the free volume theory adjustment of diffusivity when applied with an optimized B value, offers noticeable improvement in slow molecule flux predictions for Separations 2 and 3 via SBAD-1 (Figures Figure 6.12 and Figure 6.13, Sc4 vs Sc1-Sc3) but not for Separation 1 via PIM-1 (Figure 6.11, Sc4 versus Sc1-Sc3). The FH sorption model combined with Sc4 results in a serious overprediction of partial fluxes for Separation 3 via SBAD-1 (Figure 6.11) although compositions remain accurate. It was found that in this case, the application of molecule activity coefficients from ASPENTech caused a significant shift in the predictions from an ideal solution assumption where the accuracy in permeate fluxes is comparable to the other sorption models.

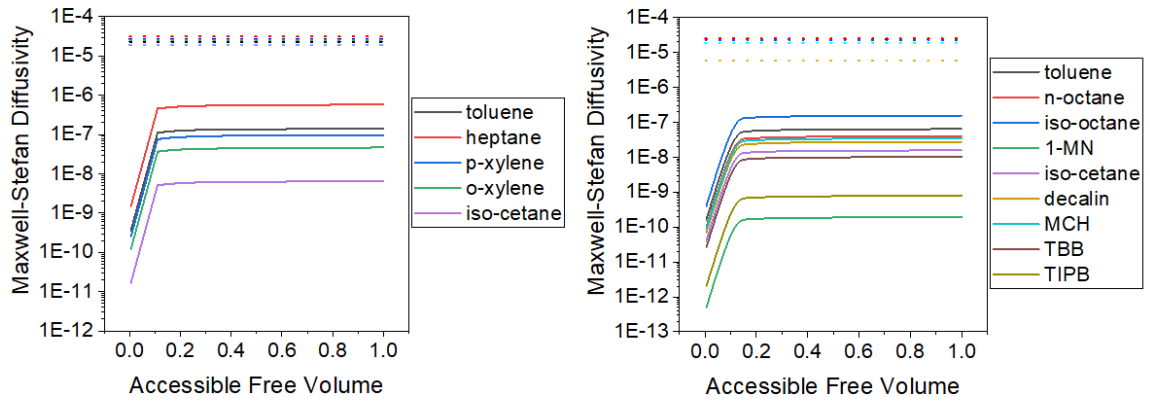


Figure 6.16. Free-volume theory-based prediction of diffusivity, $D_i^{v,m}$, as it varies with accessible free volume indicated by solid lines for PIM-1 (left) and SBAD-1 (right) assuming $B = 0.03$. Dotted lines are the self-diffusivities of molecules(38) (excluding 1-methylnaphthalene, tert-butylbenzene and 1,3,5-triisopropylbenzene) and represent an upper limit on diffusivity in the polymers.

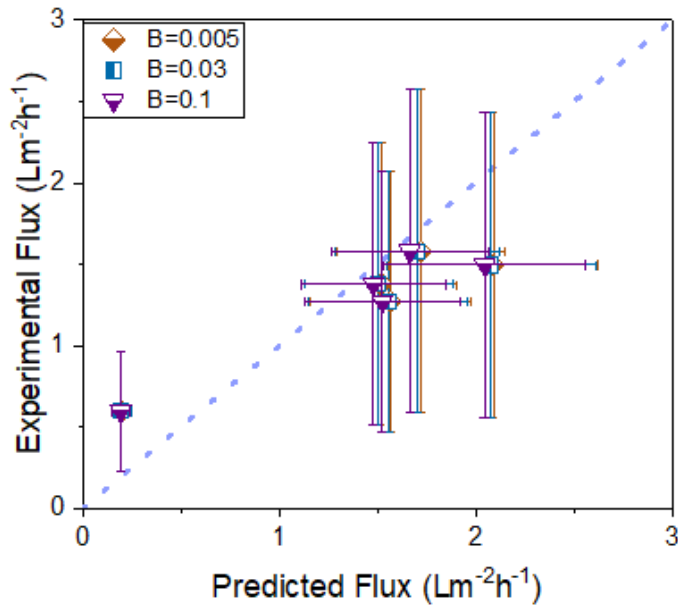


Figure 6.17. Separation 1 (via PIM-1) predicted using LM-FH, Vignes diffusion coupling, and free volume theory with varying $B =$ i) 0.005, ii) 0.03 and iii) 0.1.

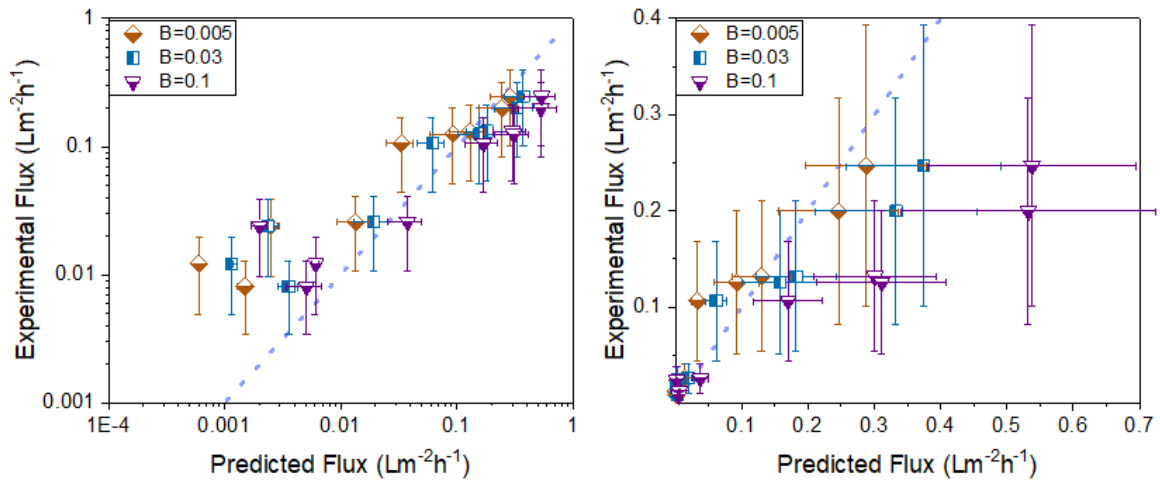


Figure 6.18. Separation 2 (via SBAD-1) predicted using LM-FH, Vignes diffusion coupling and free volume theory with varying $B =$ i) 0.005, ii) 0.03 and iii) 0.1. Left plot has log-log scale while right plot in linear.

As discussed earlier, when considering the composition-based error, the average diffusivity approach (Sc5) results in the lowest RMSPE, with small differences across the three sorption models. It appears that without sufficient diffusional coupling as described in the average diffusivity concept, the compositions of the slower molecules (decalin, 1-methylnaphthalene, 1,3,5-triisopropylbenzene and *iso*-cetane) are underpredicted in Separation 2 via SBAD-1 (Figure 6.12, Sc5 versus Sc1-Sc4). The next lowest error is when both Vignes cross-coupling and free volume theory are employed (Sc4), where an RMSPE of <30% is maintained for all sorption models. In Sc5, all molecule diffusivities are equivalent, caused by strong coupling of molecules such that they cannot diffuse independently, resulting in no diffusion selectivity. Note that this level of coupling is not possible Vignes cross-coupling approaches. On the other hand, in Sc4, a constant diffusion selectivity is maintained for each pair of molecules, but absolute diffusivities change with

polymer sorption, caused by swelling of the polymer and an increase in accessible volume. The differentiating transport mechanisms thus are i) molecules move collectively in small units versus ii) individual molecules hopping from one open site to another, which move faster when more sorption sites become available upon swelling.

Based on unary, binary and ternary sorption experiments, if we narrow down the results to just the LM-FH model, we observe a consistent decrease in composition-based RMSPE from Sc2 to Sc5. One could deduce that this aligns with increasing solvent-solvent and solvent-polymer diffusive coupling within a Maxwell-Stefan framework in the ascending order of scenarios. The error in total permeate fluxes does not follow a similar trend and cannot be correlated as easily but it remains low enough (<40%), such that preference is given to the predictions of composition based RMSPE. This point is further supported by the difficulty in precisely measuring thin film thicknesses that are on the order of hundreds of nanometers and the large relative variabilities in thicknesses across several samples during membrane production, that lead to low confidence in measured thicknesses and therefore, expected permeability (permeate flux that is normalized by the thickness of a given sample). We may therefore conclude that both the free volume theory approach and the average diffusivity approach show potential in making fast predictions of permeate compositions and fluxes of multicomponent liquid mixtures via glassy spirocyclic polymers like PIM-1 and SBAD-1.

6.8 Conclusions

Three sorption models were explored – FH, LM-FH, and DMS – as distinct conceptual approaches to the problem of membrane-based separation of complex mixtures. When

considered in combination with the unary and multicomponent sorption experiments, LM-FH is the most robust isotherm model that could be implemented with numerical and experimental ease. A variety of transport scenarios were also compared in this study. We find that the Vignes correlation did not offer significant improvements in the predictability of multicomponent transport and while the Vignes equation was included here as a stand-in for cross-coupling, such types of empirical correlations that do not have a well-defined physical significance hinder us from improving diffusional coupling correlations at this point. On the other hand, with a reasonable estimate of individual B values used in the free volume theory, varying degrees of improvements in predictions were obtained. The free volume theory improves the predictions of slow molecule fluxes but introduces more parameters that need to be fit or chosen arbitrarily, which would require further experiments or molecular dynamics simulations to evaluate fully. Critically, the average diffusivity approach based on an average guest diffusivity effectively had the best success in predicting permeate compositions in all 3 multicomponent separations and does not require the fitting of additional parameters. This is an important observation, as it has the potential to dramatically simplify deployment of this multicomponent transport framework in the case of more complex mixtures.

When drawing conclusions from the presented data, it is important to keep a few things in mind. First, the slow kinetics of bulky molecules such as 1-MN shown in Figure 6.5 could very well mean that experimental permeate compositions and fluxes were measured at what appears to be a pseudo-equilibrium state in the unary permeation testing period due to slow solvent-induced relaxations of the polymer structure. Further experiments will be needed to confirm this and accurately calculate the diffusivity of 1-

MN and other such molecules as a function of penetrant activity and polymer free volume simultaneously. Second, investigating the predictability of a small dataset of experiments is just a start – an extensive database of experimental data for a variety of solvent and polymer systems is required to validate the generalizability, accuracy, and ease of computing a multicomponent transport model. Furthermore, there is a need to standardize the success of transport models. A model with a low RMSPE for a random set of experiments (preferably >100), could be deemed a suitable framework.

Overall, it was demonstrated that complex multicomponent transport in polymers can be quantitatively predicted with some degree of accuracy, using only pure molecule-polymer sorption and diffusion parameters. While this is a complex problem, the average diffusivity simplification provides a potentially simplistic approach which could pave a practical path to multi-component diffusion modeling of complex mixtures in PIM-1 and SBAD-1. For more fundamentally accurate predictions, the diffusional and thermodynamic cross coupling of molecule pairs could be better defined with more complex approaches. Although our aim is to eventually describe the transport of real crude feeds containing thousands of molecules, less complex feeds were considered here due to the extensive experimental effort required to validate the model. Future computational efforts that can also predict pure solvent sorption and diffusion that replace experimental measurements will be needed before more complex feeds can be investigated.

Table 6.3. Nomenclature for Equations in Chapter 6.

A	fractional free volume pre-exponential factor, $\text{m}^2 \text{s}^{-1}$	N_i^V	partial volumetric flux of component i , $\text{m}^3 \text{m}^{-2} \text{s}^{-1}$
$a_{i,y}^\alpha$	activity of component i in phase α , evaluated at $z = y$, dimensionless	R	gas constant, $8.314 \text{ J mol}^{-1} \text{ K}^{-1}$
B	fractional free volume exponential parameter, dimensionless	T	system temperature, K
b_i	Langmuir affinity parameter for component i , Pa^{-1}	\bar{V}_j	partial molar volume of component j , assumed to be equal to the pure liquid molar volume in this work, $\text{m}^3 \text{mol}^{-1}$
$C_{H,sat,i}^*$	molar Langmuir free volume capacity for component i , $\text{mol} (\text{m}^3 \text{polymer})^{-1}$	\hat{V}	mixture molar volume, $\text{m}^3 \text{mol}^{-1}$
$C_{H,sat,i}$	volume Langmuir free volume capacity for component i , $(\text{m}^3 \text{penetrant}[\text{STP}]) (\text{m}^3 \text{polymer})^{-1}$	x_L^s	permeant local molar compositions in the bulk fluid within the support layer at $z = L$, dimensionless
C_i^m	molar concentration of component i normalized by total system volume (polymer and total sorbed species volume) for LM-FH and solely polymer volume basis for DMS, mol m^{-3}	z	membrane layer thickness coordinate, m
\mathfrak{D}_{ij}^m	Maxwell-Stefan diffusivity for component pair i, j , $\text{m}^2 \text{s}^{-2}$	Greek symbols	
$\mathfrak{D}_{ij}^{v,m}$	modified Maxwell-Stefan volume-based diffusivity for component pair i, j , $\text{m}^2 \text{s}^{-2}$	χ_{ij}	Flory-Huggins interaction parameter between component i and j , dimensionless
f_i^α	mixture fugacity of component i in phase α , Pa	δ_y	Hansen solubility parameters for dispersion forces ($y = D$), intermolecular forces ($y = P$), and hydrogen bonding ($y = H$), $\text{Pa}^{0.5}$
$v_{Fi,y}$	polymer free volume fraction at swollen polymer state y	ϕ_i^m	sorbed polymer phase (m) volume fraction of component i , volume component i per total system volume (polymer and total sorbed species volume)
$k_{D,i}^*$	molar Henry's law parameter for component i , $\text{mol Pa}^{-1} (\text{m}^3 \text{polymer})^{-1}$	μ_i^m	chemical potential of component i in the sorbed polymer phase (m), J/mol
$k_{D,i}$	volume Henry's law parameter for component i , $(\text{m}^3 \text{penetrant}) \text{Pa}^{-1} (\text{m}^3 \text{polymer})^{-1}$	Δp	transmembrane pressure drop, Pa
N_i	partial molar flux of component i , $\text{mol m}^{-2} \text{s}^{-1}$		

6.9 References

1. P. Marchetti, M. F. J. Solomon, G. Szekely, A. G. Livingston, Molecular Separation with Organic Solvent Nanofiltration: A Critical Review. *Chem Rev* **114**, 10735-10806 (2014).
2. P. Marchetti, A. G. Livingston, Predictive membrane transport models for Organic Solvent Nanofiltration: How complex do we need to be? *J Membrane Sci* **476**, 530-553 (2015).
3. P. Izak, L. Bartovska, K. Friess, M. Sipek, P. Uchytíl, Description of binary liquid mixtures transport through non-porous membrane by modified Maxwell-Stefan equations. *J Membrane Sci* **214**, 293-309 (2003).
4. D. Peshev, A. G. Livingston, OSN Designer, a tool for predicting organic solvent nanofiltration technology performance using Aspen One, MATLAB and CAPE OPEN. *Chem Eng Sci* **104**, 975-987 (2013).
5. S. Rosenbaum, O. Cotton, Steady-State Distribution of Water in Cellulose Acetate Membrane. *J Polym Sci A1* **7**, 101-+ (1969).
6. D. R. Paul, J. D. Paciotti, Driving Force for Hydraulic and Pervaporative Transport in Homogeneous Membranes. *J Polym Sci Pol Phys* **13**, 1201-1214 (1975).
7. J. G. Wijmans, R. W. Baker, The Solution-Diffusion Model - a Review. *J Membrane Sci* **107**, 1-21 (1995).
8. P. Silva, S. J. Han, A. G. Livingston, Solvent transport in organic solvent nanofiltration membranes. *J Membrane Sci* **262**, 49-59 (2005).
9. M. Galizia, K. P. Bye, Advances in Organic Solvent Nanofiltration Rely on Physical Chemistry and Polymer Chemistry. *Front Chem* **6**, (2018).
10. K. P. Bye, M. Galizia, Fundamental origin of flux non-linearity in organic solvent nanofiltration: Formulation of a thermodynamic/diffusion framework. *J Membrane Sci* **603**, (2020).
11. W. Mickols, Z. H. Mai, B. van der Bruggen, Effect of pressure and temperature on solvent transport across nanofiltration and reverse osmosis membranes: An activity-derived transport model. *Desalination* **501**, (2021).
12. D. R. Paul, O. M. Ebra-Lima, Pressure-Induced Diffusion of Organic Liquids through Highly Swollen Polymer Membranes. *J Appl Polym Sci* **14**, 2201-2224 (1970).

13. L. S. White, Transport properties of a polyimide solvent resistant nanofiltration membrane. *J Membrane Sci* **205**, 191-202 (2002).
14. M. H. Abdellah, C. A. Scholes, B. D. Freeman, L. Liu, S. E. Kentish, Transport of terpenes through composite PDMS/PAN solvent resistant nanofiltration membranes. *Sep Purif Technol* **207**, 470-476 (2018).
15. R. Krishna, Problems and Pitfalls in the Use of the Fick Formulation for Intraparticle Diffusion. *Chem Eng Sci* **48**, 845-861 (1993).
16. R. Krishna, J. A. Wesselingh, Review article number 50 - The Maxwell-Stefan approach to mass transfer. *Chem Eng Sci* **52**, 861-911 (1997).
17. D. R. Paul, Reformulation of the solution-diffusion theory of reverse osmosis. *J Membrane Sci* **241**, 371-386 (2004).
18. E. Habeych, A. J. van der Goot, R. Boom, Prediction of permeation fluxes of small volatile components through starch-based films. *Carbohyd Polym* **68**, 528-536 (2007).
19. A. Raisi, A. Aroujalian, T. Kaghazchi, A predictive mass transfer model for aroma compounds recovery by pervaporation. *J Food Eng* **95**, 305-312 (2009).
20. S. Postel, S. Wessel, T. Keil, P. Eiselt, M. Wessling, Multicomponent mass transport in organic solvent nanofiltration with solvent mixtures. *J Membrane Sci* **466**, 361-369 (2014).
21. C. P. Ribeiro, B. D. Freeman, D. R. Paul, Modeling of multicomponent mass transfer across polymer films using a thermodynamically consistent formulation of the Maxwell-Stefan equations in terms of volume fractions. *Polymer* **52**, 3970-3983 (2011).
22. R. Krishna, Describing mixture permeation across polymeric membranes by a combination of Maxwell-Stefan and Flory-Huggins models. *Polymer* **103**, 124-131 (2016).
23. P. M. Budd *et al.*, Polymers of intrinsic microporosity (PIMs): robust, solution-processable, organic nanoporous materials. *Chem Commun*, 230-231 (2004).
24. K. A. Thompson *et al.*, N-Aryl-linked spirocyclic polymers for membrane separations of complex hydrocarbon mixtures. *Science* **369**, 310-315 (2020).
25. F. Fornasiero, J. M. Prausnitz, C. J. Radke, Multicomponent diffusion in highly asymmetric systems. An extended Maxwell-Stefan model for starkly different-sized, segment-accessible chain molecules. *Macromolecules* **38**, 1364-1370 (2005).

26. L. Onsager, Reciprocal relations in irreversible processes. II. *Phys Rev* **38**, 2265-2279 (1931).
27. R. Krishna, J. M. van Baten, Investigating the influence of diffusional coupling on mixture permeation across porous membranes. *J Membrane Sci* **430**, 113-128 (2013).
28. S. S. Dhingra, E. Marand, Mixed gas transport study through polymeric membranes. *J Membrane Sci* **141**, 45-63 (1998).
29. A. Heintz, W. Stephan, A Generalized Solution Diffusion-Model of the Pervaporation Process through Composite Membranes .1. Prediction of Mixture Solubilities in the Dense Active Layer Using the Uniquac Model. *J Membrane Sci* **89**, 143-151 (1994).
30. A. Vignes, Diffusion in Binary Solutions - Variation of Diffusion Coefficient with Composition. *Ind Eng Chem Fund* **5**, 189-& (1966).
31. P. W. M. Rutten, Diffusion in Liquids. *Doctoral Thesis*, (1992).
32. L. S. Darken, Diffusion, Mobility and Their Interrelation through Free Energy in Binary Metallic Systems. *T Am I Min Met Eng* **175**, 184-201 (1948).
33. P. J. Flory, *Principles of polymer chemistry*. The George Fisher Baker non-resident lectureship in chemistry at Cornell University (Cornell University Press, Ithaca,, 1953), pp. 672 p.
34. R. M. Barrer, J. A. Barrie, J. Slater, Sorption and Diffusion in Ethyl Cellulose .3. Comparison between Ethyl Cellulose and Rubber. *J Polym Sci* **27**, 177-197 (1958).
35. T. H. Yang, S. J. Lue, Modeling Sorption Behavior for Ethanol/Water Mixtures in a Cross-Linked Polydimethylsiloxane Membrane Using the Flory-Huggins Equation. *J Macromol Sci B* **52**, 1009-1029 (2013).
36. C. M. Hansen, The three dimensional solubility parameter and solvent diffusion coefficient. *Doctoral Thesis*, (1967).
37. C. M. Hansen, *Hansen solubility parameters : a user's handbook*. (CRC Press, Boca Raton, Fla., 2000), pp. 208 p.
38. L. Ansaloni, L. Deng, Advances in polymer-inorganic hybrids as membrane materials. *Woodhead Publ Mater*, 163-206 (2017).
39. S. Damle, W. J. Koros, "Sorp-vection": An unusual membrane-based separation. *Aiche J* **51**, 1396-1405 (2005).

40. C. Y. Pan, Gas Separation by Permeators with High-Flux Asymmetric Membranes. *Aiche J* **29**, 545-555 (1983).
41. L. Hesse, J. Micovic, P. Schmidt, A. Gorak, G. Sadowski, Modelling of organic-solvent flux through a polyimide membrane. *J Membrane Sci* **428**, 554-561 (2013).
42. O. Suarez-Iglesias, I. Medina, M. D. Sanz, C. Pizarro, J. L. Bueno, Self-Diffusion in Molecular Fluids and Noble Gases: Available Data. *J Chem Eng Data* **60**, 2757-2817 (2015).

CHAPTER 7. FABRICATION OF MODULAR PIM-1 THIN FILM COMPOSITE MEMBRANES VIA A SCALABLE ROLL-TO- ROLL COATING PROCESS

7.1 Overview

This chapter discusses the continuous coating of PIM-1 on Torlon® hollow fiber substrates. Porous Torlon® hollow fibers are first fabricated via dry-wet spinning followed by roll-to-roll dip coating in dilute PIM-1 solutions.

7.2 Introduction

It is important to demonstrate the scalability of new materials, especially for applications that are relatively unexplored. The flat sheet membrane performance of SBAD-1 was determined via lab-scale (25 mm diameter) and spiral wound module thin film composites in Chapter 5. While spiral wound modules are attractive options for industrial applications, hollow fiber membranes are gaining increasing favorability due to their much larger surface area to occupied volume ratios. In fact, hollow fiber modules offer up to $10,000\text{m}^2/\text{m}^3$ compared to $200\text{-}1000\text{ m}^2/\text{m}^3$ for spiral wound modules.(1)

Roll-to-roll processing is a potential method for producing large-scale thin film composite hollow fibers where a flexible substrate is transferred between moving pulleys to allow a continuous additive or subtractive process to the substrate. We may use a continuous support fiber that is wound around a compact spool as the process input, which is then directed towards the coating process via pulleys and pulled through the process via

a rotating drum. Thin film coatings can be applied on membranes through various methods such as dip coating, physical vapor deposition, chemical vapor deposition, vapor phase infiltration and atomic layer deposition.(2-6) Here, continuous (roll-to-roll) dip coating was considered as the path forward due to the simplicity of design, low operating costs and low energy usage.(7) In dip coating, the film thickness and quality are dependent on the hydrodynamic and evaporative properties of the coating solutions.

Continuous hollow fiber dip coating has so far found success in aqueous and gaseous membrane separation applications. Aqueous nanofiltration hollow fiber membranes were developed by Bequet via continuous dip coating of a monomer followed by UV photografting.(8) Bequet found that by allowing a short contact time of the ultrafiltration substrate in the coating bath, the intrusion of the coating fluid into the substrate pores would be minimized. Jesswein et al. demonstrated the continuous dip coating of polyvinyl alcohols on poly(vinylidene fluoride) hollow fibers to form nano-scale to micron-scale thin film membranes for gas-to-gas humidification.(2) They detailed the strong dependence of coating thickness on the concentration and surface tension of the polymer solution as well as the coating velocity or fiber draw rate. PEG-based membranes were also created via continuous dip coating in one study for CO₂/N₂ separation.(9) It was concluded that a pre-wetting agent with low viscosity was necessary to prevent the intrusion of coating solution into substrate pores. In general, high surface porosity and small mean pore size are desired for coating substrates such that smooth thin layers can be applied without disruption while maintaining minimal support transport resistance.

SBAD-1, being a spirocyclic polymer, is expected to have similar rheological properties to PIM-1, which has previously been investigated in dip coating of hollow

fibers.(10-12) However PIM-1 has only so far been continuously processed as a thin film membrane on flat sheets via dilute chloroform solutions.(13) Therefore, it is intended to demonstrate the continuous coating of PIM-1 composite hollow fiber membranes first, followed by SBAD-1 composite hollow fiber membranes at a later time. A commercial polymer that is more easily available in bulk quantities is favored as the support layer or substrate. Torlon®, a polyamide imide, is chemically similar to polyetherimides and polyimides that have been successfully used in composites of PIM-1 in previous studies.(13, 14) It is hypothesized and investigated here that Torlon® experiences sufficient wetting of spirocyclic/chloroform solutions for defect-free coatings. Moreover, Torlon® is stable in most chemical solvents, which avoids a crosslinking step that would otherwise be necessary before dip coating in chloroform.(15) Furthermore, Torlon® exhibits high mechanical strength, ideal for our substrate that will be wound around pulleys under high tension.(16) Finally, Torlon® is a low-swelling polymer, which can prevent cracking of the thin film due to swelling or shrinkage in organic solvent separations.(15)

In Chapter 5, it was shown that although SBAD-1 is capable of discriminating molecules with Angstrom-sized differences; however, the low permeabilities impose a limitation on fabricating membranes entirely out of SBAD-1. SBAD-1 films with minimal thicknesses are desired to achieve the desirable fluxes that can compete with current separation processes. A thin film composite will allow such thicknesses along with the consumption of just small amounts of the small-scale synthesized polymer. A handful of other commercial OSN membranes sold as spiral wound modules with low MWCOs typically produce permeate at a rate of $0.1\text{--}1\text{ Lm}^{-2}\text{h}^{-1}\text{bar}^{-1}$ for a feed mixture of polystyrenes in toluene.(17) A flat thin film composite with a 300 nm SBAD-1 film results in a

permeance of $\sim 0.20 \text{ Lm}^{-2}\text{h}^{-1}\text{bar}^{-1}$ for a similar experiment at 30 bar as seen in Chapter 5. Since PIM-1 is more readily synthesized than SBAD-1, the aim of this work is to continuously produce thin film composites of PIM-1 ($\sim 100 \text{ nm}$), such that the path to similar thin film composites of SBAD-1 is recognized and can be more easily implemented in the future.

7.3 Fabrication of Torlon® Hollow Fiber Support

Torlon® hollow fibers have been created as defect-free membranes and as supports for gas permeation in previous works.^(18, 19) A previously published protocol for creating Torlon® supports with a pore size of 10 nm was closely followed to create supports with a combination of a smooth surface and sufficient porosity to avoid organic solvent transport resistance.⁽¹⁹⁾ Trial 1 in Table 7.1 resembles the spinning conditions from the reference. In this work, the fibers were spun continuously and were not cut into sections since a continuous fiber is required for the continuous roll-to-roll coating process. Fibers up to a length of 150 m were obtained on a large drum and were continuously rotated in running water overnight. The fibers were then collected on a spool and placed in a large bath of water and rinsed with fresh water daily to remove PVP, which is the pore former and residual NMP. The spool of fibers was then placed in a 3L bath of methanol and allowed to solvent exchange for 24 hours. This solvent exchange step prevents the collapse of surface pores under the high capillary forces from when water evaporates. The spool of fiber was then allowed to air dry for at least one day before roll-to-roll coating.

Table 7.1. Torlon® hollow fiber spinning parameters in Trial 1. The molecular weight (MW) of PVP used is also highlighted. The reference used Torlon® 4000T-HV while Trial 1 used Torlon® 4000T-LV.

		Reference(19)	Trial 1
Dope	Torlon®/NMP/PVP(MW)/water	25/63/7(1300k)/5	25/63/7(55k)/5
	Flow rate (mL/hr)	600	600
Bore	NMP/water	88/12	88/12
	Flow rate (mL/hr)	200	200
Operating Conditions	Air gap (cm)	0.5	1
	Take up rate (m/min)	8.5	30
	Operating temperature (°C)	55	50
	Quench water temperature (°C)	55	50

While there are slight differences in the spinning conditions, the dope composition, bore composition and air gap height, which were considered to be the deciding factors for fiber morphology, remain mostly unchanged. Importantly, 55k PVP was used in this work since 1300k PVP used in the reference incurs slow diffusion out of the fibers during the solvent exchange process. As the concentration of PVP in the dope was the same, the main difference was expected to be the size of the pores within the hollow fiber and not the porosity. The fiber take-up rate was also increased to decrease the fiber diameter and, in turn, decrease the liquid transport resistance. The spun fibers were investigated for porosity via SEM imaging shown in Figure 7.1. No detectable surface pores were observed, and permeation of pure liquid toluene measured at a pressure of 10 psi was lower than the expected permeance of the thin film coating ($0.067 \text{ L}\cdot\text{m}\cdot\text{h}^{-1}\cdot\text{bar}^{-1}$).

Torlon® is a rigid, nonporous polymer and molecules often encounter slow sorption and diffusion through it.(15, 18) The fast liquid transport that is required in a support can only be achieved via porous pathways that are connected through the entirety of the

Torlon® membrane. Therefore, in a second attempt, the concentration of polymer in the dope composition was reduced to 18wt% to simulate a higher porosity in the hollow fibers. The ratio of Torlon® to PVP was kept constant and the ratio of solvent to nonsolvent (NMP:water) was adjusted to bring the dope composition closer to the binodal line (Figure 7.2) for quick vitrification and spinodal decomposition upon contact with the quench bath.

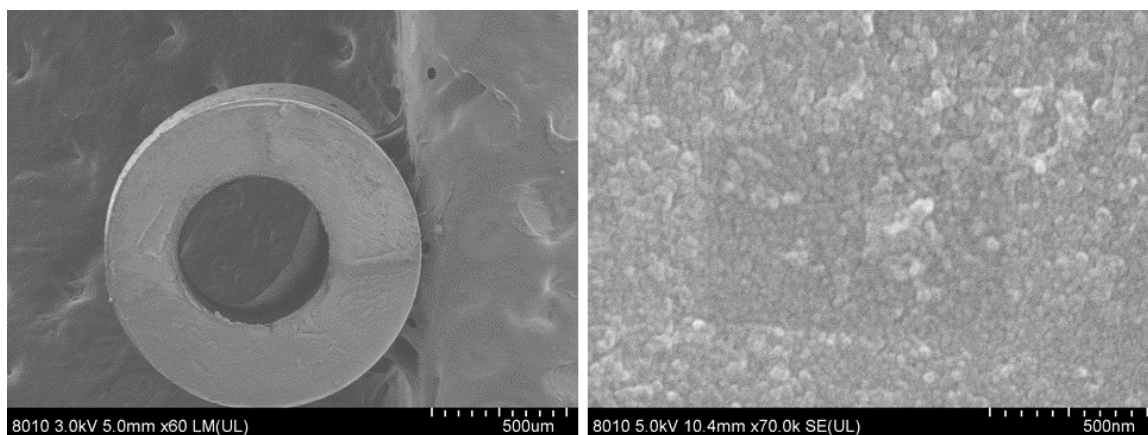


Figure 7.1. SEM images of the cross section (left) and top view (right) of Torlon® 4000T-LV fibers from Trial 1.

Before the dope was spun, a syringe extrusion was attempted to confirm that the dope was viscous enough to be drawn into a fiber. The fiber was manually pushed through a syringe and allowed to free fall into a small water bath containing hot tap water at a temperature of 45°C and air gaps varying between 2 and 10 cm. As seen in Figure 7.2, surface pores between 30-70 nm were obtained with a high density of pore population.

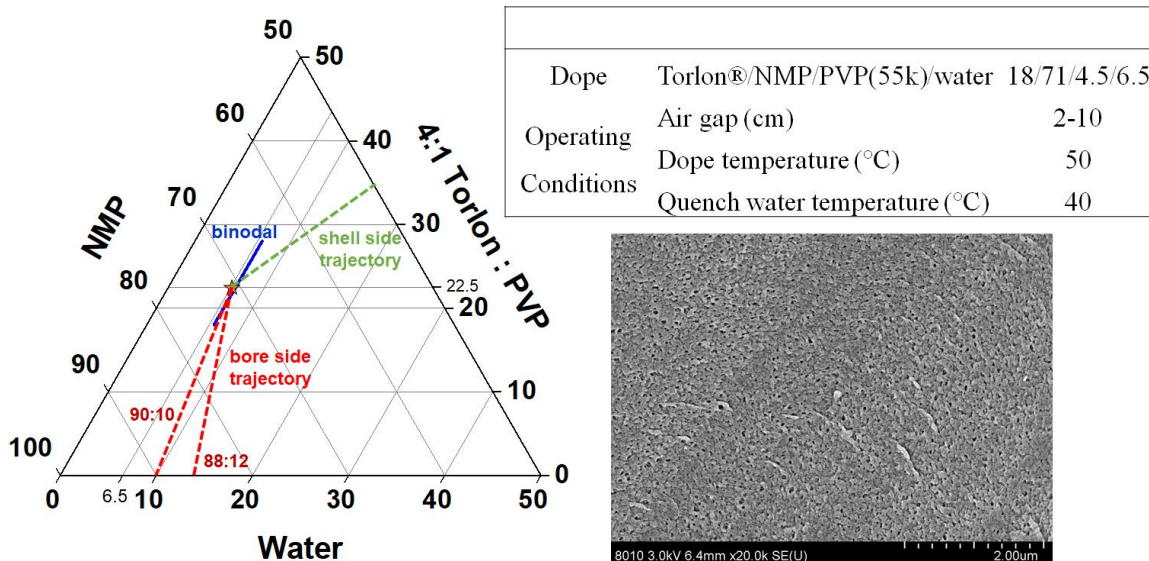


Figure 7.2. Ternary phase diagram of Torlon® 4000T-HV adapted from (20) (left). The star represents the low polymer concentration dope being considered for spinning hollow fibers. The blue, green and red lines represent the binodal line, shell side trajectory and bore side trajectory, respectively. Bore side trajectories are drawn for spinning hollow fibers in either 88:12 or 90:10 ratios of NMP:water bore fluid. Dope composition of syringe extruded Torlon® hollow fibers with a low polymer concentration (top right). SEM image (bottom right) shows the surface on the shell side of syringe extruded fibers.

For the spinning of the second Torlon® dope, Torlon 4000T-HV was opted instead of Torlon® 4000T-LV (used in Trial 1) to increase the cohesion and viscosity of the lower polymer concentration dope and therefore, increase spinnability. The bore fluid composition was also adjusted to reflect the change in dope composition (Figure 7.2). This adjustment moves the bore side trajectory closer to the binodal line which can increase the porosity on the bore side of the hollow fiber and potentially throughout the substructure. The dope flowrate was also reduced to simulate the low flowrate in the syringe extrusions, reduce the fiber outer diameter and hence, reduce the wall thickness. This should, in turn, reduce transport resistance of the support fiber. At the fixed spinning parameters, the dope

was able to free fall into the bath much like the syringe extrusion process. As seen from SEM images in Figure 7.3, pores of 10 nm were obtained with a high density of pores on the surface. The presence of the desired surface pores in Trial 2 could be due to a combination of the lower polymer concentration in the dope and the lower ratio of dope flowrate to fiber take-up speed which could have reduced the elongational stresses on the nascent fiber.

Trial 2		
Dope	Torlon®/NMP/PVP(MW)/water	18/71/4.5(55k)/6.5
	Flow rate (mL/hr)	240
Bore	NMP/water	90/10
	Flow rate (mL/hr)	60
Operating Conditions	Air gap (cm)	4
	Take up rate (m/min)	11
	Operating temperature (°C)	50
	Quench water temperature (°C)	50

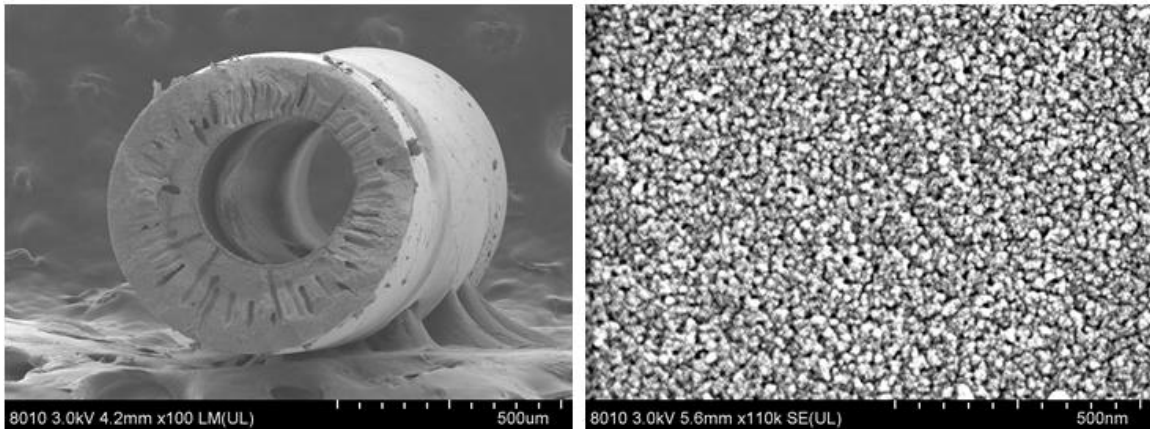


Figure 7.3. Torlon® hollow fiber spinning parameters (top) and SEM images (bottom) in Trial 2. The left image shows the cross-section of the fabrication hollow fiber and the right images shows the surface morphology on the shell of the fiber.

However, we also observe the occurrence of macrovoids throughout the substructure of this fiber which have been historically linked with low mechanical strength.(21) This is reflected in the quick decline in liquid toluene permeation through the support upon pressurization (Figure 7.4). Still, due to the desired surface porosity, fibers from this trial were used in the continuous dip coating process described in the following section as a means of demonstrating the success of coating on non-smooth surfaces, particularly to eliminate the possibility of coating solution intrusion into the pores.

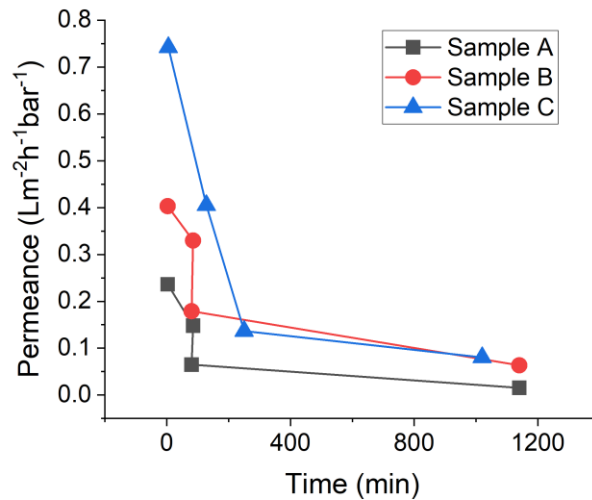


Figure 7.4. Liquid toluene permeance of Torlon® support obtained from Trial 2 at a transmembrane pressure of 10 bar for three samples (A, B and C).

7.4 Roll-to-Roll Dip Coating

7.4.1 The Landau Levich Derjaguin Law

As detailed in Chapter 2, the roll-to-roll coating method relies on fluid rheological properties to achieve thin film coatings. If inertial and gravimetric forces can be neglected,

the thickness of the wet thin film is controlled by factors such as viscosity, surface tension, and shear rate. For small fiber diameters, the dimensionless Bond number, Bo , that balances gravity and capillary forces, can be assumed to be $\ll 1$ which allows us to neglect gravity.(22)

$$Bo = \frac{\rho g r^2}{\gamma} \quad 7.1$$

Here, ρ is the coating solution density, g is the gravitational acceleration, r is the fiber radius and γ is the coating solution surface tension. For a fiber with a radius of $325\mu\text{m}$, a Bo of 0.049 is obtained. Additionally, at moderate coating speeds, inertial forces are overcome and can be determined by the dimensionless Weber number (We). (22)

$$We = \frac{\rho v^2 r}{\gamma} \quad 7.2$$

where v is the fiber draw speed. When $We < 1$, inertial forces can be neglected.(2) For a fiber with a radius of $325\mu\text{m}$, a We of 0.02 is obtained. Therefore, for small fibers, moderate coating speeds and thin films where the wet coating thickness \ll fiber radius, we can employ the Landau Levich Derjaguin law(22)

$$h_w = 1.34r Ca^{\frac{2}{3}} \quad 7.3$$

where h is the liquid film thickness and Ca is the dimensionless capillary number which is formulated as

$$Ca = \frac{\eta v}{\gamma} \quad 7.4$$

where η is the coating solution viscosity. Finally, the dry thin film thickness can be correlated with the liquid film thickness and the concentration of the coating solution as

$$t = c_p h_w \quad 7.5$$

where t is the dry film thickness and c_p is the concentration of the coating solution. We can assume the surface tension of polymer solutions to remain constant within a small range of low concentrations that will be used in this work (eg. 0.5 wt% to 2 wt% polymer in chloroform).⁽¹³⁾ Therefore, solution concentration, viscosity, and fiber draw rate may be the governing factors that determine the thickness of the thin film assuming a smooth support surface with roughness no greater than 25 nm. Viscosity is also a function of polymer concentration and therefore, we may reduce the factors to concentration and draw speed, if a relationship between concentration and viscosity can be established. The dependence of viscosity on concentrations of PIM-1 in chloroform is reported in Figure 7.5. At the low polymer concentrations tested, the fluids were observed to exhibit Newtonian behavior such that the viscous stresses were linearly correlated with the strain rate.

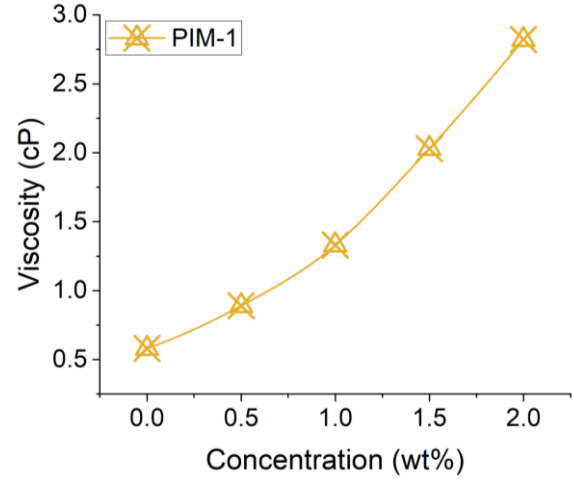


Figure 7.5. Relationship between viscosity and concentration in dilute polymer/chloroform solutions. PIM-1, MW~70k.

Figure 7.5 shows that the relationship between viscosity and concentration can be written out as a second order polynomial. Therefore, Equation 7.5 becomes

$$t = 1.34c_p r \left(\frac{(ac_p^2 + bc_p + c_p)v}{\gamma} \right)^{\frac{2}{3}} \quad 7.6$$

where a , b and c are constants that can be calculated by polynomial regression of the experimental data.

7.4.2 Minimizing the Thickness of The Film Coating

At very low withdrawal speeds, the Landau Levich Derjaguin law is not applicable. This is because the coating enters the capillary regime (described in Section 2.5) where the

evaporation of solvent is faster than the entrainment such that the wet film thickness is rarely a constant value. Therefore, the dry film thickness must be considered as a function of the wet film thickness observed at any given time.

$$t_{capillary} = \frac{c_p M E}{\alpha \rho h_w v} \quad 7.7$$

where M is the molecular weight of the polymer, E is the evaporation rate and α is the fraction of solids in the film, $\alpha = 1 - porosity$.(23) At intermediate withdrawal speeds, the thickness of the dry coating can be described by a combination of the LLD law and the capillary regime equation. Faustini et al. applied this method to theoretically validate the experimentally measured minimum film thickness of ~100 nm for a block copolymer.(23)

In the case of extremely thin films, the minimum possible film thickness may actually be controlled by intermolecular forces in the range of 100 nm.(22) By describing these Van der Waals forces in terms of a disjoining pressure, we can describe the capillary number below which the film thickness should be a constant.(22, 24)

$$Ca \sim \left(-\frac{A}{6\pi\gamma} \right)^{\frac{1}{2}} / r \quad 7.8$$

where A is the Hamaker constant and the equilibrium thickness is determined by

$$h = \left(-\frac{Ar}{6\pi\gamma} \right)^{\frac{1}{3}} \quad 7.9$$

This equilibrium thickness can be expected to be in the range of 1-10 nm(25) if only Van der Waals forces are considered. However, we must also consider the attractive forces that arise between pi-pi stacking of the aromatic rings in the support and the coating polymer. This would require a detailed analysis of interfacial phenomenon and is out of the scope of the presented work. Furthermore, the hypothesis of a minimum equilibrium thickness controlled by intermolecular forces assumes a completely smooth support surface. Based on AFM data (Figure 7.6), the Torlon® support surface possesses a pore size of 15-20 nm and an RMS roughness of 7.4 nm. However, the maximum height difference in Figure 7.6 reaches up to 50 nm. When pressure is applied during permeation testing, the soft PIM-1 thin film can be pushed into the surface pores of the substrate and result in breakage and thus, poor separation performance. Even though it has been possible to test ultrathin films of PIM-1 with a thickness of 35 nm on a polyacrylonitrile surface with RMS roughness of 3.5 nm(26), achieving a defect-free membrane with such a low thickness on the continuous Torlon® hollow fiber substrate may be difficult. We may estimate that a minimum thickness of 100 nm should be achievable via dip-coating for defect-free polymer films, provided the coating bath concentration, withdrawal speed and atmospheric conditions such as temperature and humidity are carefully controlled.

The fabricated Torlon® support fibers have an outer diameter of around 600 microns and the coating surface tension can be approximated as that of the pure chloroform at 22 °C (~0.027N-m). We can assume that a speed of 2 m·min⁻¹ is used to draw the substrate from the coating bath. Under the assumption of the LLD law (Equation 7.6), the required coating concentration for thin films with dry thicknesses of 100 – 500 nanometers must then be 1.09-3.37wt% for PIM-1.

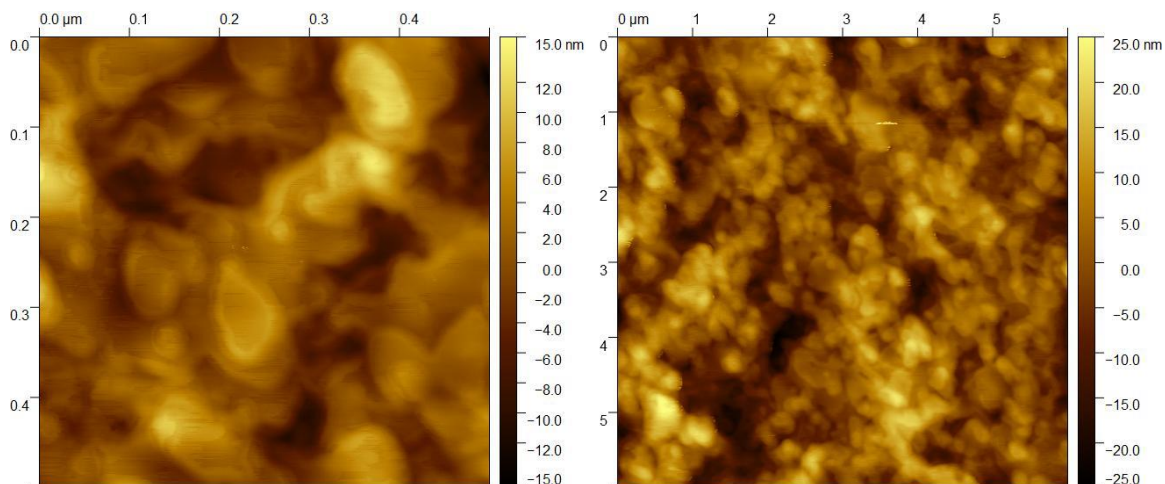


Figure 7.6. AFM height images of the Torlon® support surface used in the continuous coating of PIM-1. The image on the left has a 0.5 x 0.5 μm field of view while the image on the right has a 6 x 6 μm field of view.

7.4.3 Estimating the Marangoni Thickening Factor

Torlon® substrates were continuously coated with polymer solutions of varying concentrations of PIM-1 in chloroform to correlate the measured thin film thickness with the predicted thickness in Section 7.3.2. SEM images, shown in Figure 7.7, were used to determine the coating quality and measure the thin film thickness. It is apparent from these images that intrusion of coating into the pores is not a matter of concern and the films have adhered to the support without delamination, alluding to a favorable surface energy of the support material. The measured thicknesses from SEM images are compared with thicknesses predicted by the LLD law in Figure 7.7d. When calculating the required polymer bath concentrations, the Marangoni thickening factor was not considered. This is a swelling factor that is commonly known to occur in surfactant or polymer solutions due to favorable interparticle interactions in the dynamic meniscus regime and has been

reported to increase the coating thickness by up to 8 times.(27) Quéré hypothesized that at low enough concentrations, the thickening factor can be considered small enough to be ignored.(22)

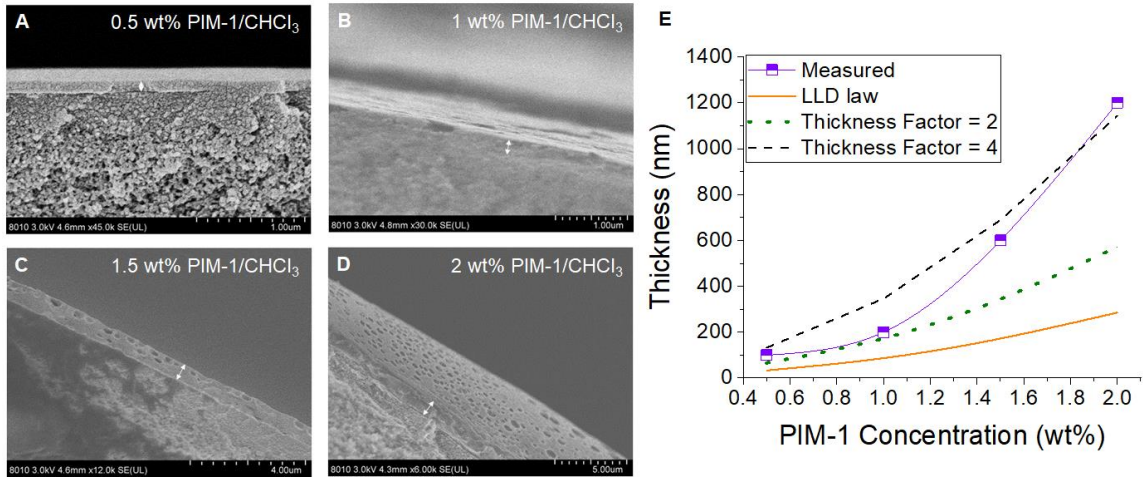


Figure 7.7. SEM images of PIM-1 coated Torlon® hollow fibers drawn at a rate of $2 \text{ m}\cdot\text{min}^{-1}$ from a bath of chloroform with PIM-1 at concentrations a) 0.5 wt% b) 1wt% c) 1.5wt% d) 2wt% e) Comparison of measured and predicted thicknesses of PIM-1 thin film coatings by the LLD law and Marangoni thickness factor of 2 and 4.

It is obvious from Figure 7.7 that the LLD law is poorly describing the PIM-1 dip coating process. In fact, even if a Marangoni swelling factor is incorporated into the LLD law, the trend of thicknesses does not obey the predictions at a single swelling factor. Upon closer inspection, large craters can be observed throughout the thin films, which could have resulted in the greater than expected thicknesses. This is reminiscent of the popping phenomenon discussed in Chapter 2. The solvent in the coating solution, chloroform, is highly volatile (boiling point = $61.2 \text{ }^\circ\text{C}$) and experiences a high driving force from the wet

fluid film to the surface-air interface. The craters observed are hypothesized to be formed due to the boiling-like rapid removal of chloroform from the film. While these craters have previously been observed in the formation of PIM-1 thin films from low boiling solvents, it was determined that they do not negatively impact the quality of the film and only reduce the effective thickness.^(11, 13) However, without the elimination of the craters, an appropriate relationship between the thickness of the films and fluid rheological properties cannot be established.

Borisov et al. eliminated crater formation during PIM-1 kiss coating by replacing pure chloroform with a 50-50 wt% mixture of chloroform and trichloroethylene (boiling point = 87.2 °C).⁽²⁸⁾ This was imitated here by dip coating with a 1 wt% solution of PIM-1 in 50-50 chloroform/trichloroethylene but upon inspection via SEM imaging (Figure 7.8), the craters could not be eliminated. The solvent was replaced again with a 50-50 mixture of chloroform and 1,1,2,2-tetrachloroethane (boiling point = 146.7 °C), and coated fibers were allowed to air dry for 24 hours. As seen from Figure 7.8, the craters were eliminated when the boiling point of the mixture was increased even further. Interestingly, the thickness of the coating remains around 200 nm. We must also consider that the fluid rheological properties have changed with the new solvent mixture. When we account for the change in viscosity and surface tension of the coating solution, an LLD thickness of 93 nm is estimated. This is still much lower than what is measured and even if we assume pure 1,1,2,2-tetrachloroethane solvent was used, the expected thickness does not increase above 120 nm. This could mean a Marangoni swelling effect is, in fact, occurring and a thickness factor of around 2 can be estimated for PIM-1 in a 50-50 solution of chloroform and

1,1,2,2-tetrachloroethane. Even low polymer concentrations can be attempted in the future to achieve the target 100 nm film thickness.

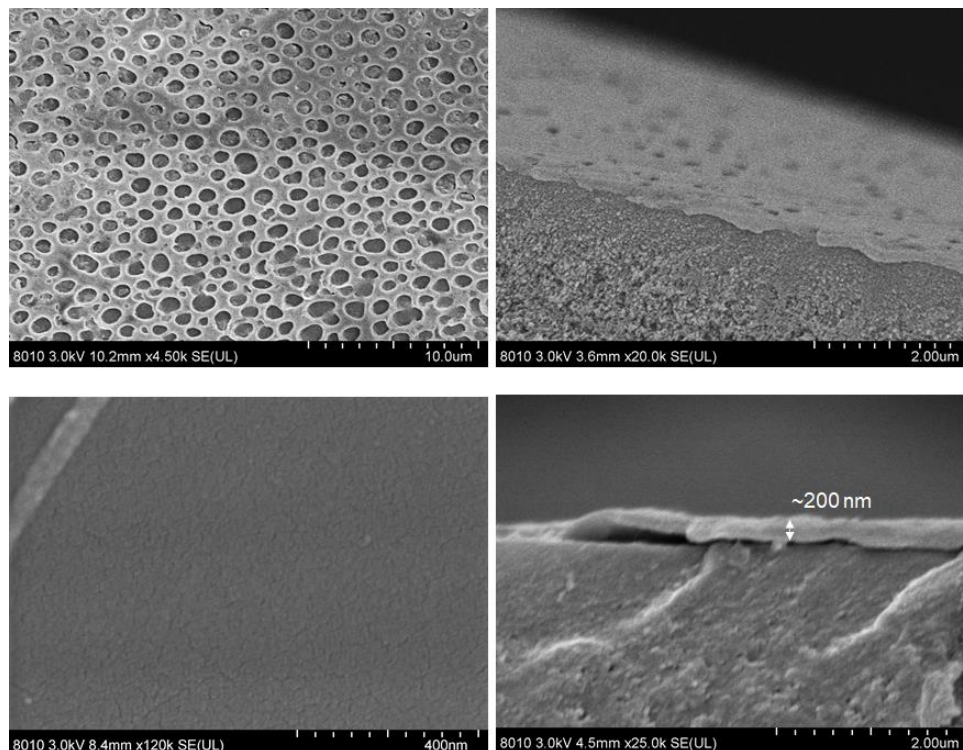


Figure 7.8. SEM images of 1 wt% PIM-1 coated Torlon® hollow fibers drawn at a rate of $2 \text{ m}\cdot\text{min}^{-1}$ from a bath of 50-50 wt% chloroform and trichloroethylene (top row) and 50-50 wt% chloroform and 1,1,2,2-tetrachloroethane (bottom row). Images of the surface are shown in the left column while images of the cross-section are shown in the right column.

7.5 Thin Film Composite Separation Analysis

As was seen in Figure 7.4, Trial 2 Torlon® support fibers showed an initial toluene liquid permeance of $\sim 0.31 \text{ Lm}^{-2}\text{h}^{-1}\text{bar}^{-1}$, which decreased to $\sim 0.04 \text{ Lm}^{-2}\text{h}^{-1}\text{bar}^{-1}$ over a

period of 48 hours. Such a sharp decrease in permeance indicates compression of large voids in the membrane, which could be due to the large macrovoids observed in Figure 7.3. This macrovoid formation is thought to be caused by fast solvent-nonsolvent exchange in the nascent fiber. Researchers have shown the appearance of macrovoids at low fiber take-up speeds and low polymer concentrations during spinning.(21, 29) It is thought that higher fiber-draw speeds cause a rapid decrease in diameter of the nascent fiber and, thus, a radial outflow of solvents which slows non-solvent intrusion into the fiber during phase inversion. The spinning dope also tends to be more viscous at higher polymer concentrations, slowing the solvent exchange rate. Thus, by decreasing both polymer content and the fiber draw rate in Trial 2, the resulting fibers became more susceptible to macrovoid formation.

The initial toluene permeance of $0.31 \text{ Lm}^{-2}\text{h}^{-1}\text{bar}^{-1}$ is lower than the permeance expected for a PIM-1 film with a nano-scale thickness ($>1 \text{ Lm}^{-2}\text{h}^{-1}\text{bar}^{-1}$).(13). So we may turn to gas separations to determine the quality of the thin-film composites. Calculating He/N₂ selectivity via pure gas permeation measurements is a standard method to assess the quality of membranes. Based on previous gas studies, PIM-1 thin films with a thickness of 200 nm are expected to have helium permeance of around 3000 GPU.(30, 31) and, in general, PIM-1 films will have a He/N₂ selectivity higher than 4.5.(32). The helium permeance of the Torlon® support varied widely between 250 – 1000 GPU, so determining the film quality via gas permeance may also be challenging. This wide range in permeances is usually uncommon and could be traced to the solvent exchange process where the fibers were cut into 20-meter spools instead of short lengths ($< 0.5 \text{ m}$), thereby decreasing the rate at which solvent exchange occurred. The solvent exchange process must be modified to reduce the external mass transfer resistance either via agitation of the nonsolvent bath,

quick movement of the spools within the bath, or more frequent replenishment of the nonsolvent. Table 7.2 summarizes the gas separation analyses of PIM-1 coated samples. All samples showed He/N₂ selectivity closer to the Knudsen value of 2.3, indicating that either a) the PIM-1 thin films are defective or b) the support resistance is limiting transport in the topcoat. Further development of the support morphology is required to decrease the transport resistance and confidently evaluate the quality of PIM-1 thin film coatings via gas or liquid permeation.

Table 7.2. Summary of gas separation analyses of PIM-1 coated Torlon® thin-film composites.

	Helium Permeance (GPU)	Nitrogen Permeance (GPU)	He/N ₂ Selectivity
1 wt% PIM-1/CHCl ₃ coated	834 ± 585	477 ± 397	1.90 ± 0.30
1 wt% PIM-1/50-50 CHCl ₃ C ₂ H ₂ Cl ₄ coated	5045 ± 3755	2525 ± 1768	1.96 ± 0.12

7.6 Conclusions

PIM-1 thin-film composites were created via continuous roll-to-roll dip coating on Torlon® hollow fiber supports with 10 nm surface pores. Micron-sized craters within the PIM-1 coating were eliminated by increasing the boiling point of the coating solution and decreasing the evaporation rate of the solvent so that the surface force exerted by the drying solvent on the soft film was minimized. Although the Torlon® supports were created with the desired surface pores, the gas and liquid permeances were either lower than or within the range of the expected PIM-1 thin-film values, so the quality of the thin film coating could not be accurately analyzed. Future work will focus on modifying the support formation so that the transport resistance is considerably reduced, and it can be determined whether the PIM-1 coatings are defect-free and reproducible.

7.7 References

1. R. W. Baker, *Advanced membrane technology and applications*. N. N. F. Li, A. G.; Winston Ho, W. S.; Matsuura, T., Ed., (Wiley, Hoboken, N.J., 2008).
2. I. Jesswein, T. Hirth, T. Schiestel, Continuous dip coating of PVDF hollow fiber membranes with PVA for humidification. *J Membrane Sci* **541**, 281-290 (2017).
3. M. E. Ivanova *et al.*, Lanthanum tungstate membranes for H₂ extraction and CO₂ utilization: Fabrication strategies based on sequential tape casting and plasma-spray physical vapor deposition. *Sep Purif Technol* **219**, 100-112 (2019).
4. Y. Ohta *et al.*, Development of pore size-controlled silica membranes for gas separation by chemical vapor deposition. *J Membrane Sci* **315**, 93-99 (2008).
5. E. K. McGuinness, F. Y. Zhang, Y. Ma, R. P. Lively, M. D. Losego, Vapor Phase Infiltration of Metal Oxides into Nanoporous Polymers for Organic Solvent Separation Membranes. *Chem Mater* **31**, 5509-5518 (2019).
6. M. Weber, A. Julbe, A. Ayral, P. Miele, M. Bechelany, Atomic Layer Deposition for Membranes: Basics, Challenges, and Opportunities. *Chem Mater* **30**, 7368-7390 (2018).
7. C. J. Brinker, G. C. Frye, A. J. Hurd, C. S. Ashley, Fundamentals of Sol-Gel Dip Coating. *Thin Solid Films* **201**, 97-108 (1991).
8. S. Bequet *et al.*, From ultrafiltration to nanofiltration hollow fiber membranes: a continuous UV-photografting process. *Desalination* **144**, 9-14 (2002).
9. H. Z. Chen, Y. C. Xiao, T. S. Chung, Multi-layer composite hollow fiber membranes derived from poly(ethylene glycol) (PEG) containing hybrid materials for CO₂/N₂ separation. *J Membrane Sci* **381**, 211-220 (2011).
10. L. Gao, M. Alberto, P. Gorgojo, G. Szekely, P. M. Budd, High-flux PIM-1/PVDF thin film composite membranes for 1-butanol/water pervaporation. *J Membrane Sci* **529**, 207-214 (2017).
11. C. Z. Liang, J. T. Liu, J. Y. Lai, T. S. Chung, High-performance multiple-layer PIM composite hollow fiber membranes for gas separation. *J Membrane Sci* **563**, 93-106 (2018).
12. H. Y. Zhao, L. Z. Feng, X. L. Ding, X. Y. Tan, Y. Z. Zhang, Gas permeation properties of a metallic ion-cross-linked PIM-1 thin-film composite membrane supported on a UV-cross-linked porous substrate. *Chinese J Chem Eng* **26**, 2477-2486 (2018).

13. M. Cook, P. R. J. Gaffney, L. G. Peeva, A. G. Livingston, Roll-to-roll dip coating of three different PIMs for Organic Solvent Nanofiltration. *J Membrane Sci* **558**, 52-63 (2018).
14. W. F. Yong, F. Y. Li, T. S. Chung, Y. W. Tong, Highly permeable chemically modified PIM-1/Matrimid membranes for green hydrogen purification. *Journal of Materials Chemistry A* **1**, 13914-13925 (2013).
15. H. Y. Jang *et al.*, Torlon (R) hollow fiber membranes for organic solvent reverse osmosis separation of complex aromatic hydrocarbon mixtures. *Aiche J* **65**, (2019).
16. S. Wickramanayake *et al.*, Mechanically robust hollow fiber supported ionic liquid membranes for CO₂ separation applications. *J Membrane Sci* **470**, 52-59 (2014).
17. P. Marchetti, M. F. J. Solomon, G. Szekely, A. G. Livingston, Molecular Separation with Organic Solvent Nanofiltration: A Critical Review. *Chem Rev* **114**, 10735-10806 (2014).
18. M. R. Kosuri, W. J. Koros, Defect-free asymmetric hollow fiber membranes from Torlon®, a polyamide-imide polymer, for high-pressure CO₂ separations. *J. Membr. Sci.* **320**, 65-72 (2008).
19. A. A. Rownaghi, D. Bhandari, S. K. Burgess, D. S. Mikkilineni, Effects of coating solvent and thermal treatment on transport and morphological characteristics of PDMS/Torlon composite hollow fiber membrane. *J Appl Polym Sci* **134**, (2017).
20. V. P. Babu, W. J. Koros, The role of polyvinylpyrrolidone in forming open-porous, macrovoid-free mixed matrix sorbents from Torlon((R)), a polyamide-imide polymer. *Polym Eng Sci* **58**, 2106-2114 (2018).
21. N. Peng, T. S. Chung, K. Y. Wang, Macrovoid evolution and critical factors to form macrovoid-free hollow fiber membranes. *J Membrane Sci* **318**, 363-372 (2008).
22. D. Quere, Fluid coating on a fiber. *Annu Rev Fluid Mech* **31**, 347-384 (1999).
23. M. Faustini, B. Louis, P. A. Albouy, M. Kuemmel, D. Grosso, Preparation of Sol-Gel Films by Dip-Coating in Extreme Conditions. *J Phys Chem C* **114**, 7637-7645 (2010).
24. J. N. Israelachvili, *Intermolecular and surface forces : with applications to colloidal and biological systems*. (Academic Press, London ; Orlando, Fla . 1985), pp. xv, 296 p.

25. D. Quere, J. M. Dimeglio, F. Brochardwyart, Making Vanderwaals Films on Fibers. *Europhys Lett* **10**, 335-340 (1989).
26. P. Gorgojo *et al.*, Ultrathin Polymer Films with Intrinsic Microporosity: Anomalous Solvent Permeation and High Flux Membranes. *Adv Funct Mater* **24**, 4729-4737 (2014).
27. A. de Ryck, D. Quere, Fluid coating from a polymer solution. *Langmuir* **14**, 1911-1914 (1998).
28. I. Borisov *et al.*, Synergistic enhancement of gas selectivity in thin film composite membranes of PIM-1. *Journal of Materials Chemistry A* **7**, 6417-6430 (2019).
29. K. Y. Wang, D. F. Li, T. S. Chung, S. B. Chen, The observation of elongation dependent macrovoid evolution in single and dual-layer asymmetric hollow fiber membranes. *Chem Eng Sci* **59**, 4657-4660 (2004).
30. P. M. Budd *et al.*, Gas separation membranes from polymers of intrinsic microporosity. *J Membrane Sci* **251**, 263-269 (2005).
31. M. L. Jue, V. Breedveld, R. P. Lively, Defect-free PIM-1 hollow fiber membranes. *J Membrane Sci* **530**, 33-41 (2017).
32. C. A. Scholes, S. Kanehashi, Polymer of Intrinsic Microporosity (PIM-1) Membranes Treated with Supercritical CO₂. *Membranes-Basel* **9**, (2019).

CHAPTER 8. CONCLUSIONS AND FUTURE WORK

8.1 Overview

This chapter discusses the major conclusions and impacts of the undertaken research related to novel spirocyclic materials for membrane-based liquid hydrocarbon separations. Critical needs for advancing research in the field of complex mixture separations, liquid hydrocarbon transport predictions and continuous coating to form large-scale thin film composites are also identified.

8.2 Conclusions and Impacts

The work presented in this dissertation focused on new polymeric materials for membrane-based separations of complex hydrocarbon mixtures such as crude oil. A series of spirocyclic polymers were created with N-aryl linkages, inspired by gas separation principles, and applied to OSN/OSRO applications. The resulting polymers exhibited enabling features for OSRO separations: non-interconnected porosities and a resistance to swelling in the presence of common polymeric plasticizers like CO₂ and toluene. The polymers' solution-processability make them attractive options for commercial membrane fabrication processes. Additionally, the glassy nature and the thermal stability of the polymers are enablers for the separation of crude oil mixtures which can be extremely viscous and will likely require high temperatures to enhance the separation productivity.

Two main spirocyclic polymers in the novel series were identified as having the most favorable separation performance characteristics for crude oil applications. SBAD-1 and DUCKY-9 were capable of low MWCOs (300-400 g·mol⁻¹) in toluene as well as good

separation factors for liquid hydrocarbons in the 100 - 350 g-mol⁻¹ range. Separations of 100 – 350 g-mol⁻¹ solutes from ~90% toluene were conducted at room temperature with a permeance of 0.15 Lm⁻²h⁻¹bar⁻¹ SBAD-1 and 0.39 Lm⁻²h⁻¹bar⁻¹ for DUCKY-9. On the other hand, the separation of shale-based crude oil was conducted at 130 °C with a permeance of 0.016 Lm⁻²h⁻¹bar⁻¹ for SBAD-1 and 0.012 Lm⁻²h⁻¹bar⁻¹ for DUCKY-9. Although the shale-based separations were observed to occur with sharp carbon cutoffs, the permeances are much lower when compared with commercial membranes for aqueous applications.⁽¹⁾ The complexity of the crude streams is responsible for non-ideal coupling forces that retard transport through the membranes and, even at high temperatures, result in low permeances. Future work must focus on increasing the productivity of these types of polymeric materials, either through further iterations of polymer structural design or optimization of membrane fabrication and morphologies.

A transport framework for complex liquid hydrocarbon mixtures in glassy polymers (SBAD-1 and PIM-1) is developed in this work. Using several sorption and diffusion model assumptions within Maxwell-Stefan flux equations, the prediction of three complex separations was attempted. The results showed that reasonable predictions of transport could be made with the Flory-Huggins sorption model and a newly proposed sorption model that combines Langmuir hole-filling and Flory-Huggins lattice interactions between polymers and solvents. It was identified that the manipulation of solvent-solvent diffusion coefficients made negligible improvements in transport predictions. However, the adjustment of solvent-polymer diffusivities with changes in the free volume of the glassy polymers due to solvent-induced swelling brought the transport predictions closer to the experimentally measured data. In another case, good predictions were obtained with

simplifications to the description of solvent-polymer diffusion; it was assumed that the similarly-sized hydrocarbon molecules are transported as a cohort and therefore, diffuse with an average diffusivity parameter. Based on this description, the separations could be viewed as being dominated by thermodynamic and solubility-based driving forces.

While the fractionation of shale-based crude mixtures was demonstrated through flat sheet thin film composites, the commercialization of new polymeric materials requires high productivities and therefore, large membrane surface areas. Due to their high surface area to volume ratios, hollow fiber membranes are often considered the pinnacle in a lab-scale membrane development process. As such, the continuous production of thin film composite hollow fibers of the spirocyclic polymer, PIM-1 was attempted. Torlon® was formed via dry-wet spinning into continuous, porous support fibers that could withstand the tension and bending in the continuous roll-to-roll dip coating process. Continuous thin films of PIM-1 were created by controlling the coating solvent evaporation and eliminating the occurrence of craters that often penetrate the entire thickness of the thin films. Such continuously processed fibers pave the way for the fabrication of large membrane modules with high surface areas and the processing of high throughput feeds.

8.3 Future Work

8.3.1 Long-term Membrane Performance in Natural Crude Streams

Widely considered the only successful membrane application in crude refining at a commercial scale, the MAX-DEWAX process was hailed as an energy-efficient method of recovering dewaxing solvent while providing higher yields of lube oil. This process is no longer in operation as refineries shifted to a catalytic cracking process that did not require

the dewaxing step.(2) While in operation at Exxon Mobil's Beaumont, Texas refinery, it boasted a 35% increase in lube oil production along with a 20,000 tons/year reduction of greenhouse gas emissions.(3) Additionally, the payback of the capital invested in the membrane process unit was less than one year. The polymer's resistance to swelling or dissolving in organic solvents was considered one of the key factors behind the success of this membrane. However, the successful commercial implementation of this membrane was only achievable after extensive long-term process studies. A one-year laboratory study and a three-year pilot plant operation were required to prove superior economic and environmental benefits before commercialization was approved. Even so, during the first year of commercial application, the permeate flow rate decreased by half before reaching a somewhat consistent flow rate during the second year. Such a performance decrease over time due to compression or fouling is one of the reasons that polymer membranes face hindrances to scale-up.(4) The path to commercialization of membrane materials requires a thorough understanding of long-term performance, and a consideration for the possibility of changing crude oil feeds.

The aging of PIMs has been tested extensively at ambient conditions. When stored in air, the gas permeability of PIMs generally continues to decrease over a period of a few years while the selectivity increases due to a gradual increase in chain packing to the equilibrium state of the polymer.(5-7) Such aging tests are less common for liquid separations, but one can assume that organic solvents, which typically swell PIMs, will undo the effects of aging during storage.(8) Therefore, a greater concern is aging during on-stream application. In the case of thin film composites, there is also a concern about the change in quality of the underlying support, especially for high-pressure OSRO

applications. The underlying support must maintain sufficient porosity and adhesion to the topcoat to ensure consistent performance. In Chapter 5, a consistent 2-month performance of SBAD-1 thin film composites was demonstrated in synthetic naphtha + kerosene (9-hydrocarbon) mixtures, suggesting that any compression that the support may experience is not detrimental to the thin film composite performance. However, future work should focus on the onstream performance of membrane candidates for at least a year in natural crude mixtures that contain small amounts of heavy polyaromatic molecules, trace metals and sulfur-containing compounds which are thought to potentially foul polymeric membranes and decrease their productivity.⁽⁹⁾ Moreover, feed properties such as metal content, sourness (sulfur content) and viscosity depend heavily on the source of crude oil used.^(10, 11) SBAD-1 and DUCKY-9 must be tested in extreme ranges of sulfur content and feed density to understand the limits of the materials and demonstrate the versatility of the novel polymer membranes, especially over long exposure periods.

8.3.2 *Extending the Modelling of OSRO/OSN to Natural Crude Oil Feeds*

The Maxwell-Stefan approach for predicting the separation of a complex system of hydrocarbons can be extended from the 9-component feed demonstrated in Chapter 6 to more complex feeds and even naturally occurring 1000+ component feeds such as crude oil. The molecules in such mixtures could be categorized by class (aliphatic, aromatic, naphthene, etc.) such that the sorption isotherms that are required for the model could be estimated theoretically. One simplification is assuming all molecules follow the Flory-Huggins sorption behaviour in polymers, which is easier to parametrize than other sorption models and is shown in Chapter 6 to lead to successful transport predictions. Then, solvent-polymer interaction parameter (χ_{ip}) can be estimated (instead of painstakingly measured)

using the Hildebrand and Scott equation for a nonpolar solvent and a nonpolar polymer(12):

$$\chi_{ip} = \frac{V_i(\delta_p - \delta_i)^2}{RT} + \beta \quad \mathbf{8.1}$$

where V_i is the liquid molar volume of the solvent, and δ_p and δ_i are the Hildebrand solubility parameters for the polymer and solvent. β is the lattice parameter and can be set as 0.34 for most polymer systems. With this equation, the sorption is a function of both the polarity/chemical structure (solubility parameter) and the size of the molecule (molar volume) of interest. An alternate and more accurate method for estimating the Flory interaction parameter is to use the Hansen solubility theory(12):

$$\chi_{ip} = \frac{V_i}{RT} \left[(\delta_{D,i} - \delta_{D,p})^2 + 0.25(\delta_{P,i} - \delta_{P,p})^2 + 0.25(\delta_{H,i} - \delta_{H,p})^2 \right] \quad \mathbf{8.2}$$

where δ_D , δ_P , and δ_H are the Hansen solubility parameters for dispersion (Van der Waals), polarity and hydrogen bonding. A constant, α , typically precedes the equation and it is fit to experimental data at different concentrations.(13) However, as a first pass, an approximate value of 1 can be assumed.

In addition to sorption of solvents in glassy polymers, the diffusivity of all molecules in the polymer would have to be estimated to employ the Maxwell-Stefan framework. At a specified temperature, the diffusion of penetrants through a glassy polymer is a function of the solvent's molar volume and its total occupied volume in the polymer system. As a first pass, the concentration dependence may be ignored and it may be assumed that the

diffusion is merely a function of the liquid molar volume and the free volume in the polymer according to the free volume theory used by gas separation researchers to predict glassy polymer permeability(14):

$$D_{ip} = A_i \exp\left(-\frac{B_i}{v_F}\right) \quad 8.3$$

where A_i is a molecule-polymer system dependent constant, B_i is a molecule-dependent constant and is related with the molecule size, and v_F is the polymer free volume. The polymer free volume can be estimated from skeletal density and bulk density measurements while A_i and B_i can be fit to a small set of solvents first before additional simplifying assumptions can be made for a larger set of solvents. Among other requirements, the framework must also be able to accommodate the computation of N molecules within a reasonable amount of time and the numerical methods employed in the simulation must be optimized to do so.

8.3.3 *Optimizing the Torlon® Support Fiber Structure*

As demonstrated in Chapter 7, the underlying hollow fiber support in a thin film composite membrane must be sufficiently optimized before successful application in high-pressure separations. It is vital to show a consistent and long-term high support permeance that does not limit transport in the topcoat. The effects of support compaction are immediately obvious in the Torlon® hollow fiber supports fabricated in Chapter7. The main reasons for this may be the presence of macrovoids and low polymer content in the fiber that weaken the integrity of the membrane. Reducing the polymer content in the spinning dope was initially identified as a route for creating surface pores on the support

(for sufficient permeation through Torlon®). While reducing the Torlon® polymer content to 18 wt% did enable the creation of surface pores, it rendered the support incapable of long-term permeation. Therefore, future work must focus on eliminating macrovoids while maintaining surface pores such that the gas and liquid permeabilities are increased by at least 10 times and do not decrease significantly over time. This may be possible by increasing the polymer content in the dope to 25 wt% and decreasing the fiber draw rate until surface pores have been obtained but before macrovoids start to form.(15)

8.3.4 Roll-to-Roll Coating of SBAD-1 and MALLARD

Following the demonstration of continuous coating of PIM-1 on a porous polymer substrate, it is of interest to extend the learnings to novel spirocyclic polymers. SBAD-1 and DUCKY-9, the candidates, recognized in Chapter 5 for complex liquid hydrocarbon separations, are expected to behave somewhat similarly to PIM-1 in the roll-to-roll coating process. This is assuming the polymer molecular weights are sufficiently high (>40,000 g/mol) to form films without cracking. It is important to note that the viscosity of the polymer solutions, and therefore the thickness of the films will be strongly dependent on the polymer molecular weight, which in turn can vary with the batch of synthesis. The viscosities of PIM-1, SBAD-1, and MALLARD are shown in Figure 8.1. MALLARD is a new spirocyclic polymer created by Dr. Nicholas Bruno (Georgia Tech, Department of Chemistry). It combines the characteristics of SBAD-1 and DUCKY-9 that give both polymers superior performance in liquid hydrocarbon separations: a more rigid spirocycle and a bulky, rigid linking group. It is apparent from Figure 8.1 that the viscosities are dependent on molecular weight and tend to be greater for polymers with higher number-based molecular weights and higher polydispersity indices (higher branching of chains).

The differential increase in viscosity with respect to concentration is also observed to be higher in these cases. This observation has important implications in the differences across polymer coatings and in controlling the thickness of desired thin film composite membranes as the film thickness is a direct function of solution viscosity and will ultimately impact the productivity of the membranes.

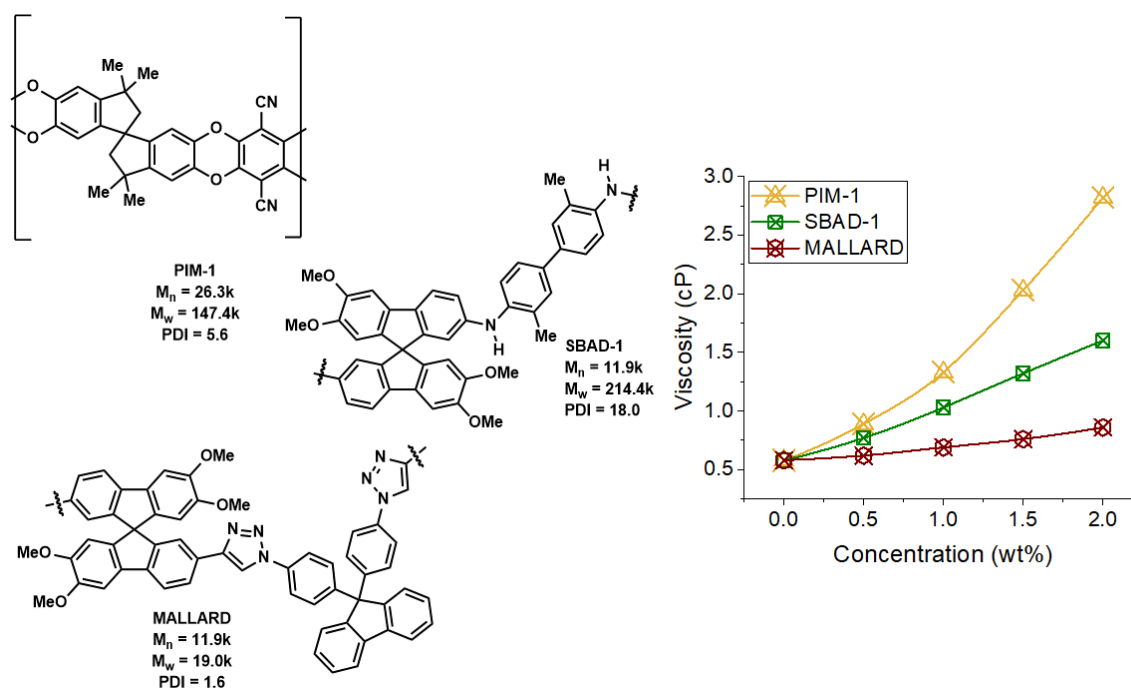


Figure 8.1. Comparison of the viscosity of PIM-1, SBAD-1 and MALLARD in chloroform solutions at 22 °C.

8.4 References

1. Z. Yang *et al.*, A Review on Reverse Osmosis and Nanofiltration Membranes for Water Purification. *Polymers-Basel* **11**, (2019).
2. M. Priske, M. Lazar, C. Schnitzer, G. Baumgarten, Recent Applications of Organic Solvent Nanofiltration. *Chem-Ing-Tech* **88**, 39-49 (2016).
3. R. M. Gould, L. S. White, C. R. Wildemuth, Membrane separation in solvent lube dewaxing. *Environ Prog* **20**, 12-16 (2001).
4. G. M. Shi, M. H. D. A. Farahani, J. Y. Liu, T. S. Chung, Separation of vegetable oil compounds and solvent recovery using commercial organic solvent nanofiltration membranes. *J Membrane Sci* **588**, (2019).
5. P. Bernardo *et al.*, Effect of physical aging on the gas transport and sorption in PIM-1 membranes. *Polymer* **113**, 283-294 (2017).
6. R. R. Tiwari, J. Y. Jin, B. D. Freeman, D. R. Paul, Physical aging, CO₂ sorption and plasticization in thin films of polymer with intrinsic microporosity (PIM-1). *J Membrane Sci* **537**, 362-371 (2017).
7. C. G. Bezzu *et al.*, The synthesis, chain-packing simulation and long-term gas permeability of highly selective spirobifluorene-based polymers of intrinsic microporosity. *Journal of Materials Chemistry A* **6**, 10507-10514 (2018).
8. M. L. Jue, C. S. McKay, B. A. McCool, M. Finn, R. P. Lively, Effect of Nonsolvent Treatments on the Microstructure of PIM-1. *Macromolecules* **48**, 5780-5790 (2015).
9. B. L. S. H.E. Johnson, "Assessment of the potential for refinery applications of inorganic membrane technology - an identification and screening analysis," (U.S. Department of Energy, Assistant Secretary for Fossil Energy, 1993).
10. U. S. E. I. Administration, Crude oils have different quality characteristics. *Energy Intelligence Group—International Crude Oil Market Handbook*. July 2012.
11. U. S. E. I. Administration, Attributes of crude oil at U.S. refineries vary by region. *Petroleum Navigator*. September 2012.
12. C. M. Hansen, *Hansen solubility parameters : a user's handbook*. (CRC Press, Boca Raton, Fla., 2000), pp. 208 p.
13. T. Lindvig, M. L. Michelsen, G. M. Kontogeorgis, A Flory-Huggins model based on the Hansen solubility parameters. *Fluid Phase Equilibria* **203**, 247-260 (2002).

14. L. Ansaloni, L. Deng, Advances in polymer-inorganic hybrids as membrane materials. *Woodhead Publ Mater*, 163-206 (2017).
15. N. Peng, T. S. Chung, K. Y. Wang, Macrovoid evolution and critical factors to form macrovoid-free hollow fiber membranes. *J Membrane Sci* **318**, 363-372 (2008).